

DAMAGE AND FAILURE OF NON-CONVENTIONAL COMPOSITE  
LAMINATES



DAMAGE AND FAILURE OF NON-CONVENTIONAL COMPOSITE  
LAMINATES

Proefschrift

ter verkrijging van de graad van doctor  
aan de Technische Universiteit Delft,  
op gezag van de Rector Magnificus prof. dr. ir. J. T. Fokkema,  
voorzitter van het College voor Promoties  
in het openbaar te verdedigen op dinsdag 23 juni 2009 om 10:00 uur

door Cláudio Saúl FARIA LOPES  
ingenieur Luchtvaart en Ruimtevaart  
geboren te Leiria, Portugal

Dit proefschrift is goedgekeurd door de promotoren:

Prof. dr. Z. Gürdal

Prof. dr. P. P. Camanho

Samenstelling promotiecommissie:

Rector Magnificus, voorzitter

Prof. dr. Z. Gürdal, Technische Universiteit Delft, promotor

Prof. dr. P. P. Camanho, Universidade do Porto, Portugal, promotor

Prof. dr. ir. L. J. Sluys, Technische Universiteit Delft

Prof. dr. P. A. Lagace, Massachusetts Institute of Technology, U.S.A.

Prof. dr. A. Torres Marques, Universidade do Porto, Portugal

Reservelid:

Prof. dr. ir. A. Rothwell, Technische Universiteit Delft

The elaboration of this thesis was financed by the *Fundação para a Ciência e a Tecnologia*, in Portugal, through the scholarship SFRH/BD/16238/2004, and by the Delft University of Technology.

Publisher: TU Delft, Faculteit Luchtvaart- en Ruimtevaarttechniek

Printed by: Ipskamp Drukkers, Enschede

ISBN/EAN 978-90-9024343-6

Keywords: Automated Fibre Placement, Variable-Stiffness Panels, Failure Criteria, Progressive Failure Analyses, Impact Damage, Damage Tolerance

Copyright 2009 by Cláudio Lopes. All rights reserved. No part of this publication may be reproduced, stored in a retrieval system, or transmitted in any form or by any means, electronic, mechanical, photocopying, recording or otherwise, without permission in writing from the author.

*to Ana and Miguel*



# Summary

THE 1960's saw the first-steps in the development of advanced composite materials and their exploitation by aeronautical engineers. In the following decades, composite laminates grew their importance in the aerospace industry but their potential as credible alternatives to the materials in use (e.g. aluminium), has been hampered mainly by (i) an insufficient practical knowledge about their structural behaviour, especially in terms of damage and failure, and (ii) an inefficient manual based production process resulting in limited part quality. As such, for a long time, the application of composite materials was restricted to military aircraft and secondary structures of commercial aircraft. Furthermore, the design possibilities offered by composite laminates were narrowed to quasi-isotropic configurations due to their closer behaviour with monolithic materials, hence with a more predictable response, and easiness of manufacturing. However, this picture is changing. Nowadays, there are automated systems capable of rapidly manufacturing large and high quality composite parts. As an example, the fuselage of the all-new long haul Boeing 787 aircraft is being built by means of Automated Fibre-Placement (AFP) machines. These highly precise systems can build laminates made of combinations of ply angles other than the conventional  $0^\circ$ ,  $90^\circ$  and  $\pm 45^\circ$ . Furthermore, AFP machines can steer the fibre tows as these are being placed, resulting in plies with variable fibre orientation and laminates whose elastic properties vary along their planar coordinates, termed *variable-stiffness panels*. In this thesis, the expression *non-conventional (composite) laminates* refers to straight-fibre laminates made of combinations of non-conventional ply angles as well as to variable-stiffness panels.

The structural behaviour of non-conventional composites is not fully understood yet, particularly their damage and failure responses. The goal of this thesis is to shed light on this field.

The stiffness and buckling properties of variable-stiffness panels have been studied in the past 10 to 15 years by means of analytical, numerical and experi-

mental approaches. In these investigations, the performance of the most promising fibre-steered designs was proven to largely exceed that of the best conventional configurations. Such results were attributed to favourable stress distributions within a given loaded panel, i.e. the curvature of the fibres has the potential to redirect the applied loads to the supported edges of the panel, hence avoiding the central sections which are critical for the buckling event. In this thesis it is demonstrated that this is not the only relevant mechanism. The superior performance of variable-stiffness panels is also due to favourable residual thermal stresses developed during the laminate curing process due to the curvature of the fibres.

This thesis also addresses the damage initiation, progression and final failure behaviour of variable-stiffness panels by means of physically sound numerical methods. These analyses include buckling considerations. The simulations are correlated with experimental tests described in the literature, with very good results. The strength of variable-stiffness panels is proven to be largely superior to that of conventional designs, however this difference is not as promising as the gains that can be achieved in terms of buckling resistance. Furthermore, it is demonstrated that it is possible to design fibre-steered panels which are insensitive to central holes.

The manufacturing of variable-stiffness panels imposes either the overlapping of some fibre tows within a ply or their cutting (dropping). While the tow-overlapping method results in local increases of the panel thickness, the tow-dropping method generates fibre-free, resin-rich regions in the laminates. Both methods have negative effects on the failure response of the structures when compared with idealised designs. However, they can be mitigated by staggering adjacent plies with similar fibre distributions, hence smearing these local ‘incidents’ across the planform, or by adopting hybrid configurations (laminates with both straight and curvilinear fibre plies).

Regarding non-conventional laminates with straight-fibres, the interest is to investigate if the dispersion of the traditional  $0^\circ$ ,  $90^\circ$  and  $\pm 45^\circ$  based lay-up over the whole  $0^\circ - 90^\circ$  range of possible fibre angles, and the avoidance of ply clustering (adjacent plies equally oriented), have some effect on their out-of-plane loading response. This investigation is also relevant for variable-stiffness panels which typically have a dispersed stacking sequence at each planar location.

The results of low-velocity impact and compression-after-impact tests revealed that the dispersion of the stacking sequence neither increases the impact resistance nor the damage tolerance of laminates. On the contrary, the compressive residual strength of impacted non-conventional laminates is most likely reduced



---

in comparison with their traditional counterparts. This is because ply clustering can divert major delaminations from occurring at the innermost interfaces of impacted specimens, which would otherwise be divided in sublaminates with overall less resistance to compressive loads. Reliable numerical models of the low-velocity impact experiments, accounting for the simulation of delaminations and intraply damage modes, predict that laminates with clustered plies can dissipate relatively less energy through delaminations, at the expense of energy dissipated by means of matrix cracking and fibre breakage, than their non-conventional counterparts. This is an added reason for their superior performance given that under compression, laminates are typically more tolerant to intraply damage modes (in general more localised around the impact area) than to delaminations.

Future research should focus on the global impact response of variable-stiffness panels, which looks more promising than the local effects of their stacking sequence dispersion.



# Samenvatting

In de jaren 60 van de 20e eeuw werden de eerste ontwikkelingen in geavanceerde composieten materialen en hun gebruik door luchtvaartingenieurs waargenomen. In de daaropvolgende decennia werden composiet laminaten steeds belangrijker in de luchtvaartindustrie, hoewel hun potentieel als geloofwaardige alternatief voor de gebruikte materialen (bv aluminium) voornamelijk werd belemmerd door (i) onvoldoende praktische kennis over hun structurele gedrag, vooral in termen van schade en bezwijking, en (ii) inefficiënte handmatige productieprocessen resulterend in kwalitatief slechte producten. Hierdoor was de toepassing van composiet materialen voor lange tijd beperkt tot militaire vliegtuigen en secundaire constructies in commerciële vliegtuigen. Verder waren de ontwerp mogelijkheden voor composiet laminaten beperkt tot quasi-isotrope configuraties omdat hun gedrag meer lijkt op dat van monolitische materialen, waardoor hun gedrag makkelijker is te voorspellen, en omdat ze makkelijker zijn te fabriceren. Maar dit beeld is aan het veranderen. Tegenwoordig zijn er geautomatiseerde systemen die snel grote composieten onderdelen met hoge kwaliteit kunnen maken. De romp van het nieuwe lange afstandsvliegtuig Boeing 787 is bijvoorbeeld gemaakt door Automated Fiber Placement (AFP) machines. Deze hoge precisie systemen kunnen laminaten produceren die zijn opgebouwd uit lamina met hoeken die afwijken van de traditionele  $0^\circ$ ,  $90^\circ$  en  $\pm 45^\circ$ . Bovendien kunnen AFP machines de vezelbanden sturen terwijl ze worden geplaatst, resulterend in lagen met varierende vezelorientaties en laminaten wiens elastische eigenschappen variëren met vlakke coördinaten, genaamd variabele stijfheidspanelen. In deze dissertatie verwijst de uitdrukking niet-conventionele composiet laminaten zowel naar laminaten met rechte vezels samengesteld uit lagen met niet-conventionele vezelhoeken, als naar variabele stijfheidspanelen.

Het structurele gedrag van niet-conventionele composieten wordt niet volledig begrepen, vooral hun schade en bezwijkgedrag. Het doel van deze dissertatie is om een beter inzicht in deze onderwerpen te verkrijgen.

De stijfheid- en knikeigenschappen van variabele stijfheidspanelen is in de afgelopen 10 tot 15 jaar bestudeerd met analytische, numerieke en experimentele methoden. In deze onderzoeken is bewezen dat de prestaties van de meest veelbelovende gestuurde vezelontwerpen die van de conventionele configuraties overtroffen. Deze resultaten worden verkregen door de gunstige spanningsverdeling in het belaste paneel, dat wil zeggen: de kromming van de vezels kan de toegepaste belasting naar de ondersteunde randen van het paneel sturen, waardoor knik in het meest kritische deel (het midden) van de plaat wordt voorkomen. In deze thesis wordt gedemonstreerd dat dit niet het enige mechanisme is dat meespeelt. De superieure prestaties van variabele stijfheidspanelen wordt mede veroorzaakt door gunstige thermische restspanningen die tijdens het uithardproces door de gekromde vezels ontstaan.

Deze dissertatie adresseert ook de schade initiatie, de schade voortgang en het bezwijkgedrag van variabele stijfheidspanelen door middel van fysisch correcte numerieke methoden. Deze analyses omvatten knikbeschouwingen. De simulaties worden vergeleken met experimenten beschreven in de literatuur, met zeer goede correlaties. Er is aangetoond dat de sterkte van variabele stijfheidspanelen superieur is ten opzichte van conventionele ontwerpen, hoewel het verschil niet zo veelbelovend is als de verbeteringen die in knik worden behaald. Verder is aangetoond dat het mogelijk is om vezelgestuurde panelen te ontwerpen die ongevoelig zijn voor centraal gepositioneerde gaten.

Het fabriceren van variabele stijfheidspanelen resulteert in panelen die f overlappende tows (vezelstrips) hebben f tows die afgeknipt zijn. Terwijl het overlappen van tows resulteert in lokale toenames van de paneeldikte, genereert het afknippen van tows lokale vezelvrije, matrixrijke gebieden in het laminaat. Beide methoden hebben negatieve effecten op het bezwijkgedrag van constructies vergeleken met gedealiseerde ontwerpen. De invloed kan echter beperkt worden door aangrenzende lagen met gelijksoortige vezelhoekverdelingen ten opzichte van elkaar te verschuiven, zodat deze lokale 'verstoringen' over het oppervlak worden uitgesmeerd, f door een hybride configuratie te gebruiken (laminaten met zowel rechte als gekromde vezellagen).

Betreffende niet-conventionele laminaten met rechte vezels is het interessant om te onderzoeken of uitbreiding van de vezelhoeken van de traditionele  $0^\circ$ ,  $90^\circ$  en  $\pm 45^\circ$  naar het volledige scala tussen  $0^\circ$  en  $90^\circ$ , en het voorkomen van clustering van vezellagen met dezelfde vezelhoeken, invloed hebben op het gedrag van het laminaat normaal op het vlak. Dit onderzoek is ook relevant voor variabele stijfheidspanelen die op elk vlaktecordinaat een gespreide laminaatopbouw hebben.

De resultaten van lage snelheidsimpact en compressie-na-impact testen onthullen dat de spreiding van de laminaatopbouw noch de impact weerstand, noch de damage tolerance van laminaten verbetert. Integendeel, de restweerstand in compressie van gempacteerde niet-conventionele laminaten neemt waarschijnlijk af in vergelijking met hun traditionele tegenhanger. Dit is omdat geclusterde lagen het ontstaan van grote delaminaties kan wegleiden van het binnenste van het laminaat, welke anders worden gesplitst in sublaminaten met een lagere weerstand tegen compressie. Betrouwbare numerieke modellen van de lage snelheidsimpacttesten die delaminaties en intraply schade modi simuleren voorspelden dat laminaten met geclusterde lagen ten opzichte van de niet-conventionele laminaten relatief minder energie kunnen opnemen door middel van delaminaties ten koste van de energie die door matrix scheuren en vezelbreuken wordt opgenomen. Dit is nog een reden voor hun superieure prestaties gegeven dat laminaten in compressie beter bestand zijn tegen intraply schade modi (over het algemeen geconcentreerd rond het impact gebied) dan tegen delaminaties.

Toekomstig onderzoek moet worden gericht op de globale responsie van variabele stijfheidspanelen, welke veelbelovender lijkt dan de lokale effecten van de spreiding in laminaatopbouw.



# Preface

THE idea of enrolling in a Ph.D. programme took form when I was about to finish my M.Sc. degree at the aerospace structures group from TU Delft, in late 2002. By that time I wanted to continue the research in the field of thermal protection systems for space reentry vehicles, at the same group. However, professor Johann Arbocz had retired and there was no replacement for him as the head of the group. Tom van Baten was temporarily filling this position until a new professor would be found. Furthermore, there was no funding available for a Ph.D. project in the field I was looking to work in. This meant I had to wait for a better day. In the meanwhile, a temporary position was found at the Adhesion Institute from TUDelft to work on the certification of bonded joints for commercial airplanes.

In June of 2003 I became the proud father of Miguel. That was a moment of change in my life, mostly for the fact that I had become a father, but also because it meant I had to travel more often back and forth from The Netherlands to Portugal where Miguel and Ana, his mother, were living. Ana had her job in Coimbra and, at that time, was additionally pursuing her own Ph.D. degree in the field of civil engineering.

In the beginning of 2004 I met Pedro Camanho, a young professor at the Faculty of Engineering from the University of Porto (FEUP) leading a research group on damage and failure of advanced composite materials. In the meanwhile, the position of the head of the group of aerospace structures had been filled by Zafer Gürdal, newly arrived from Virginia Tech (USA). The dormant idea of pursuing a Ph.D. degree surfaced, now in a reshaped form: a cooperation effort between the Faculty of Aerospace Engineering in Delft and FEUP on the subject of damage and failure of variable-stiffness panels. Such non-conventional composites were a very promising idea pursued by Zafer Gürdal since the early 1990's, and I found the subject very exciting, inspite of its divergence from my previous education. We decided to apply for a grant from the budget of the

Portuguese government through the *Fundação para a Ciência e a Tecnologia*. However, these funds were initially refused. We objected to this decision, but our objection would take about six months to be evaluated. These were definitely not good news given that my contract with the Adhesion Institute had just ended. Once again, Tom van Baten came in my rescue by finding a position as a stress analysis engineer at GlobalTechnics B.V., in Hoofdoorp. It was not until March of 2005 that the funds were unblocked and I could start this Ph.D. programme.

These last four years of my life have been fantastic. Research in the field of composite materials is a work that I enjoy doing. I foresee a bright future for the application of new material concepts in the everyday life of people, among them composite laminates. It is exciting to be a contributor to this evolution. I had the opportunity to work with extremely nice persons in two great universities, TU Delft and University of Porto, to travel to very interesting conferences around the world, and to meet highly qualified professionals of the aerospace industry and academia.

The financial support for this Ph.D. effort by the *Fundação para a Ciência e a Tecnologia*, through the scholarship SFRH/BD/16238/2004, and by TU Delft is gratefully acknowledged. With respect to the costs related with participation in international conferences, I also thank the help of the *Fundação Luso-Americana*, in Portugal.

I am thankful to my supervisors, Zafer Gürdal and Pedro Camanho, who believed in me, advised me and were patient enough to lead me to the end of this endeavour. Additionally, with their natural behaviour and humour were kind enough to nurture a relation beyond strict professional lines. I acknowledge my colleagues and friends of the aerospace structures group in Delft, where I spent most of my time, for the wonderful working environment. We had great moments together. I specially acknowledge Tom van Baten, who retired in the meanwhile. He gave me his support since I first arrived in Delft as an Erasmus exchange student, in 1999, going beyond his duties as professor and supervisor numerous times. This may not seem much for him, but in this highly chaotic world, small things can have great consequences.

Overall, I am very thankful to the Dutch people who welcomed me in their country with no reserves, and treated me all along as if I was one of their own. In spite of their natural distantness and inflexibility, as compared to southern European standards, the Dutch are persons that I became to admire and with whom I learned immensely. Their general open-mind, frontal and non-hierarchical way sets the stage for a very good working environment.

The elaboration of this thesis had the contributions of Peter Kromwijk, Yves



Coquet and Omprakash Seresta, respectively on the explicit modelling of tow-drops in variable-stiffness panels, on the carrying of the compression-after-impact tests, and on the development of the stacking sequence dispersion algorithm. The low-velocity impact and compression-after-impact experiments were performed under the laboratory supervision of Hans Verheim. The specimens required for these experiments were produced, and were later subjected to damage inspection, at the *Nationaal Lucht- en Ruimtevaartlaboratorium* (NLR), under the supervision of Bert Thuis. These contributions are gratefully acknowledged.

I am also very grateful to the advise and help of Ahmad Alhaj Ahmad, Agnes Blom, Christian Fagiano, Mostafa Abdalla, Brian Tatting, Christos Kassapoglou, Pier Marzocca, Pere Maimí and Emilio González in various subjects covered by this thesis. I address special thanks to Jan Hol, who was involved in the resolution of issues related to the computational resources required for the numerical simulations, and others. Also, I shall not forget the help of Annemarie van Lienden and Angela de Gier with all the paperwork required for different subjects during these years.

Finally, I am in great debt to Miguel and Ana. They have been immensely patient with me. I have been away for long months since Miguel was born, six years ago, and during a large part of the time I spent home I was immersed in the preparation of this thesis. Unyieldingly, Ana took care of everything necessary to our son when I was in The Netherlands. Thank you! Miguel, I am sorry for being away for such long times. I dream of a better future.



# Table of Contents

Summary	i
Samenvatting	v
Preface	ix
Table of Contents	xiii
Symbols and Acronyms	xvii
<b>1 Introduction and Objectives</b>	<b>1</b>
1.1 The Resurgence of Lightweight Structures . . . . .	1
1.1.1 Non-Conventional Laminates . . . . .	4
1.2 Damage and Failure Performance . . . . .	5
1.3 Thesis Objectives and Outline . . . . .	6
<b>2 Variable-Stiffness Panels</b>	<b>9</b>
2.1 Introduction . . . . .	9
2.2 Tailoring of Composite Laminates . . . . .	9
2.2.1 Variable Fibre Orientations . . . . .	10
2.3 Advanced Fibre Placement . . . . .	11
2.3.1 Applications . . . . .	13
2.4 Tow-Steered Laminates . . . . .	15
2.4.1 Considerations on Manufacturing . . . . .	17
2.4.2 Considerations on Design . . . . .	20
2.4.3 Structural Response . . . . .	24
2.5 Contribution to the Development of Variable-Stiffness Panels . . . . .	28
<b>3 Elastic Response of Variable-Stiffness Panels</b>	<b>31</b>
3.1 Introduction . . . . .	31
3.2 First-Ply Failure Criteria for FRP . . . . .	32
3.2.1 The LaRC Failure Criteria . . . . .	34
3.2.2 In-Situ Effects . . . . .	38
3.3 Elastic Response Characteristics . . . . .	40
3.3.1 Buckling . . . . .	42
3.3.2 First-Ply Failure in Postbuckling . . . . .	50

3.4	Performance of Manufacturable Panels . . . . .	61
3.4.1	Panels with Tow-Drops . . . . .	62
3.4.2	Panels with Overlaps . . . . .	64
3.5	Conclusions . . . . .	66
<b>4</b>	<b>Damage Propagation in Variable-Stiffness Panels</b>	<b>69</b>
4.1	Introduction . . . . .	69
4.2	Progressive Damage and Failure Analyses . . . . .	70
4.2.1	Continuum Damage Model . . . . .	73
4.3	Design Cases . . . . .	77
4.3.1	Numerical Set-Up . . . . .	77
4.3.2	FE Procedure . . . . .	78
4.3.3	Damage and Final Failure Results . . . . .	79
4.4	Test Case . . . . .	84
4.4.1	Experimental Set-Up . . . . .	84
4.4.2	FE Implementation . . . . .	86
4.4.3	Buckling Response . . . . .	88
4.4.4	Damage Initiation and Progression . . . . .	91
4.4.5	Final Failure . . . . .	93
4.5	Conclusions . . . . .	96
<b>5</b>	<b>Failure of Variable-Stiffness Laminates with Tow-Drops</b>	<b>99</b>
5.1	Introduction . . . . .	99
5.2	Tow Dropping and Resin-Rich Spots . . . . .	100
5.3	Numerical Set-Up . . . . .	101
5.4	Damage and Failure Predictions . . . . .	104
5.4.1	Influence of the Tow Width . . . . .	106
5.4.2	Influence of the Laminate Thickness . . . . .	109
5.5	Conclusions . . . . .	110
<b>6</b>	<b>Low-Velocity Impact: Experimental Testing</b>	<b>113</b>
6.1	Introduction . . . . .	113
6.2	Damage-Tolerant Laminate Design . . . . .	115
6.2.1	Non-Conventional Laminates with Dispersed Stacking Sequences . . . . .	118
6.3	Drop-Weight Impact Tests . . . . .	122
6.3.1	Specimen Preparation, Setup and Test Procedure . . . . .	122
6.3.2	Experimental Results . . . . .	124
6.4	Compression-After-Impact Tests . . . . .	136
6.4.1	Test Setup and Procedure . . . . .	137
6.4.2	Experimental Results . . . . .	138
6.5	Discussion . . . . .	141
6.6	Conclusions . . . . .	143

---

<b>7</b>	<b>Low-Velocity Impact: Numerical Simulations</b>	<b>145</b>
7.1	Introduction . . . . .	145
7.2	Impact Damage Models . . . . .	146
7.2.1	Continuum Damage Model for 3-D Plies . . . . .	146
7.2.2	Cohesive Zone Model for 3-D Interfaces . . . . .	148
7.3	Simulations of the Low-Velocity Impact Tests . . . . .	151
7.3.1	Numerical Set-Up . . . . .	151
7.3.2	Numerical Results and Correlation with Experiments . . . . .	157
7.4	Additional Non-Conventional Laminates . . . . .	168
7.5	Conclusions . . . . .	170
<b>8</b>	<b>Conclusion</b>	<b>173</b>
8.1	Lessons Learned . . . . .	173
8.1.1	Variable-Stiffness Laminates . . . . .	173
8.1.2	Laminates with Dispersed Stacking Sequences . . . . .	175
8.2	Perspectives and Recommendations . . . . .	176
<b>A</b>	<b>Stacking Sequence Dispersion</b>	<b>179</b>
A.1	Introduction . . . . .	179
A.2	Dispersion of Ply Orientations . . . . .	179
A.3	Dispersion using Genetic Algorithms . . . . .	180
A.3.1	Lamination Parameters . . . . .	181
	<b>List of References</b>	<b>181</b>
	<b>Curriculum Vitae</b>	<b>195</b>



# Symbols and Acronyms

## Acronyms

ADL	Allowable Damage Limit
AFP	Automated Fibre Placement
BVID	Barely Visible Impact Damage
CAI	Compression-After-Impact
CDT	Critical Damage Threshold
CFRP	Carbon Fibre Reinforced Plastics
CLT	Classical Lamination Theory
DCDT	Direct Current Displacement Transducer
DTL	Delamination Threshold Load
FE	Finite Elements
FPI	Fluorescent Penetrant Inspection
FRP	Fibre Reinforced Plastics
GA	Genetic Algorithm
GFRP	Glass Fibre Reinforced Plastics
LVI	Low-Velocity Impact
NCL	Non-Conventional Laminate
NDI	Non-Destructive Inspection
PFA	Progressive Failure Analyses
VSP	Variable-Stiffness Panel(s)

## Subscripts

<i>c</i>	cohesive (layer)
<i>i</i>	impact
<i>l</i>	laminate
<i>m</i>	matrix
<i>p</i>	ply
1±,2±,6	longitudinal tension (1+), longitudinal compression (1-), transverse tension (2+), transverse compression (2-), in-plane shear

	(6)	
$cr$	critical	
$ff$	final failure	
$fpf$	first ply failure	
$I, II, III$	loading modes (mode I, mode II, mode III)	
$x, y$	global directions	
<b>Superscripts</b>		
$m$	misalignment frame	
$eq$	equivalent, overall	
$is$	in-situ	
<b>Variables</b>		
$\alpha$	fracture angle	deg
$\alpha_{ii}$	coefficients of thermal expansion	$^{\circ}\text{C}^{-1}$
$\beta$	mixed mode loading ratio	
$\Delta$	relative displacement (between cohesive surfaces)	mm
$\eta$	loading mode interaction parameter	
$\gamma$	shear strain	
$\kappa$	material shear stress - shear strain non-linearity parameter	
$\mathcal{D}$	laminate stacking sequence dispersion	
$\mathcal{G}_c, \mathcal{G}_{M, M=1\pm, 2\pm, 6}$	fracture toughnesses (critical values of the strain energy release rate)	N/mm
$\mu$	friction coefficient	
$\nu$	Poisson's ratio	
$\phi$	orientation of the axis of fibre angle variation in a VSP	deg
$\phi_{N, N=1\pm, 2\pm}$	LaRC failure criteria	
$\rho$	density	$\text{kg}/\text{m}^3$
$\sigma_{ij}$	stress tensor	
$\tau$	shear stress	MPa
$\mathbf{H}$	compliance tensor	
$\theta$	fibre angle	deg
$\varepsilon_{ij}$	strain tensor	
$A$	acceleration	$\text{m}/\text{s}^2$
$a, b$	panel dimensions	mm
$A_{ij}, B_{ij}, D_{ij}$	CLT stiffness matrices	
$b$	bonus parameter associated with stacking sequence dispersion	
$d$	distance	mm
$d_{M, M=1\pm, 2\pm, 6}$	material damage variables	



---

$E$	Young's modulus	MPa
$E$	energy	J
$E_{1mm}$	impact energy corresponding to a permanent indentation of 1 mm	J
$F$	force	N
$G$	shear elasticity modulus	MPa
$h$	thickness	mm
$K$	stiffness	MPa
$l$	length	mm
$l^*$	FE characteristic length	mm
$M$	mass	kg
$N$	stress resultant	N/mm
$P$	pressure	MPa
$T$	temperature	°C
$t$	time	s
$T_0$	fibre angle at the centre of a VSP	deg
$T_1$	fibre angle at a characteristic distance, $d$ , in a VSP	deg
$u, v, w$	displacements	mm
$V$	velocity	m/s
$W_i$	lamination parameters	
$X_{M, M=1\pm, 2\pm, 6}$	ply strengths	MPa
<b>Constants</b>		
$g$	acceleration due to the gravitational force	9.81 m/s <sup>2</sup>



# Chapter 1

## Introduction and Objectives

### 1.1 The Resurgence of Lightweight Structures

**I**N the context of materials science, the term *composite* is generally associated to a heterogeneous material composed of two or more distinct phases. Composite materials have long been used for structural and non-structural applications. Wood, a natural composite material, is known to be used by humans since we consider ourselves an intelligent species. Initially, and still, employed in the construction of huts (together with reed, another natural composite material), wood has accompanied human evolution through all times. Either to build the most varied tools, weapons, animal pulled transportation systems (e.g. horse-wagons), buildings, bridges or even planes, wood is certainly the most versatile composite material known to exist. Another example of an ancient composite material are construction bricks. Initially composed of mud reinforced by straw, bricks were already in use for house building by the ancient Egyptian civilisation, known to exist from as early as 4000 B.C.<sup>1</sup>.

The use of materials in structures is related with transportation in one way or another, and transportation is related with energy consumption. Either the structures have to be loaded for at least part of their useful lives or themselves constitute the means of transportation. In the distant past when most humans still lived nomadic lives, all structures (shelters, hunting and food preparation tools, etc.) had to be carried by hand, i.e. with little energy expenditure. Therefore, they had to be light and were mostly built of natural polymers (bone, skin, horn and hair) and composites (wood and straw-brick)<sup>2</sup>. With the first human settlements and animal domestication, the energy available increased and the opportunity to use stronger, but heavier, materials to build larger and more com-

plicated structures arose. Starting from stone, civilised people soon discovered the melting of metals such as copper, bronze and iron and their benefits in construction. With the industrial revolution and the use of the combustion engine, the potential for energy use increased enormously and heavy metals such as steel became dominant as an engineering material. A bathtub shaped graph, as drawn by Ashby<sup>3</sup>, illustrating the relative importance of materials in the human civilisation throughout history is plotted in Figure 1.1. In comparison with other materials, the use of metals in constructions reached a peak around 1960. With the increase of world population and the gradual depletion of fossil fuel reserves, the cost of energy is increasing and a pressure for lighter structures is on. In the aeronautical and space industry, where energy efficiency is crucial, metals with a high strength/density ratio such as aluminium and titanium found temporary prosperity. However, this is just slowing down the decline of metals as major construction materials. Maybe in a last agonising push, metals are trying to keep some vital space as alloys (e.g. Al-lithium). In the meanwhile there is a resurgence of lightweight structures based on low density synthesised polymeric and composite materials such as Fibre Reinforced Plastics (FRP). Advanced composites such as FRP offer the best values of specific stiffness (stiffness/density) and specific strength (strength/density) amongst engineering materials. That is why they are starting to be used in advanced applications, not only in the aeronautical and space industries but also in specific sectors as the automotive (e.g. F1 cars with high specific stiffness) and military (e.g. woven helmets with high specific impact strength)<sup>4</sup>.

FRP are advanced composites where long fibres (e.g. glass - GFRP, carbon - CFRP) are embedded in a polymer matrix. Characterised by their high stiffness and strength, the role of the fibres is to reinforce the relatively low-strength matrix. Therefore, it is possible to combine the properties of a lightweight matrix with the ones of the strong fibres. Overall, this technique results in a lighter material than its monolithic counterparts (e.g. metal), while still maintaining high-stiffness and high-strength properties along a predetermined direction, the direction of the fibres.

Advanced composites are often fabricated in the form of *laminates*. A laminate consists of one or more thin layers (*laminae*) stacked together. Traditionally, within each lamina or ply, the fibres are placed straight and parallel in the resin material. The structural properties of each lamina can, therefore be tuned by changing the fibre and resin constituent materials as well as their relative amount (the volume fraction). Additionally, specific stiffness properties of a laminate can be achieved by correctly choosing the fibre angles, the thickness of each ply,

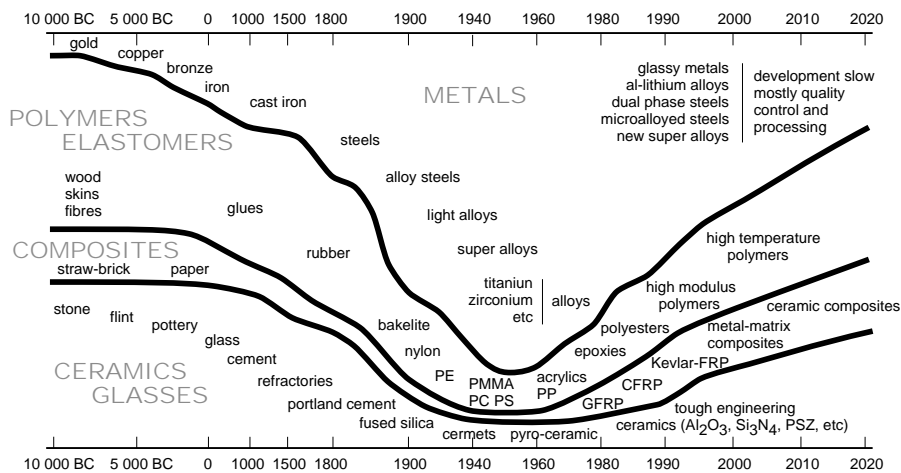


Figure 1.1: The evolution of the relative importance of engineering materials with time<sup>3</sup>. Data in the stone and bronze ages is based on assessments by archeologists. Data in the 1960's is based on allocated teaching hours on US and UK universities. Data in the 2020's is based on predictions of material usage in automobiles by manufacturers. The time scale is non-linear. The rate of change is far faster today than at any previous time in history.

the number of plies and their stacking sequence. A composite laminate defines an orthotropic material whose properties can be tailored in each orthogonal direction individually in order to achieve the best structural performance.

Since the emergence of advanced composites materials, during the 1960's, structural engineers have been given all the above described possibilities in the design of composite structures. In spite of that fact, practical reasons have dictated that, in most cases, the design variables are reduced to the number of plies, the fibre angle within each ply and the stacking sequence. Furthermore, the fibre angles are often chosen from a small number of discrete values:  $0^\circ$ ,  $90^\circ$  and  $\pm 45^\circ$ . More than often, by proper selection of the percentages of the plies with different orientations, they exhibit also quasi-isotropic properties in the plane of the laminate. Conventional design practices have the purpose of simplifying and generalising the application of composites; however they limit the potential of composites to improve the efficiency of traditional structures. The full potential of advanced composites can only be achieved by *tailoring* each laminate to each specific structural application. One way to do this is by turning to *non-conventional laminates*.

### 1.1.1 Non-Conventional Laminates

The designation *non-conventional laminates* refers to two types of configurations: (i) laminates that explore the whole range of possible ply orientations, hence using more than the conventional  $0^\circ$ ,  $90^\circ$  and  $\pm 45^\circ$  fibre angles, and (ii) composite panels with lay-ups that continuously vary from point to point. A continuously varying lay-up is achieved by steering the fibres within each ply. In such cases, the laminate stiffness also varies with the in-plane coordinates of the laminate, hence these configurations are termed Variable-Stiffness Panels (VSP). The illustration in Figure 1.2 shows that at each point in the planform of a VSP there is a distinct non-conventional lay-up of type (i). Besides these characteristics, it is considered that in both types of non-conventional laminates there are no plies clustered at the same fibre orientation. The exploitation of non-conventional ply angles and the absence of ply clustering can be coupled in a single property of non-conventional laminates: *stacking sequence dispersion*.

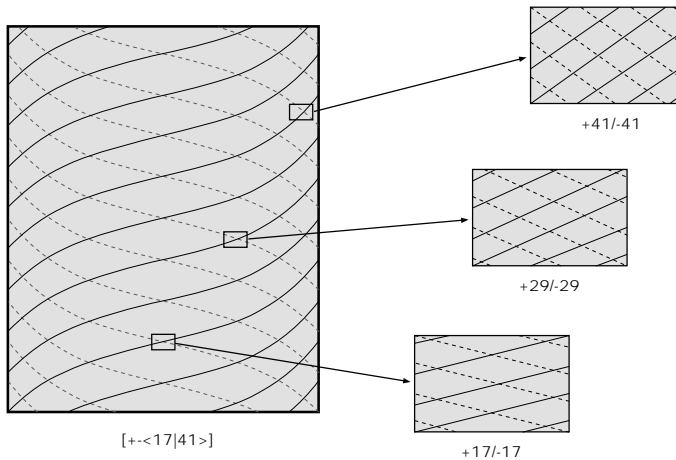


Figure 1.2: Example of a 2-ply VSP. The non-conventional lay-up varies continuously from point to point on the laminate.

Non-conventional laminates are possible nowadays thanks to the recent developments on Advanced Fibre-Placement (AFP) systems. This technology allows a fully automated manufacturing of complex composite laminate parts and shows a high potential for aeronautical applications. The precision of AFP systems allows the production and repeatability of laminates with non-traditional stacking sequences. Furthermore, their fibre-steering capability makes VSP possible. The full details of the AFP technology are explained in Chapter 2.

The idea behind non-conventional laminates is to improve the structural ef-

iciency of composite laminates designed according to the conventional way. In particular, the present thesis is focused on their damage and failure performances under in-plane and (out-of-plane) Low-Velocity Impact (LVI) loads. Previous research works<sup>5-10</sup> have proven the advantages of VSP in terms of stiffness and buckling responses to in-plane static loading. This thesis focus on the failure response of such configurations and their potential for increasing the strength performance of composite laminates. Furthermore, due to the manufacturing process, these configurations are deemed to have characteristics other than simply curvilinear fibres. These are fully explained in Chapter 2. As an example, the fibre-tows laid by the AFP machine may have to be cut at certain locations. This cutting procedure leaves small fibre-free areas in the panels, termed tow-drops, that will eventually be filled with resin material during the curing process, hence becoming resin-rich spots which may have a degrading influence on the strength of the panel. The effect of this and other characteristics of VSP on their in-plane strength performance is investigated in Chapters 3, 4 and 5.

Until the present moment, the impact damage performance of VSP has not been investigated. It is likely that the extent of the LVI damage on these laminates is small as compared with their fibre radius. Hence, for the sake of simplification of the research, configurations of type (i) may be considered representative of VSP in terms of impact response. Furthermore, the results can be generalised for non-conventional laminates of straight or curvilinear fibres. The impact damage resistance as well as the residual strength, or damage tolerance, of non-conventional laminates is investigated in Chapters 6 and 7.

## 1.2 Damage and Failure Performance

The non-destructive evaluation of the damage and failure performance of non-conventional laminates, and FRP in general, requires the use of advanced analysis tools recently developed within the frameworks of fracture and damage mechanics.

Advanced composites are orthotropic materials. Not only they respond differently under tension and compression, they respond according to the direction of the applied stress. Composite laminates fail at much higher loads when loaded in the longitudinal direction, the direction of the fibres, than when loaded in the transverse direction. In this thesis, non-conventional designs are proposed which take into account this mismatch in an optimal way. That is, in such panel configurations, the local ply orientations are such that most of the load is carried along the longitudinal direction. This can be achieved with fibre-steering and VSP.

In spite of their apparent brittleness, fracture in FRP does not correspond to

the sudden and complete loss of structural stiffness. Rather, there is a damage process, generally over a small strain range, corresponding to a gradual decrease of stiffness which is associated with energy dissipation in the form of matrix cracks and fibre breakage. The onset of damage in a laminate corresponds to the first ply reaching the elastic limit. It can be predicted by means of first-ply failure criteria. In this thesis the Finite Element Method (FEM) is used together with special purpose first-ply failure criteria for FRP developed at NASA - Langley Research Centre (LaRC). The damage process can be simulated by means of intralaminar and interlaminar damage models implemented in the FEM. In composite laminates, these models can take into account the energy dissipation associated with the different failure modes of a ply (longitudinal/transverse, tension/compression) and loss of cohesion between plies (delamination). Hence, the final failure loads, i.e. the loads corresponding to the total loss of stiffness of a composite structure, can be predicted. These numerical simulation procedures are commonly known as Progressive Failure Analyses (PFA). In the work reported in this thesis, PFA's are carried to simulate the behaviour of non-conventional laminates under static compressive loads and LVI loads, with good correlation with experimental results.

### 1.3 Thesis Objectives and Outline

The main goal of this thesis is to investigate the performance of non-conventional laminates, specifically in terms of buckling, strength, damage resistance and damage tolerance, and compare them with composites designed in the conventional way. In order to evaluate the behaviour of non-conventional laminates and achieve this objective, experimental tests are carried out and state-of-the-art numerical simulation tools are employed.

Chapter 2 presents a literature review on AFP technology and the development of the concept of VSP, an idea pursued for the past 15-20 years. The most relevant aspects of these non-conventional laminate designs in terms of design and manufacture are presented.

In Chapter 3, the possibilities offered by variable-stiffness designs in terms of buckling and failure are explored. Parametric studies are presented which involve numerical analyses of the behaviour of these structures under in-plane static compression loads until the onset of damage, with consideration for buckling. Chapter 3 also covers the investigation of the effects of some manufacturability issues presented in Chapter 2 in the failure response of VSP.

In Chapter 4, the numerical analyses performed in Chapter 3 are extended beyond the elastic limit by carrying PFA on the most promising variable-stiffness de-



signs. In order to evaluate the accuracy of the modelling and simulation strategy, PFA are also carried on previously tested constant-stiffness and variable-stiffness panels.

Chapter 5 covers the numerical analysis of VSP with the explicit geometrical inclusion of tow-drops. In Chapters 3 and 4, the FE models are simplified with respect to tow-drops. However, the comparison between experimental and numerical results in Chapter 4 indicate that the effect of these might not be negligible. Parametric studies are carried in Chapter 5 to investigate the consequences of tow-dropping under several conditions.

In Chapters 6 and 7 the effects of stacking sequence dispersion on the impact damage resistance and tolerance of laminates are investigated. Chapter 6 reports an experimental programme of LVI and Compression-After-Impact (CAI) tests on a few conventional and non-conventional configurations. In Chapter 7 the impact problem is addressed by three-dimensional PFA which cover the simulation of intraply and interlaminar damage.

This thesis is concluded in Chapter 8 with an exposition of the lessons learned from the work reported in the previous chapters and a perspective on the research to be carried in the future based on the present contribution to the knowledge of the behaviour of non-conventional laminates.



## Chapter 2

# Variable-Stiffness Panels

### 2.1 Introduction

THIS thesis is focused on the damage and failure behaviour of non-conventional laminates, which can be divided in two groups: (i) straight-fibre laminates having non-conventional ply orientations, and (ii) curvilinear-fibre laminates with continuously varying non-conventional lay-ups. The elements of this last group are specifically designated VSP. Not only the design and analysis of such composite panels needs special attention, their manufacture is only possible with the recent advances on automated fibre-placement technology. Hence, the present chapter defines the state-of-the-art in terms of the development of VSP and sets the stage for the research work carried in this thesis.

### 2.2 Tailoring of Composite Laminates

The traditional way to tailor composite laminates is by changing their stacking sequence. Here, 'stacking sequence' is used in the wide sense which can be translated in information on the number of layers, the fibre angle of each individual layer and the way they are arranged through the thickness of the laminate. According to this definition, it is generally assumed that the fibre angle within each ply is maintained constant at all locations in the plane of the laminate. There is an infinite number of configuration possibilities with these laminate variables which respond in a varied number of different ways to a given applied load. This means that the best design, or designs, can be found to respond in the best possible manner to a structural solicitation. However, the design space is still rather limited because it only allows for configurations with constant properties along the laminate planar

dimensions. This means that it is not possible to tailor a panel to respond in the most efficient manner to non-uniformly distributed in-plane stresses caused, for instance, by holes and notches. In the case of such geometries, either the whole laminate has to be manufactured with the properties required to bear the highest loads, which eventually only occur in a small part of the panel, or it can be locally reinforced or patched by addition of plies, hence changing their lay-up. For example, Biggers et al.<sup>11;12</sup> tailored laminates by redistributing the layers with specified orientations across the planform of rectangular plates in order to create beneficial stiffening patterns against compression and shear buckling. The major drawbacks of this solution are eventual stress concentrations and delaminations. DiNardo and Lagace<sup>13</sup> achieved in-plane laminate tailoring by dropping off plies. Experimental and analytical investigations showed that ply dropoffs have a marked effect on plate buckling and postbuckling behaviour.

### 2.2.1 Variable Fibre Orientations

A more flexible method of tailoring a composite laminate is to vary the orientation of fibres from point to point by steering them throughout each lamina, hence varying the laminate properties along its planar coordinates. With this method it is possible to respond more adequately to planar stress variations and, more importantly, it is possible to divert loads from the most sensitive regions of a composite structure such as holes and notches.

One of the first theoretical investigations on the effects of changing the elastic properties of laminates by varying the fibre orientations was carried out by Muser and Hoff<sup>14</sup>. These authors provided a closed-form solution for the stress concentration around a hole for an orthotropic plate subjected to uniaxial tension that contained a radial variation of the elastic properties. Their example shows that the introduction of a  $\pm 45^\circ$  fibre arrangement in the vicinity of the hole, that gradually varies to quasi-isotropic lay-up at the outer edges of the plate, is very effective in reducing the stress concentrations.

Yau and Chou<sup>15</sup> inserted metal pins into woven fabric prior to curing, effectively pushing the fiber tows apart to create a molded hole. The resulting laminates possessed curvilinear fibers around the hole and exhibited improved open-hole strength compared to similar laminates with drilled holes.

Kuo et al.<sup>16</sup> analysed the elastic behaviour of *flexible composites* with waving fibres. These are defined as elastomeric polymer based composites for which the usable range of deformation is much larger than that of the conventional thermosetting or thermoplastic polymer based composites. Due to the waving

fibres embedded in an elastomeric matrix, flexible composites can elongate at low stresses but stiffen when the fibres become fully extended.

Hyer and Charette<sup>17</sup> applied the concept of waving fibres to a plate with a central hole and studied its tensile and compressive behaviour. The authors claimed that improved laminate designs would result from aligning the fibres with the principal stress directions. According to them, having fibres aligned with the applied tensile loading is making good use of the concept of fibre reinforcing. The interacting stress-based Tsai-Wu failure criterion<sup>18</sup> applied on a Finite Element (FE) solution predicted marked improvement of the failure behaviour of these panels over their traditional, straight-fibre counterparts. Although the tension behaviour was improved with the variable fibre-orientation format, the same tendency was not observed with respect to the buckling response. In a follow-up work by Hyer and Lee<sup>19</sup>, both a sensitivity analysis and a gradient search technique were employed, and the buckling loads were actually increased as compared to the traditional straight-fibre design. It was shown that it is possible to place the fibres in such orientations that the loads are transferred away from the unsupported hole region of the plate to the supported edges, thus increasing the buckling capacity. By combining both straight and curvilinear fibre formats within a laminate, hence resulting in *hybrid laminates*, the best buckling and failure results were achieved.

Other examples of fiber orientation angle tailoring include theoretical and numerical studies by Banichuk<sup>20;21</sup>, Pedersen<sup>22;23</sup>, Duvaut et al.<sup>24</sup> and Crothers et al.<sup>25</sup>. The motivation for these studies was the optimisation of the spatial variation of fiber orientation within the domain of a composite panel in order to improve its stiffness, buckling or strength characteristics.

## 2.3 Advanced Fibre Placement

The fibre-steered laminate designs discussed in the previous paragraphs are not easily manufactured by traditional hand laying methods, mostly because of the degree of precision required in laying the fibres at the correct angles and keeping them during curing. Production of these laminates requires an accurate fibre placement system. Advanced Fibre Placement (AFP) is an emerging technology combining the differential tow payout capability of filament winding and the compaction and cut-restart capabilities of automated tape laying. An AFP machine is a high-precision robot, capable of wide freedom of movement, computer-controlled to produce a composite component without any human intervention<sup>26;27</sup>. Off-line programming is used to implement the desired configurations. Their feasibility is confirmed by simulations. AFP technology allows the design and production

of components that would be extremely difficult or even impossible with other automated methods, let alone hand laying. Despite the novelty of the process and high machinery costs, the availability of tow-placement systems is rapidly growing<sup>28-31</sup>.

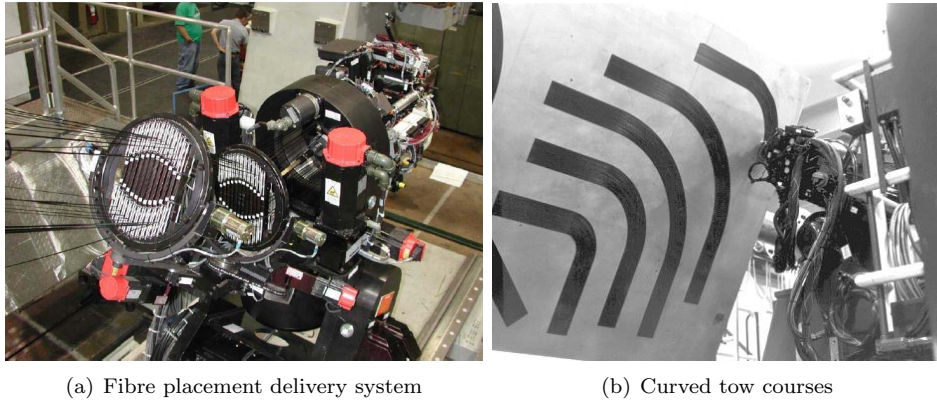


Figure 2.1: Typical Advanced Fibre Placement (AFP) system characteristics (courtesy of Ingersoll Machine Tools<sup>31</sup>).

The primary advantage of fibre-placement over manual lay-up of a composite part results from the automation of the manufacturing process. By automating the fibre laying procedure, the process repeatability is greatly improved, hence its speed is increased. Bullock et al.<sup>26</sup> estimate the AFP process to be as much as seven times faster than hand laying. Additionally, a part produced by a machine can be more faithful to the intended design, therefore showing better quality, than if produced by hand.

With the fibre-placement process, individual prepreg tows are fed through a fibre delivery system (Figure 2.1.a) into a fibre placement head (Figure 2.2) where they are laminated onto a work surface as a single fibre band. The tow-placement head can accommodate up to 32 tows. Typically, the tows have widths of 3.175mm (1/8in), 6.35mm (1/4in) or 12.7mm (1/2in) which result in fully-filled tow-bands or courses of 101.6mm, 203.2mm and 406.4mm, respectively. When starting a course, the individual tows are fed through the head and compacted onto a surface. As the course is being laid down, the processing head can cut or restart any of the individual tows. Hence, the width of the fibre band can be increased or decreased allowing the elimination of excessive gaps or overlaps between adjacent courses. At the end of the designed course, the remaining tows are cut to match the shape of the ply boundary. This reduces the amount of material scrap and of post-cure machining required for a finished product<sup>32;33</sup>.

A tow-placement head can move in seven degrees of freedom: three position axes, three orientation axes and an axis to rotate the work mandrel. The range of motion described by the tow-placement head allows the tows to be aligned in any direction, consequently enabling the production of doubly-curved parts which might be impossible to fabricate by other automated methods<sup>32;33</sup>.

During the placement of a course, each tow is dispensed at its own speed, allowing it to independently conform to the surface of the part. Because of this differential payout system the fibres can be steered to meet specified designs, as shown in Figure 2.1.b. This is a totally innovative capability in comparison with other automated methods. Because they rely on the friction and the tension of the material to hold individual fibre paths in place, filament winding and automated tape laying are confined to near-geodesic paths<sup>32;33</sup>.

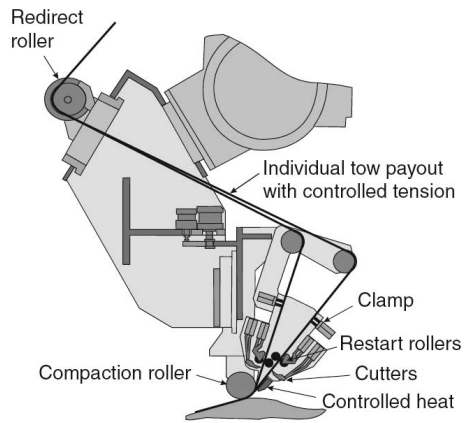


Figure 2.2: Typical tow-placement head (courtesy of Evans<sup>34</sup>).

A rolling compaction device, combined with heat for tack enhancement, laminates the tows onto the lay-up surface. The action of pressing the tows onto the work surface, or a previously laid ply, removes trapped air minimising the need for vacuum debulking. Compaction combined with low-tension positioning allows the fibres to be laid onto concave surfaces. With traditional methods, such as filament winding, the concave surfaces would be bridged over because of the high tension necessary to hold the fibres in place<sup>32;33</sup>.

### 2.3.1 Applications

The AFP technology was developed during the mid 1980's, hence the use of tow-placement machines is still relatively new. However, AFP machines have already demonstrated the capability to produce large and complicated structures. The

first company to implement this novel system on a production aircraft was Boeing Helicopters, in the early 1990's. Hercules, Inc. proved that their machine can produce parts ranging from wing spars to primary fuselage structures<sup>29</sup>. Boeing and Hercules conducted a program to develop the design and process for fibre-placing the aft fuselage for the Bell/Boeing V-22 Osprey<sup>35</sup>. This part was designed to take advantage of the unique capabilities of the AFP production method. The first four prototype V-22 aft fuselages were made from nine hand-laid sections. By switching to fibre-placed monolithic structure, the number of fasteners was cut by 34%<sup>34</sup>. Trim and assembly labour was also reduced by 53%. Through the combination of design optimisation and fibre-placement, Boeing also reduced the material scrap by 90%. Another military aircraft that takes advantage of the unique capabilities of the fibre placements is the F/A-18 E/F Super Hornet<sup>36</sup>. When compared to hand lay-up, the application of this technology to the fuselage skin saved 38% in labour time and 80% in process time.

The AFP technology is also being used in commercial aircraft. Raytheon Aircraft uses the Cincinnati Milacron's FPX machine to fabricate fuselage sections for the Premier I and Hawker Horizon business jets<sup>34</sup>. The honeycomb sandwich design creates a fuselage shell free of frames and stiffeners. The shells are also free of rivets, skin joints and frames, which frees more usable space for passengers or cargo. By using the fibre-placement process to fabricate the fuselages, Raytheon Aircraft achieved weight savings, material savings, reduced part count, reduced tool count, reduced shop flow time, and managed to increased part quality.

The application of high performance composite laminates to large aerospace structures was also made possible by the introduction of AFP machines<sup>31</sup>. Currently, this technology is being used to produce the fuselage barrels and main wing boxes of large commercial airplanes<sup>37</sup>. The revolutionary Boeing 787 Dreamliner is making use of the tow-placement technology to reduce production costs and part weight, overall increasing structural performance. The manufacturing of a couple of sections of this aircraft is shown in Figure 2.3.

Although AFP machines allow the steering of fibre tows, hence increasing structural design flexibility, this capability is not explored in the applications mentioned above which, in most cases only take advantage of the accuracy and convenience of an automated process. The development of composite laminates with steered fibres is mostly still at the academic research level.



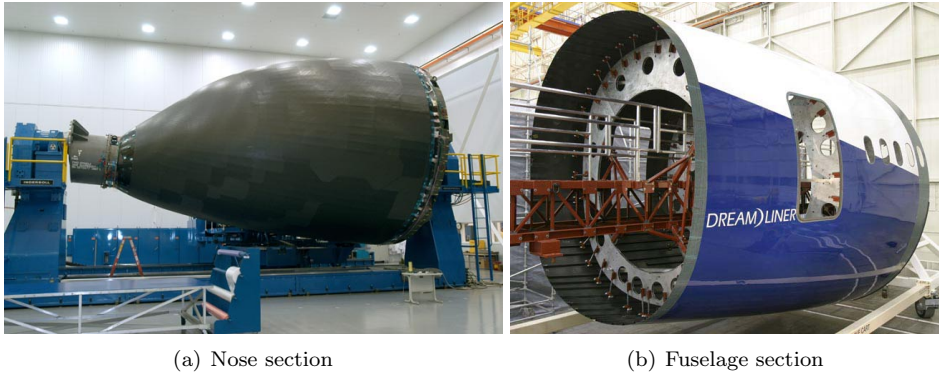


Figure 2.3: Boeing 787 nose and fuselage sections manufactured by advanced tow-placement technology (courtesy of Boeing<sup>38</sup>).

## 2.4 Tow-Steered Laminates

The potential of fibre-steered laminates, made possible by AFP technology, led to the birth of a new branch of research in laminated composite materials. The increased freedom of design also increases the complexity and requires novel approaches to many common problems in composite laminates engineering. As described above, several different approaches have been used to attempt to adequately model and predict the response of curvilinear-fibre laminates. The motivation in each case was that by spatially varying the fibre orientations within a ply it should be possible to improve the structural performance of a laminate.

A simple method of modelling complete tow paths was developed in the research initiated by Gürdal and Olmedo<sup>5;6;39</sup>. The original idea was that the response of fibre-reinforced laminates could be significantly altered by allowing the fibre orientation angle to vary spatially throughout the structure. The variation of fibre orientations within a lamina determines a planar variation in its stiffness. Hence, these composites were termed *variable-stiffness laminates* or *Variable-Stiffness Panels* (VSP). The work led by Gürdal resulted in the formulation of a tow steered ply definition with a minimum number of parameters. A simple formulation is not only necessary for the attractiveness of the concept, but also to allow for fast optimisation algorithms to produce the best manufacturable structural designs. Being manufacturable implies that the curvilinear ply paths can be fabricated using existing fibre placement technology, so that the range of possible designs is bounded by the constraints of the machine used.

In the formulation proposed by Gürdal and Olmedo<sup>5;6;39</sup>, it was assumed that the fibre angle of a reference fibre path varied linearly from the value  $T_0$  at a fixed

position in the panel (typically, its geometrical centre) to  $T_1$  at a specified distance  $d$ , as illustrated in Figure 2.4. This distance is often taken as a characteristic dimension of the composite panel being designed. In the case of a rectangular laminate, this is generally half of the panel width in the direction along which the fibre orientation variation takes place. With this formulation the orientation of a single curvilinear fibre path can be denoted by  $\langle T_0|T_1 \rangle$ . This curve is the *reference path* for the course followed by the AFP machine head when laying a band of tows. Eventually, similar courses have to be described in order to cover a full ply. Since a ply is made of fibres oriented similarly to the reference fibre path, the description of this curve is sufficient to describe the ply. A "±" sign in front of this term means that there are two adjacent layers with  $T_0$  and  $T_1$  angles of equal magnitudes but opposite sign.

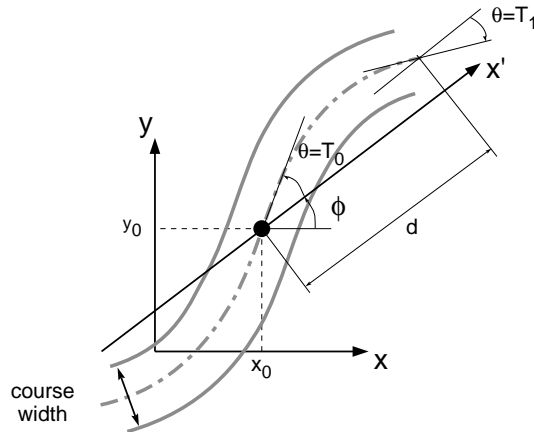


Figure 2.4: Linear fibre angle variation reference path.

A more general fibre path definition can be achieved by rotating the axis of variation of the fibre orientation by an angle,  $\phi$ , from the geometric axis of the panel. This rotation defines a new fibre orientation variation axis denoted by  $x'$ . According to the formulation, the fibre path defined by  $\phi \langle T_0|T_1 \rangle$  varies linearly along the  $x'$  direction, rotated from the  $x$ -axis by an angle  $\phi$ . A "±" sign in front of the rotation angle means that the reference fibre paths for two successive layers are rotated by equal and opposite amounts. A smooth reference curve, illustrated by the dashed line in Figure 2.4, is constructed starting at the origin  $(x_0, y_0)$ . In general, the origin of variation is located at the centre of the panel. The reference curve is assumed to be anti-symmetric about the origin of variation. The function which defines the fibre orientation can be determined in

terms of  $\phi$ ,  $T_0$ ,  $T_1$  and  $x'$ :

$$\theta(x') = \phi + (T_1 + T_0) \frac{|x'|}{d} + T_0 \quad (2.1)$$

For the remaining domain, the fibre orientation angle repeats indefinitely with period  $2d$  so that  $\theta(x')$  is periodic and continuous. Thus the variation of the fibre orientation angle follows a linear saw-tooth pattern with limits  $T_0$  and  $T_1$ .

In order to construct the remainder of the ply, Gürdal and Olmedo<sup>5;6;39</sup> suggested shifting the reference path in a direction perpendicular to its axis of fibre orientation variation, i.e. the fibre direction is assumed to vary only in one spatial direction. With this method they claimed increases of up to 50% in the axial stiffness and up to 80% in the critical buckling load of VSP when compared to traditional straight-fibre laminates. The reason for these remarkable results was attributed to the load redistribution from the centre of the panels to the higher-stiffened edge regions. The best buckling results were found for the designs where the fibre orientation,  $\theta$  varied in a direction perpendicular to the direction of the applied load<sup>10;40</sup>.

### 2.4.1 Considerations on Manufacturing

The AFP system offers the capability of reducing material and labour costs while enabling the production of structures capable of increased performance. However, the theorised benefits, e.g. by Gürdal et al.<sup>10</sup>, may be bounded by the real manufacturing conditions and limitations imposed AFP machines. The most important are described in the following paragraphs.

#### Fibre Angle Deviations

In the idealised variable-stiffness ply definition presented above (Equation 2.1), the fibre angle varies continually as a function of one of the planar coordinates. However, this formulation only defines the reference path orientation, i.e. the centreline of the AFP machine head course. Typically, an automated tow-placement head has the capability of accommodating up to 36 fibre tows within a 76.2mm (3in) course width. This means that within each head pass or course, up to 36 tows are placed parallel to each other. Therefore, the shifting of the reference path occurs discretely at multiples of the course width. Within a given course, the fibre orientation deviates from the reference path which is only followed by the course centreline. The maximum deviation is at the edges of the course. Furthermore, the wider the course, the larger the deviation is. As an example, the

difference between a laminate ply where all the tows follow the reference path and a ply manufactured with a finite-width course is illustrated in Figure 2.5. The discontinuities visible in Figure 2.5.b. correspond to fibre angle mismatches at the course edges. The designer of VSP should be aware that these geometric discontinuities can be the cause of stress concentrations, and these can hinder the performance expected from the idealised structure, i.e. one with a continuous variation of the fibre orientation along one of the planar coordinates.

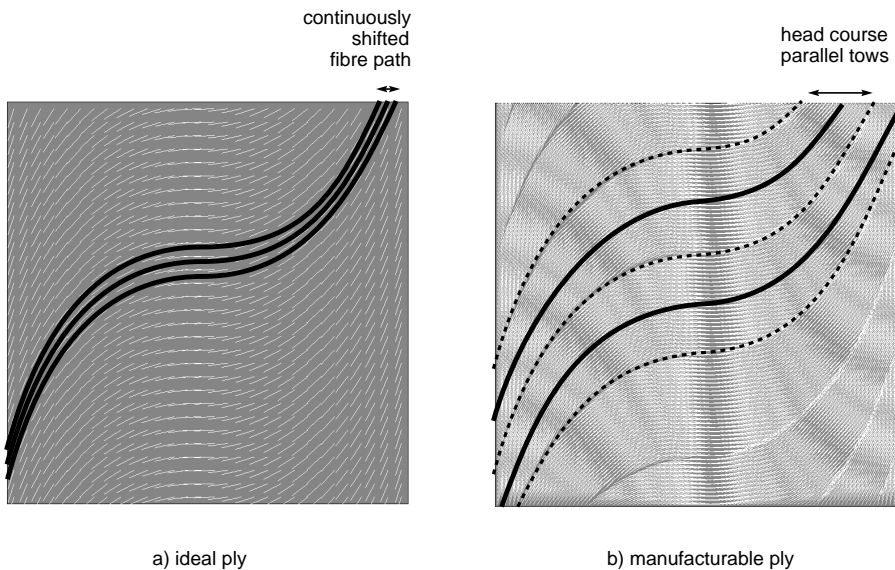


Figure 2.5: Fibre directions on ‘ideal’ and ‘manufacturable’ 300mm×300mm tow-steered plies ( $T_0 = 0^\circ$ ,  $T_1 = 80^\circ$ ,  $\phi = 0^\circ$ ). The course width on the manufacturable ply is 72.6mm (3in).

### Tow-Drops and Tow-Overlaps

As a consequence of the discrete tow course shifting, the boundaries of constant-width neighbouring courses do not match for all locations along the  $x'$ -axis. That is, fibre gaps are created. This leads to irregular regions between tow courses that can be accounted for by prescribing the shift distance so that no gaps occur. However, for curved reference paths, this practice produces regions where tows overlap each other. By allowing tows to overlap, thicker regions are created within the laminate. The smaller the fibre radius, the larger is this local thickness buildup effect. Furthermore, the thickness grows with  $|x'|$ . This effect may not be desirable, for example, in parts that act as control surfaces. However, for other

parts this effect can be advantageous since these thicker regions can act as ‘integral stiffeners’ that improve the load-carrying capability of the structure. Since a VSP is built on a mandrel with a smooth surface, these thickness buildups can only develop on one of the laminate surfaces, rendering the resulting laminate locally asymmetric, which might not be desired.

To prevent the overlapping regions, the tow-placement machine can be instructed to cut the tows individually so that no thickness builds up. This is referred to as the *tow-drop method*, in opposition to the *tow-overlap method* described previously. It results in constant-thickness panels that contain small wedge-like areas free of fibres due to the cutting of the individual, finite thickness tows perpendicular to their axis. These small fibre-free areas are likely to create resin-rich regions during the panelcuring process, and may be hot-spots for damage initiation. The decision on when to drop tows from each course is based on the minimisation of these gaps. Examples of panels manufactured by the tow-drop and overlap methods are shown in Figure 2.6.

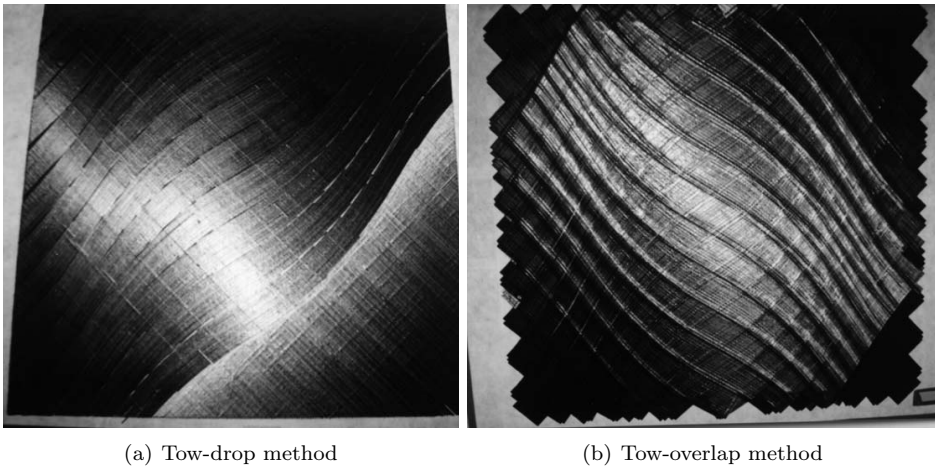


Figure 2.6: Examples of variable-stiffness composite panels manufactured according to two fabrication methods.

### Minimum Cutting Length

The designer of VSP needs to take into consideration where the tows are added and dropped, making sure there are not too many gaps and overlaps within a small area. However, there is a tow length limit for a tow to be correctly placed by the tow-placement head. Because the tow cutter is located between the restart roller and the compaction roller (see Figure 2.2), it would be possible to restart

and cut a tow before it is correctly fed into the compaction roller. In such a case, the tow would not be properly placed onto the part being manufactured. In order to prevent this, a *minimum cutting length*, i.e. the shortest tow length the machine can properly lay down, must be imposed. This length is equal to the distance from the start of the lay-down point to the tow-cutting mechanism in the fibre-placement head and varies according to the tow-placement machine considered. Therefore, in a VSP manufactured according to the tow-drop method, the decision on when to drop tows from each course should be based not only on the minimisation the fibre gaps but also on the compliance with the minimum cut length manufacturing constraint.

### Minimum Turning Radius

Another AFP manufacturing limitation concerns the turning radius of the tow-placement head. In order to avoid local fibre buckling, Nagendra et al.<sup>41</sup> suggest a *minimum turning radius* of 635mm. If the turning radius is too small, the inner tows in the course tend to wrinkle out-of-plane, which leads to imperfections and degrades the load carrying capability of the cured laminate. Therefore, the VSP design process must be able to monitor the turning radius of each configuration in order to reject combinations of the fibre path parameters that produce infeasible designs.

The value of the minimum turning radius proposed by Nagendra et al.<sup>41</sup> is a conservative value valid for a wide range of tow and tow-course widths. In a curved course, the radius of curvature decreases towards the concave side. That means that if the course is wide, the radius of curvature of the inner tows can be severely reduced and they can wrinkle. On the other side, if the course is narrow, the tows are not as prone to wrinkling. Similar reasoning could be applied to the tow width. Therefore, turning radius much smaller 635mm are probably feasible for configurations manufactured with narrow tows and courses. Furthermore, the evolution of the AFP systems may eventually allow for smaller fibre steering radius anyway.

### 2.4.2 Considerations on Design

Since the work initiated by Gürdal and Olmedo<sup>5;6;39</sup>, several authors have devoted their efforts to the development of the tow-steering concept. Either due to the manufacturing constraints imposed by tow-placement machines or due to the increased number of design variables, as compared to straight-fibre laminates, curvilinear-fibre laminates require extra care in the design phase.

### Construction Methods

Waldhart et al.<sup>42;43</sup> divided the formulation of variable-stiffness laminates in two possible methods for construction of tow-steered panels. The first method was the same shifted method used by Gürdal and Olmedo, where the reference fibre is repeatedly shifted a prescribed distance to form the remainder of the ply. By the second method, new courses parallel to the reference path are created. In the *parallel method*, as opposed to the *shifted method*, the outer edges of each course are exactly aligned with the outer edges of the neighbouring courses. This produces a ply with no gaps or overlaps. However, this method also leads to undesirable effects. The reference path is not copied from course to course, hence the fibre curvatures can vary significantly within a lamina. The radius of curvature increases for a path in the convex side of another path, and decreases for a course in the concave side of another course. This effect can lead to kinking of the tow paths. Kinks occur whenever a fibre path passes sufficiently close to the centre of curvature of the reference path. In order to prevent fibre kinking, extra constraints on the curvature of the reference path must be imposed. From a manufacturing standpoint, this implies that each course must be examined individually to ensure that the minimum radius of curvature does not go below the allowed minimum turning radius. Besides this propensity for infeasibility, the parallel construction method creates an undesirable stiffness variation in the direction perpendicular to the fibre angle variation direction. This detracts from the effectiveness of the stiffness tailoring concept. Overall, the parallel method also tends to produce smaller variations in stiffness than the shifted method, hence the the same degree of load redistribution is not possible. This results in smaller structural performance improvements.

More recently, Blom et al.<sup>44;45</sup> expanded the range of possible path definitions to a total of four: a geodesic path, a constant angle path, a linearly varying angle path and a path with constant curvature. Manufacturability of the paths using AFP machines was checked as function of the geometry of the composite part and fibre orientation variables.

### Balancing and Symmetry

Wu and Gürdal<sup>46;47</sup> discussed laminate balancing and symmetry. A laminate is symmetric when its stacking sequence is symmetric about the middle surface with respect to material properties, ply thicknesses and orientation angles, i.e., using the standard notation of the Classical Lamination Theory (CLT)<sup>1</sup>,  $[B] = [0]$ . This can be advantageous in a design because it removes coupling between extension

and bending. Balanced laminates are those for which coupling between in-plane extension and shear is removed ( $A_{16} = A_{26} = 0$ ), so that normal loading does not produce shearing effects, and vice-versa. Due to the fact that balancing requires a symmetric variation of stiffness about both in-plane axes, in general four plies are required for the overall balancing of an arbitrary tow-steered ply within a laminate, as illustrated in Figure 2.7. Since the fibre orientation angle configuration of a structure may be asymmetrical, a reflection about both axes is often required. However, if the original ply configuration possesses some symmetry about either the horizontal or vertical axis, then only two plies are needed for the totally balanced laminate configuration.

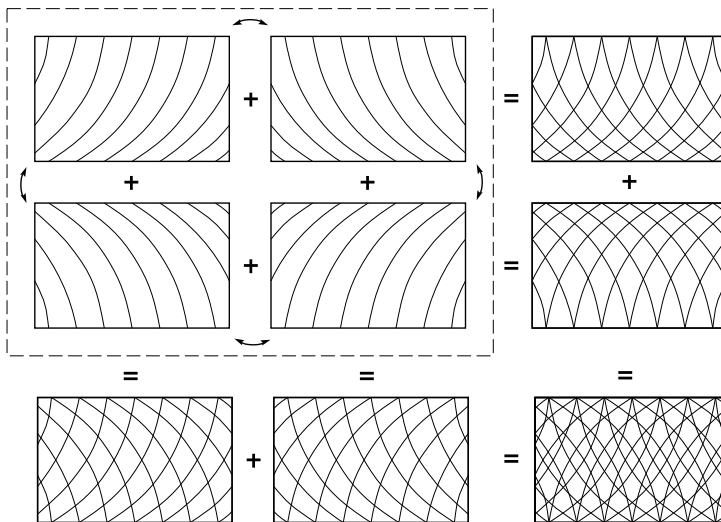


Figure 2.7: Balancing of tow-steered plies.

### Ply Staggering

In a review paper of the tow-placement technology and fabrication of tow-steered laminates, the technique of ply shifting or *staggering* was approached by Gürdal et al.<sup>48</sup>. This technique, illustrated in Figure 2.8, has the purpose of avoiding the collocation of course edges, tow-drops or tow-overlaps, that would occur at the same places through-the-thickness of a laminate in clustered plies i.e. adjacent plies with the same fibre angle distribution.

Collocation of course edges has two different effects depending on the manufacturing method. If the tow-drop method is used, local resin-rich regions can occur throughout the panel thickness, and this can degrade the laminate strength. In



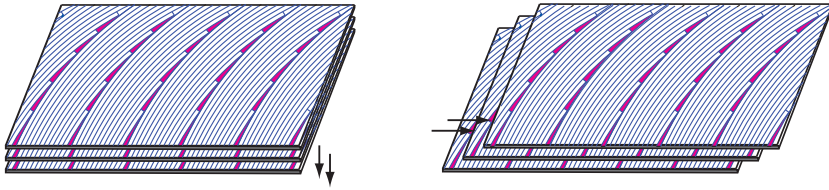
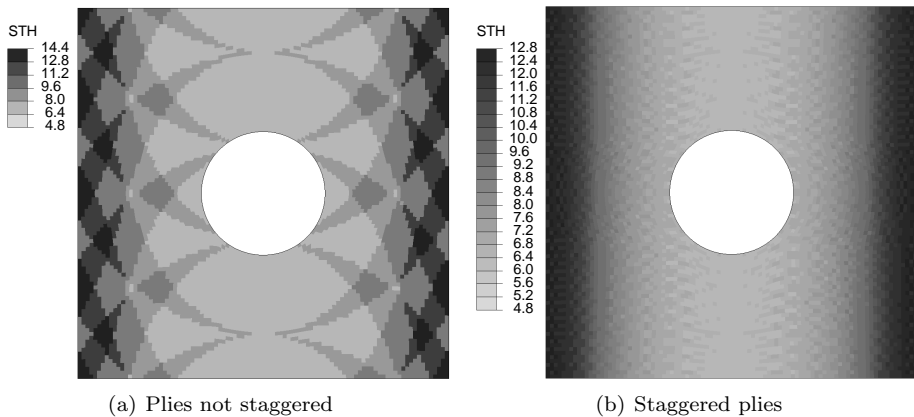


Figure 2.8: Staggering of tow-steered plies.

addition, coincident course edges generate the highest thickness buildups which can be smoothed by ply staggering, hence allowing the production of smooth thickness laminates manufactured by the tow-overlap construction method. As an example, the thicknesses of panels with overlaps manufactured with both methods are illustrated in Figure 2.9. When compared to the traditional overlapping, panels built using this technique showed no appreciable decrease in performance<sup>8</sup>. Unfortunately, ply staggering causes the actual lay-up for a curvilinear-fibre laminate to be locally asymmetric and unbalanced. Several options to achieve the same benefits of staggering with a reduced impact on panel performance were presented by Gürdal et al.<sup>48</sup>. One of these was the alternation of the shifting direction.

Figure 2.9: Thickness distributions for the  $[\pm < 0 | 80 >]_{6s}$  laminate panels with overlaps.

### Stacking Sequence Dispersion

The fibre angle difference between any two adjacent tow-steered plies based on distinct tow paths is not constant in the plane of the laminate. This secondary

effect of adopting the variable-stiffness format can be described using Figure 2.7. Considering the two-ply configuration  $\pm < 0|45 >$ , as an example, the difference in orientation between the layers, or *fibre dispersion*, is  $0^\circ$  at  $x = 0$ , and  $90^\circ$  at  $x = d$  according to the definition given by Equation 2.1. Even in the case of neighbouring plies with the same fibre path definition, the use of the staggering technique results in fibre dispersion. Generalising, the local stacking sequence of tow-steered laminates is typically dispersed. Contrary to the traditional straight-fibre format where the clustering of plies (the placement of adjacent layers at the same orientation) is frequent, in fibre-steered laminates this is neither common nor wanted.

The characteristic stacking sequence dispersion of VSP was never investigated in the past although it may, by itself, have an effect in the response of these laminates, namely in situations that involve interlaminar damage such as lateral impacts. A reason to suspect of possible effects is the difference in number of ply interfaces, plausible of delamination, between clustered and dispersed stacking sequences. The effects of stacking sequence dispersion are investigated in Chapters 6 and 7 of this thesis.

### 2.4.3 Structural Response

The primary objective of varying the orientation of fibres within the plane of laminates is the increase of the structural performance of fibre-reinforced composites in terms of stiffness, buckling and failure characteristics, when compared to traditional straight-fibre laminates. Since the creation of the concept, the structural response of variable-stiffness laminates has been analysed by several authors, whose investigations are briefly described in the following paragraphs.

#### Stiffness and Buckling Performance

Gürdal and Olmedo<sup>5;6</sup> used a numerical iterative technique to solve the system of coupled elliptic partial differential equations governing the in-plane response of VSP. The results showed increases in the axial stiffness of VSP of up to 50% as compared to straight-fibre laminates. Further work by the same authors<sup>39</sup> employed the Rayleigh-Ritz Method to find the buckling loads and modes for two different cases of fibre angles variation. In the first case the fibre orientation varied in the direction of the applied load, whilst in the second the fibre orientation varied perpendicularly to the loading direction. Improvements in the buckling load of up to 80% over straight-fibre configurations were found for the second case while the first case resulted in lower performance improvements. The reason for these

remarkable results was attributed to the load redistribution from the centre of the panel to the higher-stiffened edge regions.

In the follow-up work carried out by Waldhart et al.<sup>42;43</sup> the buckling loads of compression and shear loaded tow-steered panels was analysed by solving the elliptical partial differential equations governing the panel behaviour. Increased buckling performance, as compared to the straight-fibre counterparts, was reported. This was attributed to the stiffness variation, which caused redistribution of the internal loads toward the supported panel edges and favourable transverse stresses that provided additional mechanisms to improve the panel buckling load.

Wu et al.<sup>7;47</sup> conducted experimental and FE studies to characterise the structural response of two different compression-loaded variable-stiffness composite panels. The panels were designed and manufactured according to the tow-drop method and the tow-overlap method, respectively<sup>49</sup>. A baseline cross-ply laminate was also analysed and tested for comparative purposes. VSP, especially the ones with overlapping tows, showed significantly better structural efficiency than the baseline laminate. Experimental data showed transition loads up to 5 times that of the baseline panel. A portion of this increase in performance was attributed to the use of a fibre-steered lay-up. Differences in structural response between the two variable-stiffness were attributed to the regions of overlapping tows which act as local stiffeners, hence increasing the load-carrying capability of the panel manufactured according to the tow-overlap method.

Wu et al.<sup>7;47</sup> found that, for variable stiffness panels, the experimental buckling loads far exceeded the FE predictions. It was determined that the difference between predicted and actual performance was the result of the residual stresses induced by the curing process, which are also responsible for the superior performance demonstrated by tow-steered laminates in comparison with straight-fibre composites. Residual stresses arise during cooling of the composite laminate to the room temperature and can be defined as the stress distribution that persists in a material that is free of external forces or temperature gradients<sup>40</sup>. Non-linear FE analyses with thermal prestresses were performed to correlate better the predictions with the test results. Another approach consisted in simulating the prestresses resulting from mechanical edge straightening that is necessary because of the large anticlastic imperfections which are present in the cured VSP. The analyses with thermal prestresses resulted in a more consistent correlation with test results than the analyses with mechanical prestresses.

Tatting and Gürdal<sup>50</sup> optimised a panel with central hole for compressive buckling load. First, a panel without the hole was considered for the optimisation study. Then, the hole was added to the best lay-up and the panel analysed in the

FE code STAGS (S**T**ructural **A**nalysis of **G**eneral **S**hells)<sup>51</sup>. As compared to the baseline panel with lay-up  $[\pm 45_2 / \pm 30 / \pm 45 / \pm 15]_s$ , the best curvilinear-fibre panel ( $[\pm 45 / 0 \pm < 45 | 60 >_2 / 0 \pm < 30 | 15 > / 0 \pm 45 | 60 >]_s$ ), achieved an improvement in load-carrying capability of over 60% with no appreciable increase in weight. These results were attributed, once again, to the capacity of tow-steered panels to divert stresses away from the panel centre sections towards the supported edges. This kind of analysis was carried for three different hole sizes<sup>52;53</sup>. Then, the chosen configurations, as well as baseline panel and a curvilinear-fibre panel without central hole, were manufactured and tested by Jegley et al.<sup>8;9</sup>. Reasonable agreement was observed for the straight-fibre specimens but buckling and post-buckling behaviour was not as accurately predicted for the tow-steered specimens. The tow-drop specimens showed buckling loads about 10% greater than the comparable straight-fibre specimens, while the tow-overlap panels almost doubled the constant-stiffness panels buckling loads. Jegley et al. also analysed and tested tow-steered panels under shear-loads<sup>8;9</sup>. Despite not being optimised for shear solicitations, variable-stiffness composite specimens reached higher buckling loads than their straight-fibre counterparts. However, the results were not as expressive as for the compressive buckling behaviour.

An overview of the effects of fibre-steering on the in-plane stiffness and buckling responses of tow-steered panels was presented by Gürdal et al.<sup>10</sup>. Stiffness variations in the direction parallel and perpendicular to the direction of the loading were analysed. A much higher degree of improvement (as high as 80%) due to the redistribution of the applied loads is predicted for the second case, as mentioned previously. This work also demonstrates that the variable stiffness concept provides design flexibility for trade-offs between overall panel stiffness and buckling load, meaning that there are many configurations with equal buckling loads yet different global stiffness values, or vice versa. The analyses performed by Gürdal et al.<sup>10</sup> were further refined by Abdalla et al.<sup>40</sup> with the inclusion of residual thermal stresses which were responsible for a duplication of the buckling performance differential between variable and constant-stiffness panels.

The variable-stiffness concept has been extended to structures other than plates. Tatting<sup>54</sup> investigated the application of the variable-stiffness concept to thin cylindrical shells of various lengths. Conical shells have been studied by Blom et al.<sup>44;45</sup>. It was shown that the variable-stiffness concept is most effective at improving the bending response of long cylinders through the use of a circumferential stiffness variation.

### Failure Performance

First-ply failure analyses and failure tests were the subject of a few works on variable-stiffness laminates. However, the damage mechanisms that lead to the final failure of these structures were not thoroughly studied. The reason for this may be found on the fact that the potential applications of tow-steered composite panels are compression-loaded structural parts for which the buckling loads are generally the limiting factor. By guaranteeing that laminates fail at much higher loads than buckling level, a rather easy task when considering thin-shelled structures under compression, designers assure that all damage and catastrophic phenomena take place outside of the loading envelope.

Waldhart et al.<sup>42;43</sup> considered failure, along with the minimum turning radius, as a constraint on the production of tow-steered panels. The Tsai-Hill first-ply failure criterion<sup>55</sup> was applied to rule out configurations with first-ply failure loads lower than buckling loads. The use of this criterion was chosen over other failure prediction methods, such as the maximum stress and maximum strain theories, because it offers a more continuous strength variation that accompanies changes in orientation angle and it incorporates interactions between the failure strengths that some other theories completely neglect. The drawback found in using the Tsai-Hill criterion is that it does not reveal the mechanisms of failure. Langley<sup>56</sup> used several failure criteria implemented in the Genesis FE solver to find the limit compressive load allowed on VSP. For an edge-displaced laminate with a  $[\pm < 0|45 >]_s$  lay-up, Langley concluded that failure would occur due to a shearing mode along the displaced edge.

Wu et al.<sup>7;47</sup> analysed and tested tow-steered panels, as well as a baseline cross-ply plate, under compression loads up to failure. The tests performed on the variable stiffness panels showed a linear pre-buckling load-deflection response, followed by a nonlinear response until failure, which occurred at load levels about three times greater than the buckling loads. The weight-normalised failure loads were found to be approximately 28% and 8% greater than the baseline panel, respectively for the tow-steered laminates with and without overlapping tows. Attempts to numerically simulate the nonlinear postbuckling response relying solely on geometrically nonlinear analysis resulted in inaccurate results. The introduction of nonlinear shear behaviour allowed the correct simulation of the postbuckling path<sup>57</sup>. However, the parameters of the nonlinear material model were neither characterised nor estimated *a priori* but determined based on the best fitting of the experimental results.

Jegley et al.<sup>8;9</sup> tested compression and shear-loaded VSP up to global struc-

tural failure, and compared the results with straight-fibre configurations. The geometries included central holes of various sizes. The Tsai-Hill first-ply failure criterion<sup>55</sup> was initially applied on candidate designs to guarantee that the panels produced would fail at loads much higher than the buckling loads. The panels manufactured by the tow-overlap method carried loads more than three times their buckling loads while shear-loaded specimens reached at least twice their buckling load levels before failure. Overall, VSP had a failure performance up to 60% higher than the constant-stiffness configurations.

More recently, Alhajahmad<sup>58-60</sup> designed tow-placed pressurised fuselage panels with and without cutouts for maximum strength performance. The Tsai-Wu first ply failure criterion<sup>18</sup> was used in the optimisation algorithm. Improvements in panel load carrying capacity of 50% and above were achieved.

### Thermal Behaviour

Analyses on the thermal behaviour of variable stiffness laminates were carried by Wu and Gürdal<sup>46;47</sup>. One of the research goals was to experimentally evaluate the structural response of curvilinear and straight-fibre panels when subjected to thermal loads and compare it with the results predicted by the CLT. The correlation between the measured and predicted coefficients of thermal expansion ranged from excellent to poor. The best correlation was achieved for laminates that are close to an orthotropic cross-ply laminate, i.e. for a  $\pm 45^\circ$  lay-up.

## 2.5 Contribution to the Development of Variable-Stiffness Panels

The research carried in the framework of this thesis has the objectives of expanding the present knowledge about the structural behaviour of VSP, and of promoting the development of the variable-stiffness laminate concept. Specifically, the potential in terms of strength improvements, in comparison with conventional laminate designs, is investigated more thoroughly than before. In a first approach (Chapter 3), the elastic limits of the structural response of idealised VSP are defined. This is achieved by means of state-of-the-art, physically-based failure criteria and reliable FE models. Then, manufacturability issues, such as the residual thermal stresses due to panel curing, the fibre angle deviations from the reference path due to the finite width of the machine head course, tow-drops and tow-overlaps are investigated in terms of their effects on the panel failure response. In the attempt to mitigate eventual degradation of the expected performance, design

techniques such as ply staggering and laminate hybridisation are attempted and their accomplishments described.

The potential for damage accumulation before final failure is explored (Chapters 4 and 5) by simulating the progressive failure behaviour of VSP by means of continuum damage models. The reliability of this methodology is ascertained by correlation with experimental results.

Finally, the research focuses on the effects of stacking sequence dispersion (Chapters 6 and 7), one of the characteristics fibre-steered laminates. However, the stacking sequence dispersion is looked at not by being an aspect concerning only VSP, but is approached in a broader sense, by being a possible characteristic of other non-conventional laminates, for example the ones built exclusively with straight-fibre plies. Therefore, this thesis derives from the specific subject of variable-stiffness composite laminates to contemplate non-conventional laminates in general.





## Chapter 3

# Elastic Response of Variable-Stiffness Panels

### 3.1 Introduction

PREVIOUS analytical investigations<sup>5;6;10;39</sup> predicted significant advantages offered by VSP in terms stiffness and buckling loads. Experimental research<sup>7-9;46</sup> demonstrated the superiority of these designs concerning stiffness and buckling response as well as strength. The improvements were attributed, in cases where the fibre orientation variation is perpendicular to the loading, to the redistribution of the applied in-plane loads to the stiff support regions and, in the cases where the fibre orientation variation is parallel to the loading, to the favourable distribution of the transverse in-plane stresses. The best results were achieved through the redistribution of the applied loads. Furthermore, it was found that the residual thermal stresses due to the laminate curing cycle can have a significant positive effect on the buckling response of VSP<sup>7</sup>. Numerical investigations in which thermal stresses were taken into account<sup>7;40;61</sup> achieved good correlation between simulated and experimental results.

The knowledge about the variable-stiffness configurations that lead to the highest ultimate loads is still rather limited. Furthermore, the full details about the mechanisms that lead to failure of VSP are not known yet, particularly the influence of local effects such as tow-drops or tow-overlaps. The few analyses on these designs that involved failure considerations<sup>8;9;42</sup> were mostly restricted to the application of the Tsai-Hill first-ply failure criterion<sup>55</sup> for the sole purpose of guaranteing that buckling rather than failure would be the design driver for these

structures, i.e. that failure would occur well in the postbuckling regime of the panels with the best buckling response. Although the Tsai-Hill criterion takes into account quadratic interaction between stress components, its formulation is based on curve-fitting techniques that do not account for the effect of the ply thickness on the strength. Furthermore, it does not identify the failure mode. The same considerations apply to the Tsai-Wu criterion<sup>18</sup> used by Alhajahmad<sup>58</sup> in the design tow-placed pressurised fuselage panels, with and without cutouts, for maximum strength performance.

The typical elastic response envelope allowed by fibre-steered panel designs under compression is characterised in this chapter. This means evaluating the boundaries of the behaviour of VSP under edge shortening, in the elastic regime, up to the onset of damage which eventually occurs in postbuckling. This task involves the evaluation of the response characteristics of VSP, for all possible combinations of the fibre orientations, concerning buckling response and first-ply failure in the postbuckling regime. Furthermore, the influence of a central circular hole on these responses is predicted. To achieve these purposes, numerical analyses are carried out using the commercial FE package ABAQUS<sup>62</sup>. The onset of damage in the laminates is evaluated using stress-interactive, physically-based first-ply failure criteria which identify the failure mechanisms occurring within the plies of the laminate. This means that out-of-plane failure events, such as interply delaminations, are not considered herein. Hence, the current work is a preliminary assessment of tow-steered configurations compared with straight-fibre laminates, based only on their in-plane behaviour.

As a first approach, only ‘ideal’ variable-stiffness configurations are analysed i.e. designs where the reference fibre path is continuously shifted to cover the full ply. A second, and more refined approach, consists in introducing the manufacturing effects described in Section 2.4, such as tow-drops and tow-overlaps, and evaluating their influence on the panel failure response. The effects of ply staggering on VSP buckling and first-ply failure responses are also assessed.

## 3.2 First-Ply Failure Criteria for FRP

Strength-based criteria are the usual methodology for predicting the onset of failure events in composite structures due to their ease of use with the FE method. A large number of criteria relating stresses and experimental measures of material strength to the onset of failure have been proposed in the past decades. París<sup>63</sup> discusses thoroughly the failure criteria proposed by Tsai<sup>18;55</sup>, Hashin<sup>64</sup>, Puck<sup>65</sup>, Sun<sup>66</sup>, and several others. The World Wide Failure Exercise (WWFE) was con-

ceived and conducted by Hinton and Soden<sup>67</sup> in order to assess the predicting capability of the available failure criteria. One important conclusion from this event was that the mechanisms that lead to failure of laminated composite materials were not fully understood at the time. Meanwhile, new physically-based failure criteria have been developed and proposed. These represent a step further in the quest to identify the phenomena at the origin of the failure process. Phenomenological-based criteria are widely applicable, as opposed to curve-fitting based criteria whose applicability is restricted to the particular load cases from which they were derived.

A set of physically-based criteria, developed at the NASA - Langley Research Centre (LaRC), is used in this chapter for the analysis of first-ply failure behaviour of constant and variable-stiffness composite panels in the postbuckling regime<sup>68;69</sup>. The LaRC failure criteria<sup>70;71</sup> are capable of accurately predicting the main failure modes of FRP: matrix compression failure, fibre compression failure, matrix tensile failure, and fibre tensile failure.

The correct prediction of first-ply failure using all components of the stress tensor would require the combination of LaRC04<sup>71</sup>, a three-dimensional failure criterion, with fully three-dimensional FE models. There are several situations where the correct prediction of failure onset requires three-dimensional failure criteria. For example, the well-know effect of hydrostatic pressure on the composite compressive strength<sup>71</sup> can only be represented using a fully three-dimensional analysis. The combination of LaRC04 with a criterion for the initiation of ply delamination, such as the quadratic stress criterion proposed by Brewer and Lagace<sup>72</sup> would provide a complete assessment of the failure performance of composite laminates. For the sake of simplification and efficiency, the analyses performed in this work are based on two dimensional shell elements. The set of failure criteria LaRC04 is simplified to the LaRC03 version<sup>70</sup>, which does not use the out-of-plane components of the stress tensor. Panel failure in the postbuckling regime is certainly influenced by components of the stress tensor other than  $\sigma_1$ ,  $\sigma_2$  and  $\sigma_{12}$ , namely by the transverse shear stress components  $\sigma_{13}$  and  $\sigma_{23}$ . However, it is considered herein that first ply failure is mainly driven by the membrane components of the stress tensor. Furthermore, the occurrence of delaminations, traditionally caused by interlaminar stresses that arise due to differences in ply compliance (and out-of-plane loading), is not considered.

Delamination, caused or potentiated by interlaminar stresses<sup>73</sup>, is a key failure mode in laminated materials. A VSP has, by definition, a nonuniform in-plane stiffness distribution that might result, as will become clear, in large in-plane stress gradients. Such gradients contribute to the amplification of the interlami-

nar stresses, as demonstrated by Saeger et al.<sup>74</sup>, and possibly to render delamination the dominant failure mode in these configurations. Furthermore, VSP have manufacturing characteristics, such as course edges, tow-drops and overlaps, as described in Section 2.4, which may act as discontinuities and stress concentration zones that locally excite the interlaminar stresses further. Similar mechanisms develop in material discontinuities<sup>75</sup> such as free edges (e.g. in holes), notches and ply drop-offs<sup>76</sup>.

Hence, the current work is a preliminary assessment of tow-steered configurations, based only on their in-plane behaviour. In this way the analyses are substantially simplified, the modelling difficulties are kept low, and a sound basis for the comparison of VSP with straight-fibre laminates is still achieved. However, care should be taken in drawing definite conclusions about their failure performance.

### 3.2.1 The LaRC Failure Criteria

The following paragraphs describe the LaRC first-ply failure functions<sup>77</sup>,  $\phi_N$ , corresponding to the in-plane loading modes in FRP plies: longitudinal tension ( $N = 1+$ ), longitudinal compression ( $N = 1-$ ), transverse tension ( $N = 2+$ ), and transverse compression ( $N = 2-$ ).

**Transverse Compressive Fracture** Under compressive transverse loads, the matrix fails by transverse shear. For pure compression, the angle of the fracture surface with respect to the through-the-thickness direction is generally  $\alpha_0 = 53 \pm 2^\circ$  for most composite materials<sup>70;71</sup>. The existence of compressive stresses acting on the potential fracture surfaces with associated friction stress explain why this angle differs from the angle of maximum shear stresses,  $\alpha = 45^\circ$ . For a general loading case, the fracture plane might assume a different orientation,  $\alpha$ , as is illustrated in Figure 3.1, that depends on the particular combination of shear and normal tractions in that plane.

In a plane stress situation, the tractions are obtained from the components of the stress tensor defined in the material coordinate system as:

$$\begin{aligned}\sigma_n &= \frac{\sigma_{22}}{2} [1 + \cos(2\alpha)] \\ \tau_T &= -\frac{\sigma_{22}}{2} \sin(2\alpha) \\ \tau_L &= \sigma_{12} \cos(\alpha)\end{aligned}\tag{3.1}$$

wherein  $\sigma_{22}$  and  $\sigma_{12}$  are the in-plane transverse stress and shear stresses, respectively. The subscript  $n$  denotes the direction normal to the fracture plane,  $L$  holds

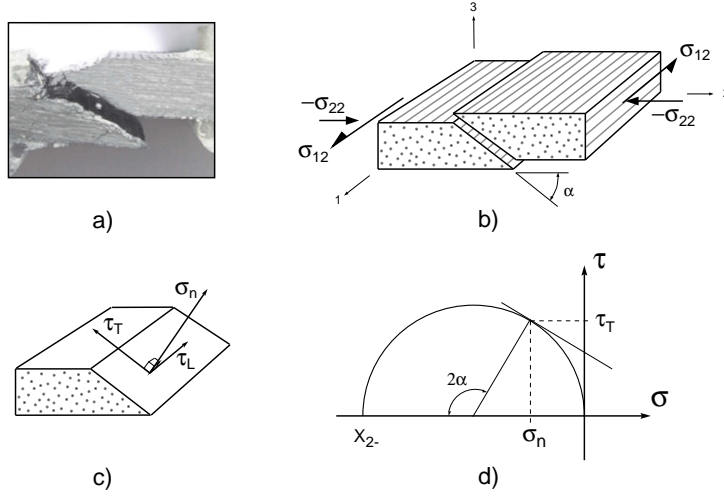


Figure 3.1: a) Pure transverse compression failure for a CFRP specimen; b) Fracture plane for a ply subjected to transverse compression and in-plane shear; c) Stresses in the fracture plane; d) Geometrical representation of the Mohr - Coulomb criterion.

for the longitudinal direction or the direction of the fibres and  $T$  is the direction transverse to the fibres and parallel to the fracture plane. The criterion for matrix compression failure is a function of these three components. The failure surface associated with transverse compression is represented by:

$$\phi_{2-} = \left( \frac{\tau_T}{X_{6T} - \mu_T \sigma_n} \right)^2 + \left( \frac{\tau_L}{X_{6L}^{is} - \mu_L \sigma_n} \right)^2 = 1 \quad (3.2)$$

where the longitudinal shear strength  $X_{6L}^{is} = X_6^{is}$  accounts for the in-situ effects according to the closed-form solutions proposed by Camanho et al.<sup>78</sup> and presented later in this section. The shear strength transverse to the fibres is calculated using:

$$X_{6T} = X_{2-} \cos \alpha_0 \left( \sin \alpha_0 + \frac{\cos \alpha_0}{\tan(2\alpha_0)} \right) \quad (3.3)$$

wherein  $X_{2-}$  is the ply transverse compressive strength. The angle of the fracture surface with the through-the-thickness direction for a pure compression case,  $\alpha_0$  should be determined experimentally. Again, for most composite materials  $\alpha_0 = 53 \pm 2^\circ$ . The coefficient of transverse friction,  $\mu_T$ , is given by:

$$\mu_T = -\frac{1}{\tan(2\alpha_0)} \quad (3.4)$$

and for the longitudinal friction coefficient,  $\mu_L$ , the following relation is generally applied:

$$\frac{\mu_L}{X_{6L}} = \frac{\mu_T}{X_{6T}} \quad (3.5)$$

**Transverse Tensile Fracture** The LaRC criterion for matrix tensile failure, corresponding to a fracture plane perpendicular to the ply plane, is defined as:

$$\phi_{2+} = (1 - g) \left( \frac{\sigma_{22}}{X_{2+}^{is}} \right) + g \left( \frac{\sigma_{22}}{X_{2+}^{is}} \right)^2 + \left( \frac{\sigma_{12}}{X_6^{is}} \right)^2 = 1 \quad (3.6)$$

The variable  $g$  is the fracture toughness ratio defined by

$$g = \frac{\mathcal{G}_{Ic}}{\mathcal{G}_{IIc}} \quad (3.7)$$

wherein  $\mathcal{G}_{Ic}$  and  $\mathcal{G}_{IIc}$  are the mode I and II fracture toughness, respectively, and  $X_{2+}$  is the transverse tension strength. The in-situ effects are taken into account by calculating the in-situ strengths  $X_{2+}^{is}$  and  $X_6^{is}$  as a function of the ply thickness<sup>78</sup>.

**Longitudinal Compressive Fracture** Under compressive loads, fibres fail by kinking. The most recent advances in the study of the process of kink-band formation suggest that kinking is initiated by local microstructural defects, such as fibre misalignments and longitudinal or interfacial, matrix cracking rather than triggered by a global microbuckling mode<sup>70;71</sup>. In the present model, an initial fibre misalignment is assumed to exist in the lamina, which leads to shearing stresses between the fibres. These further rotate the fibres which, in turn, lead to further increase the shear stresses. This mechanism, illustrated in Figure 3.2, can lead to the formation of a kink-band, i.e. fibre compressive failure<sup>79;80</sup>.

In a plane stress situation, the stresses in the misalignment frame of a lamina being compressed are calculated by:

$$\begin{aligned} \sigma_{11}^m &= \frac{\sigma_{11} + \sigma_{22}}{2} + \frac{\sigma_{11} - \sigma_{22}}{2} \cos(2\varphi) + \sigma_{12} \sin(2\varphi) \\ \sigma_{22}^m &= \frac{\sigma_{11} + \sigma_{22}}{2} - \frac{\sigma_{11} - \sigma_{22}}{2} \cos(2\varphi) - \sigma_{12} \sin(2\varphi) \\ \sigma_{12}^m &= -\frac{\sigma_{11} - \sigma_{22}}{2} \sin(2\varphi) - \sigma_{12} \cos(2\varphi) \end{aligned} \quad (3.8)$$

where  $\sigma_{11}$  is the longitudinal stress and the superscript  $m$  denotes the frame misaligned by an angle  $\varphi$  from the principal fibre direction. The failure criteria expressed in Equations 3.2 and 3.6 can now be used within this stress state to check for matrix failure. For a pure compression case, the misalignment angle at

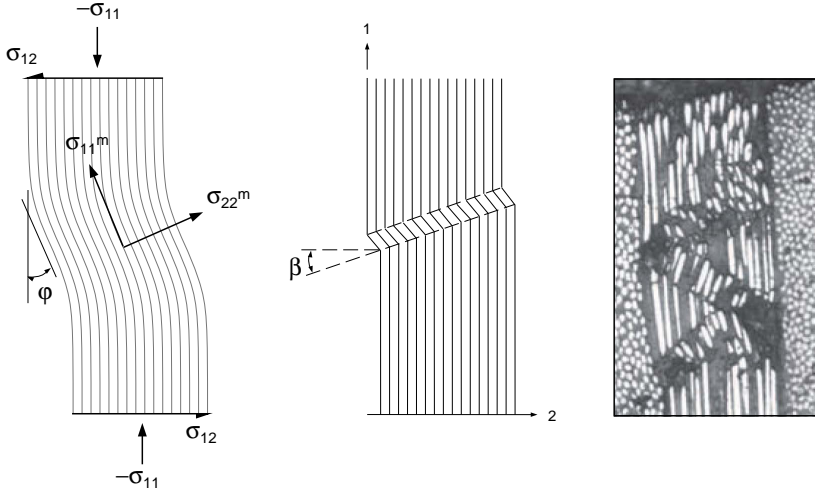


Figure 3.2: Illustration of fibre kink-band formation and misalignment frame.

failure,  $\varphi_c$ , can be found by applying Equations (3.8) into Equation (3.2). This yields:

$$\varphi_c = \arctan \left( \frac{1 - \sqrt{1 - 4 \left( \frac{X_6}{X_{1-}} + \mu_L \right) \frac{X_6}{X_{1-}}}}{2 \left( \frac{X_6}{X_{1-}} + \mu_L \right)} \right) \quad (3.9)$$

wherein  $X_{1i}$  is the ply longitudinal compressive strength and  $\varphi_c$  is the sum of an initial misalignment with the rotation due to loading  $\gamma_c^m$ . The initial misalignment angle can be regarded as a material property that embodies an actual initial misalignment or simply microstructural defects which may lead to kinking, like variations in the fibre volume fraction, poor bonding to the resin or microcracks in the resin<sup>79;80</sup>.

The criteria for fibre failure are constituted by the Equations (3.2) and (3.6) applied in the misalignment frame, i.e:

$$\phi_{1-} = (1 - g) \left( \frac{\sigma_{22}^m}{X_{2+}^{is}} \right) + g \left( \frac{\sigma_{22}^m}{X_{2+}^{is}} \right)^2 + \left( \frac{\sigma_{12}^m}{X_6^{is}} \right)^2 = 1 \quad (3.10)$$

for  $\sigma_{22}^m \geq 0$  and

$$\phi_{1-} = \left( \frac{\sigma_{12}^m}{X_6^{is} - \eta_L \sigma_{22}^m} \right)^2 = 1 \quad (3.11)$$

for  $\sigma_{22}^m < 0$ . The quadratic term with  $\tau_T$  is not considered here because, in this case, fracture is assumed to occur in the through-the-thickness plane ( $\alpha = 0^\circ$ ).

**Longitudinal Tensile Fracture** In the case of fibre tension, it is assumed that only the longitudinal stress contributes to promote failure. Therefore, the maximum stress criterion for fibre failure is defined by:

$$\phi_{1+} = \frac{\sigma_{11}}{X_{1+}} = 1 \quad (3.12)$$

wherein  $X_{1+}$  is the ply longitudinal tension strength.

In summary, the failure surfaces determined by the LaRC failure criteria (Equations 3.2, 3.6, 3.10, 3.11 and 3.12) are represented in Figure 3.3.

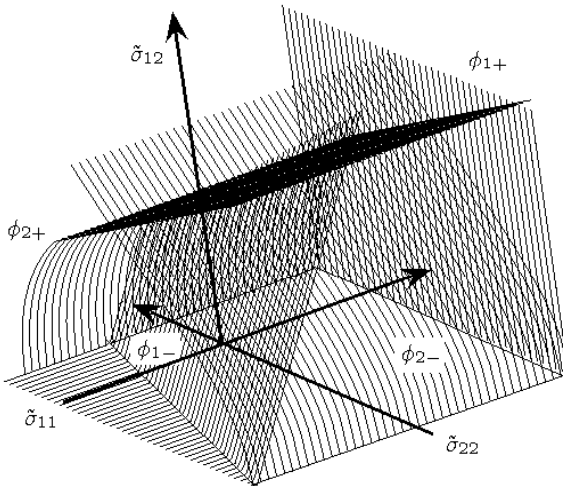


Figure 3.3: Typical failure surfaces determined by the LaRC failure criteria.

### 3.2.2 In-Situ Effects

The LaRC failure criteria take into account the *in-situ effect* characterised by higher transverse tensile and shear strengths of a ply when it is constrained by plies with different fibre orientations in a laminate, as compared with the strength of the same ply in a unidirectional laminate<sup>78</sup>. This means that when evaluating the strength of a laminate, the unidirectional strength values of each lamina should be adjusted to take into account for its position within the laminate and its thickness ( $h_p$ ), or the overall number of plies clustered at the same fibre orientation.



The in-situ transverse tensile and in-plane shear strengths follow from the respective critical energy release rate for crack propagation. The concept of interaction energy, which is defined as the energy released by the introduction of a crack in a ply subjected to in-plane transverse tensile and shear stresses, is used to calculate the individual components of the energy release rate from which the in-situ strengths are obtained<sup>78</sup>. Three distinct cases need consideration: thin embedded plies, thick embedded plies and laminate face plies.

**Thin Embedded Plies** For thin embedded plies, the transverse tensile strength is given by:

$$X_{2+}^{is} = \sqrt{\frac{8G_{Ic}}{\pi h_p \Lambda_{22}^0}} \quad (3.13)$$

wherein

$$\Lambda_{22}^0 = 2 \left( \frac{1}{E_2} - \frac{\nu_{12}^2}{E_1} \right) \quad (3.14)$$

The in-plane shear strength is:

$$X_6^{is} = \sqrt{\frac{(1 + \kappa \chi G_{12}^2)^{1/2} - 1}{3\chi G_{12}}} \quad (3.15)$$

with

$$\chi = \frac{12X_6^2}{G_{12}} + 18\kappa X_6^4 \quad (3.16)$$

wherein  $\kappa$  defines the non-linearity of the shear stress - shear strain behaviour in the polynomial relation

$$\gamma_{12} = \frac{1}{G_{12}} \sigma_{12} + \kappa \sigma_{12}^3 \quad (3.17)$$

**Thick Embedded Plies** The in-situ transverse tensile strength of thick embedded plies is given by:

$$X_{2+}^{is} = 1.12\sqrt{2}X_{2+} \quad (3.18)$$

The in-situ shear strength is obtained by solving

$$\frac{(X_6)^2}{G_{12}} + \frac{6}{4}\kappa(X_6)^4 = \frac{(X_6^{is})^2}{2G_{12}} + \frac{3}{4}\kappa(X_6^{is})^4 \quad (3.19)$$

which has two imaginary roots and two real roots with opposite signs. The in-situ shear strength of a thick ply,  $X_6^{is}$ , corresponds to the positive real root of Equation 3.19.

**Laminate Face Plies** The in-situ strength of laminate face plies, constrained only at one of the surfaces, is lower than that of their embedded counterparts since less energy is required to propagate cracks at a free surface. Then, the transverse tensile strength is:

$$X_{2+}^{is} = 1.79 \sqrt{\frac{\mathcal{G}_{Ic}}{\pi h_p \Lambda_{22}^0}} \quad (3.20)$$

and the in-plane shear strength is given by equation (3.15) with

$$\chi = \frac{24\mathcal{G}_{IIc}}{\pi h_p} \quad (3.21)$$

### 3.3 Elastic Response Characteristics

Gürdal et al.<sup>10;40</sup> investigated the stiffness and buckling response characteristics of ‘ideal’ VSP configurations with linearly varying fibre orientations, by considering the whole range of possible angles  $T_0$  and  $T_1$ . The present investigation follows the same procedure as Gürdal et al. to determine the first-ply failure response characteristics of panels with holes in the postbuckling regime. Herein, residual thermal stress, eigenvalue extraction and nonlinear postbuckling, and failure calculations are carried out using the commercial FE package ABAQUS<sup>62</sup>. This approach allows more versatility in the geometries under consideration (e.g. a panel with a hole) as well as offering extended analysis capabilities. The failure criteria introduced in the previous section are implemented in a special-purpose FORTRAN subroutine `UARM` to obtain `User defined VARIables` at FE `Material` points. This subroutine is run at every load increment along the prebuckling and postbuckling regimes for every integration point of the FE model, postprocessing the stress field components and calculating the values of the LaRC failure indices. A refined step-wise load incrementation ensures that the load level at which the first criterion equals unity is captured with enough accuracy. This point corresponds to the onset of damage in the laminate. Further load incrementation would cause a degraded stiffness response, eventually leading to final collapse. However, this non-linear progressive damage behaviour is only analysed in the next chapter.

FE calculations are performed discretely at each  $5^\circ$  for each  $T_0$  and  $T_1$  in the  $0^\circ - 90^\circ$  range, where  $T_0$  and  $T_1$  are, respectively, the fibre angles at the centre

and at the edges of VSP with linear fibre orientation variation, as described in Chapter 2. The FE models make use of shell elements of reduced integration (S4R). For fibre-steered laminates, each element of the FE model is associated with a particular lay-up, as opposed to straight-fibre formats where the same lay-up applies to the entire mesh. The local stacking sequence is calculated with Equation 2.1 at the centroid of each element, i.e. in practical terms the fibre orientation variation is discrete. Between each two neighbouring elements, the maximum fibre angle difference is  $6^\circ$ .

Following Gürdal et al.<sup>10;40</sup>, the results presented here are in non-dimensional form in order to simplify the comparison between straight-fibre and variable-stiffness laminates. Furthermore, they refer to 24 ply laminates of the form  $[\phi \pm < T_0 | T_1 >]_{6s}$ , made of the carbon-epoxy material system AS4/9773, with nominal ply properties presented in table 3.1. The layer thickness,  $h_p$ , is 0.2mm and the total laminate thickness,  $h_l$ , is 4.8mm. The in-situ strengths, as calculated for this configuration with the presented formulation, are shown in table 3.2.

Table 3.1: AS4/9773 nominal material properties

Elastic properties:	$E_1=129.8$ GPa; $E_2=9.2$ GPa; $G_{12}=5.1$ GPa; $\nu_{12}=0.36$
Thermal expansion [ $^\circ C^{-1}$ ]:	$\alpha_{11} = -34.2 \cdot 10^{-8}$ ; $\alpha_{22} = 34.4 \cdot 10^{-6}$
Ply strengths [MPa]:	$X_{1+}=2070$ ; $X_{1-}=1160$ ; $X_{2+}=29.0$ ; $X_{2-}=157.9$ ; $X_6=91.0$

Table 3.2: In-situ strengths for the present problem

Ply position	$X_{2+}^{is}$ [MPa]	$X_6^{is}$ [MPa]
embedded ply ( $h = h_p$ )	135.1	141.1
embedded ply ( $h = 2h_p$ )	95.5	116.3
outer ply ( $h = h_p$ )	85.4	116.3

Within the framework of the parametric studies presented in this section, the finite width of the tow-course, i.e the course of the AFP machine head pass, is not considered. Instead, in a simplified approach, each course is considered to have an infinitesimal width, or the width of a single fibre. This means that there is a continuous shifting of the reference path in the direction perpendicular to the fibre orientation variation instead of a discrete shifting as imposed by a finite

width tow-course, as illustrated in Figure 2.5. In this ‘ideal’ design, the fibre paths do not have a constant distance between them, and appear to converge and diverge from one another. Such a fibre path variation can only be possible if the fiber volume fraction of the laminate changes. However, since the fibre placement machines that are used to build panels of the type studied here have finite width machine heads with a fixed number of fiber tows, the fibre paths are parallel within a given course. These aspects will be addressed in Section 3.4, wherein the response of ‘ideal’ and ‘manufacturable’ configurations are compared.

### 3.3.1 Buckling

The first case under analysis is a simply supported flat square plate under uniform edge shortening,  $v(x, b/2) = v_0$ , as depicted in Figure 3.4. The transverse edges are free to expand in the  $x$  direction. The fibre orientation,  $\theta$ , is a function of the  $x$ -coordinate only ( $\theta = \theta(x)$ ,  $\phi = 0^\circ$ ). Thus, the laminate takes the general form  $[\pm < T_0 | T_1 >]_{6s}$ . This set-up is different from the one adopted in previous works by Gürdal et al.<sup>10;40</sup>, where the loading was applied along the  $x$ -axis and the fibre orientation varied with the  $y$ -axis. Hence, the whole panel was rotated by  $90^\circ$  with respect to the one herein, and the configuration was of the form  $[90 \pm < T_0 | T_1 >]_{6s}$ .

For the purpose of this study, the panel can be treated in a non-dimensional form in the  $x - y$  plane. Should it be produced, however, it would have to cope with minimum manufacturable dimensions. The most restrictive parameter is the *minimum turning radius* already explained in the previous chapter. If the value of 635mm suggested by Nagendra et al.<sup>41</sup> is followed, the panel would have to be at least 1270×1270mm in size to allow for variations of  $T_0$  and  $T_1$  in the  $0 - 90^\circ$  range.

In this loading case, the transverse stress resultant,  $N_x$ , and the in-plane shear resultant,  $N_{xy}$ , are zero over the entire panel, and it expands uniformly in the  $x$  direction leaving the transverse edges straight. However, unlike a traditional straight-fibre laminate, the variation of the  $u$  displacement is not linear along the  $x$  direction but depends on the variation of the in-plane stiffness terms along this coordinate<sup>10</sup>. One of the most important consequences of the present configuration ( $v(x, b/2) = v_0$ ,  $\theta = \theta(x)$ ) is a favourable stress resultant along the load direction. As an example, the schematic representation of the  $N_y = N_y(x)$  variation, for a laminate with small angle  $T_0$  and a larger angle  $T_1$ , under uniform edge shortening,  $v_0$  is shown in Figure 3.5.

Although uniform edge displacements are used for loading the panels, the fol-

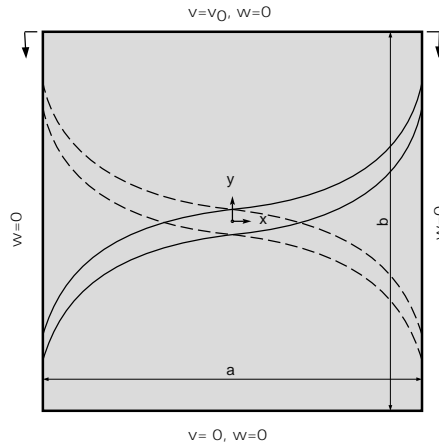


Figure 3.4: VSP geometry and boundary conditions ( $a/b=1$ ). Transverse edges free in in-plane deformations. Stiffness variation in the  $x$  direction, perpendicular to the loading direction.

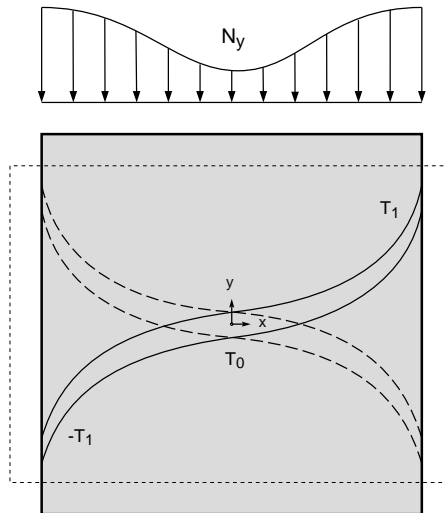


Figure 3.5: In-plane deformation of a laminate with  $\phi = 0^\circ$  under uniform edge shortening,  $v_0$ .

lowing results of the buckling analyses are compared to the straight-fibre format panels by using the axial stress resultant  $N_y$  corresponding to the lowest eigenvalue,  $N_{y,cr}$ . As  $N_y = N_y(x)$ , in order to describe the critical loading in terms of the axial stress resultant, an average critical load is defined as:

$$N_{cr}^{av} = \frac{1}{a} \int_{-a/2}^{a/2} N_{y,cr}(x, b/2) dx \quad (3.22)$$

The overall panel stiffness modulus is also function of the  $x$ -coordinate,  $E_y = E_y(x)$ . Similarly to  $N_y$ , for a laminate with small angle  $T_0$  and a larger angle  $T_1$ ,  $E_y$  is larger at  $x = \pm a/2$  than at  $x = 0$ . In order to compare it to the constant-stiffness value of straight fibre panels, the overall stiffness,  $E_y^{eq}$ , is defined by:

$$E_y^{eq} = \frac{b \int_{-a/2}^{a/2} N_y(x, b/2) dx}{h_l a v_0} \quad (3.23)$$

The critical axial stress resultants of panels normalised by  $b^2/(E_1 h_l^3)$  as a function of the respective overall axial stiffness normalised by the longitudinal ply stiffness,  $E_y^{eq}/E_1$ , are plotted in Figure 3.6.a. The thick line in the figure corresponds to straight-fibre configurations with a  $\pm\theta$  lay-up, and shows the variation of both the panel buckling load and the stiffness as the fiber angle,  $\theta$ , is changed from  $0^\circ$  to  $90^\circ$  (measured from the  $x$ -axis), respectively at the left and the right ends of the line.

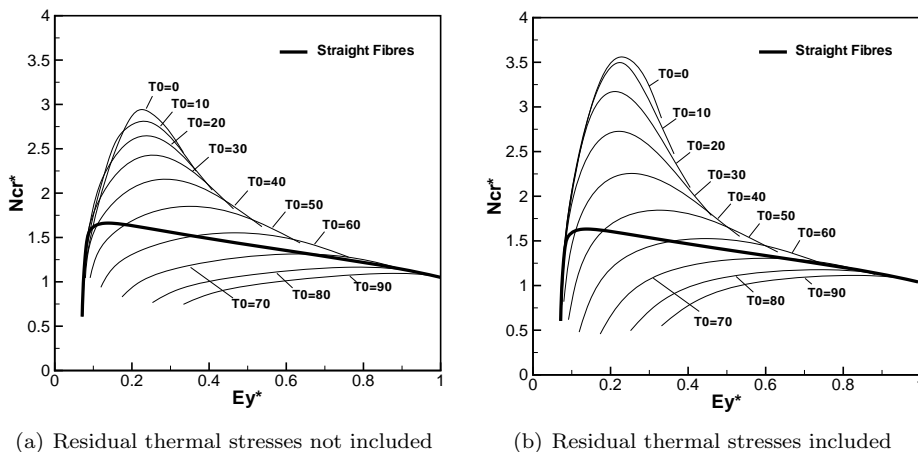


Figure 3.6: Buckling and stiffness performance of VSP under uniform edge shortening,  $v_0$  ( $N_{cr}^* = \frac{N_{cr}^{av} b^2}{E_1 h_l^3}$ ,  $E_y^* = \frac{E_y^{eq}}{E_1}$ ).

For constant-stiffness laminates, the maximum stiffness is achieved for an all  $90^\circ$  laminate, i.e with fibres parallel to the loading direction. The maximum normalised buckling load is 1.66 and corresponds to a  $[\pm 45^\circ]_{6s}$  laminate with overall normalised stiffness value  $E_y^{eq}/E_1 = 0.14$ .

For VSP, Figure 3.6.a. shows a family of curves corresponding to various

values of  $T_0$ , from  $0^\circ$  to  $90^\circ$  with increments of  $10^\circ$ . Each curve is generated by varying the value of  $T_1$  between  $0^\circ$  and  $90^\circ$ , in intervals of  $5^\circ$ , for a given value of  $T_0$ . Points to the left of the intersection of these curves with the curve corresponding to straight-fibre panels, identify configurations where  $T_1 > T_0$  and vice-versa. The maximum normalised value of the critical load is 2.92, obtained for the configuration  $[\pm < 0|75 >]_{6s}$ . This corresponds to a 76% improvement in critical load when comparing variable and constant-stiffness designs. Furthermore, the overall axial stiffness of the best VSP in terms of buckling load,  $E_y^{eq}/E_1=0.21$ , is about 54% higher than the best straight-fibre format panel. Most VSP with  $T_0 = 0^\circ$  have a higher buckling load than straight-fibre configurations. Typically, there are many variable-stiffness configurations that have a critical load greater than the straight-fibre configuration with the same  $E_y^{eq}$ . Additionally, for a given value of  $N_{cr}$ , there is only one or two configurations with straight fibres but many with a steered fibre configuration. This provides an added advantage in the design process by allowing more freedom to tailor the stiffness and critical load of the structure simultaneously<sup>10</sup>.

The reason for the increase in the critical load is a favourable distribution of the applied load across the panel height as a function of the  $x$ -coordinate, as shown in Figure 3.7. The configurations for which the value of  $N_{cr}$  is high are characterised by small values of the fibre orientation angle at the panel centreline ( $x = 0$ ) and large values at  $x = \pm a/2$ , just as the configuration shown in Figure 3.5. The local axial stiffness of the regions of the panel is high at locations where the fibres are closely aligned with the loading direction. As a result, most of the applied load introduced via uniform edge shortening is carried by the high stiffness regions of the panel that are located near the simply-supported edges of the panel where out-of-plane deflections are suppressed, i.e. the central section of the panel carries only a small fraction of the applied load. This makes the panel highly resistant to buckling.

### Effect of the Residual Thermal Stresses

The analyses described above, referring to the results shown in Figure 3.6.a, neglect the effect of the residual thermal stresses due to the curing of the laminates. As mentioned above, these were found to significantly influence the structural performance of variable-stiffness laminates<sup>7</sup>.

During the curing process, stress-free laminates at an elevated temperature are gradually brought down to room temperature. Since the carbon-fibre laminas have orthotropic thermal expansion behaviour, residual stress states are induced

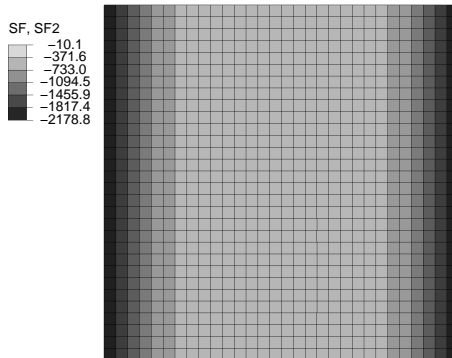


Figure 3.7: Through-the-thickness stress resultant  $N_y$  on the VSP  $[\pm < 0|75 >]_{6s}$  at buckling load.

after curing multi-ply laminates. For VSP, the thermal residual stresses are not uniform layerwise like they are for straight-fibre laminates. This generates non-zero section forces throughout the laminates which influence the bifurcation loads. Therefore, the first step required for the correct analysis of tow-steered composite panels is the computation of the stress/displacement state resultant of the curing process.

Figure 3.6.b shows the results of the buckling analyses similar to those presented in Figure 3.6.a but performed on panels which have been previously prestressed by undergoing a thermal step  $\Delta T = -137.5^\circ\text{C}$ , which is the indicated by the manufacturer for this material system. Residual thermal stresses have little effect on the normalised stiffness values but clearly amplify the critical load of VSP. The  $[\pm < 0|75 >]_{6s}$  configuration, with a normalised buckling load of 3.53, is still the best fibre-steered design in this case. The same occurs for the  $[\pm 45]_{6s}$  straight fibre panel. However, in this last case the residual thermal stresses do not contribute to the increase of the buckling load. Therefore, the realistic advantage of fibre steered format, in terms of  $N_{cr}$ , is 117% instead of the 76% previously calculated.

Examples of the magnitude of the deformations, after curing, for the  $[\pm 45]_{6s}$  straight fibre and for the  $[\pm < 0|75 >]_{6s}$  VSP are shown in Figure 3.8. For comparison, the panel shapes before cooldown are plotted on top of the deformed shapes. The straight-fibre panel shrinks in both directions in a uniform way, i.e. the edges remain straight after deformation. On the contrary, for the fibre steered panel the deformations are not uniform. As an example, in the specific case of the  $[\pm < 0|75 >]_{6s}$  configuration, the panel contracts along its centreline  $x = 0$  to a maximum value of 0.37mm at  $y = \pm b/2$ , and expands along the edges



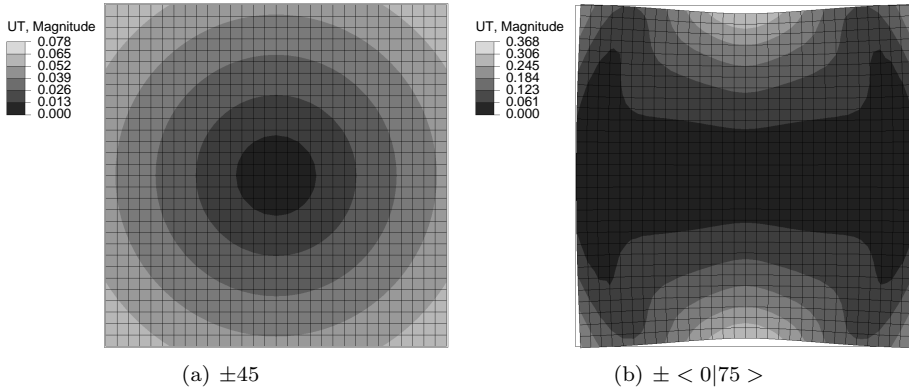


Figure 3.8: Displacement resultants after a thermal step  $\Delta T = -137.5^\circ\text{C}$ . The dark lines represent the pre-curing panel shape. The deformed shape is exaggerated by a factor of 20.

$x = \pm a/2$  to a maximum value of 0.04mm also at  $y = \pm b/2$ . This behaviour is both due to the fibre steering and the mismatch in thermal expansion coefficients between fibres and matrix. The laminate arrangement at the centre of the panel is dominated by fibres aligned along the  $x$ -axis. Therefore, the thermal loading response in the  $y$ -coordinate is determined by the transverse properties. That is, with cooldown, the positive transverse thermal expansion factor of the material system used determines a contraction of the centre of the laminate along the  $y$ -axis. On the other hand, the laminate arrangement at edges  $x = \pm a/2$  is dominated by fibres closely aligned with the  $y$ -axis. As the fibres expand during cooldown, although with a much lower magnitude, these edges also tend to expand in the  $y$ -coordinate.

The nonuniformity of the deformations in tow-steered panels due to curing is associated with the non-zero residual section forces shown in Figure 3.9. Negative forces develop close to the panel edges while positive forces, as high as 151.3N/mm along the loading direction, and 118.3N/mm in the transverse direction, arise at its inner sections. These are beneficial because they reduce the mechanical compressive forces on the most critical region of the panel which is the unsupported central section. That is, when these residual thermal forces are added to the applied mechanical forces, the resulting stress distribution in the panel is even more favourable in the resistance to buckling than the stress distribution resulting from in-plane stiffness variation alone.

The normalised critical load, for the flat squared panels under consideration, as a function of the fibre orientation angles  $T_0$  and  $T_1$  is shown in Figure 3.10. These results take into account the beneficial effects of the residual thermal stresses.

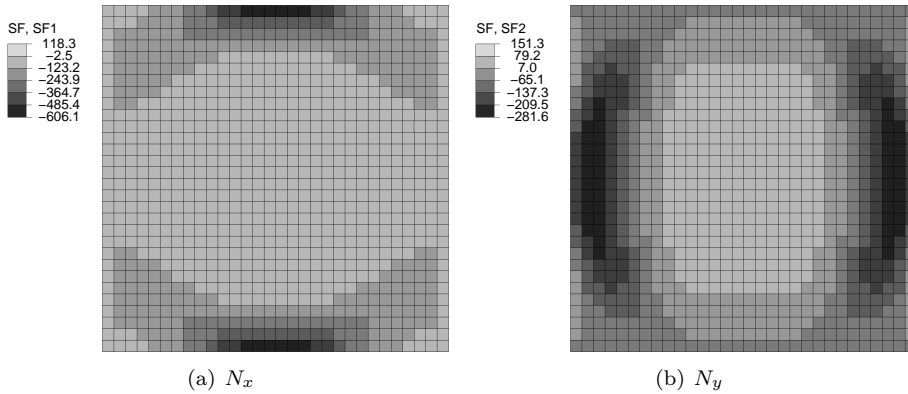


Figure 3.9: Residual thermal stress resultants on the VSP  $[\pm <0|75 >]_{6s}$  after a thermal step  $\Delta T = -137.5^\circ\text{C}$ .

Typically, for the best results, VSP need a low  $T_0$  and a high  $T_1$  in order to attract the highest portion of the applied loads to the supported edges. All the configurations with a  $T_1$  lower than  $30^\circ$  perform poorly. The most critical design variable is, therefore, the fibre orientation angle  $T_1$ . The variation in results is as high as 600%. In the specific cases of constant-stiffness panels, the best results are obtained for fibre angles between  $40^\circ$  and  $65^\circ$ .

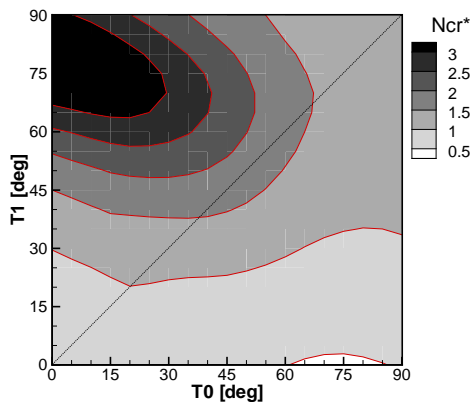


Figure 3.10: Normalised critical load ( $N_{cr}^* = \frac{N_{cr}^{av} b^2}{E_1 h_l^3}$ ) field contours in the linear fibre angle variation domain (residual thermal stresses taken into account). The straight line identifies straight fibre panel solutions.

### Effect of a Central Hole

VSP offer the ability to control the distribution of the in-plane stress resultants, which can be used to redistribute the loads to the rigid supported edges, hence increasing the critical loads of VSP. Then, it is interesting to investigate how the presence of a central cutout influences the buckling loads of VSP.

A new case study is considered here, consisting of a simply supported square plate with a central hole, under uniform edge shortening,  $v(x, b/2) = v_0$ , as illustrated in Figure 3.3.2. The transverse edges are free to expand in the  $x$  direction. The fibre orientation,  $\theta$ , is a function of the  $x$ -coordinate only ( $\theta = \theta(x)$ ,  $\phi = 0^\circ$ ) and the laminates are of the  $[\pm \langle T_0 | T_1 \rangle]_{6s}$  family. The problem is similar to the one considered before except for the presence of a central circular hole with a diameter equal to one third of the panel width.

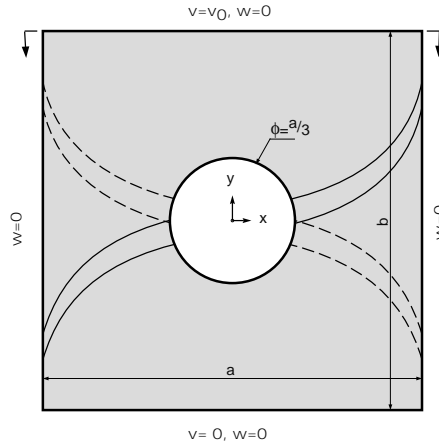


Figure 3.11: Cutout panel geometry and boundary conditions ( $a/b=1$ ). Transverse edges free in in-plane deformations. Stiffness variation in the  $x$  direction, perpendicular to the loading direction.

The normalised critical stress resultants for a range of laminate configurations, as a function of their overall normalised axial stiffness, are plotted in Figure 3.12.b. As in previous figures, the thick line in the figure corresponds to straight-fibre designs. For comparison purposes, Figure 3.12.a repeats the results for the flat panel analysed previously. The shape of the curves is similar between both cases but, due to the hole softening effect, the maximum normalised stiffness has now a value much lower than 1.0. This, however, only affects significantly the configurations with high  $T_0$  (typically,  $T_0 > 50^\circ$ ) and low  $T_1$ . For these laminates, the  $E_y$  (and  $N_y$ ) distributions on flat panels are qualitatively opposite

to that represented in Figure 3.5. i.e. the central sections of the panels are more loaded than the edges. Therefore, the axial stiffness (and stress resultant) for such designs is greatly reduced by the presence of the cutout. On the opposite side, for configurations with low  $T_0$  and high  $T_1$ ,  $E_y$  and  $N_y$  are much less affected by the hole.

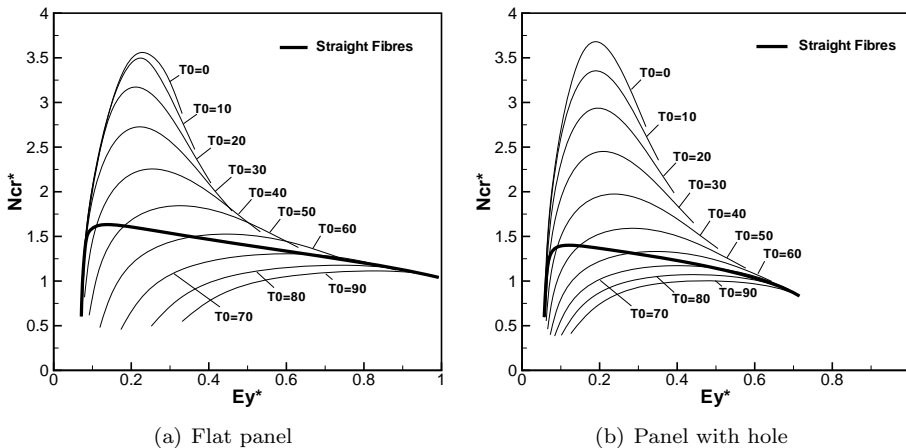


Figure 3.12: Buckling and stiffness performance of square VSP under uniform edge shortening,  $v_0$  ( $N_{cr}^* = \frac{N_{cr}^{av} b^2}{E_1 h_1^3}$ ,  $E_y^* = \frac{E_y^{cq}}{E_1}$ ).

The above considerations are also reflected on the values of the critical loads. This means that, concerning the buckling behaviour, variable-stiffness designs with low  $T_0$  and high  $T_1$  are nearly insensitive to the presence of the central hole. The constant and variable-stiffness optimum configurations for buckling resistance are the same for panels with and without a central hole. However, while for the  $[\pm < 0 | 75 >]_{6s}$  configuration,  $N_{cr}$  is unaffected by the existence of the hole, for the  $[\pm 45]_{6s}$  design it is reduced by 14%, increasing the ratio between the buckling performance of both designs to 2.62.

### 3.3.2 First-Ply Failure in Postbuckling

It was demonstrated that fibre-steering offers the possibility to control the distribution of the in-plane loads in a panel. This can be used to increase the panel critical loads and make its buckling response insensitive to a central cutout. It is likely that the panel failure response is improved as well. That is, the flexibility offered by fibre-steering may be used to tailor the laminates for the purpose of reducing the stress concentrations around holes and notches, henceforth increasing the panel failure loads. The following paragraphs are dedicated to the

first-ply-failure analysis of fibre steered panels with holes.

The LaRC failure criteria<sup>70;71</sup> described in section 3.2 is used herein to study the first-ply failure characteristics of VSP with a central hole, as illustrated in Figure and previously described. The first-ply failure eventually occurs in the nonlinear postbuckling regime. In order to generate the nonlinear solutions along the loading path, a linear bifurcation analysis is performed at first, just as in the previous analyses, and the first two buckling modes for the structure are calculated. Then, the FE model is re-defined with the buckling modes introduced as initial imperfections with small amplitudes as compared to the panel thickness (typically, 1-5%). Finally, geometrically nonlinear solutions are determined for loads up to first-ply failure, as predicted by the LaRC failure criteria. The Riks path following method<sup>81</sup> is used to find accurate solutions even if the structure shows negative stiffness due to mode jumping and eventual postbuckling collapsing behaviour.

Similarly to the buckling analyses, the following results of the failure analyses are compared to the straight-fibre format panels by using the average axial stress resultant  $N_y$  corresponding to the first-ply failure load,  $N_{fpf}^{av}$ , defined by:

$$N_{fpf}^{av} = \frac{1}{a} \int_{-a/2}^{a/2} N_{y,fpf}(x, b/2) dx \quad (3.24)$$

The  $N_{fpf}^{av}$  of panels is, in the same way as before, normalised by  $b^2 = E_1 h_f^3$  in order to compare critical buckling and first-ply failure loads.

The normalised first-ply failure stress resultant as a function of the overall normalised axial stiffness,  $E_y^{eq}/E_1$ , for a range of configurations, is plotted in Figure 3.13.a. The thick line in the figure corresponds to straight-fibre designs. The family of curves has now substantially different shapes than seen previously, indicating that the mechanisms that trigger buckling and failure are different. Under compressive loads, not only the laminate longitudinal stiffness but also the transverse stiffness terms play an important role in the resistance to buckling. Therefore, unidirectional laminates, and those that are close to such configuration, are poor designs in terms of critical loads. On the other hand the better the alignment of fibres with the loading, the stronger the laminate is, because of the great disparity between longitudinal and transverse (or shear) strengths. However, Figure 3.13.a. shows that the best variable-stiffness designs in resisting first-ply failure roughly coincide with the best configurations in terms buckling.

The maximum normalised value of the failure load is 3.51, obtained for the configuration  $[\pm < 0|80 >]_{6s}$ . A very close value (3.38) is obtained for the optimum design for buckling resistance, corresponding to the  $[\pm < 0|75 >]_{6s}$  lami-

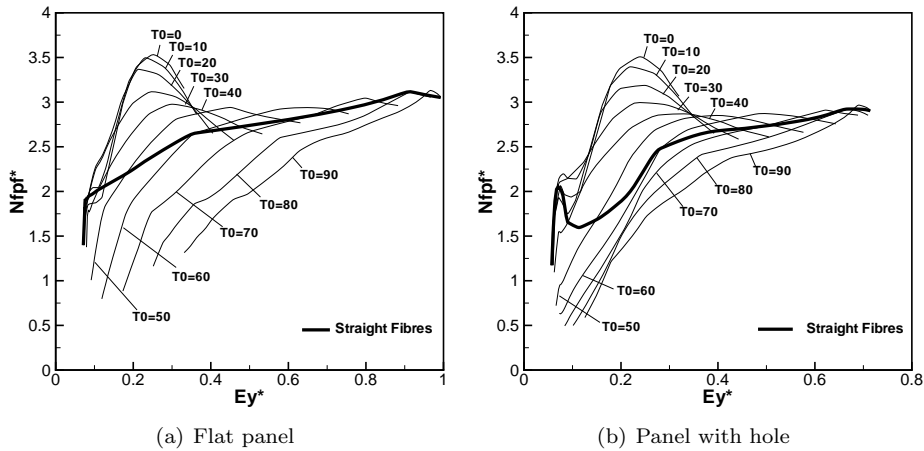


Figure 3.13: First-ply failure and stiffness performance of square VSP under uniform edge shortening,  $v_0$  ( $N_{fpf}^* = \frac{N_{fpf}^{av} b^2}{E_1 h^3}$ ,  $E_y^* = \frac{E_y^{eq}}{E_1}$ ).

nate. The differences between these two configurations are a  $5^\circ$  in fibre angle  $T_1$  and overall axial stiffness of 0.24 versus 0.20. On the other hand, for constant-stiffness panels, the best configuration for failure resistance is the  $[\pm 80]_{6s}$  laminate ( $E_y^{eq}/E_1=0.66$ ), with a normalised failure load of 2.92, which is quite different from the best straight-fibre panel for buckling resistance, the  $[\pm 45]_{6s}$  laminate ( $E_y^{eq}/E_1=0.11$ ), with a normalised failure load of 1.60. This corresponds only to a 20% improvement in the first-ply failure load when comparing VSP with constant-stiffness configurations, a value much lower than the 117% improvement in the critical buckling load. Furthermore, the overall axial stiffness of the best VSP in terms of failure load is about 64% lower than the best straight-fibre format panel. However, for most values of  $E_y^{eq}$ , there are many variable-stiffness configurations that have a failure load greater than the corresponding straight-fibre configuration. Additionally, for a given value of  $N_{fpf}^*$ , there is only one, two or at most three configurations with straight fibres but many with steered. This provides an added advantage in the design process by allowing more freedom to tailor the stiffness, buckling load and failure load of the structure simultaneously.

For the panel geometry and material considered in this research, the buckling and failure loads of the best variable-stiffness configurations look similar. However, first-ply failure of the panels analysed here always occurs in the post-buckling regime. This is because the critical loads presented above are the result of linear eigenvalue extraction analyses and correspond to predictions of the bifurcation loads which are typically higher than the transition loads predicted by nonlinear

analyses (with panel imperfections).

The normalised failure load, for the cutout VSP as a function of the fibre orientation angles  $T_0$  and  $T_1$  is plotted in Figure 3.14. Typically, for the best results, VSP need a low  $T_0$  and a high  $T_1$ , similarly to the buckling case. On the opposite side of the scale are the configurations with high  $T_0$  and a low  $T_1$ . The variation in results is as high as 600%. In the specific cases of constant-stiffness panels, the best results are obtained for fibre orientation angles above  $60^\circ$ . For fibre orientation angles between  $35^\circ$  and  $55^\circ$ , the failure load of constant-stiffness panels is reduced. This is also evident from the depression in the corresponding curve in Figure 3.13.b. This dip in the  $N_{fpf}$  distribution corresponds to panels that fail (prematurely) due to stress concentrations around the hole edge. For the sake of comparison, Figure 3.13.a shows the failure response curves for the flat panel version, which is depicted in Figure 3.4. Here, the curve representing straight-fibres designs does not show a depression.

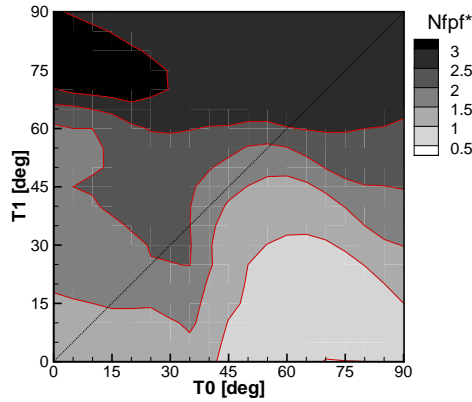


Figure 3.14: Normalised first-ply failure load ( $N_{fpf}^* = \frac{N_{fpf}^{2v} b^2}{E_1 h_1^3}$ ) field contours in the linear fibre angle variation domain. The straight line identifies straight fibre panel solutions.

The location of panel failure, in a binary scale, is shown in Figure 3.15, in which the black field represents failure around the hole edge. The cutout on the panel develops stress concentrations which can trigger panel failure at lower applied loads than those for flat panels. Roughly, there are as many configurations that fail by the hole edge as the ones that do not. Typically, values of  $T_1$  lower than  $20^\circ$  cause hole-edge failure. Values of  $T_0$  higher than  $35^\circ$  combined with values of  $T_1$  lower than  $55^\circ$  also drive the panels to fail by the hole, in the majority of the cases. It is likely that the failure loads for these configurations is even lower than predicted here because of eventual free edge delaminations, a failure mechanism

that is generally more critical than any of the intraply failure modes.

The most promising VSP in terms of buckling and failure under pure compressive loads do not fail by the hole edge. Neither do the best straight-fibre designs if failure is the only critical event. On the other hand, the constant-stiffness panels that perform better in terms of buckling end up by failing by the hole edge. Actually, with exception from a small range of fibre orientation angles around  $30^\circ$ , all straight-fibre panels typically with  $\theta < 60^\circ$  fail at this location.

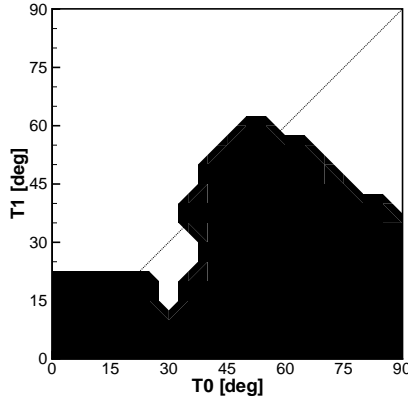


Figure 3.15: First-ply failure location. The black field identifies failure by the hole edge. The white field identifies failure at any other location. The straight line identifies straight fibre panel solutions.

The failure modes, for square cutout panels, as a function of the fibre orientation angles  $T_0$  and  $T_1$  are shown in Figure 3.16. For maximum strength, the most desired failure mode for composite panels under compression is fibre kinking. This leads to relatively high failure loads because the longitudinal strength of a ply under compression (as well as for tension) is much higher than their transverse strength (see Table 3.1). The disadvantage is that fibre kinking is generally a very explosive (brittle) failure mode. The fibre kinking failure mode is predicted for most of the panel configurations analysed, including the best performing constant and variable-stiffness designs. A smaller number of configurations, mainly with low or high values of  $T_1$ , is prone to fail by transverse compressive or tensile cracking. The latter failure mode is caused by the high bending induced transverse tensile stresses in one of the laminate face plies due to a buckle.

As in the case of buckling, the reason for the superior performance of VSP in terms of failure load, as compared to the straight-fibre counterparts, is a favourable distribution of the applied load across the panel height as a function of the  $x$ -coordinate, as shown in Figure 3.17. The configurations for which



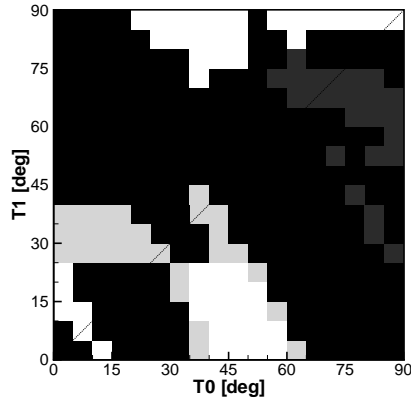


Figure 3.16: Failure mode for possible panel designs with linear fibre angle variations. The black field represents first-ply failure by fibre kinking. The white and grey fields represent first-ply failure by matrix cracking. The straight line identifies straight fibre panel solutions.

the value of  $N_{f_{pf}}$  is high are characterised by small values of the fiber orientation angle at the panel centreline ( $x = 0$ ) and large values at the edges  $x = \pm a/2$ . The local axial stiffness of the regions of the panel is high at points where the fiber orientation is closer to  $90^\circ$ . As a result, most of the applied load introduced via uniform edge shortening is carried by the highly stiff regions of the panel located near their simply-supported edges. The introduction of the central hole does not greatly disturb the stress field and does not create stress concentrations higher than the ones forming near the panel transverse edges. Due to the favourable fibre alignment, at these locations the load is mostly supported along the local longitudinal directions. This architecture leads to strong laminates since the longitudinal strength of plies is much higher than their transverse strength.

There is a second reason for the superior failure performance of the tow-steered format: their superior buckling response. First-ply failure in the  $[\pm < 0 | 80 >]_{6s}$  panel, as an example, occurs where the added influences of the directly applied longitudinal compressive stresses and the bending induced ones (due to buckling) is the highest, i.e. fibre kinking is triggered by bending-induced compressive stresses on the concave side of the buckles, in regions close the transverse edges where the direct compressive loads are higher. Furthermore, failure initiates at the laminate face plies. This occurs due to two reasons: (i) the bending induced stresses are higher and (ii) the in-situ strengths of these plies is lower than for the embedded (constrained) laminae, as reported in Table 3.2. These considerations lead to the conclusion that, for failure in the postbuckling regime in general, high

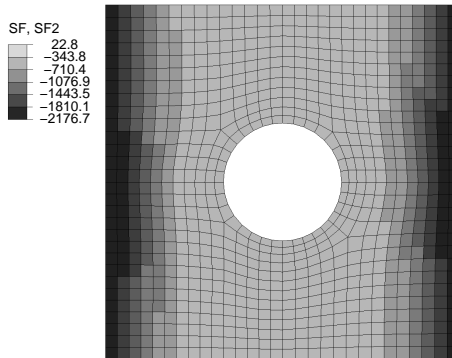


Figure 3.17: Through-the-thickness stress resultant  $N_y$  on the  $[\pm < 0|80 >]_{6s}$  panel with a central hole, at first-ply failure loading.

buckling loads lead to high failure loads. Hence, the improved failure performance of VSP is also a consequence of their improved buckling response. The  $[\pm 80]_{6s}$  laminate, for instance, has a favourable fibre distribution in terms of strength but its critical buckling load is rather low. As a consequence, face ply fibres at the concave side of the buckle start to kink prematurely due to added effects of direct and bending induced compressive loads. For values of  $T_1$  typically higher than  $85^\circ$ , first-ply failure may occur by transverse tension (see Figure 3.16) because the bending induced stresses become more critical for this failure mode.

The analyses carried out lead to the conclusion that the curvilinear-fibre format has less potential for increasing the postbuckling failure resistance of composite panels than for improving their buckling response. However, the analyses performed focused only on compressive loading. It is probable that, if different load cases are considered, the advantage of tow-steered designs might be extended. For example, under shear loads it is unlikely that the  $[\pm 80]_{6s}$  laminate performs as well as the panel under compression. Typically, under this type of loading, the best designs are oriented at  $\pm 45^\circ$  and unidirectional laminates perform poorly. Therefore, the best performing straight-fibre configuration in terms of first-ply failure would probably be the  $[\pm 45]_{6s}$  laminate, which is already the optimum with respect to buckling performance. That is, for a realistic application, it is likely that the optimum straight-fibre configuration resembles more the  $[\pm 45]_{6s}$  than the  $[\pm 80]_{6s}$ . On the other hand, the  $[\pm < 0|80 >]_{6s}$  laminate might perform reasonably well under shear loads because it contains regions with a  $\pm 45^\circ$  arrangement. This means that the structural advantages of using tow-steered formats might be proven to be higher than what is suggested by the results presented in this thesis. This claim, however, requires further analysis.

### Effect of the Residual Thermal Stresses

The residual thermal stresses due to laminate curing were taken into account in the previous analysis. It is interesting, however, to quantify their effect. The normalised failure stress resultant, neglecting the residual thermal stresses, as a function of the overall normalised axial stiffness is plotted in Figure 3.18.b. For the sake of comparison, the characteristic curves for the case where the residual stresses are taken into account are repeated in Figure 3.18.a. The data curves are qualitatively similar in both figures but the values of normalised  $N_{fpf}$  reported are somewhat different. Similarly to the influence on buckling loads, the curing process has the effect of stretching the difference in strength between constant and variable-stiffness laminates. Figure 3.18 shows that, in general, residual thermal stresses have the effect of reducing the performance of straight-fibre panels and increasing that of the most promising curvilinear-fibre configurations. Without their inclusion in the analysis, the best tow-steered design, the  $[\pm < 0|80 >]_{6s}$  laminate, performs only 9.7% better than the most promising constant stiffness configuration, the  $[\pm 70]_{6s}$  laminate.

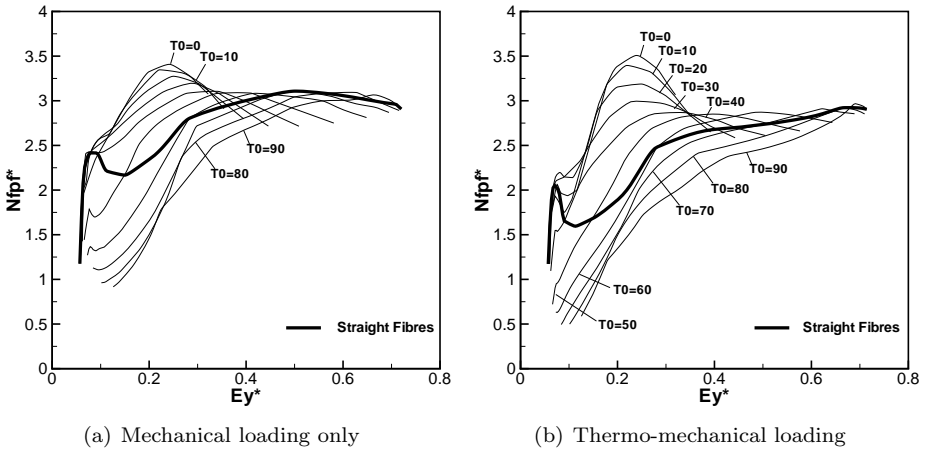


Figure 3.18: First-ply failure and stiffness performance of VSP under uniform edge shortening,  $v_0$  ( $N_{fpf}^* = \frac{N_{fpf}^{av} b^2}{E_1 h_1^3}$ ,  $E_y^* = \frac{E_y^{eq}}{E_1}$ ).

The fibre compression failure index fields on face plies of  $[\pm < 0|80 >]_{6s}$  laminates, where either mechanical or thermo-mechanical loads are taken into account, are plotted in Figure 3.19. At the load level represented,  $\frac{N_y b^2}{E_1 h_1^3} = 1.24$ , the panels are still in the prebuckling regime. The fields are different in each case. The maximum failure index is 0.15 for the case of mechanical loading only, and 0.50 for the case of thermo-mechanical loading. This means that, if panel buckling is not con-

sidered, the residual thermal stresses actually promote first-ply failure. Then, the reason for the positive effect of the curing in the panel strength must have to do with the buckling event. Since low buckling loads promote poor failure response, and these are increased by the residual thermal stresses, in an indirect way, curing stresses are also responsible for improvements in strength performance.

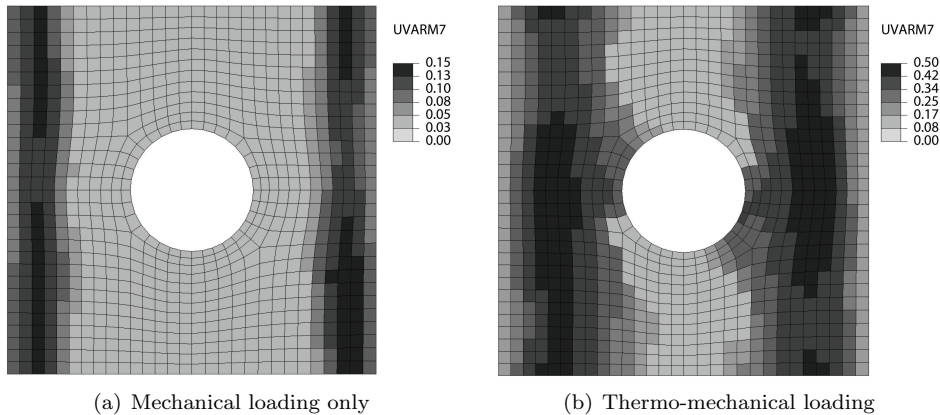


Figure 3.19: Fibre compression failure index for a face ply of the  $[\pm < 0 | 80 >]_{6s}$  panel at an applied normalised  $N_y$  equal to 1.24 (in the prebuckling regime).

### Other Cases

Besides the benchmark case of a square composite panel with stiffness variation perpendicular to the axis of loading, there are two other cases worth being analysed, namely: (i) a squared panel with fibre orientation variation along the loading axis and (ii) a rectangular panel with  $b/a = 2$ . In both cases, the panels have a central circular hole. The analyses performed herein on these configurations take into account the residual thermal stresses.

**(i) panel with stiffness variation along the loading direction** Previous investigations<sup>10;40</sup> have analysed the compressive buckling response of flat VSP with fibre angle variation along a direction parallel to the loading axis. The results showed that the advantages of using tow-steered formats are less expressive if such configurations are adopted. This is also evident from the analyses reported below.

The critical axial stress resultant of panels normalised by  $b^2/(E_1 h_l^3)$  as a function of the axial stiffness normalised by the longitudinal ply stiffness,  $E_y/E_1$  is plotted in Figure 3.20.a. The panel laminae material, geometry, loading and boundary conditions are the same as for the cases considered previously and il-

illustrated in Figure 3.3.2. However, in the present case the fibre orientation,  $\theta$ , is a function of the  $y$ -coordinate only ( $\theta = \theta(y)$ ,  $\phi = 90^\circ$ ). Then, the laminate takes the form  $[90 \pm < T_0 | T_1 >]_{6s}$ , i.e. the  $T_0$  and  $T_1$  fibre angles are now measured relatively to the  $y$ -axis. Contrary to the cases of fibre orientation variation as function of the  $x$ -coordinate only, here the in-plane stiffness  $E_y$  and stress resultant  $N_y$  are constant everywhere and the transverse characteristics  $E_x$  and  $N_x$  vary with the  $y$ -coordinate.

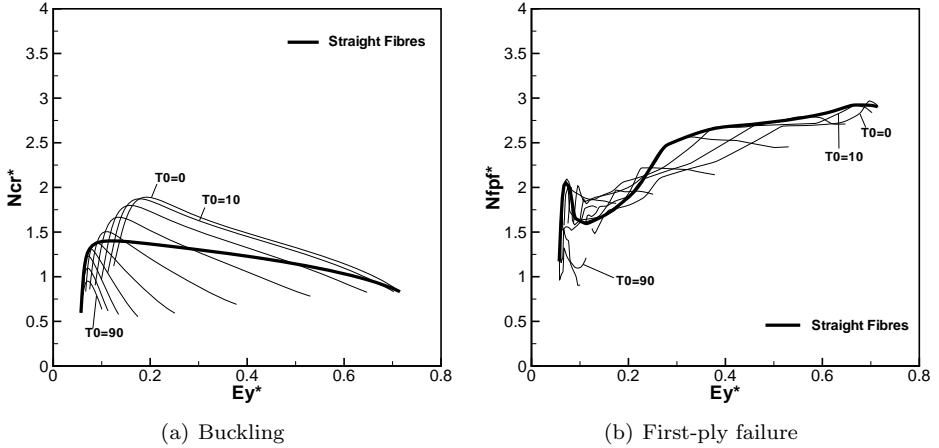


Figure 3.20: Performance of VSP under uniform edge shortening ( $v_0$ ), and stiffness variation along the loading axis ( $N_{cr}^* = \frac{N_{cr}^{av} b^2}{E_1 h_i^3}$ ,  $N_{fpf}^* = \frac{N_{fpf}^{av} b^2}{E_1 h_i^3}$ ,  $E_y^* = \frac{E_y^{eq}}{E_1}$ ).

The maximum normalised value of the critical load is 1.89, obtained for the configuration  $[90 \pm < 0 | 60 >]_{6s}$ . This value is 35% higher than the maximum value of 1.40 obtained with a straight-fibre configuration, the  $[\pm 45]_{6s}$  laminate. Furthermore, the overall axial stiffness of the best VSP in terms of buckling load,  $E_y/E_1=0.20$ , is about 81% higher than the best straight-fibre format panel,  $E_y/E_1=0.11$ . The maximum increase in critical load of VSP over the straight-fibre format (35%) is largely due to a favourable distribution of the transverse stress resultant  $N_x$  at the panel edges along the height of the panel<sup>10</sup>. Although the variable-stiffness configuration has a higher axial stiffness, its transverse stress resultant is very small near the panel centre (the region that triggers buckling) compared to the large transverse compressive stresses at the same location in the straight-fibre panel.

The first-ply failure performance is represented in Figure 3.20.b. Although panel failure always occurs in the postbuckling regime, variable-stiffness laminates of this format do not outperform constant-stiffness designs. The normalised failure

load for the panels under analysis, as a function of the fibre orientation angles  $T_0$  and  $T_1$ , are shown in Figure 3.21. Typically, the best responses are achieved for low values of  $T_0$  and  $T_1$ , with maximum strength values corresponding to the straight-fibre configurations.

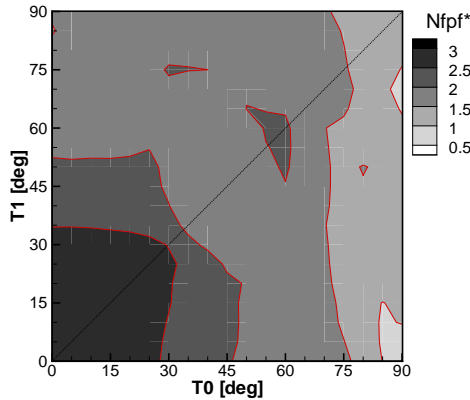


Figure 3.21: Normalised first-ply failure load ( $N_{pfp}^* = \frac{N_{pfp}^{av} b^2}{E_1 h_1^3}$ ) field contours in the linear fibre angle variation domain for squared panels with stiffness variation along the loading axis. The straight line identifies straight fibre panel solutions.

The disappointing results achieved by curvilinear-fibre panels are mainly related to local stresses. The laminate failure modes are shown in Figure 3.22. In most of the cases, failure occurs by matrix cracking which is an indication that these configurations have highly transversely stressed laminae. Laminate designs predominately loaded along the local transverse directions are poor designs in terms of failure because the transverse strength of a ply, either in tension or compression, is much lower than its longitudinal strength (see Table 3.1). A large number of panels that fail by longitudinal compression correspond either to straight-fibre designs or to designs with large fibre curvature radius.

**(ii) panel with  $b/a = 2$**  The consequences of varying the panel geometry, by deviating from the squared configuration, are addressed in this paragraph. The family of laminate configurations studied herein is similar in laminae material, geometry, loading, boundary conditions and fibre orientation variation ( $\theta = \theta(x)$ ,  $\phi = 0^\circ$ ) to the cases illustrated in Figure 3.3.2 except that the panel height which is now double of its width. The central hole dimensions are maintained.

The normalised critical and first-ply failure axial stress resultants as functions of the normalised axial stiffness are plotted in Figures 3.23.a and 3.23.b, respectively. In terms of buckling loads, the advantage of using the fibre-steered instead

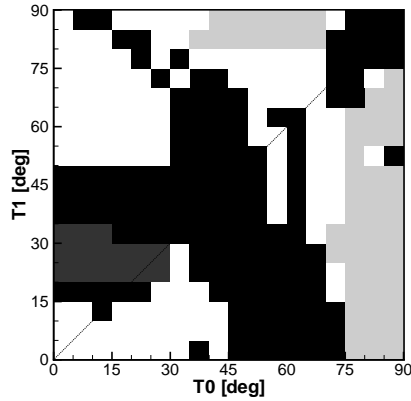


Figure 3.22: Failure modes for possible panel designs with linear fibre angle variations along the loading axis. The black field represents first-ply failure by fibre kinking. The white and grey fields represent first-ply failure by matrix cracking. The straight line identifies straight fibre panel solutions.

of straight-fibre format is reduced both due to a lower performance of the former and a better response of the later. The maximum normalised value of the critical load is 3.45, obtained for the optimal configuration  $[\pm < 0|75 >]_{6s}$  (the same as for the square panel). This value is 97% higher than the maximum value of 1.75 obtained with the  $[\pm 50]_{6s}$  laminate, the best constant-stiffness configuration. In terms of first-ply failure loads, the optimal configurations for variable and constant-stiffness formats, the  $[\pm < 0|80 >]_{6s}$  and  $[\pm 80]_{6s}$  laminates respectively, are the same as the ones found for squared panel geometries. The maximum benefit of using tow-steered designs is also unchanged: 20%.

### 3.4 Performance of Manufacturable Panels

The analyses reported in the last section concern fibre-steered designs with ‘ideal’ fibre courses, i.e. where there is a continuous shifting of the reference path in the direction perpendicular to the fibre orientation variation. As explained in Chapter 2, the practical manufacturing of variable-stiffness laminates imposes a discrete shifting of the reference path at a frequency equal to the tow-course width. Within each course, the fibres are placed parallel to each other. The differences between ‘ideal’ and ‘manufacturable’ fibre-steered plies are exemplified in Figure 2.5.

In this section, the most promising designs, in terms of first-ply failure performance, are analysed in detail. That is, the  $[\pm < 0|80 >]_{6s}$  VSP is compared with the  $[\pm 80]_{6s}$  straight-fibre laminate. Additionally, the  $[\pm < 0|80 >]_{6s}$  VSP

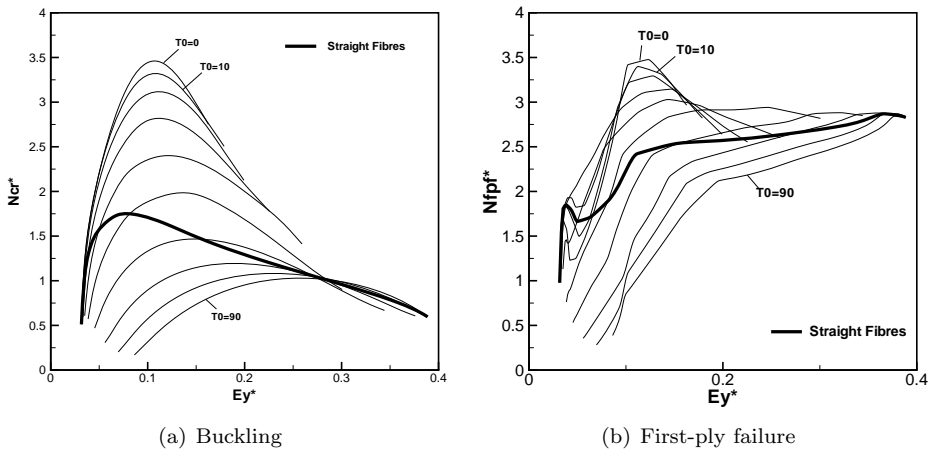


Figure 3.23: Performance of VSP ( $a/b = 2$ ) under uniform edge shortening ( $v_0$ ) and stiffness variation perpendicular to the loading axis ( $N_{cr}^* = \frac{N_{cr}^{av} b^2}{E_1 h_1^3}$ ,  $N_{fpf}^* = \frac{N_{fpf}^{av} b^2}{E_1 h_1^3}$ ,  $E_y^* = \frac{E_y^{eq}}{E_1}$ ).

is also compared with the  $[\pm 45]_{6s}$  straight-fibre design, since this configuration may be preferable to the  $[\pm 80]_{6s}$  laminate due to its buckling and shear failure performance. Some of the issues that arise due to the practical manufacturing of these panels are taken into account. As described in Chapter 2, one of these respects the laying of each ply in several machine head tow-placement courses. Here, a nominal course width approximately equal to 1/4th of the panel height is adopted. This means that, on average, each ply can be laid completely with four machine head passes. For each configuration studied, both the tow-drop and the tow-overlap manufacturing methods are addressed. The effects of ply staggering and local asymmetry on panel response are also analysed. These manufacturing issues are thoroughly explained in Chapter 2. The results, for all the cases studied in this section, are reported in Table 3.3.

In order to capture the panel geometric discontinuities in more detail than in the previous section, and accurately evaluate their influence on the first-ply failure result, the FE meshes used herein are refined such that the maximum fibre angle difference between neighbouring elements is  $1.2^\circ$ .

### 3.4.1 Panels with Tow-Drops

The predicted overall first-ply failure load,  $N_{fpf}^{av}$ , for the  $[\pm < 0 | 80 >]_{6s}$  panel with tow-drops is 469.5N/mm, only 1.2% higher than the 464.1N/mm calculated for the  $[\pm 80]_{6s}$  laminate, and much lower than what was expected, given the results



Table 3.3: Buckling and strength results for the  $[\pm < 0|80 >]_{6s}$  design according to several manufacturing methods. The strength performance is compared with the results predicted for the  $[\pm 80]_{6s}$  and  $[\pm 45]_{6s}$  laminates.

Design	$N_{cr}^{av}$ [N/mm]	$N_{fpf}^{av}$ [N/mm]	vs. $[\pm 80]_{6s}$ [%]	vs. $[\pm 45]_{6s}$ [%]
Straight fibres ( $[\pm 45]_{6s}$ )	232.7	244.7	-47.2	-
Straight fibres ( $[\pm 80]_{6s}$ )	148.8	464.1	-	89.7
Ideal variable-stiffness	555.8	559.6	20.0	120.5
Tow-drops	548.6	469.5	1.2	91.9
Tow-drops (staggering)	543.9	523.4	12.8	113.9
Tow-overlaps	2440.0	733.2	58.0	200.0
Tow-overlaps (staggering)	2395.2	1226.6	164.3	401.3
Tow-overlaps (asymmetric)	2502.1	600.5	29.4	145.4
Tow-overlaps (stag. + asym.)	2448.0	543.6	17.1	122.1

achieved by the ‘ideal’ design. In terms of predicted critical buckling loads, the difference between ‘ideal’ ( $N_{cr}^{av}=555.8\text{N/mm}$ ) and ‘manufacturable’ designs with tow-drops ( $N_{cr}^{av}=548.6\text{N/mm}$ ) is only about 1%, hence the buckling behaviour is not the cause for the mismatch in the first-ply failure loads.

The longitudinal compressive failure index ( $\phi_{1-}$ ) field for the critical surface ply of the  $[\pm < 0|80 >]_{6s}$  panel with tow-drops, for  $N_{fpf}^{av}=469.5\text{N/mm}$ , is depicted in Figure 3.24.a. The figure shows values of the failure index near the course edges of the respective and neighbouring layers approaching 1.0. This means that stress concentrations develop in those areas, because of the fibre angle mismatch between adjacent courses. These discontinuities trigger premature first-ply failure. The repeatability of plies in the laminate determine that the layerwise stress concentrations develop at the same  $(x,y)$ -coordinates through-the-thickness of the panel, therefore there are no alternative paths for stress relief.

In the attempt to lower stress concentration regions, by smearing the course edges over wider areas of the panel and promoting alternative load paths, the technique of ply staggering is applied to the  $[\pm < 0|80 >]_{6s}$  laminate with tow-drops, as illustrated in Figure 2.5. The first-ply failure is now predicted at  $N_{fpf}^{av}=523.4\text{N/mm}$ , 12.8% higher than for the  $[\pm 80]_{6s}$  laminate, while the critical buckling load is kept nearly the same (less than 1% difference). This failure load is still lower than the value predicted for the ‘ideal’ case, but higher than for the non-staggered configuration. The fibre compression failure index for this design, for  $N_{fpf}^{av}=523.4\text{N/mm}$ , is shown in Figure 3.24.b. The highly stressed

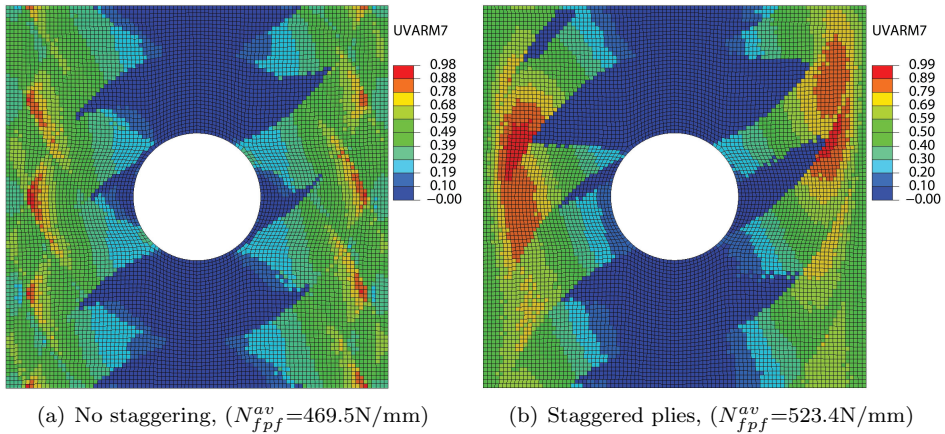


Figure 3.24: Longitudinal compressive failure index ( $\phi_{1-}$ ) field at first-ply failure load for the critical surface ply of the  $[\pm < 0 | 80 >]_{6s}$  panel with tow-drops.

regions are now dispersed over wider areas resulting in a more uniform loading of the panel. This lowers the peak stresses and postpones failure to higher applied loads. Compared with the  $[\pm 45]_{6s}$  panel, the optimal ply-shifted variable-stiffness configuration offers a 113.9% increase in strength.

### 3.4.2 Panels with Overlaps

By letting the fibre tows overlap during laminate manufacturing, regions of increased thickness are produced. The thickness field for the  $[\pm < 0 | 80 >]_{6s}$  laminate panel constructed according to the overlap technique is shown in Figure 2.9.a. Most of its central section has the nominal 24-ply thickness. As the edges are approached, thicker regions with up to 72 stacked plies, in steps of 12 layers, are produced. Besides the thickness increase, tow-overlapping also has the consequence of increasing the panel mass, in this case by as much as 59%. The thicker regions stiffen the panel and its critical buckling load, which is affected by  $Eh_t^3$ , increases by 340% ( $N_{cr}^{av} = 2440.0 \text{ N/mm}$ ). The benefit in terms of failure performance is not nearly as pronounced. First-ply failure is predicted at an applied load of  $733.2 \text{ N/mm}$ , well below the buckling load.

The introduction of staggering in the design of panels with overlaps has two effects. The first is the prevention of layerwise stress concentration zones from overlapping each other through-the-thickness of the panels, lowering peak stress values by smoothing the loads over wider regions of the panel. This effect is visible in Figure 3.25. The second consequence of staggering is the smoothing of panel thickness, as shown in Figure 2.9.b. The maximum thickness is now of 64

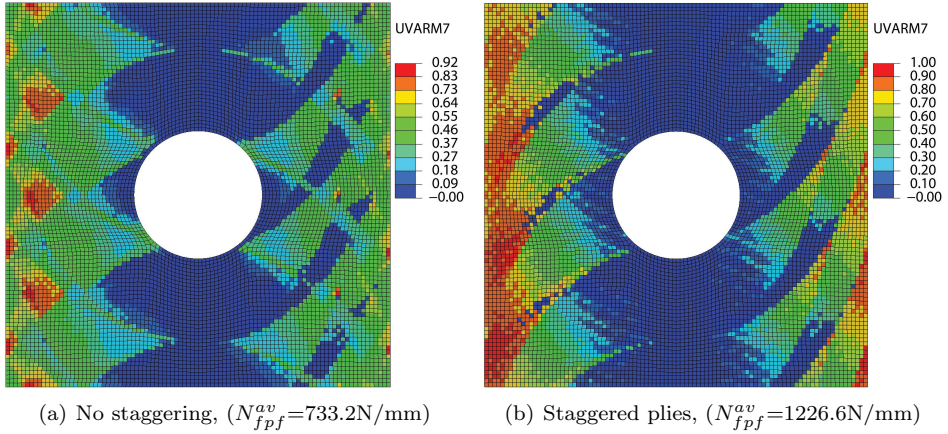


Figure 3.25: Longitudinal compression failure index ( $\phi_{1-}$ ) field at first-ply failure load for the critical surface ply of the  $[\pm < 0|80 >]_{6s}$  panel with overlaps.

plies and increases from the nominal value, in a more gradual way, in steps of 2 plies. The critical load slightly decreases (-1.9%) but the failure performance is significantly benefited ( $N_{fpf}^{av}=1226.6\text{N/mm}$ , +67.3%). This amounts to a total of 164.3% and 401.3% improvements over the  $[\pm 80]_{6s}$  and  $[\pm 45]_{6s}$  configurations, respectively.

Another issue with panels with tow-overlaps is their local asymmetry due to the single-sided thickness buildup, i.e as the tows are laid down over a flat mandrel, the overlapping occurs only towards the free face of the laminate. This aspect is taken into account in FE modelling by offsetting the midsection of each shell element, as shown in Figure 3.26.

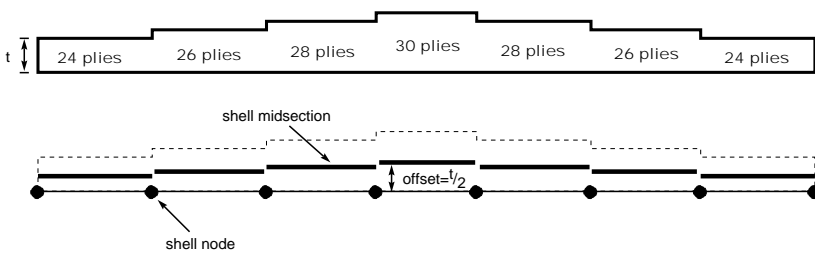


Figure 3.26: Modelling of asymmetries with shell elements.

The lay-up asymmetry due to tow-overlapping seriously affects the buckling and first-ply failure performance of VSP. It constitutes a dominant imperfection in the panel that forces it to buckle prematurely. This means that the effect

of imperfection introduced in the buckling mode shape is small when compared with the destabilising effect of the lay-up asymmetry. Besides, the eccentricity in load introduction causes premature failure of the thicker edge regions, as shown in Figure 3.27, and the value of  $N_{fpf}^{av}$  reduces to 543.6N/mm, only 17.1% higher than for the optimal straight-fibre configuration.

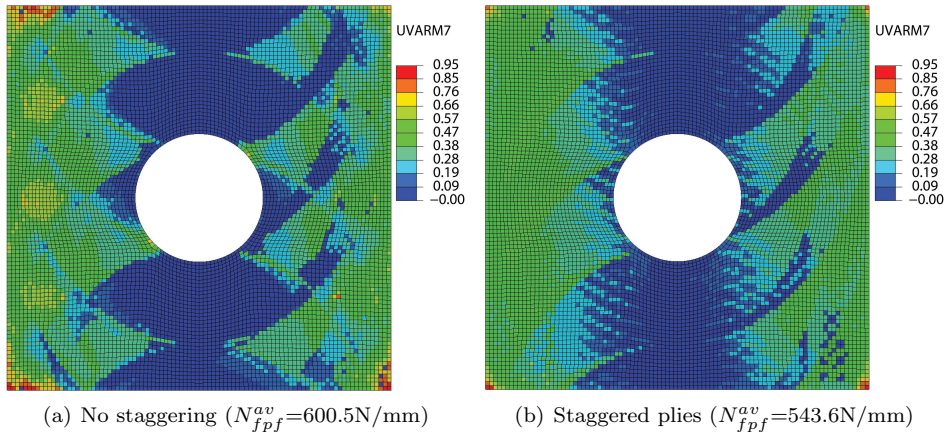


Figure 3.27: Longitudinal compression failure index ( $\phi_{1-}$ ) field at first-ply failure load for the critical surface ply of the  $[\pm < 0|80 >]_{6s}$  panel with overlaps where the asymmetry in the thickness buildup is taken into account.

### 3.5 Conclusions

The response characteristics in terms of buckling and first-ply failure in the post-buckling phase of VSP were analysed in this chapter. Important advantages in comparison with constant-stiffness formats were found in both indicators. The effects of the residual thermal stresses resulting from the laminate curing process were also quantified.

Fibre-steered panels offer significant performance improvements in terms of critical buckling loads. This is due to a favourable redistribution of the applied loads towards the supported panel edges resulting in an unloading of its central section, the region that eventually triggers the buckling event. This effect is so pronounced that the optimum cutout VSP designs have barely the same critical loads as equivalent flat panels, i.e. with the same distribution of fibre orientations.

Additionally, results of the buckling study revealed an extended design flexibility due to the decoupling between the buckling load and the overall axial in-plane stiffness. For straight-fibre laminates, changing the fibre orientation angle in or-

der to change the panel in-plane stiffness causes the buckling load to change as well. Moreover, the trends of the buckling load and the in-plane stiffness as a function of the fibre orientation angle diverge from one another. For variable stiffness-panels, it is possible to change either the buckling load or the in-plane stiffness while keeping the other one constant. This is an added advantage in the design process because there is more flexibility to tailor the stiffness and critical load of the structure simultaneously.

Part of the advantage in buckling performance offered by fibre-steered configurations is caused by favourable residual thermal stresses. By creating beneficial section forces, these stresses amplify the mechanisms of load redistribution, towards the supported edges, that favour VSP in terms of mechanical response.

Results of the postbuckling first-ply failure study on cutout panels show similar design flexibility to that revealed by the buckling study. Additionally, there are clear benefits in using tow-steered designs in terms of nominal panel strength, although not as pronounced as in terms of critical buckling loads. These improvements have two different reasons. One is the load redistribution towards the panel supported edges and a favourable fibre alignment at these locations such that the load is mostly supported along the local longitudinal direction, the one that offers the highest strength. The other reason is related to the higher buckling loads. The postbuckling regime adds bending induced stresses to the directly applied loads, therefore, the high buckling loads of some VSP also postpones their failure to even higher loads.

Residual thermal stresses benefit the failure response of VSP, but only in an indirect way, by improving their buckling response. For the specific case of a panel under compression, the advantage of in-plane stiffness variation is less pronounced than in terms of critical loads due to the relatively high performance of unidirectional laminates loaded longitudinally.

The most promising variable-stiffness configurations are insensitive to a central hole either in terms of buckling response as with respect to first-ply failure performance. This is one of the major advantages of two-steered designs in comparison with traditional configurations. This characteristic can be exploited in different loading situations. One example is impact loading. Actually, impact damage is often represented as a circular hole.

The manufacturability of fibre-steered laminates imposes some design constraints that limit their advantages in terms of first-ply failure performance, specifically the fibre angle mismatches at course edges due to the finite width of the AFP machine head passes that create zones of elevated stresses, which can be mitigated by using narrower tow courses or ply staggering. Additional analyses

involving the progressive failure response of such laminates up to final failure will provide more accurate predictions of their response. That is the focus of the following chapter.

In the failure assessment analyses performed herein, the prediction of the occurrence of ply delaminations was neglected altogether. This is as a reasonable simplification, considering the computational costs involved and the expected improvements in the accuracy of the simulations. However, these considerations are based on the typical behaviour of conventional laminates. It is clear at this stage that VSP behave very differently from straight-fibre panels. Specifically, due to the stiffness variation, large in-plane stress gradients arise that may contribute to the amplification of the interlaminar stresses and possibly to the initiation of delaminations. Furthermore, it has been observed that VSP develop residual stresses during the curing process, and local stress concentrations due to tow-dropping and overlapping which certainly contribute to excite the interlaminar stresses further, potentially rendering delamination the dominant failure mode in these structures. Finally, the presence of a cutout in some of the configurations analysed creates a free edge where interlaminar stresses are typically high, and delaminations a concern<sup>73</sup>. Then, the results presented herein should be analysed carefully. An efficient modelling strategy for the problem of deaminations in VSP is being pursued by Fagiano et al.<sup>82</sup>.

## Chapter 4

# Damage Propagation in Variable-Stiffness Panels

### 4.1 Introduction

**T**HE previous chapter focused on the elastic behaviour of VSP. That is, their linear prebuckling and nonlinear postbuckling responses up to the onset of failure in the laminate. If a panel is unloaded from a loading state within this range, it returns to its original stress state prior to the application of mechanical stresses with no damage whatsoever. This chapter is focused on the panel response under applied loads higher than those that cause first-ply failure, hence resulting in permanent damage to the laminates<sup>61;83;84</sup>. As a consequence, the structures are unlikely to retake their initial state after unloading. The damage progression as the load increases is modelled within a FE framework, as done before for the damage onset, and the final failure loads and modes are predicted. The material damage model used in this research was developed by Maimí et al.<sup>85;86</sup> and is based on continuum damage mechanics, a methodology well suited for the simulation of damage evolution and ultimate failure of composite structures.

PFA are carried on the most promising panel configurations, as determined from the first-ply failure study in the previous chapter. Additionally, this chapter reports postbuckling, damage and failure simulations of experimental tests on VSP carried in the past by Jegley et al.<sup>8;9</sup>. In these tests, laminates with steered and non-steered fibres were loaded in compression and shear up to final failure. Jegley et al.<sup>8;9</sup> tried to simulate these experiments through FE analyses as well. However, the models failed to predict the buckling loads with acceptable accuracy,

and the damage and failure modes were not studied in detail. Wu et al.<sup>7</sup> also performed numerical simulations of compression tests on flat tow-steered panels. Accurate predictions of transition loads were obtained but only by taking into account the residual thermal stresses resulting from the curing process. Damage simulations or failure load predictions were not performed. In the work presented in this chapter, all the appropriate measures are taken into account in order to simulate the behaviour of VSP under compression up to their global structural failure.

## 4.2 Progressive Damage and Failure Analyses

The ability to predict the initiation and growth of damage in fibre reinforced plastic structures is essential to evaluate their performance, residual strength, and to develop reliable, safe designs which exploit the advantages offered by composites. Since most composite materials exhibit quasi-brittle failure with little or no margin of safety through ductility, as offered by many metals, the mechanisms of propagation of quasi-brittle damage in composite structures are worth understanding in detail.

Under normal operating conditions, laminated composite structures can exhibit local damage mechanisms such as matrix cracks, fibre breakage, fibre-matrix debonding, and delaminations which contribute to final failure. Strength-based failure criteria are commonly used to predict these phenomena. A large number of continuum-based criteria have been derived to relate stresses and experimental measures of material strength to the onset of failure<sup>63;67</sup>. In most cases, however, first-ply failure criteria can only predict the onset of the different damage mechanisms, and are inaccurate in predicting the ultimate structural failure of composite structures that can accumulate damage before structural collapse. To bridge this gap, the past recent years have seen the development of numerical methodologies to address the progressive failure of composite materials<sup>87</sup>.

A typical methodology for PFA is illustrated in Figure 4.1. At each load step, a nonlinear analysis is performed to account for the geometrically nonlinear response of the structure (e.g. a panel in postbuckling). Using this nonlinear solution, the local lamina stresses are determined and checked against failure criteria to determine whether any damage has occurred for this load increment. If no failure is detected, the applied load is increased and the analysis continues. When failure in the lamina occurs, a change in the stiffness tensor is calculated based on the material degradation model. This adjustment accounts for the nonlinearity associated with material damage. Static equilibrium needs to be re-established



by repeating the geometrically nonlinear analysis at the current load step, using the new material properties. The load step is then incremented and the process repeated until final failure of the structure is detected. In most models, final structural failure is identified at the load level at which static equilibrium can no longer be reached. Due to its convergence rate, the most popular iterative scheme for the solution of the nonlinear FE equations is the Newton-Raphson procedure. However, in structures showing negative stiffness, for instance due to mode jumping phenomena and postbuckling collapsing behaviour, the Riks path following method may be preferable<sup>81</sup>.

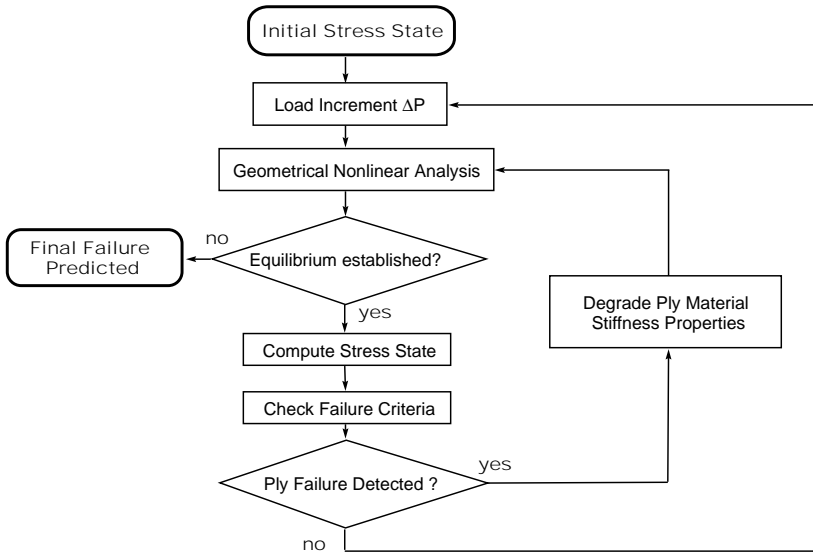


Figure 4.1: Typical PFA methodology (after Sleight<sup>87</sup>).

At loads close to structural collapse due to material failure, static equilibrium ceases to be achieved because fracture is in itself a dynamic process, with sudden dissipation of energy and conversion into kinetic energy of a great part of the accumulated strain energy. In this event, the solution of the static problem defined by

$$[K]\{u\} = \{F\} \quad (4.1)$$

becomes undetermined. However, if the inertia and damping of the structure is taken into account, the system

$$[M]\{\ddot{u}\} + [C]\{\dot{u}\} + [K]\{u\} = \{F\} \quad (4.2)$$

can still be solved for most cases. Therefore, structural collapse due to fracture is often possible to be numerically simulated through dynamic analyses. In the last equations,  $[M]$ ,  $[C]$  and  $[K]$  are the system mass, damping, and stiffness matrices,  $\{F\}$  is the applied force vector,  $\{u\}$ ,  $\{\dot{u}\}$ , and  $\{\ddot{u}\}$  are the system displacements, velocities and accelerations, respectively.

The most simple damage model for laminated composites is the ply discount method: when first-ply failure is detected the whole stiffness of the lamina is removed from the laminate stiffness matrix, as illustrated in Figure 4.2. This method, and other simplified methods, can be used to get rough estimates of the final failure of a composite structure. However, continuum damage mechanics is a more accurate methodology to predict the quasi-brittle failure of composites. In this way, the more realistic gradual unloading of a ply after the onset of damage is simulated by means of a material degradation model.

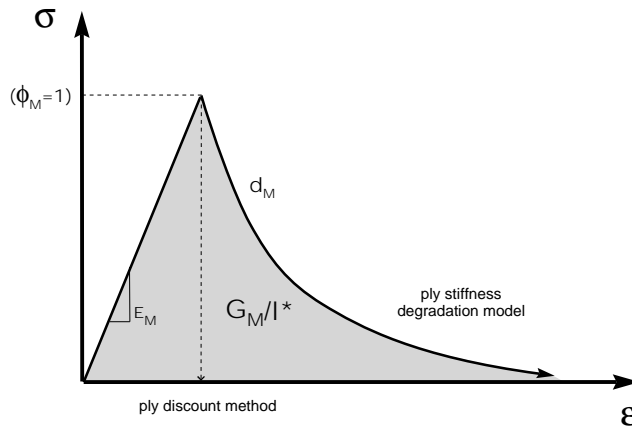


Figure 4.2: Idealised damage behaviours in composite laminae.

Nonlinear constitutive models defined in the context of the mechanics of continuum mediums have been developed and implemented in FE codes in the past<sup>87</sup>. The damage model used in this work for the prediction of the post-buckling response and structural collapse of VSP was developed by Maimí et al.<sup>85;86</sup>. There are three main differences between this and the damage models for composites previously developed by other authors. First, the use of physically-based criteria to predict the onset of matrix cracking and fibre fracture, the LaRC first-ply failure criteria<sup>70;71</sup> described in Chapter 3, which account for the in-situ effect<sup>78</sup> of the thickness of a ply on its transverse tensile and shear strengths. Second, the simulation of crack-closure effects under load reversal cycles. Third, the im-

plementation of the crack band model proposed by Bažant<sup>88</sup> to ensure a mesh independent solution. An alternative method to ensure a mesh-independent solution is, for example, the viscoplastic regularisation proposed by van der Meer and Sluys<sup>89</sup>.

The majority of the material properties required for the definition of the damage model can be measured using standard test methods that are defined at ply level. This represents a clear improvement over damage models that are defined at laminate level and that require the measurement of properties for each lay-up. The main aspects of the damage model used in this work are presented in the following paragraphs.

### 4.2.1 Continuum Damage Model

The complementary free energy density of a ply is defined by:

$$G = \frac{\sigma_{11}^2}{2(1-d_1)E_1} + \frac{\sigma_{22}^2}{2(1-d_2)E_2} - \frac{\nu_{12}}{E_1}\sigma_{11}\sigma_{22} + \frac{\sigma_{12}^2}{2(1-d_6)G_{12}} + (\alpha_{11}\sigma_{11} + \alpha_{22}\sigma_{22})\Delta T + (\beta_{11}\sigma_{11} + \beta_{22}\sigma_{22})\Delta M \quad (4.3)$$

where  $d_1$  and  $d_2$  are the non-dimensional damage variables ( $0 \leq d_M \leq 1$ ) associated with longitudinal (fibre) failure and transverse matrix cracking, respectively. They take an initial value of 0 when the material is undamaged, and increase with damage evolution up to a value of 1, representing complete material failure. The damage variable  $d_6$  is influenced by longitudinal and transverse cracks;  $\alpha_{ii}$  and  $\beta_{ii}$ , ( $i = 1, 2$ ) are, respectively, the coefficients of thermal and hygroscopic expansion in the longitudinal ( $i = 1$ ) and transverse directions ( $i = 2$ );  $\Delta T$  and  $\Delta M$  are the temperature and moisture content variations with respect to the corresponding reference values.

The strain tensor results from the derivation of the complementary free energy density with respect to the stress tensor:

$$\varepsilon = \frac{\partial G}{\partial \sigma} = \mathbf{H} : \sigma + \alpha \Delta T + \beta \Delta M \quad (4.4)$$

Here,  $\mathbf{H}$  is the lamina compliance tensor represented as:

$$\mathbf{H} = \frac{\partial^2 G}{\partial \sigma \otimes \partial \sigma} = \begin{bmatrix} \frac{1}{(1-d_1)E_1} & -\frac{\nu_{21}}{E_2} & 0 \\ -\frac{\nu_{12}}{E_1} & \frac{1}{(1-d_2)E_2} & 0 \\ 0 & 0 & \frac{1}{(1-d_6)G_{12}} \end{bmatrix} \quad (4.5)$$

The longitudinal and transverse damage variables are identified using:

$$\begin{aligned} d_1 &= d_{1+} \frac{\langle \sigma_{11} \rangle}{|\sigma_{11}|} + d_{1-} \frac{\langle -\sigma_{11} \rangle}{|\sigma_{11}|} \\ d_2 &= d_{2+} \frac{\langle \sigma_{22} \rangle}{|\sigma_{22}|} + d_{2-} \frac{\langle -\sigma_{22} \rangle}{|\sigma_{22}|} \end{aligned} \quad (4.6)$$

where  $\langle x \rangle$  is the McCauley operator defined as  $\langle x \rangle := (x + |x|)/2$ . Damage caused by tension loads ( $d_+$ ) is tracked separately from damage caused by compression loads ( $d_-$ ). In this way, the eventual closure of transverse cracks under load reversal is taken into account. Depending on the sign of the corresponding normal stress, a damage mode can be either active or passive. The model assumes that the shear damage variable,  $d_6$  is not affected by the closure effect. Shear damage occurs mainly in the form of transverse cracks and these do not close under shear stresses<sup>77</sup>.

### Damage Activation Functions

The elastic domain is assumed to be bounded by four distinct damage activation functions based on the LaRC failure criteria<sup>71</sup>: longitudinal and transverse fracture under tension and compression. The four damage activation functions,  $F_N$ , associated with damage in the longitudinal ( $N = 1+, 1-$ ) and transverse ( $N = 2+, 2-$ ) directions, represented in Figure 4.3, are defined as:

$$F_{1+} = \phi_{1+} - r_{1+} \leq 0 \quad ; \quad F_{1-} = \phi_{1-} - r_{1-} \leq 0 \quad (4.7)$$

$$F_{2+} = \phi_{2+} - r_{2+} \leq 0 \quad ; \quad F_{2-} = \phi_{2-} - r_{2-} \leq 0$$

where the loading functions,  $\phi_N$  ( $N = 1+, 1-, 2+, 2-$ ), depend on the strain tensor and material constants (elastic and strength properties) and are explained in the previous chapter. The elastic domain thresholds,  $r_N$  ( $N = 1+, 1-, 2+, 2-$ ), are related to the damage variables  $d_M$  ( $M = 1+, 1-, 2+, 2-, 6$ ) by the damage evolution laws. They take an initial value of 1 for a material behaving elastically and increase with damage. The elastic domain thresholds are obtained applying the Kuhn-Tucker and consistency conditions, assuming that the elastic domains in

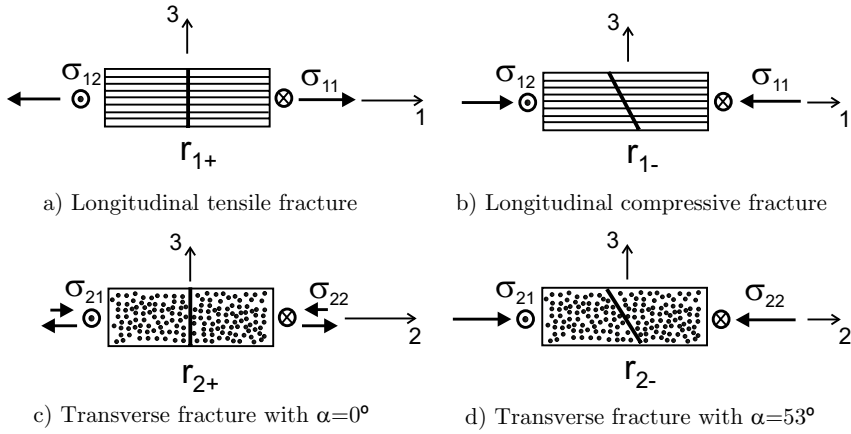


Figure 4.3: Fracture surfaces and corresponding internal variables for four different failure modes.

tension and in compression are coupled and that the transverse and longitudinal elastic domains are uncoupled<sup>85;86</sup>:

$$\begin{aligned}
 r_{N+} &= \max \left\{ 1, \max_{s=0,t} \{ \phi_{N+}^s \}, \max_{s=0,t} \{ \phi_{N-}^s \} \right\}, \quad N = 1, 2 \\
 r_{N-} &= \max \left\{ 1, \max_{s=0,t} \{ \phi_{N-}^s \} \right\}, \quad N = 1, 2
 \end{aligned} \tag{4.8}$$

### Damage Evolution and Mesh Regularisation

The standard implementation of strain-softening constitutive models results in mesh-dependent results, i.e. the solution is non-objective with respect to the mesh refinement, and the computed energy dissipated decreases with the reduction of the element size.

An effective solution to assure objective solutions consists in using the characteristic length of the finite elements,  $l^*$  (corresponding to the square root of the area represented by one integration point), in the definition of the constitutive model<sup>88</sup>. As schematically shown in Figure 4.4, the post-peak response of the material is scaled as a function of the element size to keep the computed energy dissipation independent of the size of the element, and equal to the material fracture energy. The energy regularisation scheme proposed requires the values of the fracture energies per unit surface associated with the four failure modes shown in Figure 4.3.

The exponential damage evolution laws proposed by Maimí et al.<sup>85;86</sup> are expressed in the following general form:

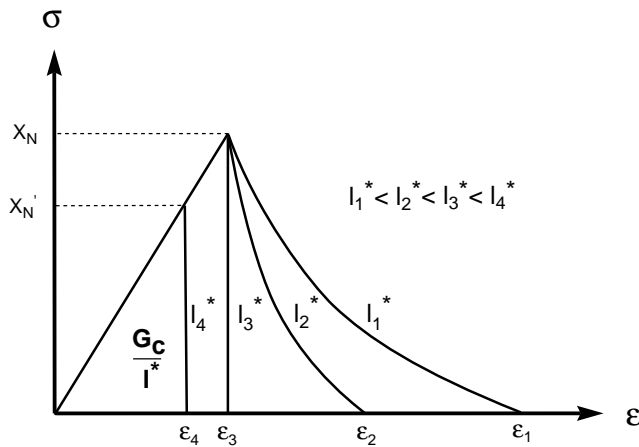


Figure 4.4: Scaling of constitutive model for different element sizes.

$$d_M = 1 - \frac{1}{f_N(r_N)} \exp \{A_M [1 - f_N(r_N)]\} f(r_K) \quad (4.9)$$

where the function  $f_N(r_N)$  is selected to force the softening of the constitutive relation. The damage law parameters,  $A_M$  ( $M = 1+, 1-, 2+, 2-, 6$ ), assure that the dissipated energy computed by the numerical model is independent of mesh refinement.  $f(r_K)$  is the coupling factor between damage laws and elastic threshold domains. The damage evolution laws for each damage variable are described by Maimí et al.<sup>85;86</sup>.

The parameters  $A_M$  ( $M = 1+, 1-, 2+, 2-, 6$ ) used in Equation (4.9) are not defined a priori, but are instead calculated internally by the model to ensure that the computed energy dissipation is independent of the element size. The equality between the rate of energy dissipation ( $l^* g_M$ ) for each failure mode and the corresponding fracture toughness ( $\mathcal{G}_M$ ) is imposed by:

$$l^* g_M = l^* \int_1^\infty \frac{\partial G}{\partial d_M} \frac{\partial d_M}{\partial r_M} dr_M = \mathcal{G}_M, \quad M = 1+, 1-, 2+, 2-, 6 \quad (4.10)$$

Equations (4.10), used together with Equations (4.9), are numerically integrated to calculate the parameters  $A_M$ .

### Material Properties

The independent material properties required to define the damage model are:

- Ply elastic properties ( $E_1, E_2, G_{12}, \nu_{12}$ ) and ply strengths ( $X_{1+}, X_{1-}, X_{2+}, X_{2-}, X_6$ ). These properties can be measured using test standards defined by the American Society for Testing and Materials (ASTM)<sup>90–92</sup>.
- Four components of the fracture toughness, associated with longitudinal failure in tension and compression ( $\mathcal{G}_{1+}$  and  $\mathcal{G}_{1-}$ , respectively) and with transverse failure in tension and shear ( $\mathcal{G}_{2+}$  and  $\mathcal{G}_6$ , respectively).  $\mathcal{G}_{2+}$  can be measured using a standard test procedure devised by the ASTM<sup>93</sup>.  $\mathcal{G}_{1+}$  and  $\mathcal{G}_{1-}$  are measured using compact tension and compact compression tests developed by Pinho et al.<sup>94</sup>.  $\mathcal{G}_6$  can be measured using the four-point bending end-notched flexure test proposed by Martin et al.<sup>95</sup>.

The fracture toughness  $\mathcal{G}_{2-}$  is dependent on  $\mathcal{G}_6$  and on the angle  $\alpha_0$  in the form  $\mathcal{G}_{2-} = \mathcal{G}_6 / \cos \alpha_0$ . Additionally, the model requires the input of the in-situ strengths  $X_{2+}^{is}$  and  $X_6^{is}$ , which are functions of the independent material properties. The in-situ strengths can be calculated by means of closed-form equations presented in Chapter 3<sup>78</sup>.

## 4.3 Design Cases: Square Cutout Panels Under Edge Shortening

The study initiated in the previous chapter on constant and variable-stiffness cutout square panels is resumed in this section. Here, the first-ply failure analyses on the most promising configurations in terms of buckling and strength is extended to the progression of damage and final structural failure. The damage model described in the previous section, developed and implemented by Maimí et al.<sup>85;86</sup> in the commercially available ABAQUS FE code<sup>62</sup> as a FORTRAN User defined MATerial (UMAT) subroutine, is used for this purpose.

### 4.3.1 Numerical Set-Up

The cases under analysis consist of simply supported square panels with a central hole under uniform edge shortening, as described in the previous chapter and depicted in Figure 3.3.2. The transverse edges are free to expand in the  $x$ -direction. The typical FE model consists of a mesh of fully integrated, **S4**, shell elements with a typical characteristic length  $l^*=2\text{mm}$ . Such a small element size guarantees a maximum fibre angle difference of  $1.2^\circ$  between elements, and a correct energy dissipation.

The configurations chosen for analysis are those which obtained the best buckling and first-ply failure results: the constant-stiffness designs  $[\pm 45]_{6s}$  and  $[\pm 80]_{6s}$ ; and the variable-stiffness laminate  $[\pm < 0|80 >]_{6s}$ . For the tow-steered design, two construction methods are studied: the tow-drop and the tow-overlap methods. Asymmetric thickness build-up is taken into account in the case of panels with overlaps. The technique of ply staggering is used in the design of all the curvilinear-fibre laminates except for one of the configurations.

In practical cases,  $\pm 45$  plies are added as face plies of tow-steered laminates in order to smooth abrupt thickness variations and cover resin-rich regions at tow-drop locations. Therefore, this type of formats is worth being investigated. Hence, a hybrid design, the  $[\pm 45/\pm < 0|80 >_4]_s$  laminate, is added to this study.

The laminate material simulated is the carbon-epoxy material system AS4/9773 whose elastic and strength properties are summarised in Table 3.1. The nominal ply thickness,  $h_p$ , is 0.2mm and the total 24-ply laminate thickness,  $h_l$  is 4.8mm. The in-situ strengths are reported in table 3.2. The fracture toughness properties for the material AS4/9773 are not available. The mode I and mode II components of the fracture toughness for matrix cracking used herein,  $\mathcal{G}_{2+}$  and  $\mathcal{G}_6$  respectively, were measured by Reeder<sup>96</sup> for the material IM7/9772 using interlaminar test methods. There is no standard test method to measure the fracture toughness associated to failure in the longitudinal direction,  $\mathcal{G}_{1+}$  and  $\mathcal{G}_{1-}$ . Pinho et al.<sup>94</sup> proposed new test methods, based on compact tension and compact compression specimens, to measure  $\mathcal{G}_{1+}$  and  $\mathcal{G}_{1-}$ . These methods were used in a previous characterisation of the IM7/8552 carbon-epoxy material<sup>97</sup> and the values measured then are used here. All the required independent values of the fracture toughness are reported in Table 4.1.

Table 4.1: Fracture toughness properties used to model the material AS4/9773 [N/mm].

$\mathcal{G}_{1+}$	$\mathcal{G}_{1-}$	$\mathcal{G}_{2+}$	$\mathcal{G}_6$
81.5	106.3	0.31	1.68

### 4.3.2 FE Procedure

In order to generate the nonlinear solutions in the buckling path using ABAQUS<sup>62</sup>, a linear bifurcation analysis is performed at first and the first two buckling modes for the structure are calculated. Then the FE model is redefined with the buckling



modes introduced as initial imperfections with small amplitudes as compared to the panel thickness (typically 1-5%). Finally, geometric and material nonlinear solutions are determined for loads up to structural failure as predicted by the damage model. Panel inertia is taken into account by using a dynamic solution procedure. The progressive damage problem is stabilised by the introduction of the mass matrix, and the mode jumping phenomenon, where a significant part of the model strain energy is suddenly released, can be accurately predicted.

Taking into account the findings of Chapter 3, residual thermal stresses resulting from the laminate curing process are simulated by means of the application of thermal steps previous to the linear bifurcation and the nonlinear dynamic loading steps. In these thermal steps a linear cooldown ( $\Delta T = -137.8^\circ C$ ) is prescribed<sup>7</sup>.

The user-developed FORTRAN routine UMAT, which implements of the continuum damage model, is run at each equilibrium iteration for each of the integration points in the model. This routine can also handle thermal loading events such as curing cooldown.

### 4.3.3 Damage and Final Failure Results

The prebuckling and postbuckling load versus edge shortening behaviour for the panel configurations analysed, including damage progression, are plotted in Figure 4.5. The dashed segments initiate at the damage onset loads reported in Table 3.3 and terminate after the sudden load drops indicating final structural failure. The load values corresponding to final panel failure are given in Table 4.2 which also compares the performance of constant and variable-stiffness designs.

The onset of damage on the  $[\pm 45]_{6s}$  panel occurs at a relatively low load, by longitudinal compression, due to the stress concentration around the hole. However, this structure seems to accumulate a considerable amount of damage before final failure which occurs at a load almost 70% higher than the failure of the first ply. The average final failure load,  $N_{ff}^{av}$  is 409.6N/mm while the average first-ply failure load,  $N_{fpf}^{av}$ , is only 244.7N/mm. The corresponding displacement values more than double (2.85mm versus 1.22mm). The final failure mode for this panel is illustrated in Figure 4.6.a. Cracks oriented at  $\pm 45^\circ$  are triggered by shear loads at the transverse edges propagating to the inner regions of the panel. Although they are initiated at the face plies in the form of matrix cracking, these shear bands also propagate through-the-thickness of the laminates involving extensive damage in the form of fibre kinking. The occurrence of several locations of damage accumulation before global failure may justify, in part, the extensive damage range. Another reason is that the onset of damage occurs at the hole

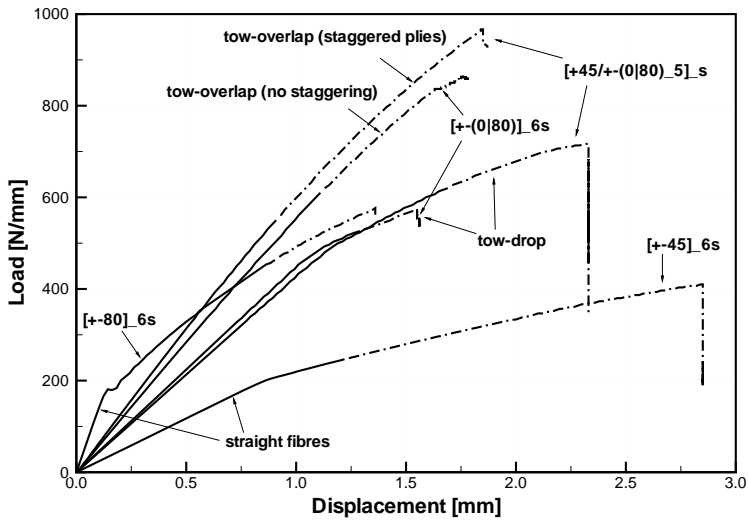


Figure 4.5: Load versus displacement curves for the configurations simulated. The curves cover the elastic (solid line) and progressive damage (dashed line) response of the panels up to final structural failure (sudden load drop).

edge and some damage accumulates at this location, but the structural collapse is not triggered by the hole. As the load increases and the buckle grows, the central section of the panel unloads relatively to the edges where the  $\pm 45^\circ$  shear cracks eventually start. This change in failure mode acts as a buffer for load increase and damage growth before final collapse. The described process only occurs due to the particular properties of the panel considered. Should it be stiffer, either due to different dimensions, boundary conditions or material properties, buckling would be delayed to higher loads and the panel would actually fail by the cutout.

Table 4.2: Strength results for the best designs with straight and steered fibres. Comparative results are mass-normalised.  $N_{ff}^{av}$  is the average final failure load.

Design	$N_{ff}^{av}$ [N/mm]	vs. $[\pm 80]_{6s}$ [%]	vs. $[\pm 45]_{6s}$ [%]
Straight fibres ( $[\pm 45]_{6s}$ )	409.6	-28.8	-
Straight fibres ( $[\pm 80]_{6s}$ )	575.8	-	40.6
Tow-drops	571.9	-0.7	39.6
Tow-drops ( $\pm 45^\circ$ faceplies)	716.2	24.4	74.9
Tow-overlaps (no staggering)	863.5	-5.7	32.6
Tow-overlaps	966.9	5.6	48.5
Tow-overlaps ( $\pm 45^\circ$ faceplies)	980.5	7.1	50.6

On the other hand, the process of failure of the  $[\pm 80]_{6s}$  panel is quite brittle. This configuration is close to a unidirectional laminate. There is only a  $20^\circ$  difference in fibre angle between neighbouring plies. Transverse cracks initiated by bending induced tensile stresses easily propagate with little resistance offered by the fibres i.e. contrary to the  $[\pm 45]_{6s}$  case, the mechanism of fibre bridging over the matrix cracks has little effect and there is little damage by fibre kinking. This effect can be visualised in Figure 4.6.b. No more than two sharp through-the-thickness cracks trigger the final failure of this structure at a load 40.6% higher than for the  $[\pm 45]_{6s}$  laminate. This contrasts with a first-ply failure performance advantage of 89.7%. Furthermore, the onset of damage is predicted to be triggered by fibre kinking, as seen in Chapter 3, while global failure is dominated by transverse cracking. Visibly, first-ply failure criteria can not only seriously under-predict the real strength of structures but also lead to a erroneous ranking of the performance of different configurations in terms of final failure load.

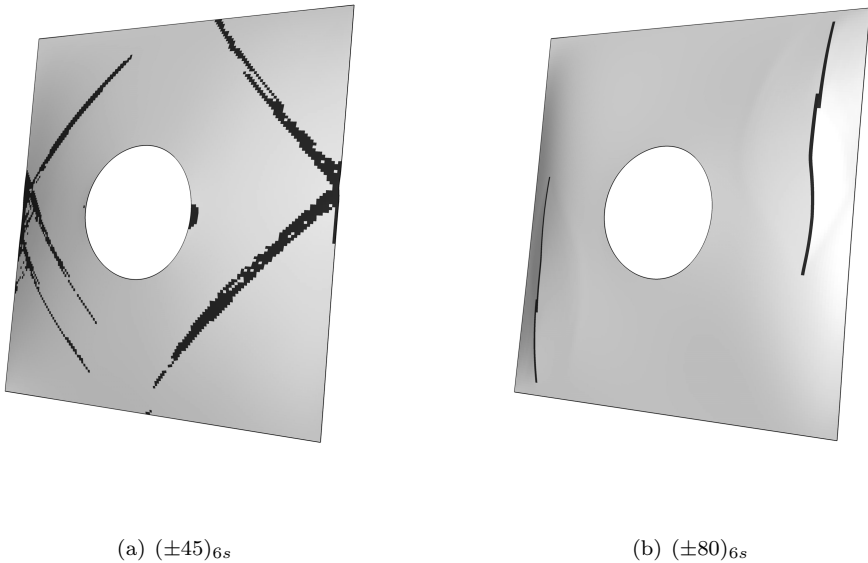


Figure 4.6: Failure modes for the simulated straight-fibre panels. The dark regions represent final material failure. Out-of-plane displacements are amplified by a factor of 2.

The failure mode of the fibre-steered panel with the  $[\pm < 0 | 80 >]_{6s}$  configuration with staggered tow-drops is shown in Figure 4.7.a. This laminate buckles in a two half-wave mode. Two matrix cracks start developing by the action of transverse tension at the convex sides of the buckles, close to the side edges where the bending induced stresses are the highest. It is interesting to notice that the ma-

trix cracks have a curved shape, parallel the local fibre orientation. This mode is different than the one identified as the onset of damage, which also occurs close to the side edges but by fibre kinking at the concave faces. The whole failure process, however, progresses in a quite brittle fashion. The first-ply and global failure loads are only 9.3% apart ( $N_{fpf}^{av}=523.4\text{N/mm}$  and  $N_{ff}^{av}=571.9\text{N/mm}$ ). Furthermore, the failure performance of the optimal constant-stiffness and variable-stiffness configurations is about the same. This means that the differences found in terms of first-ply failure are not reflected in final failure response.

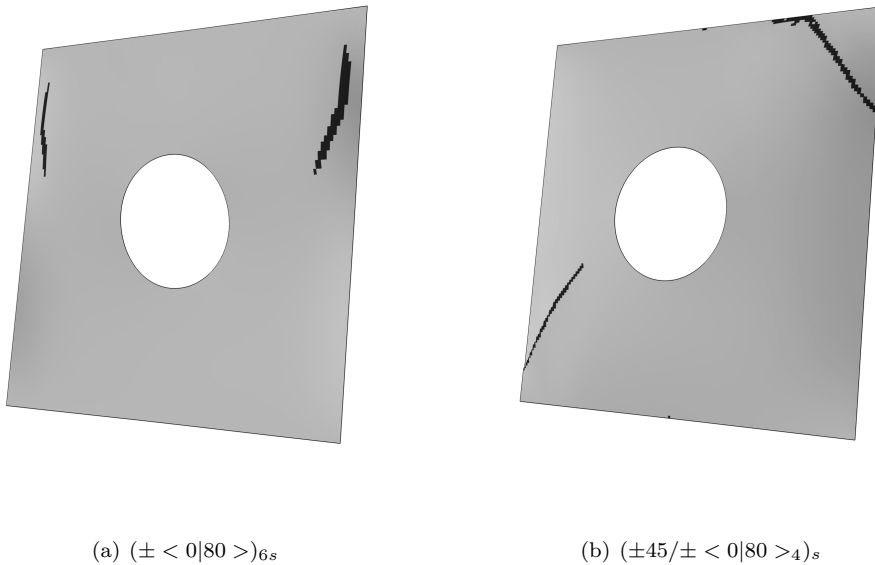


Figure 4.7: Failure modes for the simulated fibre-steered panels with tow-drops. The dark regions represent final material failure. Out-of-plane displacements are amplified by a factor of 2.

Replacement of the outer layers of the  $[\pm(T_0|T_1)]_{6s}$  type laminates by  $\pm 45$  plies produces advantageous results. The first-ply and the structural failure loads are increased, the latter by 25.1%. This means that the straight-fibre plies have a notable structural effect in smoothing the stress concentrations caused by the mismatch in fibre angles at the edges of the machine head-courses and in reducing the failure indexes. The predicted failure mode for the hybrid panel is depicted in Figure 4.7.b. It consists of structural cracks developing at an angle from the panel transverse edges in a non-symmetrical way. The first to initiate is a kink band, driven by shear stresses, that propagates towards the loaded edge. It is followed by a second shear crack, perpendicular to the first, initiated at the opposite edge and involving mostly transverse damage.

The  $[\pm < 0|80 >]_{6s}$  panels with overlapping tows do not change failure mode as damage progresses. Structural failure eventually occurs by the accumulation of distributed fibre compressive damage within the overlapping tows, near the side edges where the transferred loads are higher, as illustrated in Figure 4.8. This is the failure mode that leads to the highest failure loads due to the superior longitudinal strength of plies, as compared to their transverse or shear strengths, and due to the distribution of loads over a wide panel area. Contrary to the tow-drop case, hybridisation does not seem to noticeably improve the strength of these panels. On the other hand, ply staggering is responsible for an increase around 12% in panel strength. This is opposite to the trend observed in terms of first-ply failure loads. The absolute increase in failure performance offered by VSP with overlaps is around 70%. However, if the results are normalised by the panel mass, which is 59% higher than their constant-thickness counterparts, the advantage is severely reduced to 7.1%. This is much lower than the results achieved with the  $[\pm 45 / \pm (0|80)_4]_s$  panel with tow-drops.

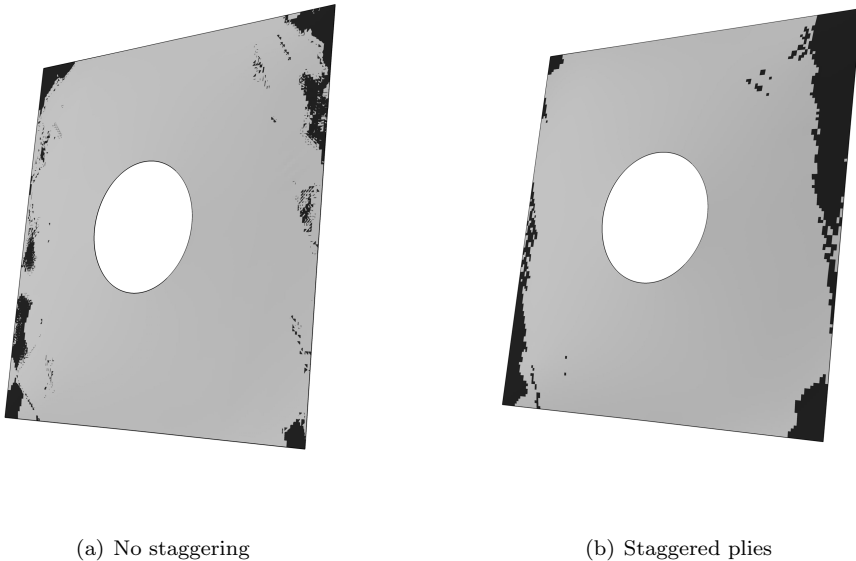


Figure 4.8: Failure modes for the  $[\pm < 0|80 >]_{6s}$  laminates with overlaps. The dark regions represent material damage. Out-of-plane displacements are amplified by a factor of 2.

## 4.4 Test Case: Rectangular Cutout Panels Under Edge Shortening

In this section, PFA are carried on previously tested constant and variable-stiffness panels manufactured by an AFP system. The results of the simulations are correlated with the experimental data obtained by Jegley et al.<sup>8;9</sup>.

The tow-steered laminates investigated here were optimised by Tatting et al.<sup>50;52</sup> for optimal buckling response. Laminate failure was taken into account in the design by using the Tsai-Hill failure criterion<sup>55</sup>, with the only purpose of guaranteeing that first-ply failure would occur well after the transition loads. Lopes et al.<sup>69</sup> carried first-ply failure analyses on the same panels, by using the set of phenomenological failure criteria LaRC developed at NASA Langley Research Centre<sup>71</sup>. According to the numerical solutions, tow-steered panels showed improvements as great as 34% when compared with classical straight-fibre laminates. The objective of the work presented in this section is to extend these analyses with the complete progressive damage process onto the final failure loads of such panels and compare the performance of constant and variable-stiffness configurations.

### 4.4.1 Experimental Set-Up

The structures simulated consist of 20-layer composite panels, 508mm×381mm in size, (20in×15in) with and without central holes, 76.2mm (3in) in diameter, under edge shortening, as illustrated in Figure 4.9. The laminates were built with the carbon-epoxy system AS4/9773 whose elastic and strength properties are summarised in Table 3.1. The nominal ply thickness,  $h_p$ , is 0.1397mm (0.054in). The total laminate thickness,  $h_l$ , is 2.794mm (1.08in). The in-situ strengths for this laminate, as calculated with the formulation presented in Chapter 3, are reported in Table 4.3. The values of the fracture toughness assumed for this problem are given in Table 4.1. Constant and variable-stiffness panels were manufactured, the latter ones with a nominal course width of 76.2mm (3in).

In previous experiments carried out by Jegley et al.<sup>8;9</sup>, the applied load was gradually increased in the prebuckling and postbuckling regime until global structural failure occurred. Edge shortening and out-of-plane displacements were measured by Direct Current Displacement Transducers (DCDT's) attached to the panels, as shown in Figure 4.10. The advantages of tow-steered designs over straight-fibre configurations were clearly demonstrated. Not only the buckling loads increased by up to a factor of 2 but also failure loads showed a maximum increase of 56%.

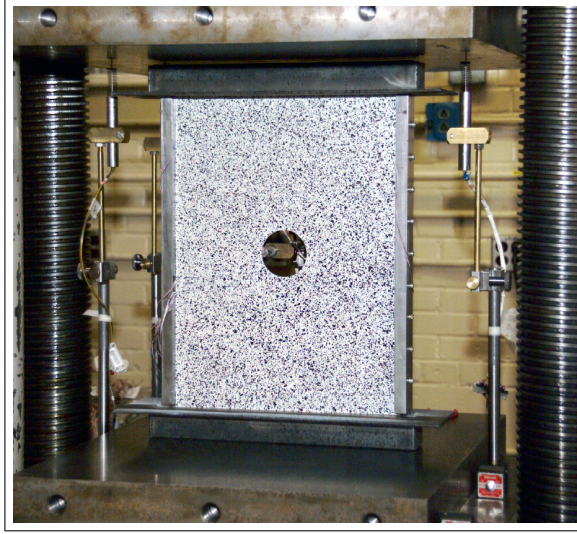


Figure 4.9: Experimental set-up (courtesy of Jegley et al. <sup>8;9</sup>).

Table 4.3: In-situ strengths for the present problem

Ply position	$X_{2+}^{zs}$ [MPa]	$X_6^{zs}$ [MPa]
embedded ply ( $h = h_p$ )	161.7	155.7
embedded ply ( $h = 2h_p$ )	114.2	128.7
outer ply ( $h = h_p$ )	102.2	128.7

Three variants of the composite panel specimens are considered, corresponding to three construction methods: i) the straight-fibre method, ii) the fibre-steered method with dropped tows and iii) the fibre-steered method with overlapping tows. The layups chosen for the analysis were the ones previously determined by Tatting et al. <sup>50;52;53</sup> based on the optimal buckling response, with the requirement that the optimised configurations should fail at a reasonably higher load than the buckling load. This request was verified using the Tsai-Hill first-ply failure criterion <sup>55</sup>. The design optimisation was only performed for the plates without holes. The same stacking sequence was used for the cutout panels. For the straight-fibre configuration, the best configuration was found to be the one with the stacking sequence  $[\pm 45_2 / \pm 30 / \pm 45 / \pm 15]_s$  whilst for the steered-fibre variants the best lay-up is the hybrid  $[\pm 45 / \pm < 45 | 60 >_2 / \pm < 30 | 15 > / \pm < 45 | 60 >]_s$ . In the external plies of the variable-stiffness laminates, the straight-fibre format was adopted so that gaps and overlaps were avoided at the exterior of the laminate. In the remaining plies, the maximum fibre angle variation was constrained to  $15^\circ$

so that the minimum turning radius of 625mm, i.e. the smallest reference path radius that results in an acceptable laminate quality (see Section 2.4), was not violated. The tow-steered plies were staggered in order to smear the tow-drops or the tow-overlaps, hence reducing eventual stress concentrations and laminate thickness variations.

#### 4.4.2 FE Implementation

The models simulate the boundary conditions used in the experiments and illustrated in Figure 4.10. On the lower edge, the built-in condition is modelled by restraining all degrees of freedom. On the top edge, displacements are only allowed in the vertical direction. The load is introduced by incrementing the top edge displacement. Out-of-plane displacements are restrained at both side edges to simulate the effect of the knife edges in the experiments.

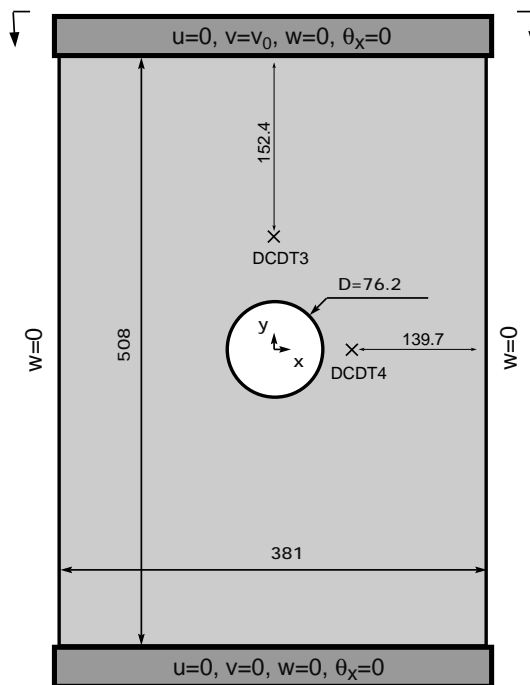


Figure 4.10: Panel geometry and boundary conditions (dimensions in mm).

The FE meshes make use of fully integrated **S4** shell elements with a typical characteristic length  $l^*=2\text{mm}$ . Such small elements are required mainly to guarantee a correct computation of the dissipated energy. Between each two neighbouring elements, the maximum fibre angle difference is  $0.16^\circ$ . For curvilinear-fibre



layers it is necessary to define a specific stacking sequence for each individual element according to the linear variation of the fibre orientation angle in Equation 2.1. Depending on the fabrication method used, the local stacking sequence can be calculated for an arbitrary point in the panel and a generic FE model can be transformed into a tow steered design merely by redefining the lay-up property entry, the \*SHELL SECTION card for each element. For the case of designs with overlapping tows, the laminate thickness is also updated by stacking extra layers at the overlap locations. In order to represent the asymmetrical thickness buildup in these configurations, the midsection of each shell element is offset, as shown in Figure 3.26.

The thickness of tow-steered panels with overlapping tows is at least equal to the nominal thickness corresponding to the desired laminate design. The plies are staggered in order to interweave the overlaps as most as possible. However, the resulting panels still show a variation on the local number of layers that ranges from 20 to 26. Roughly, 99% of the panel area has a thickness between 20 and 24 plies (20 plies: 33%, 22 plies: 33%, 24 plies: 33%) and only about 1% corresponds to the thickness of 26 plies. Hence, the mass of the panel increases 10.2% in comparison to its constant thickness counterparts. It is interesting to notice that neither the thickness buildup nor the mass increase are comparable to the values obtained for the  $[\pm < 0|80 >]_{6s}$  laminate investigated previously. This is due to the smaller fibre angle variations herein. Figure 4.11 shows the thickness distribution of the cutout panel designed according to the tow overlapping method.

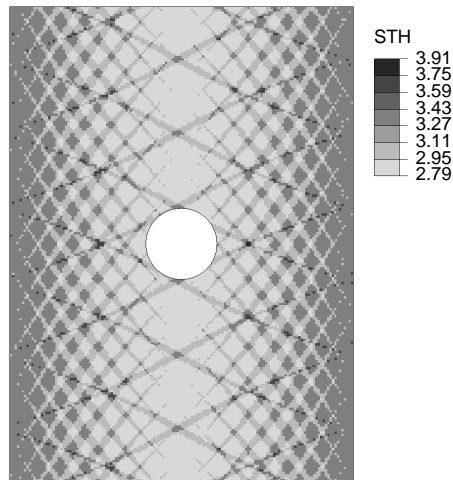


Figure 4.11: Thickness distribution of the cutout panel with overlapping tows. The number of plies varies from 20 to 26.

The numerical procedure for the PFA of the panels is similar to the one described previously for the cases of cutout square panels.

### 4.4.3 Buckling Response

As demonstrated in the previous chapter, the residual thermal stresses due to laminate curing have an important influence in the buckling and failure responses of fibre-steered panels. For these laminates, the residual stresses are not uniform layerwise as in straight-fibre laminates. This generates non-zero section forces throughout the laminates which influence mainly the buckling behaviour.

As an example, the sections forces developed due to curing in the VSP manufactured by the tow-drop method are illustrated in Figure 4.12. Negative forces develop close to the edges of the panels while positive forces, as high as 18.5N/mm, in the loading direction and 7.7N/mm in the transverse direction, arise in the central sections of the panel. These are beneficial because they reduce the mechanical compressive forces in this unsupported region which is the most critical in terms of buckling.

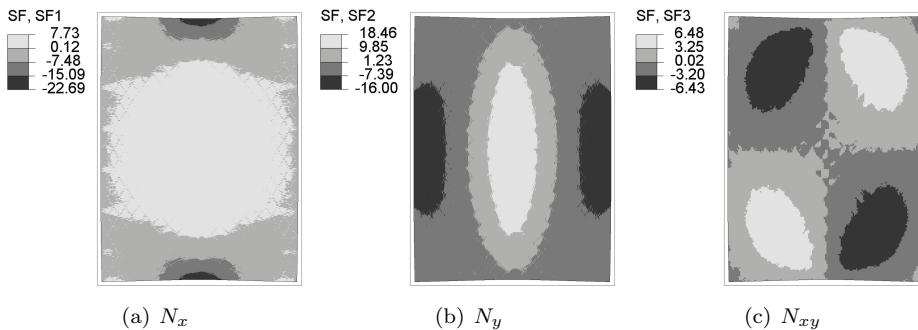


Figure 4.12: Residual thermal section forces (N/mm).

As observed experimentally, under progressive edge shortening, the flat panels buckle in a half-wave pattern and remain on this buckling mode as the load increases up to structural failure of the panel. On the other hand, a central hole triggers a change of buckling mode from half-wave to a full-wave pattern, as shown in Figure 4.13.

The bifurcation points, mode change behaviour and displacements can be analysed through the load-displacement curves plotted in Figure 4.14. Taking, as an example the cutout straight-fibre panel under compression, out-of-plane displacements are not observed until the transition point is reached at an applied overall load approaching 36.5N/mm. As the panel buckles in a half-wave pattern, the

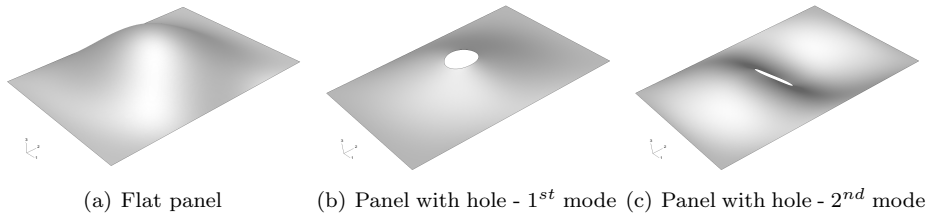


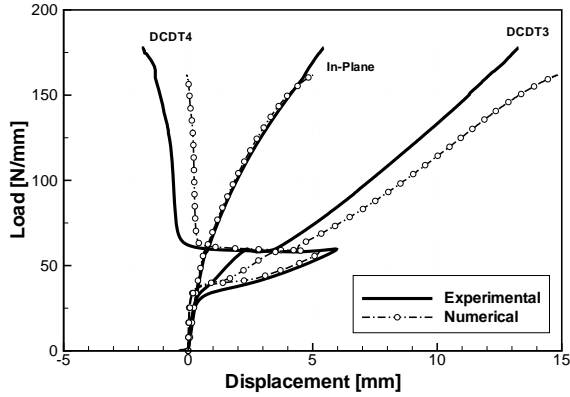
Figure 4.13: Buckling modes for the panel configurations analysed.

displacements measured by DCDT3 and DCDT4 grow in the same (positive) direction. Also, a decrease of structural stiffness is revealed by the edge shortening load-displacement curve. At an applied overall load of 59.8N/mm the panel finds another equilibrium path by changing its shape to a full-wave buckle. The displacements measured by DCDT3 still grow in the same direction but DCDT4 is taken to a slightly negative displacement path. The in-plane displacement curve shows that between these two equilibrium states, the load carrying capability of the panel slightly decreases. This panel mode shape is kept stable until the structure finally fails. The response is similar for the remaining cutout configurations. The respective transition loads are summarised in Table 4.4. All the predictions fall within an interval of 5% difference from the experimental results.

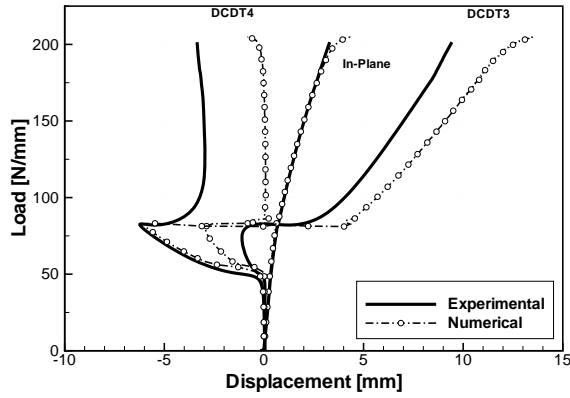
The predicted and measured displacements are compared in Figure 4.14. There is good agreement between the edge shortening curves. However, the out-of-plane displacements observed in the experiments are replicated by FE analyses with less accuracy, mainly for the tow-steered panels.

The benefit of steering fibres in the plane of the laminate is clearly visible by analysing the buckling load results presented in Table 4.4. According to the experimental results, the linear response range is extended by 42% for tow-steered laminates with dropped tows and 90.3% for the case of overlapping tows. Here, the 10.1% extra mass of the steered laminates with overlapping tows is taken into account by mass-normalisation of the results.

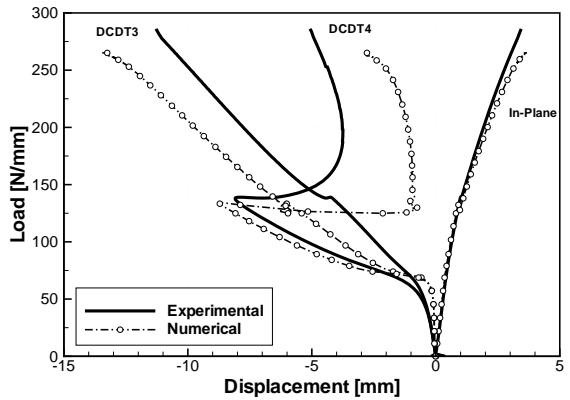
As demonstrated in the previous chapter, this beneficial effect is due to the capacity of variable-stiffness laminates for redistribution of the applied load fluxes to the supported edges. Since the buckling critical central sections of these panels are kept relatively unloaded, mode transition occurs only at overall applied loads higher than those for constant-stiffness configurations. Another cause for the higher buckling loads in tow-steered panels is the curing-induced residual thermal stress field, as explained in Chapter 3. If no pre-stresses were taken into account herein, the initial bifurcation loads would be under-predicted by 30% on average.



(a) Straight fibres



(b) VSP - dropped tows



(c) VSP - overlapping tows

Figure 4.14: Edge shortening and out-of-plane displacement curves for the panels with central holes.

Table 4.4: Buckling load results. Comparative results are mass-normalised. Exp. - Experimental results, SF - Straight Fibres, TD - VSP, Tow-Drop method, TO - VSP, Tow-Overlap method, Num. - Numerical results, TL - Transition load, MT - Mode transition load, Diff. - Difference between experimental and numerical results, Imp. - Improvement due to variable-stiffness design.

Config.		TL (Exp.) [N/mm]	TL (Num.) [N/mm]	Diff. [%]	Imp. [%]	MT (Exp.) [N/mm]	MT (Num.) [N/mm]	Diff. [%]
	No hole	SF	40.9	38.2	-6.8	-	-	-
TD		-	57.7	-	50.7	-	-	-
TO		-	81.4	-	93.0	-	-	-
Hole	SF	36.5	36.0	-1.4	-	59.8	58.5	-2.2
	TD	51.7	54.1	+4.6	42.0	82.9	83.2	+0.3
	TO	76.4	75.6	-0.7	90.3	139.1	134.4	-3.4

In addition to these general effects, tow-overlaps act as ‘integral stiffeners’ which help increasing the buckling loads further. It is interesting to notice that, contrary to what occurs with the square  $[\pm 45/\pm (0|80)_4]_s$  laminate analysed previously, the regions of thickness build-up due to overlapping tows on the  $[\pm 45/\pm < 45|60 >_2 / \pm < 30|15 > / \pm < 45|60 >]_s$  panel do not have a dominant effect in triggering buckling.

#### 4.4.4 Damage Initiation and Progression

By progressively increasing the applied loads in the postbuckling regime, the increasing stresses on the panels eventually lead to damage initiation and propagation at specific locations in some of the panel layers. This means that the combination of local longitudinal, transverse, and shear stresses is such that one of the first-ply failure criteria described in Chapter 3 is fulfilled. This corresponds to the initiation of damage. As seen before, the outmost layers are the most critical in terms of damage initiation. On one hand, the panel deforms in the out-of-plane direction with increasing bending forces due to the installed buckling mode. As a result, the bending induced strains and stresses are higher in the outer layers of the panels: tension and compressive stresses are generated on the convex and concave sides of the buckles, respectively. On the other hand, the in-situ strength of the face plies of a laminate is lower than that of their inner counterparts. As they become damaged and their load-carrying capability decreases, the load is transferred to the adjacent layers. Eventually these also start

to damage as a consequence of increased stress levels.

Most of the load is transferred along the longitudinal direction, such that the first damage onset criterion to be fulfilled is the one corresponding to longitudinal compression or fibre kinking. On average, damage initiates when about 75-80% of the panel load capacity is reached. With the increasing applied loads and bending induced stresses, the transverse damage initiation criteria are eventually fulfilled as well. As examples, the longitudinal and transverse damage variable fields ( $d_1$  and  $d_2$ ) at maximum applied load, for the four outmost layers at each side of the tow-steered panels with tow-drops and a central hole, are plotted in Figures 4.15 and 4.16. The damage fields are similar for the other panels. In spite of the central hole, the regions of the panels where damage accumulates and that eventually lead to their final failure are close to the knife edges, as happens to the panels without the cutouts. At those locations the out-of-plane curvature of the panel is generally higher, hence the in-plane compressive loading is added to bending-induced compression. The bending-induced stresses are such that, as the applied load levels increase, the transverse tension damage initiation criterion is fulfilled. However, this phenomenon is only observed at the last loading stages and only at the outer plies.

The comparison of the damage response of the laminates built according to the three different construction methods is best done by analysing the damage initiation load values presented in Table 4.5. As expected, damage initiation is postponed to higher loads as the laminate construction method is changed from straight to steered fibres. The benefit is, however, quite remarkable for the panels with overlapping tows for which damage is initiated at up to a 63.3% higher load level (normalised by panel mass) than for its straight-fibre counterpart. Curvilinear-fibre designs show the added benefit of reducing the degrading influence of the hole on the panel elastic load range. For traditional straight-fibre panels the central hole causes a decrease higher than 23% on the damage onset load. For tow-steered panels this difference is reduced to an average 17.6%.

By comparing Tables 4.4 and 4.5 it can be concluded that, for the constant-stiffness laminates, damage initiation occurs at a load around 3.4 times higher than buckling. This factor is reduced to 3.2 and 2.75, respectively for the fibre-steered designs with tow-drops and tow-overlaps. As explained before, although the onset of damage is due to fibre kinking, matrix cracks due to transverse tension also occur at a higher load level. The combination of these two damage modes eventually leads to the final failure of the composite panels.

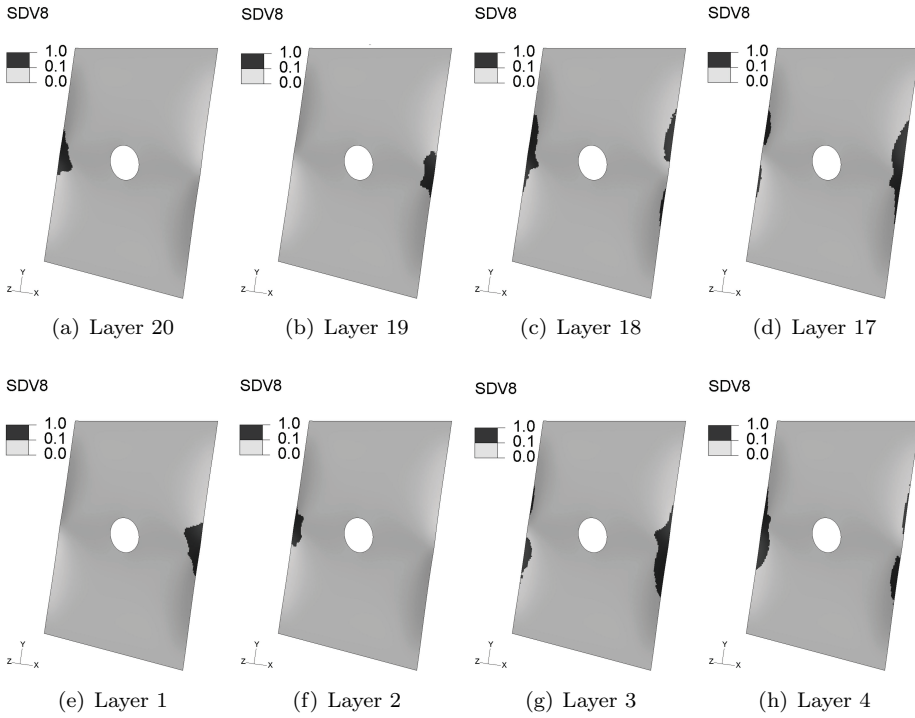


Figure 4.15: Longitudinal (fibre) damage variable ( $d_1$ ) on the four outmost layers at each tow-steered (tow-drop method) panel side, at maximum load level (216.1N/mm). Note: Layer 1 has the lowest out-of-plane coordinate value.

Table 4.5: Damage onset loads. Comparative results are mass-normalised. Imp. - Improvement due to variable-stiffness design.

Configuration	Const. Method	Damage Onset	Imp.	Hole effect
		[N/mm]	[%]	[%]
No Hole	Straight Fibres	161.4	-	-
	Tow-Drops	202.1	+25.2	-
	Tow-Overlaps	255.9	+53.2	-
Hole	Straight Fibres	123.9	-	-23.3
	Tow-Drops	166.9	+34.7	-17.4
	Tow-Overlaps	210.2	+63.3	-17.8

#### 4.4.5 Final Failure

The load versus edge shortening curves for the tested and simulated panels with central holes is plotted in Figure 4.17. The lines terminate at the predicted fail-

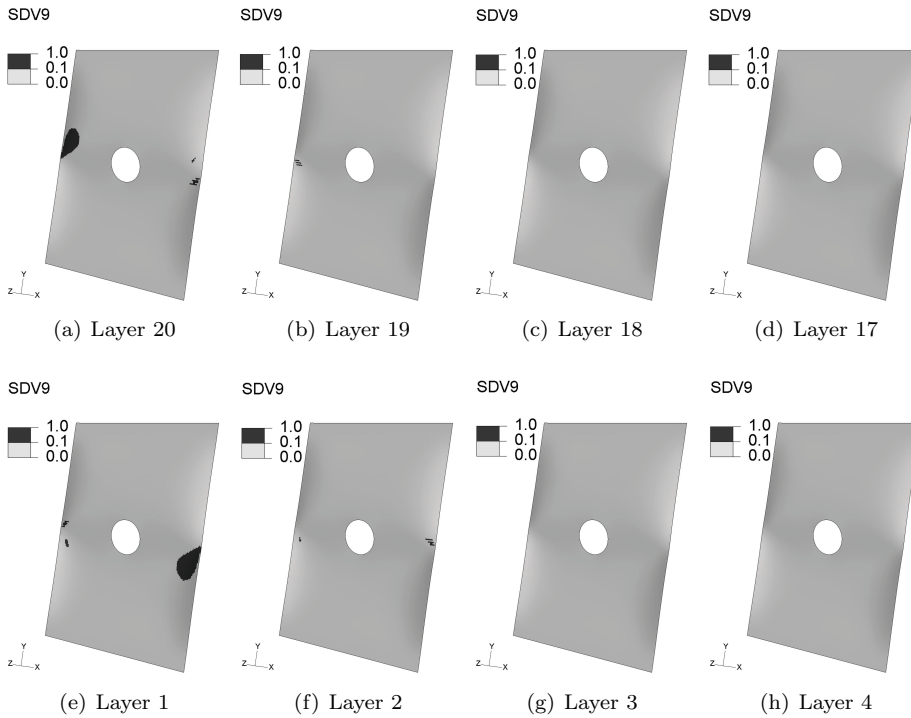


Figure 4.16: Transverse (matrix) damage variable ( $d_2$ ) on the four outmost layers at each tow-steered (tow-drop method) panel side, at maximum load level (216.1N/mm). Note: Layer 1 has the lowest out-of-plane coordinate value.

ure load levels. The load-displacement behaviour of the simulated cutout panels correlates very well with the experimental results except for the design with tow-overlaps and only after mode transition. Here, the predicted equilibrium path and panel stiffness after mode transition are slightly different from the experimental results. The extra stiffness observed in the experiments is probably caused by three-dimensional effects associated with the overlapping tows. These effects are neglected in the simplified shell models.

There are also visible differences between experimental and numerical results at the end of the load paths. The simulations predict a slight material softening while this behaviour was not observed in the experiments, i.e. the composite panels failed catastrophically without visible damage. This softening is coincident with the load interval in which matrix damage occurs. Here, the fracture toughness properties being used may be playing a role, mainly for the transverse direction. The fracture energy for the 9773 resin used in the fabrication of the laminates, but whose properties were not measured, may be higher than for the



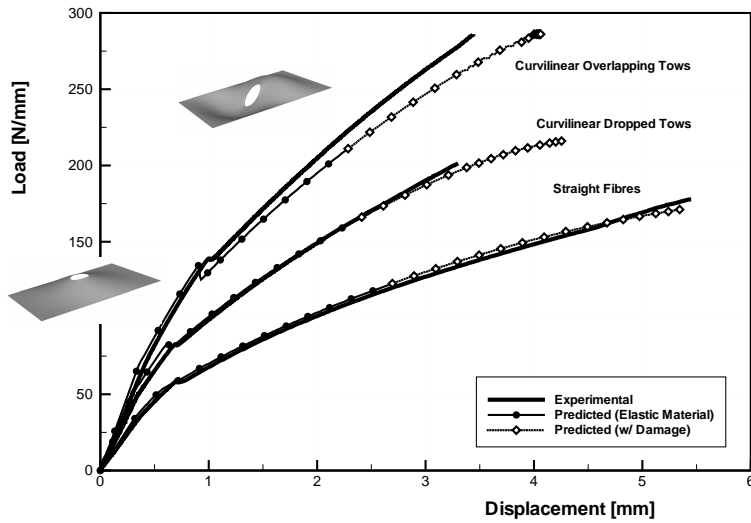


Figure 4.17: Load versus edge shortening curves for the simulated and tested panels. Hollow symbols identify damage progression.

9772 resin whose properties are used instead.

The predicted global failure loads are within 10% difference of the experimental failure loads. The accuracy on the prediction of the edge-displacement levels at which failure occurs is also fairly good except in the case of the tow-drop design technique. Here, the mismatch is probably due to the effects of tow-dropping. The individual dropping of tows results in fibre-free, resin-rich areas that can trigger damage initiation. Tow-drop areas are potential spots for the initiation matrix cracking or even delaminations, similarly to what occurs in regions of ply drop-offs in conventional laminates. The concern with delamination was already raised in Chapter 3 due to the high in-plane stress gradients in VSP which contribute to the amplification of interlaminar stresses<sup>74</sup>. The tow-drop areas can further excite the interlaminar stress distributions and potentially cause delamination to be the dominant failure mode in these designs<sup>98</sup>. However, these ‘hot-spots’ are not represented in the FE models used herein. Therefore, the prediction of their effects is not possible.

The strength performance obtained for the different panels are compared in Table 4.6. Fibre steering improves the strength performance of the analysed configurations up to a maximum of 55.5% (normalised by panel mass), achieved with the cutout tow-steered panel constructed according to the tow-overlap method. Also here, the detrimental effect of the hole on strength is reduced from around 17.5%, for constant-stiffness panels to 6.6% in the case of curvilinear and over-

lapping tows.

Table 4.6: Strength results. Comparative results are mass-normalised. Exp. - Experimental results. Num. - Numerical results, Diff. - Difference between experimental and numerical results. Imp. - Improvement due to variable-stiffness design.

Configuration	Const. Method	Strength (Exp.) [N/mm]	Strength (Num.) [N/mm]	Diff. [%]	Imp. [%]	Hole effect [%]
No Hole	Straight Fibres	~203.9	207.3	+1.7	-	-
	Tow-Drops	-	259.6	-	+25.2	-
	Tow-Overlaps	-	301.3	-	+41.2	-
Hole	Straight Fibres	177.7	171.0	-3.8	-	-17.5
	Tow-Drops	201.6	216.1	+7.2	+13.4	-16.8
	Tow-Overlaps	286.1	281.5	-1.6	+55.5	-6.6

The shape and fibre damage variable ( $d_1$ ) of straight and curvilinear fibre panels at collapse are represented in Figure 4.18. Numerical solutions at this load-displacement stage are only possible with dynamic analyses in which inertia effects are taken into account. The panels built with straight fibres and curvilinear fibres with dropped tows collapse along two folds which start at symmetrical locations at each side edge and develop around the hole. The VSP with overlapping tows shows an asymmetrical collapsing behaviour because of small asymmetries in the panel construction (see Figure 4.11). As it was cut from a bigger panel and the cutting was not made exactly at the intended locations, the origin of the tow angle variation is not coincident with the centre of the panel.

## 4.5 Conclusions

Numerical nonlinear postbuckling analyses of constant and variable-stiffness composite panels, taking into account the progressive material damage process and final structural failure, were carried out in this chapter. The use of a continuum damage model in the commercially available FE code ABAQUS<sup>62</sup> allowed the simulation of the full panel response when subjected to edge shortening loads.

Two series of laminates were investigated. The first series corresponds to hypothetical design cases which were selected in the parametric study performed in Chapter 3. The second series is constituted by panels actually tested in laboratory for buckling and failure under edge shortening conditions. Herein, the numerical

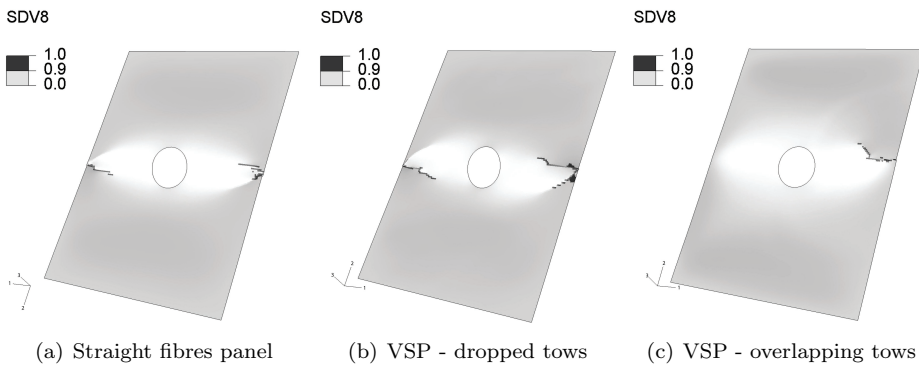


Figure 4.18: Through-the-thickness laminate cracks developing during collapse of three panel configurations.

procedure and damage model were validated with these experimental cases. The simulations agree well with experimental data, either in terms of buckling loads as in terms of strength performance.

Laminates with curvilinear-fibre topology demonstrated, through experimentation, remarkable improvements in terms of buckling and failure performance. The improvements were also predicted by the numerical simulations. It was observed in the previous chapter that the potential of the variable-stiffness format for improvements in the first-ply failure performance was not as promising as in terms of critical load. It was demonstrated in this chapter that, although the damage process offers a buffer for load increase before final structural failure, the possible strength improvements are still lower than they can be in terms of buckling.

The maximum difference in transition loads, normalised by weight, between constant and variable-stiffness panels is 90%. A better buckling performance was achieved by some designs considered in the previous chapter. This is due to their higher degree of fibre steering, hence higher potential for load redistribution. This effect is also reflected in the strength performance.

The maximum difference in specific strength between panels optimised for maximum buckling load is 55%. This advantage achieved by VSP with tow-overlaps is similar for the panels of both series. However, in what concerns the normalised failure performance of panels optimised for strength, the tow-overlap method may not to be the best option because of the shorter margin for strength improvements and because of the the extra mass associated with this construction method. According to the numerical simulations, the higher specific strength improvements are achieved with the tow-drop method. They range from 24% to

75%, respectively for designs optimised for strength and for buckling.

In the case of the tested specimens, due to the buckling mode, the central hole is not the main geometrical cause for failure. The prescribed boundary conditions in combination with the panel curvature due to buckling originate higher stress concentrations that eventually lead to final structural failure due to a combination of fibre kinking and transverse tensile cracks. However, the stress redistribution due to the cutout is not negligible and it promotes panel failure. As demonstrated in the previous chapter, the effect of the hole can be eliminated altogether if more freedom for fibre steering is allowed.

The case where the comparison between simulations and experiments shows the highest difference is the variable-stiffness laminate manufactured according to the tow-drop method. This may be because the wedge fibre-free regions, resulting from a perpendicular cutting of tows, are neglected from the numerical analyses. These resin-rich spots may trigger damage initiation and promote structural failure. The effects of dropping tows are investigated in the following chapter.

## Chapter 5

# Failure of Variable-Stiffness Laminates with Tow-Drops

### 5.1 Introduction

LAMINATES that have variations of the fibre orientation across its planform can be manufactured using advanced tow-placement technology, as described in Chapter 2. To manufacture such configurations, successive passes of the fibre placement head need to be made resulting in overlapping fibre tows and thickness buildup regions. If a constant thickness is desired, tows have to be cut at the course boundaries. In the analysis of the tow-placed structures with constant thickness, by Tatting and Gürdal<sup>50;52;53</sup>, Blom et al.<sup>44;45</sup>, Lopes et al.<sup>61;69</sup>, as well as in the numerical simulations described in the previous chapters, the course boundaries were assumed to be smooth. In reality, tows are cut perpendicular to the fibre directions, resulting in small triangular resin-rich areas.

A theoretical, numerical investigation of the influence of these tow-drop areas on the strength and stiffness of variable-stiffness laminates is carried out in this chapter. The influence of the tow width, laminate thickness and ply staggering, in combination with tow-drop areas, on the in-plane failure performance of variable-stiffness laminates is studied by means of parametric studies. The commercially available FE package ABAQUS<sup>62</sup> is used together with the user-developed continuum damage model<sup>85;86</sup>, in a similar way as performed in the previous chapter.

## 5.2 Tow Dropping and Resin-Rich Spots

As described in Chapter 2, manufacturable fibre-steered laminates exhibit overlapping tows if the tow-course width is kept constant i.e. for a constant number of tows within each machine head pass. These overlaps can be eliminated by using the tow-cutting and restarting capability of the tow-placement machines. By applying this technique, a constant thickness fibre-steered panel can be produced.

The tows are cut perpendicular to the fibre direction, resulting in a jagged edge. If the tow-drop method is used, different tow-coverage levels can be chosen, as described by Tatting and Gürdal<sup>53</sup>. A coverage of 0% indicates that a tow is cut as soon as its first edge reaches the boundary of the adjacent course. This results in a small fibre-free triangular area that is likely to be filled with resin during curing, therefore creating a 'resin-rich' region which may be termed a *tow-drop area*. At 100% coverage, the tow is cut only when both tow-edges cross the boundary, hence creating a small triangular overlap area. Coverage values between 0% and 100% represent the intermediate cases. Three examples are given in Figure 5.1.

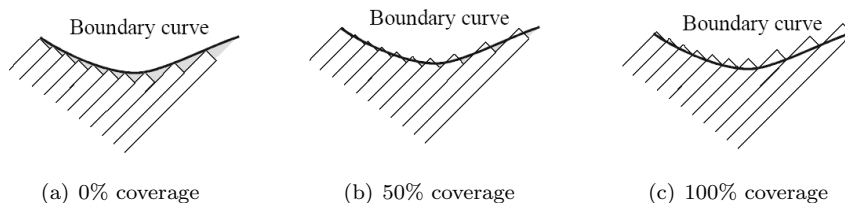


Figure 5.1: Tow-dropping with different coverage parameters (courtesy of Tatting and Gürdal<sup>53</sup>).

Resin-rich areas may be hot-spots for damage and failure due to their low stiffness and fracture toughness, hence tow-drops are potential crack initiators. Therefore, the study of the influence of these in the global failure performance of VSP is of great relevance.

The tow-dropping method was included in the design of the tow-steered panels manufactured by Tatting and Gürdal<sup>52;53</sup>. Therefore, some of these panels exhibited small triangular resin-rich regions between courses, as shown in Figure 5.2. However, these resin-rich spots were not taken into account in the numerical analyses carried out by most researchers, i.e. perfectly smooth course boundaries were assumed. Similarly, all the analyses performed on VSP (e.g. 7;10;44–46;61;69), including the studies presented in the previous chapters, neglect the discrete resin-rich spots.

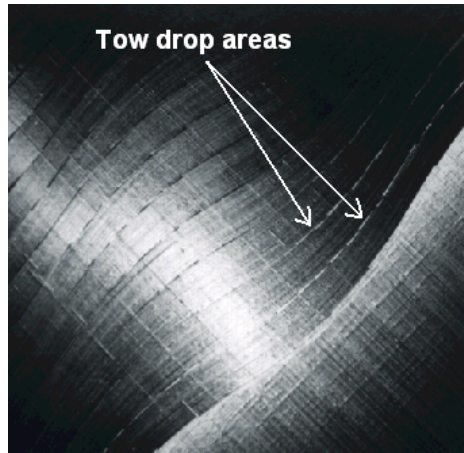


Figure 5.2: Manufactured VSP exhibiting tow-drop areas.

In this chapter, the effects of tow-drop regions are simulated by physically including them in the numerical models. The method used to calculate the locations of tow-drops is described by Blom et al.<sup>99;100</sup>. The influence on the failure performance of variable-stiffness laminates of different fibre angle combinations, tow widths, laminate thicknesses and ply staggering, in combination with tow-dropping, is investigated. Different tow widths result in different sizes of the resin-rich areas. Therefore, the influence of the tow width on laminate performance is worth investigating. The laminate thickness that results from the number of plies is expected to have some effect on the relative influence of tow-drops. Ply staggering (the relative shifting of adjacent plies with the same fibre orientation distribution in order to avoid collocation of tow-drop regions) is applied in combination with both tow width and laminate thickness variations, i.e. the influence of staggering is discussed simultaneously with the influence of the other variables. For comparison purposes, perfect laminates with continuous course boundaries are analysed as well and taken as reference cases.

### 5.3 Numerical Set-Up

The numerical simulations are carried out on a simply supported flat square panels ( $a$  (height) =  $b$  (width) = 300mm) under progressive edge shortening until final failure. These dimensions allow a representative fibre angle variation within the domain of the model while keeping the amount of computation time acceptable.

Compression is foreseen to be the critical load condition for this type of tow-

steered laminates as the combination of tow-drops and fiber curvature can trigger the fibre kinking failure mode. Therefore it is considered the most interesting load case to be investigated. As the objective of the study is the representation of the material system configuration rather than the structural response, out-of-plane displacements are prevented, hence avoiding buckling of the simulated thin-walled coupon.

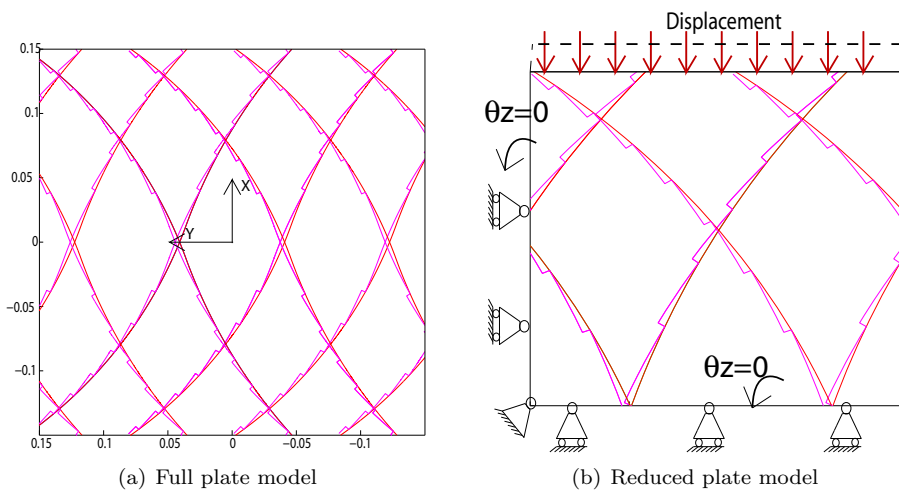


Figure 5.3: FE model of the simply supported 300mm $\times$ 300mm variable-stiffness laminate, designed according to the tow-drop method, under edge shortening.

The laminates are globally balanced and symmetric, belonging to the  $[\pm < T_0|T_1 >_n]_s$  family and having a nominal ply thickness  $t=0.181\text{mm}$ . In this notation,  $< T_0|T_1 >$  represents a variable-stiffness ply with a fiber orientation angle  $T_0$  at  $x = 0$  and  $T_1$  at  $x = \pm a/2$ , wherein the coordinate axes are centered on the panel. Between these values, the fibre angle varies according to a constant curvature path, and is function of both  $x$  and  $y$  coordinates. Definition of the fibre angle at one location, e.g.  $T_0$ , and the radius of curvature of the reference path also completely characterises a layer. The minimum turning radius of 625mm, i.e. the smallest reference path radius that results in an acceptable laminate quality (see Section 2.4), is adopted for all configurations in this study. Hence, the fibre angle  $T_1$  is dependant on  $T_0$ , which is varied between  $0^\circ$  and  $40^\circ$  at  $5^\circ$  intervals. An example of such a design, including the tow-drop areas, is illustrated in Figure 5.3.a. Computational effort is reduced by modelling only  $1/4^{\text{th}}$  of the panel ( $0 \leq x \leq a/2$ ,  $0 \leq y \leq b/2$ ), and by applying symmetry conditions to two of the model edges ( $x = 0$  and  $y = 0$ ). A displacement is prescribed at the edge  $x = a/2$  while the remaining edge ( $y = b/2$ ) is left simply supported



and free to expand in the  $y$ -direction, as shown in Figure 5.3.b.

The continuum damage model developed by Maimí et al.<sup>85;86</sup> and described in Chapter 4 is used herein as a user subroutine of the commercially available FE package ABAQUS<sup>62</sup>. The IM7/8552 carbon-epoxy system was chosen as the ply material for the simulated composite laminate specimens because its full characterisation has been done in previous investigations, therefore all the properties required by the damage model are available. The property values measured by Camanho et al.<sup>97</sup> are summarised in Table 5.1. The in-situ ply strengths for this laminate, as calculated with the formulation presented in Chapter 3 for a ply thickness  $h_p=0.181\text{mm}$ , are reported in table 5.2.

Table 5.1: Hexply IM7/8552 ply properties.

Elastic Properties:	$E_1=171.4$ GPa; $E_2=9.1$ GPa; $G_{12}=5.3$ GPa; $\nu_{12}=0.32$
Thermal Expansion [ $^{\circ}C^{-1}$ ]:	$\alpha_{11} = -5.5 \cdot 10^{-6}$ ; $\alpha_{22} = 25.8 \cdot 10^{-6}$
Ply strength [MPa]:	$X_{1+}=2323.5$ ; $X_{1-}=1200.1$ ; $X_{2+}=62.3$ ; $X_{2-}=199.8$ ; $X_6=92.3$
Fracture toughness [N/mm]:	$\mathcal{G}_{1+}=81.5$ ; $\mathcal{G}_{1-}=106.3$ ; $\mathcal{G}_{2+}=0.28$ ; $\mathcal{G}_6=0.79$

Table 5.2: In-situ ply strengths for the present problem

Ply position	$X_{2+}^{is}$ [MPa]	$X_6^{is}$ [MPa]
embedded ply ( $h = h_p$ )	126.6	114
embedded ply ( $h = 2h_p$ )	89.5	93.1
outer ply ( $h = h_p$ )	80.1	93.1

The FE model consists of a mesh of fully integrated **S4** shell elements, with a typical characteristic length  $l^*=1.5\text{mm}$ . The element size is governed by the requirement of a correct representation of the dissipated energy in the damage propagation model, as explained in Chapter 4. Furthermore, in the present model, the elements should be small enough to properly capture the tow-drop areas. The typical tow width used in this study is  $3.125\text{mm}$ . Hence, an element size of  $1.5\text{mm}$  is adequate to capture the resulting tow-drop areas. The local stacking sequence is calculated by the method described by Blom et al.<sup>99;100</sup>, at the centroid of each element and inserted in the **\*SHELL SECTION** property card of the ABAQUS input file. If the element centroid is found to be located in a resin-rich area, the ply transverse material properties are used in both directions (transverse and

longitudinal), as an approximation of the resin material properties. The numerical effect of this procedure is the severe point-wise reduction of the longitudinal ply stiffness and fracture toughness as if the material was locally damaged which is, as intended, a way of simulating crack initiation spots.

## 5.4 Damage and Failure Predictions

The longitudinal ( $d_1$ ) and transverse ( $d_2$ ) damage variable field plots at face plies of 8-ply thick laminates are shown in Figure 5.4. The plots represent the last load increment prior to global structural failure. Two configurations are shown, one corresponding to  $T_0 = 0^\circ$  ( $[\pm < 0|13.7 >_2]_s$ ) and another corresponding to  $T_0 = 30^\circ$  ( $[\pm < 30|47.4 >_2]_s$ ), without staggered plies. In the plots, the blue field represents non-damaged material i.e. behaving elastically. The red field corresponds to regions with some level of damage. Because of their lower in-situ strength, damage is initiated at the laminate face plies.

Depending on the fibre angles, two different damage and failure responses can be devised. For the  $[\pm < 0|13.7 >_2]_s$  configuration, most of the applied load is supported along the longitudinal direction. As a result, the first damage mode to initiate and the one that will eventually dominate the final failure of the panel is fibre kinking. For the  $[\pm < 30|47.4 >_2]_s$  configuration, the larger fibre angles at the top edge lead to higher loads being directly supported along the transverse direction. Damage initiates by matrix cracking because of the relatively low transverse strength values. However, most of the applied load is still transferred through the longitudinal direction, hence the final failure occurs with the development of fibre kink bands. By increasing  $T_0$  to higher angles, matrix cracking becomes the dominating final failure mode.

For the  $T_0 = 0^\circ$  case, damage at the outer plies occurs at the tow-drop locations in the adjacent layers. This means that these fibre-free areas locally disturb the load paths, in similar ways to notches and slits, and cause stress concentrations at nearby regions which eventually trigger the onset of damage. For the  $T_0 = 30^\circ$  case, damage is initiated exactly at the resin-rich spots in the face plies. In both the  $T_0 = 0^\circ$  and  $T_0 = 30^\circ$  cases, damage is initiated close to the load introduction edge because the angle between the loading vector and the fibre direction is higher there. For the  $T_0 = 0^\circ$  case, fibre kinking is favoured higher shear stresses. For the  $T_0 = 30^\circ$  case, matrix cracking is favoured by the higher loading in the transverse direction.

In non-staggered laminates, the tow-drops occur at the same locations through-the-thickness of the laminates in plies with the same fibre orientation distribu-

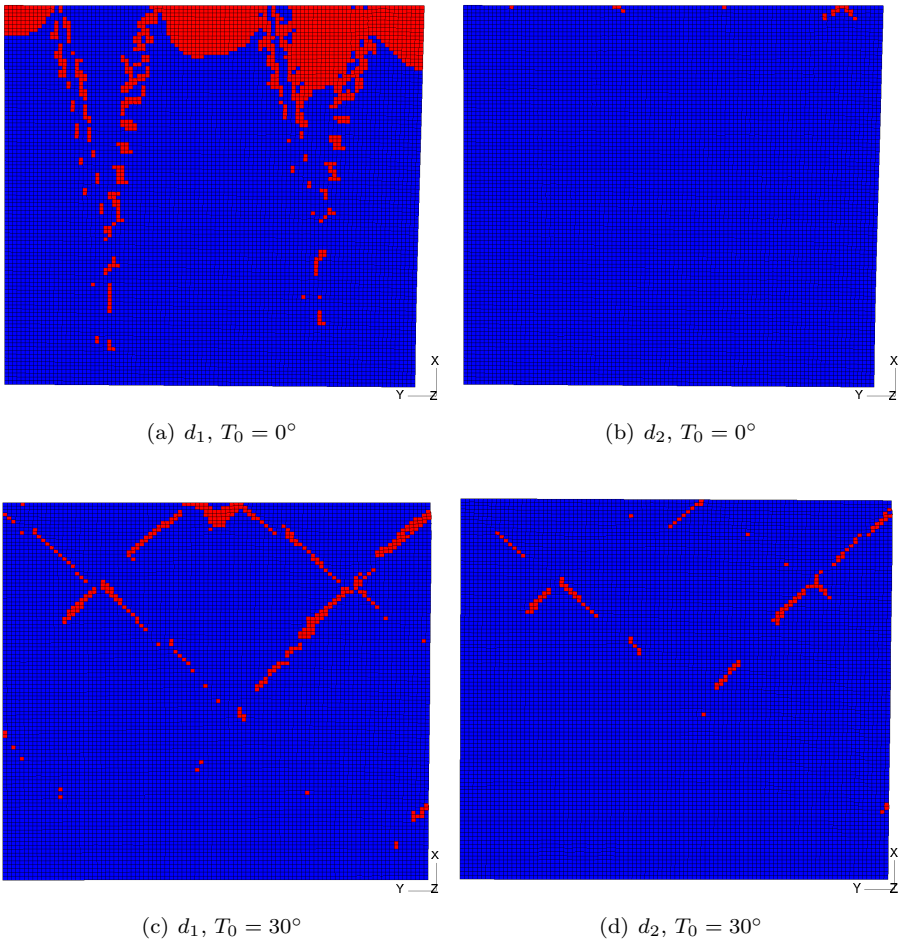


Figure 5.4: Longitudinal ( $d_1$ ) and transverse ( $d_2$ ) damage variables for the face plies of the  $[\pm < 0 | 13.7 >_2]_s$  and  $[\pm < 30 | 47.4 >_2]_s$  laminates, with no staggered plies (tow width is 3.125mm) at final failure loading. Legend: Red field - damaged material; Blue field - non-damaged material.

tions. Hence, there is low capacity for stress relief around these stress concentration spots. This can be changed by staggering the plies with the same fibre orientation distributions. In such way, the stress concentrations are mitigated. That is, by staggering the layers, a smoother stress distribution results, thereby postponing final panel failure. This effect, already described in Chapter 3, can be observed here by comparing Figures 5.5.a and 5.5.b with Figures 5.4.c and 5.4.d, respectively. The damage region is spreader in the staggered laminate, but the actual failure load is higher.

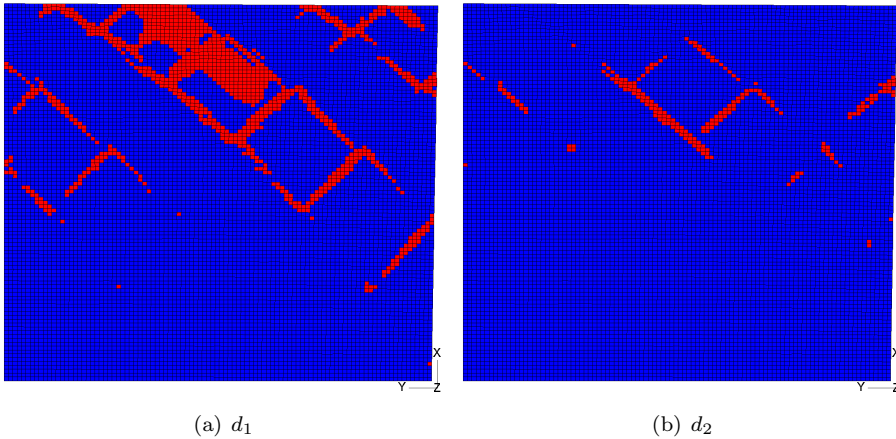


Figure 5.5: Longitudinal ( $d_1$ ) and transverse ( $d_2$ ) damage variables for the outer layer of the  $[\pm < 30|47.4 >2]_s$  laminate with staggered plies (tow width is 3.125mm) at final failure loading. Legend: Red field - damaged material; Blue field- non-damaged material.

#### 5.4.1 Influence of the Tow Width

Typically, AFP machines have the capability of placing different numbers of tows while keeping the tow width constant. In the parametric study reported here, the tow width is assumed to vary while the total course width is kept constant at 76.2mm (3in), which is accomplished by varying the number of tows. As described in Chapter 2, the local fibre orientation angle is a function of the distance to the course centerline. Hence, by maintaining a constant course width, the effects of fiber angle variations due to different course widths are ruled out. The courses are chosen to contain 8, 12 or 24 tows, respectively of 9.525mm, 6.25mm or 3.125mm in width. For the cases studied herein, the sum of tow-drop areas in a lamina as a percentage of the total ply area is approximately 2.5% for the thinnest tows, 5% to 6.5% for the 6.25mm tows, and between 7.5% and 12% for the widest tows.

As examples, the overall applied stress versus strain curves, for staggered and non-staggered 16-ply panel configurations with  $T_0 = 30^\circ$  and different tow widths, are plotted in Figure 5.6. The strength values as function of the tow width, corresponding to the configurations represented in Figure 5.6, are plotted in Figure 5.7. The results for a 4-ply, non-staggered laminate are also reported. Both stiffness and strength decrease with increasing tow widths, however the effect is more pronounced on the strength performance.

The results above can be plotted as function of the total fibre-free area in the laminates. In this way, tow width and  $\langle T_0|T_1 \rangle$  variations are condensed

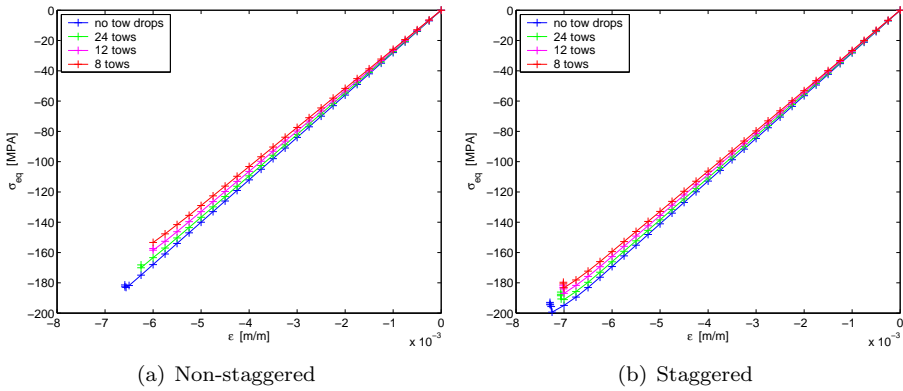


Figure 5.6: Stress versus strain curves for 16-ply laminates with different tow widths ( $T_0 = 30^\circ$ )

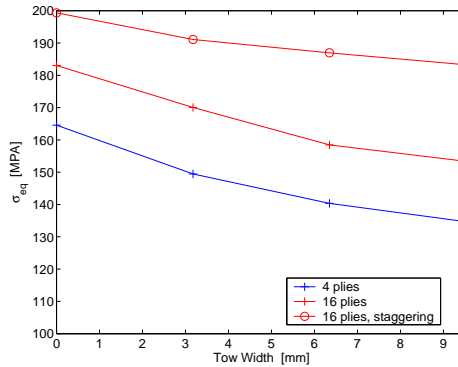


Figure 5.7: Compressive strength of laminates with different thicknesses and tow widths ( $T_0 = 30^\circ$ )

in one variable. The stiffness and strength reductions, for all the configurations analysed, as functions of the total tow-drop area are presented in Figure 5.8. There is a nearly linear relationship between the tow drop area and the overall stiffness of non-staggered laminates, as indicated by the straight line in Figure 5.8.a. Furthermore, the total resin-rich area as a percentage of laminate area corresponds roughly to the overall stiffness reduction. This result was expected since the resin alone does not have a major contribution to the laminate stiffness. Still, the use of staggering reduces this dependency. A similar plot for the reduction in strength (Figure 5.8.b) does not show the same linear trend, however the strength reduction with tow width or total fibre-free area is appreciable.

Ply staggering is generally beneficial to the strength (and overall stiffness) of fibre-steered panels with tows of any width including infinitesimal, i.e a constant-

thickness VSP where no resin-rich regions are generated, as considered in the previous chapters. This effect was already observed in Chapter 3. Even without the tow-drops, stress concentrations develop at the course boundaries due to fibre angle mismatches. If the plies are staggered, these stresses can be redistributed to the neighbouring plies. On the other hand, if the layers are not staggered, stress concentrations develop at the same planar coordinates in all of them and there is little flexibility for alternative load paths. The introduction of tow-drops amplifies the stress concentrations which can be largely mitigated by staggering the plies in the laminate, i.e staggering is more effective in the presence of tow-drops than in the case of perfect course edges. In general, the improvements in strength performance due to staggering increase with increasing tow-drop area, as shown in Figure 5.8.b. The improvements in stiffness seems to be more scattered.

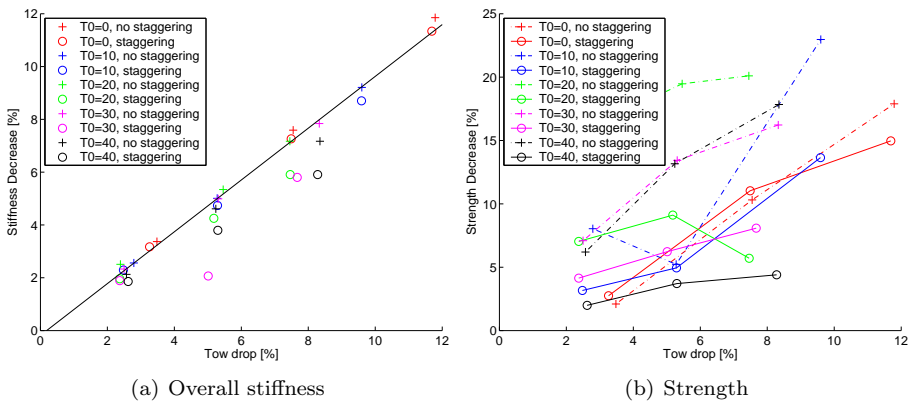


Figure 5.8: Panel overall stiffness and strength reductions as functions of the total tow-drop area.

The results presented herein show that the panel strength is a function the laminate fibre orientation distribution and of the tow width. The reductions in strength, when comparing with panels with ideal course edges, range from 3% to 15% for the smallest tow width, from 5% to 24% for the intermediate tow width, and from 15% to 29% for the largest tow width. In a design environment, these values could be translated into lower allowables in the design of the laminates. In this way, the numerical simulations would become unnecessary in the preliminary design phase. To be conservative, the allowables for the 3.125mm tows should be in the order of 15% lower than the reference case (no tow-drop areas). This value increases, respectively to 25% and 30% for the 6.25mm and 9.525mm wide tows. If staggering is applied, these values can be reduced to 7%, 11% and 15%, respectively.

### 5.4.2 Influence of the Laminate Thickness

The surface plies of a laminate are often the weakest ones within a laminate due to their lower in-situ strength, as explained in Chapter 3. By varying the number of plies within the laminate, any additional effects of tow-drop areas on the laminate strength are investigated. For this study, the course is set to have 24 tows of 3.125mm in width, resulting in a total width of 76.2mm. The number of plies is 8, 16, 24 or 32.

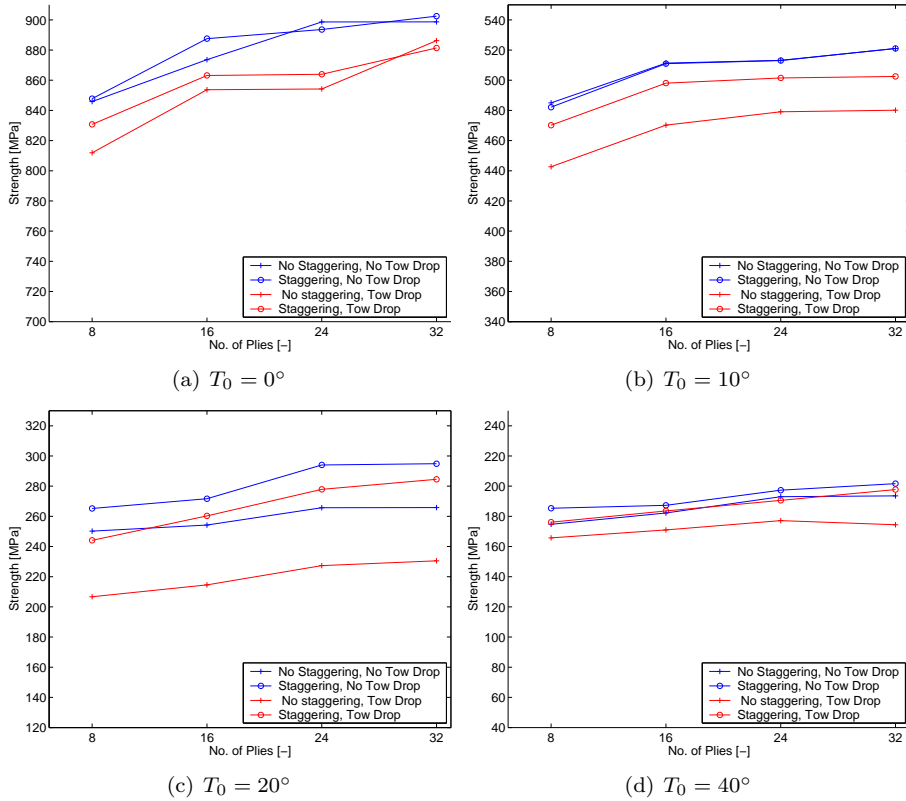


Figure 5.9: Panel strength performance for different fibre distributions and laminates thicknesses (tow width is 3.125mm). Tow Drop: resin-rich areas taken into account. No Tow Drop: resin-rich areas not taken into account.

Figure 5.9 displays the panel strength for four different  $T_0$  angles as function of the number of plies in the laminate, both for laminates with smooth course edges and laminates with tow-drop areas. The effects of ply staggering are also included. Again, the panel strength is shown to decrease with increasing values of  $T_0$ . The overall final failure load is as high as 900MPa, for configurations where  $T_0 = 0^\circ$ , and it decreases to less than 200MPa for  $T_0 = 40^\circ$ . Additionally,

it is shown that the thinnest laminates are the weakest. In general, the failure performance of a laminate is increased by increasing its thickness (while keeping constant the ply thickness). This is due to the relatively large influence of the face plies which have a lower in-situ strength. However, the strength reduction due to the fibre-free areas does not seem to vary with the number of plies. By staggering the plies, the laminate strength performance is generally improved. However, a clear relation between staggering and laminate thickness can not be drawn.

## 5.5 Conclusions

The effects of the discrete dropping of tows on the overall stiffness and strength characteristics of constant-thickness tow-steered laminates were investigated by means of numerical simulations. The tow-drop areas caused by the individual cutting of tows was explicitly modelled and simulated in a FE framework. In this way, the influence of these geometrical details on the in-plane stiffness and strength of the panels was investigated more thoroughly than in the previous chapters. Variations of fibre orientation distributions, tow width, laminate thickness, and ply staggering, in combination with tow-drop areas, were studied as well.

Based on the research presented herein, it can be concluded that the failure of VSP are inevitably affected by the presence of tow-drops. Damage can be triggered by the resin-rich areas, preferentially in regions where the angle between the loading vector and fibre orientations is the largest. The usage of wider tows results in larger tow drop areas which further decrease the laminate strength. The application of staggering improves the panel failure performance by mitigating the stress concentrations in the neighbourhood of course edges and fibre-free areas. The effects of tow-dropping do not show any coupling with laminate thickness.

Based on the present numerical studies, it can be concluded that for the sake of simplification of the laminate design, the influence of tow-drop areas can be accounted by reducing the values of allowable loads. This reduction depends mainly on the width of the tows used in the manufacturing of the laminate and on whether the plies are staggered or not, i.e. not only the size of the tow-drop areas but also their distribution over the panel planform and thickness play a role in the failure process. These results are inline with the ones obtained in the previous chapter. In the case of the VSP with tow-drops, the experimental failure results were overpredicted by 7.2% which is precisely the effect on laminate strength of dropping 3.125mm wide tows, predicted by the analyses carried in the present chapter.



The total course width was kept constant in this study. However, it is likely that the total number of tows is kept constant when the tow width is varied. This actually reduces the number of course boundaries and thus the amount of tow-drop area. On the other hand, the mismatch on the fibre angle between neighbouring machine head courses increases and stress concentrations are amplified. These will further reduce the failure loads. Hence, the best failure performance is achieved with the lowest number of tows per course with the smallest tow width.

In the PFA performed herein, the prediction of the occurrence of ply delaminations was neglected altogether. However, tow-drop areas are potential spots for the initiation this failure mode, similarly to what occurs in regions of ply drop-offs<sup>98</sup>. Hence, delamination might actually be the primary and dominant damage mode in VSP configurations constructed according to the tow-drop method. As mentioned in Chapter 3, the simulation of delaminations would decrease the efficiency of the computations substantially. Then, the results presented herein should be analysed carefully. Also, in other loading situations such as cyclic loading, the failure initiation around tow-drop regions may primarily be delamination<sup>98;101</sup>. This problem will require a more comprehensive treatment. An efficient modelling strategy for the issue of deaminations in VSP is being pursued by Fagiano et al.<sup>82</sup>. In any way, the numerical predictions would require validation by experimental testing. In the future, an appropriate experimental programme should be devised for this purpose.



## Chapter 6

# Low-Velocity Impact: Experimental Testing

### 6.1 Introduction

THIS and the following chapters diverge from the line of work of the previous ones to focus on the behaviour of laminates under a different type of loading, specifically Low-Velocity Impact (LVI) loading in the direction transverse to the plane of the laminate. It was mentioned, in Chapter 2, that one of the characteristics of tow-steered laminates is their dispersed stacking sequence, i.e. typically, at different spatial locations of a variable-stiffness laminate, the layers have different fibre orientations. For example, in the  $\pm < 30|75 >$  configuration, the stacking sequence is  $\pm 30$  at the origin of the fibre path but gradually changes to  $\pm 75^\circ$  at a characteristic distance (typically the panel edge). If a  $\pm < 45|60 >$  stack is added to the laminate, then the local stacking sequence changes from  $[\pm 30/\pm 45]$  to  $[\pm 75/\pm 60]$ , at the same locations. This dispersion is obvious in plies that have different fibre path definitions, but occurs also due to the staggering of adjacent plies with the same orientation distributions (see Chapter 2). Therefore, the clustering of plies at the same fibre angle, frequent in traditional constant-stiffness laminates, is avoided altogether in VSP. This dispersion of ply orientations may have a beneficial effects, namely in terms of impact damage resistance. The reason for this postulate is explained in the following.

In laminates with dispersed stacking sequences, matrix crack propagation through-the-thickness may be prevented because of the increased fibre bridging effect. That is, in traditional laminates with clustered plies, a considerable fraction

of the total impact energy is expected to be dissipated in cracking the relatively weak matrix, whilst in laminates with dispersed stacking sequences, part of this energy may be directed to load the stronger fibres which may be bridging the matrix cracks. Additionally, the extent of delaminations may be reduced. Since delaminations do not usually propagate between plies of the same orientation, the interlaminar shear stresses at interfaces with clustered plies, which act as a single ply, are relatively high<sup>73</sup>. These have the potential to cause wide delaminations that split the laminate into sublaminates having, overall, a lower resistance to buckling. This can greatly reduce the residual strength of a panel, i.e. its damage tolerance is compromised<sup>102–104</sup>. In laminates with dispersed stacking sequences, not only unidirectional layers are thinner but also more interfaces with the potential for delamination become available. This means that the same impact energy can be dissipated in more delaminations of controlled extension, hence reducing the impact footprint and hopefully leading to lower reductions in the residual strength of the impacted specimens.

In order to efficiently analyse the effects of the dispersion of the stacking sequence of VSP, it is assumed that the curvature of the fibres does not have, by itself, an influence in the local damage response of the impacted laminate. This is a reasonable assumption since the panel area damaged by a LVI can typically be bounded by a circumference of 100mm in diameter which is small compared to the minimum tow-steering radius of 635mm suggested by Nagendra et al.<sup>41</sup> for acceptable quality of a VSP. That is, the fibre angle variation in the damaged area is, at most, of 10°. It is not expected that such a small curvature significantly influences damage initiation loads, matrix cracking, fibre failure or the propagation of delaminations. Therefore, for the purpose of this investigation, laminates with dispersed stacking sequences but with straight-fibres are considered. These can be treated in general terms as *non-conventional laminates*, as opposed to traditional configurations based on a few ply orientations and eventually having several clustered layers. The behaviour of these non-conventional laminates under impact loading will be studied in this and the following chapters.

By considering non-conventional laminates in general, the focus of this thesis is broadened without compromising the specific study on VSP. Configurations with dispersed stacking sequences are compared to traditional designs based on a few ply orientations, some of them clustered. The specific effects due to the stacking sequence dispersion are isolated from the effects due to the stiffness of the laminate by comparing configurations with similar global stiffness properties.

It would be a enormous endeavour to evaluate, either by testing or by credible predictions, the effects related to all the possibilities allowed by the dispersion of

the stacking sequence. Therefore, this research is narrowed to a few representative configurations from which reasonable conclusions can be extrapolated. A stacking sequence dispersion method is proposed and applied to one configuration designed according to conventional practices, resulting in two non-conventional laminates. The three configurations are manufactured using carbon/epoxy material by means of an AFP system. The impact resistance of specimens laid according to each lay-up is evaluated by analysing their response to drop-weight impact loads of different energies. Then, their damage tolerance is ascertained by conducting experimental Compression-After-Impact (CAI) tests and the results of such experiments are compared.

## 6.2 Damage-Tolerant Laminate Design

Damage tolerance is the ability of a damaged structure to retain sufficient residual strength until such damage is detected through regular inspections and corrective action, such as repairing, is taken<sup>105</sup>. Damage can be inflicted by repeated loading (e.g. fatigue, acoustic, dynamic), environmental effects, handling or accidental impacts. In particular, the damage resulting from accidental impacts during manufacturing, handling and operation are the most likely to appreciably reduce the strength capability of laminated composite structures<sup>106;107</sup>.

The philosophy for impact damage tolerance of composite structures is defined by regulations such as the FAR 25 and JAR 25 (USA) and is illustrated, along general lines, in Figure 6.1. For a given configuration there is an energy threshold below which an impact does not result in any reduction of the structural residual strength. Above that impact energy value, the laminate suffers some damage affecting its strength. The most critical failure mechanism in LVI is delamination. Delaminations can occur at several interfaces through-the-thickness of a laminate and spread over large areas. This splits the original laminate into sublaminates which are more prone to buckle under compressive loading. Hence, the CAI test is the adequate tool for the evaluation of the residual strength of an impacted laminate.

Delaminations are typically invisible to exterior eye inspection. Therefore, if no other sign that an impact has occurred, damage can stay undetected for a long period of time. Nonetheless, the structure has to sustain the operational loads, accounting for a safety margin, without failing. Furthermore, this damage shall not grow under a certain level of fatigue loading (e.g. load cycles with amplitude bounded by 50% of the ultimate loading)<sup>106</sup>. At a certain energy level, an impact becomes detectable by the local indentation that results from matrix crushing and

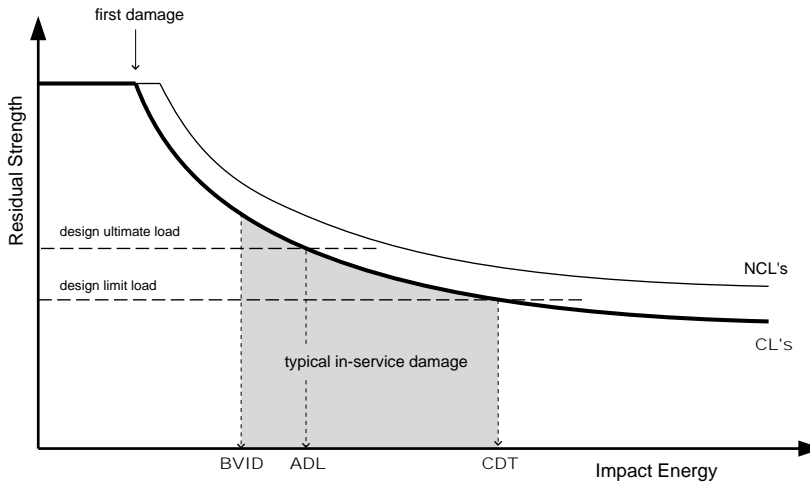


Figure 6.1: Damage tolerance concept. BVID - Barely Visible Impact Damage; ADL - Allowable Damage Limit; CDT - Critical Damage Threshold.

shear nonlinearity. This is commonly referred to as Barely Visible Impact Damage (BVID). Although the indentation itself is not critical to the integrity of the part, it indicates underlying extensive damage which may need to be repaired. This corrective action shall occur before this damage eventually grows (e.g. under the action of fatigue) to a Critical Damage Threshold (CDT) and the margin of safety for the design limit load is reduced to 0%<sup>107</sup>. Impact damage might not need extensive repair if it is safe to assume that it is not larger than (and it will not grow above) the Allowable Damage Limit (ADL), corresponding to a margin of safety of 0% with respect to the design ultimate load. These regulations implicate a regular inspection procedure. The residual strength limit, corresponding to the CDT, is such that it should not be violated by impacts within realistically admissible energy levels. In general aeronautical applications, realistic impacts are bounded by a 50J energy level, except for the horizontal tailplane root that typically must tolerate impacts up to 140J<sup>106</sup>. Stronger impacts may be able to cause sufficient matrix cracking and fibre breakage to perforate the laminate altogether and reduce its CAI strength even further. However, there is a lower asymptotic limit for which an increase in impact energy does not result in a larger strength reduction.

The objective of this chapter is to verify whether the damage tolerance of traditional laminates can be improved uniquely by changing their lay-up. Although this means an attempt to promote lower decreases in the residual strength of lam-

inates subjected to a given impact energy, laminates with a lower energy BVID can also be understood as advantageous in terms of damage tolerance because the window of detectability and repair would be enlarged, eventually leading to less frequent inspections.

In industrial practice the stacking sequence of laminates is often limited to combinations of  $0^\circ$ ,  $90^\circ$ , and  $\pm 45^\circ$  fibre angle plies which is in line with the limitations of traditional lay-up processes in assuring a precise fibre placement. Furthermore, in order to comply to certain directional stiffness requirements, clustering of plies becomes unavoidable. This practice, in spite of being advantageous due to its simplicity and readiness, can be inefficient in terms of structural behaviour. Although a laminate might have good stiffness properties, it may show a poor response to impact loads, in particular when plies with the same orientations are clustered together. The optimisation of composite laminate designs towards a better impact damage resistance and tolerance is often overlooked in favour of efficient in-plane, statically loaded designs. The response to impact damage is, in general, not accounted for in the early design phase but evaluated for those designs that meet the static load requirements. More than often, there is margin to improve the impact response of a laminate previously designed to withstand in-plane loads in a optimal way, just by changing its stacking sequence.

Extensive experimental research on the impact response of composite laminates has been carried out by many authors. For example, Lagace and Wolf<sup>108</sup> studied the impact damage resistance of several laminated material systems. Various laminate configurations were tested in order to better understand the role of stacking sequence and fibre orientation. The results indicated that the impactor force is a key parameter in the assessment of impact damage resistance, particularly the force needed to initiate damage, which is generally in the form of matrix cracks followed by delamination at the interfaces with the cracked plies. Cantwell and Morton<sup>109</sup> made an extensive review of the research work on impact damage and identified the fundamental parameters determining the impact damage resistance of CFRP. The mode II delamination strength and fracture toughness are the variables found to have a higher influence in the control of the impact induced delaminations while the fibre fracture toughness greatly controls the amount of fibre damage. Cantwell and Morton<sup>109</sup> also concluded that the laminate lay-up determines both the elastic energy absorbing capability of the composite as well as its failure mode and, for the sake of damage containment, laminates with abrupt changes in fibre orientations should be avoided.

In particular, the issue of the influence of the stacking sequence on the impact response of laminated composites was addressed in several investigations. Dost et

al.<sup>110</sup> investigated the damage resistance and residual strength for several quasi-isotropic laminates under LVI. Post-impact compressive behaviour was found to be a strong function of the laminate lay-up. Strait et al.<sup>111</sup> carried instrumented drop-weight impact tests on cross-ply, quasi-isotropic and  $0^\circ / \pm 45^\circ$  fibre angle based laminates. The lay-up was found to have a significant effect on the impact resistance, particularly at higher impact energies. Fuoss et al.<sup>112;113</sup> studied the influence of three parameters on the impact damage resistance of composite laminates: interface angle, ply orientation relative to a fixed axis and ply grouping. The guidelines given in their work for a better damage resistance include the avoidance of ply clustering or small interface angles. It should be noted that the work of Fuoss et al.<sup>112;113</sup> was based on transverse quasi-static loading and their conclusions were based on simplified FE models that were not able to accurately simulate delamination.

### 6.2.1 Non-Conventional Laminates with Dispersed Stacking Sequences

In previous investigations, the stacking sequence of laminates was changed with no regard for the changes in laminate stiffness. LVI events can often be approximated to quasi-static loads. In such situations, the delaminated area is highly dependant on the out-of-plane displacement of the plate during impact<sup>103</sup>. This means that the bending stiffness plays an important role on the way damage develops on an impacted laminate. To avoid misinterpretations of the results, in this work both the in-plane and the bending stiffness of the studied laminates are maintained while redesigning the stacking sequence. Using optimisation tools based on Genetic Algorithms (GA), alternatives to the traditional  $0^\circ$ ,  $90^\circ$ , and  $\pm 45^\circ$  fibre angle based laminates are designed where the plies are dispersed through the  $0^\circ - 90^\circ$  fibre angle range at intervals of  $5^\circ$ . These non-conventional laminates maintain similar in-plane and bending stiffness properties with the baseline configuration from which they were derived. This procedure, described in detail in Appendix A<sup>114;115</sup>, is possible since in the design of composite laminates multiple optima exist, i.e. there is more than one stacking sequence that satisfies a given design criterion. It is also highly efficient due to use of *lamination parameters*, that represent the laminate stiffness properties with fewer parameters than traditional design practices wherein ply orientations, thicknesses and relative locations within the laminate are accounted explicitly. Furthermore, manufacturing of such laminates is practical nowadays as the industry switches from hand laying processes to accurate automated fibre-placement and tape-laying technologies.



In order to compare the impact damage resistance and tolerance of composite laminates with traditional and dispersed stacking sequences, a two-step approach is proposed herein. In the first step, a configuration is designed according to conventional practices, to cope with the expected static loads on the structure. The second step consists of redesigning this laminate by dispersing its stacking sequence, as described in Appendix A<sup>114</sup>. This is done without compromising the initial stiffness properties. This second stage of design is cost efficient since the candidate laminates will be those with known stiffness properties, thus minimising the number of designs for which impact testing and/or PFA are required.

Laminated plates with three different stacking sequences, from which several specimens were cut and tested, were produced by means of an AFP. One of the stacking sequences constitutes the baseline conventional configuration. The other two designs have dispersed stacking sequences and are the proposed non-conventional laminates. The plates were fabricated with Hexply AS4/8552 carbon epoxy tows resulting in a nominal ply thickness of 0.182mm. The nominal ply properties used to model this material are summarised in Table 6.1.

Table 6.1: Nominal ply properties used to model the material Hexply AS4/8552.

Density [kg/m <sup>3</sup> ]:	$\rho=1590$
Elastic Properties:	$E_1=135\text{GPa}; E_2=9.6\text{GPa};$ $G_{12}=5.3\text{GPa}; \nu_{12}=0.32; \nu_{23}=0.487$
Thermal Expansion [ $^{\circ}C^{-1}$ ]:	$\alpha_{11}=-3.42 \cdot 10^{-7}; \alpha_{22}=2.58 \cdot 10^{-5}$
Ply strengths [MPa]:	$X_{1+}=2207; X_{1-}=1531;$ $X_{2+}=80.7; X_{2-}=199.8; X_6=114.5$
Fracture Toughness [N/mm]:	$\mathcal{G}_{1+}=81.5; \mathcal{G}_{1-}=106.3; \mathcal{G}_{2+}=0.28; \mathcal{G}_6=0.79$

The baseline conventional laminate constitutes an example of a configuration that could be the result of the traditional industrial practice in designing a laminate to comply with certain stiffness requirements. In this work, it is assumed that such requirements have led to a symmetric and balanced 24-ply laminate having about 60% of plies in the main loading direction ( $0^{\circ}$ ), 10% of  $90^{\circ}$  plies to add transverse stiffness and another 30% at  $\pm 45^{\circ}$  to counteract shear loads and improve buckling resistance. Placing  $\pm 45^{\circ}$  plies on the surface of laminates is also the best strategy to improve impact resistance<sup>109</sup>. Mimicking industrial practice in avoiding large interlaminar stresses, the ply contiguity was limited to four plies. Thus, the following conventional laminate is proposed:

$$\text{Baseline: } [\pm 45/90/0/45/0_4/ - 45/0_2]_s$$

In spite of its good elastic performance, the damage tolerance of the baseline laminate may be poor due to the relative high number of  $0^\circ$  clustered layers allowing for an easy propagation of through-the-thickness matrix cracks degenerating in wide delaminations at interfaces with neighbouring plies due to the high interlaminar shear stresses. The low number of interfaces can lead to the occurrence of wide delaminations which may become necessary to dissipate the impact energy. The application of the stacking sequence dispersion method described in Appendix A results in the following non-conventional laminates:

$$\text{NCL1: } [\pm 45/0/70/-70/0/15/10/-10/-15/15/-15]_s$$

$$\text{NCL2: } [\pm 45/80/5/20/-20/10/-80/-10/-5/15/-15]_s$$

These two configurations were generated through two different runs of the dispersion algorithm. To generate the NCL1, a value of the dispersion bonus parameter  $b = 10^{-17}$  was used in the objective function, as described in Appendix A. The NCL2 was generated with  $b = 10^{-13}$ . This means that there was more freedom to disperse the stacking sequence when generating NCL2.

The inplane and bending stiffness matrices are: (i) for the baseline laminate,

$$A^B = \begin{bmatrix} 41.3 & 5.66 & 0 \\ 5.66 & 13.7 & 0 \\ 0 & 0 & 6.62 \end{bmatrix} \cdot 10^4 \text{ N/mm},$$

$$D^B = \begin{bmatrix} 46.5 & 13.0 & 2.74 \\ 13.0 & 32.8 & 2.74 \\ 2.74 & 2.74 & 14.6 \end{bmatrix} \cdot 10^4 \text{ N} \cdot \text{mm};$$

(ii) for the NCL1,

$$A^{NCL1} = \begin{bmatrix} 40.8 & 5.72 & 0 \\ 5.72 & 14.1 & 0 \\ 0 & 0 & 6.68 \end{bmatrix} \cdot 10^4 \text{ N/mm},$$

$$D^{NCL1} = \begin{bmatrix} 47.0 & 13.2 & 2.04 \\ 13.2 & 32.0 & 1.62 \\ 2.04 & 1.62 & 14.7 \end{bmatrix} \cdot 10^4 \text{ N} \cdot \text{mm};$$

and (iii) for the NCL2,

$$A^{NCL2} = \begin{bmatrix} 39.7 & 5.50 & 0 \\ 5.50 & 15.6 & 0 \\ 0 & 0 & 6.46 \end{bmatrix} \cdot 10^4 \text{ N/mm},$$

$$D^{NCL2} = \begin{bmatrix} 46.7 & 13.0 & 2.88 \\ 13.0 & 32.8 & 2.72 \\ 2.88 & 2.72 & 14.5 \end{bmatrix} \cdot 10^4 \text{ N} \cdot \text{mm}$$

The bending-stretching coupling matrices  $B^B$ ,  $B^{NCL1}$  and  $B^{NCL2}$  are identically zero since the laminates are symmetric about their midplane. The baseline laminate axial modulus, transverse modulus, shear modulus and Poisson's ratios are:

$$E_x^B = 89.2\text{GPa}, \quad E_y^B = 29.6\text{GPa}, \quad G_{xy}^B = 15.2\text{GPa}, \quad \nu_{xy}^B = 0.413$$

As for the laminates with dispersed stacking sequences, the same engineering constants take the values:

$$E_x^{NCL1} = 88.1\text{GPa}, \quad E_y^{NCL1} = 30.4\text{GPa}, \quad G_{xy}^{NCL1} = 15.3\text{GPa}, \quad \nu_{xy}^{NCL1} = 0.406$$

and

$$E_x^{NCL2} = 86.4\text{GPa}, \quad E_y^{NCL2} = 34.0\text{GPa}, \quad G_{xy}^{NCL2} = 14.8\text{GPa}, \quad \nu_{xy}^{NCL2} = 0.352$$

respectively for the NCL1 and NCL2. The axial and shear moduli of the alternative laminates are within 3% difference from the baseline configuration. The transverse moduli are very similar between the baseline and the NCL1 but the NCL2 shows a 15% shift. A similar comparison can be made for the Poisson's ratio. This means that, despite the differences in  $D_{13}$  and  $D_{23}$ , the NCL1 can be considered a better match to the baseline than the NCL2. This is most likely due to the higher freedom to disperse the stacking sequence of NCL2. Overall, the algorithm is successful in generating laminates having dispersed stacking sequences but stiffness properties very similar to those of the baseline.

### 6.3 Drop-Weight Impact Tests

The experimental programme follows the *standard test method for measuring the damage resistance of a fiber-reinforced polymer matrix composite to a drop-weight impact event*<sup>116</sup>, as devised by the American Society for Testing and Materials (ASTM). A similar procedure is proposed by the aircraft manufacturing company AIRBUS<sup>117</sup>. The objective of the test is the evaluation of the level of damage induced by an impact event on a laminated composite plate. The specimen geometry and dimensions for this test are depicted in Figure 6.2. A complete representation of the test setup is available in the document defining the standard test procedure<sup>116</sup>.

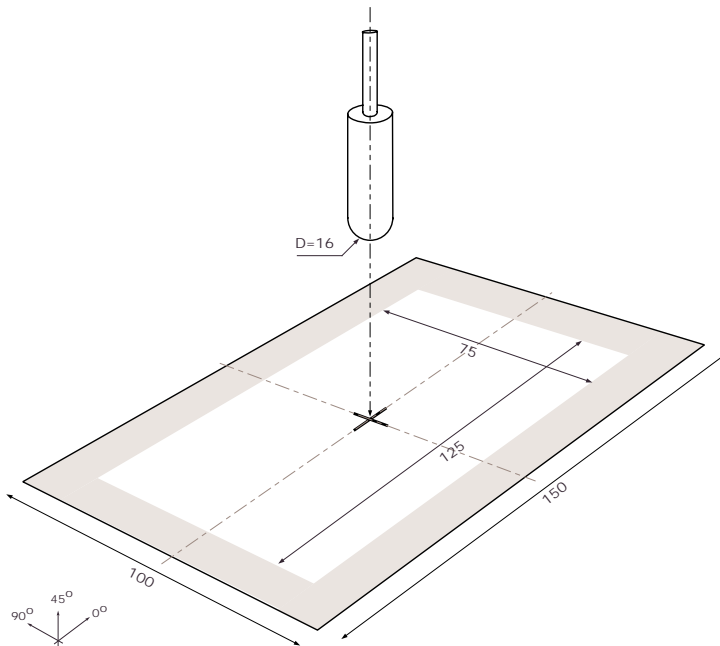


Figure 6.2: Illustration of the devised impact test setup (dimensions in mm).

#### 6.3.1 Specimen Preparation, Setup and Test Procedure

Laminated composite plates, about 500mm×500mm in size, were fabricated with Hexply AS4/8552 carbon epoxy tows at the Dutch National Aerospace Laboratory (NLR) by means of an AFP system (Automated Fibre Placement Workcell from Automated Dynamics). The curing cycle was performed according to a standard autoclave procedure. A two-step 3-hour cycle at 7bar was followed. In the first 1-

hour step a temperature of 110°C was maintained and the second step took 2 hours at 180°C. Nondestructive Inspection (NDI) by means of through-transmission ultrasonics (C-scan) was carried on the cured plates. C-scan results did not reveal delaminations or porosities of significative size. Overall, the achieved laminate quality was higher than for traditional hand-laid laminates. Each panel was cut in 15 test specimens with a water-cooled disk saw to a tolerance of 0.5% with respect to the standard dimensions<sup>116</sup>. The specimen thickness was measured at 3 specimen locations and determined to be 4.37mm, on average, with a standard deviation of 0.7%.

The standard impact test consists of dropping a spherically shaped steel dart on a free fall, guided by two rails, onto a 150mm×100mm composite laminate specimen supported on all sides in such a way that the specimen region free for an impact is a rectangular area of 125mm×75mm in size, as shown in Figure 6.2. The mass of the impactor and the height at which it is dropped in a free fall were chosen to meet the impact energy required. According to the standard procedure<sup>116</sup>, four toggle clamps should be installed along the longer specimen sides in order to prevent any in-plane movement. In the present case, the clamps are replaced by a 10mm thick steel plate with a 125mm×75mm rectangular hole that completely covers the supported side areas preventing movement in the out-of-plane direction, and constraining the displacements in the in-plane directions by means of friction. In Figure 6.2, the supported areas are drawn in grey. Either the standard or the adopted procedures simulate the supported conditions found in a typical structural composite panel<sup>118</sup>. The latest was found simpler to produce and mechanically more robust.

The drop height,  $H$ , is related with the impact energy,  $E_i$ , with  $H = \frac{E_i}{M_i g}$  where  $M_i$  is the mass of the impactor and  $g$  is the acceleration due to the gravitational force (9.81m/s<sup>2</sup>). The impactor velocity at the moment of contact with the specimen,  $V_i$ , is related with the impact energy by  $E_i = \frac{1}{2} M_i V_i^2$ . In this experimental programme, specimens of the three different stacking sequence configurations were impacted with energies varying between 5J and 50J, according to the procedure proposed by AIRBUS<sup>117</sup>. The test matrix is shown in Table 6.2. The drop heights ranged from 77cm to 168cm and the impactor mass was either 951g, 1.331kg, 2.441kg or 4.186kg, as function of the impact energy required.

The specimens were impacted on the laminate tool side. A rebound impact on the specimens was prevented by means of a manually controlled device. The impact velocity was calculated as a function of the travelled time between two sensors placed close to the impact surface. The impact force as function of the impact contact time,  $t$ , was recorded digitally by reading the output of a load-cell

Table 6.2: Test matrix for the drop-weight impact experimental programme.  $E_{1mm}$  corresponds to the energy necessary to produce a 1mm dent depth, considered to be the threshold for BVID, and is found by interpolation of the results of the remaining tests.

Number of Specimens	Target Impact Energy [J]	Drop Weight ( $M_i$ ) [kg]
1	5	0.95
1	10	1.33
1	15	1.33
2	20	2.44
1	25	2.44
3	$E_{1mm}$	2.44
3	30	2.44
1	40	2.44
1	50	4.19

installed inside the impactor. The indentation originated on the impact face of the specimens was measured once, immediately after each test, and again after a relaxation time of one week. The visible damage was characterised and the specimens were again inspected to evaluate the extent of the delaminated projected area, commonly referred to as *impact footprint*. The location of major delaminations through-the-thickness of the specimens was identified by means of Fluorescent Penetrant Inspection (FPI).

### 6.3.2 Experimental Results

With the goal of finding the differences between the impact response of the three configurations tested, the data pertaining impact force and dynamics as well as the resulting impact damage is analysed in the next paragraphs.

#### Impact Dynamics

In a typical LVI process, the initial impactor velocity is gradually reduced as its movement is opposed by the deforming composite specimen. This deceleration is associated to a reaction force on the impactor. The kinetic energy is transferred to the laminate and part of it temporarily stored as elastic strain energy. Another part is dissipated by means of friction between the impactor and the laminate. If the local stresses are such that at least one of the failure criteria for the material is fulfilled, still another fraction of the impact energy is dissipated through irreversible damage. An impacted specimen can dissipate the energy of impact

by means of various failure mechanisms including indentation at the impact face (indicative of local matrix plasticity and crushing), interlaminar delaminations, tensile matrix cracking and fibre breakage, and back face splitting and fibre peeling. As the impactor movement is resisted by the impacted specimen, its velocity is eventually reduced to zero as the indentation reaches a maximum value. Gradually, part of the accumulated elastic strain energy is transferred back to the impactor. The impactor accelerates and is impelled away from the specimen, but the restituted energy is lower than the impact energy. A fraction of the accumulated energy is kept in the form of panel vibrations and eventually dissipated by damping.

The impactor reaction force histories during for 5J, 10J, 20J and 30J impacts on the baseline configuration and non-conventional laminate specimens are shown in Figure 6.3. For the remaining impact cases, the three designs compare in a similar way. By integrating the force history, the impactor acceleration ( $A$ ), velocity ( $V$ ) and displacement ( $S$ ) can be calculated, respectively by:

$$V(t) = V_i + \int_0^{\Delta t} A(t)dt = V_i + g\Delta t - \frac{1}{M_i} \int_0^{\Delta t} F(t)dt \quad (6.1)$$

$$S(t) = S_i + \int_0^{\Delta t} V(t)dt \quad (6.2)$$

with<sup>103</sup>  $V_i = \sqrt{2E_i/M_i}$ .  $S_i$  is the impactor position at the moment of contact with the specimen and  $\Delta t$  is the total impact time. The impactor force versus displacement plots, shown in Figure 6.4, are helpful in evaluating the behaviour of the specimens in terms of damage, i.e. loss of stiffness. The impactor transferred energy histories, calculated with  $E(t) = \frac{1}{2}M_i V(t)^2$ , are plotted on Figure 6.5. The curves represent the energy lost by the impactor during the impact process. The maximum loss of energy, equal to the total impact energy, is reached at the maximum indentation moment when the impactor is immobilised. After that instant, part of the energy is restituted to the impactor as it bounces back. The difference between the impact and restitution energies corresponds to dissipations in the form of vibration damping, friction and damage.

The load histories for impacts with energy levels around 5J on the baseline configuration and non-conventional laminates is plotted in Figure 6.3.a. The load peaks, visible up to the global peak load, are primarily due to elastic wave responses and vibration of the specimen<sup>118</sup>. This behaviour indicates that the response of the specimens diverts from being quasi-static. The dashed line in the

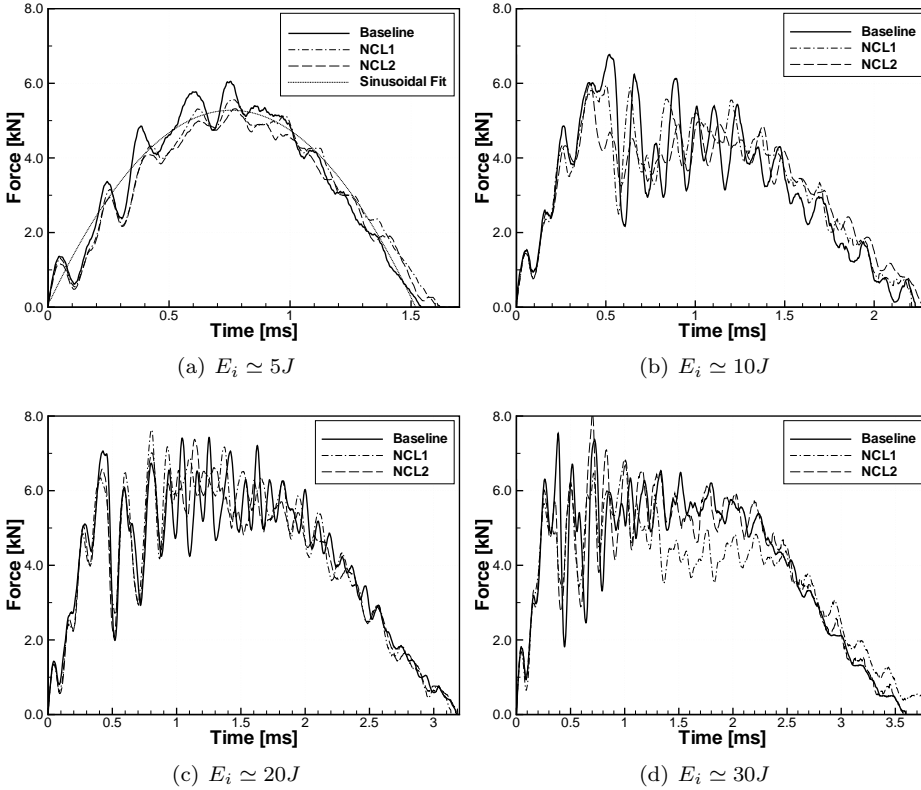


Figure 6.3: Impactor reaction force histories for impacts on the baseline (conventional) and non-conventional laminates. DTL - Delamination Threshold Load.

figure is a half sine wave fitted to the experimental results, which represents a model for the typical contact load from an impact by a relatively heavy mass on a lightweight specimen in which no damage occurs, i.e. the stiffness behaviour remains linear. Such an event can generally be accurately approximated by a single degree-of-freedom system as

$$F = V_i \sqrt{KM_i} \cdot \sin \sqrt{\frac{K}{M_i h_l}} \quad (6.3)$$

wherein  $K$  and  $h_l$  are, respectively, the stiffness and thickness of the specimen<sup>103</sup>. This model predicts that the contact load should vary sinusoidally with the contact time.

The similarity between the experimental results and the sinusoidal approximation leads to the conclusion that the specimen response is linear with little or no indication of impact damage. However, in the load-displacement curves



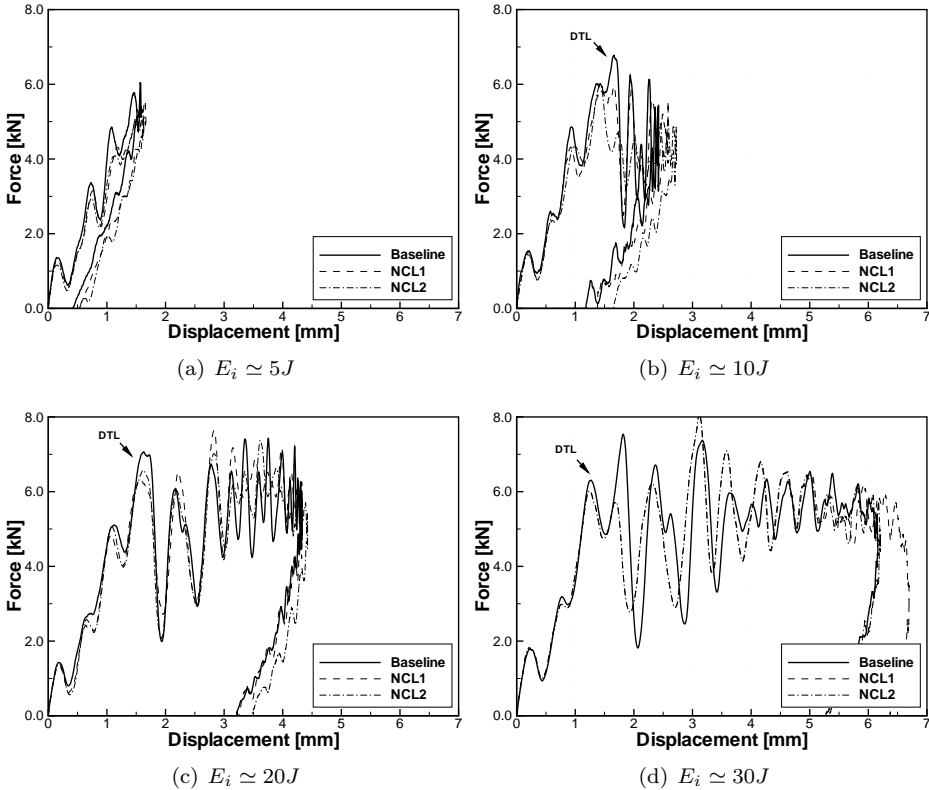


Figure 6.4: Impactor force versus displacement for impacts on the baseline (conventional) and non-conventional laminates. DTL - Delamination Threshold Load.

shown in Figure 6.4.a. for an impact energy level of 5J, some hysteresis is visible between the loading and unloading phases, which is an indication of some energy loss during the impact event. This is explicitly represented in Figure 6.5.a. The energy lost by the impactor during the loading phase is not totally transferred back during unloading. The damping of vibrations introduced in the specimens could explain the behaviour shown in Figure 6.5.a but not the one in Figure 6.4.a. The hysteresis indicates energy dissipation by means of material damage which may be occurring in the form of matrix cracking or localised indentation. Sjöblom et al.<sup>119</sup> showed that these phenomena affect the overall laminate stiffness only slightly. However, matrix crack tips can act as initiation points for delaminations, and these can dramatically change the global stiffness of the impacted composite specimen<sup>120</sup>. In the experimental results herein, this effect is only visible for impacts at higher energies.

The load histories for impacts with energy levels around 10J on the base-

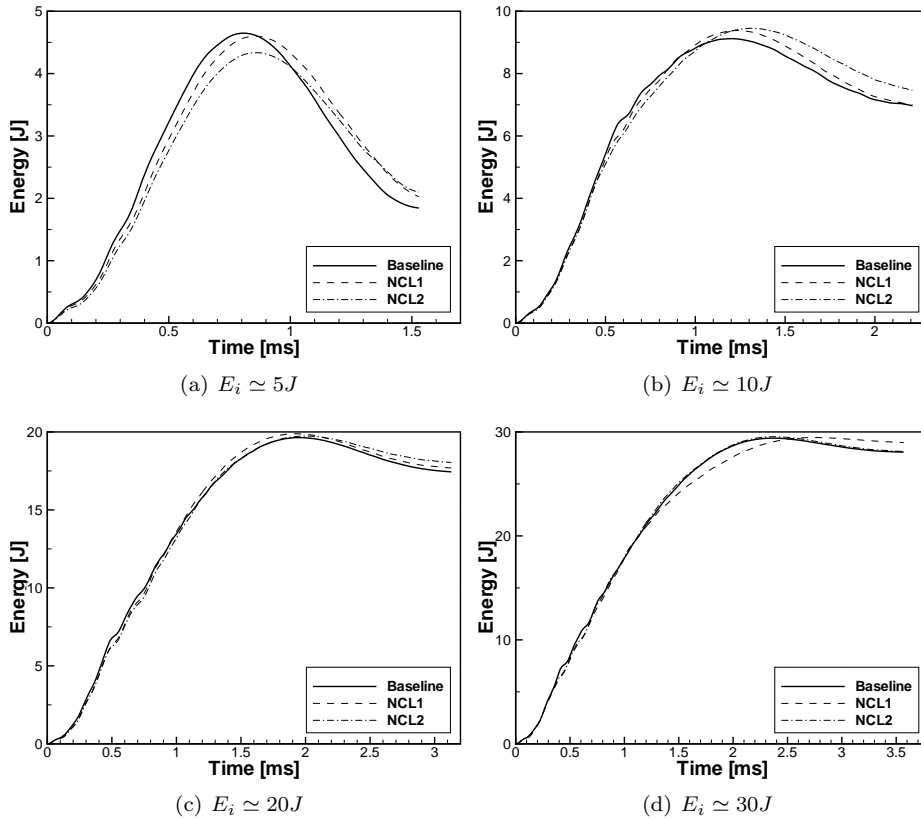


Figure 6.5: Impactor transferred energy versus time for impacts on the baseline (conventional) and non-conventional laminates.

line configuration and non-conventional laminates is plotted in Figure 6.3.b. The corresponding load-displacement curves are shown in Figure 6.4.b. Initially, the loading paths follow a trend similar to the one implicit in Figure 6.4.a. However, a peak impact load close to 7kN is recorded at approximately 0.5 milliseconds followed by a sudden and dramatic decrease in load. Further load increases and dramatic drops are followed by an oscillatory behaviour of high amplitude. Schoeppner and Abrate<sup>118</sup> attributed the sudden drops in load to the unstable propagation of delamination. The first peak load is termed the Delamination Threshold Load (DTL) and represents the load at which *significant damage* occurs. The higher the impact energy, the longer the oscillatory behaviour lasts before unloading, possibly due to the propagation of wider delaminations. Similarly, the higher the impact energy is, the larger is the separation between the loading and unloading paths in Figure 6.4, indicating larger amounts of energy dissipation. This mechanism is explicit in Figure 6.5. After a certain moment in

time before the unloading phase the oscillations seem to be damped. This effect, visible in Figures 6.3.c and 6.3.d, is possibly due to the interference with other damage modes such as fibre breakage.

As observed by Schoepner and Abrate<sup>118</sup>, the DTL does not vary significantly with impact energy. The stacking sequence does not seem to have a noticeable effect either. In this investigation, the average DTL's were found to be 6.8 kN, 6.4 kN, 6.5 kN, respectively for the baseline configuration, NCL1 and NCL2. In fact, Schoepner and Abrate<sup>118</sup> showed that the DTL is directly proportional to  $h_l^{3/2}$ .

In general, the differences between the baseline design and the non-conventional laminates are not easily noticeable from Figures 6.3 and 6.4. The energy plots in Figure 6.5 show a slight advantage to the baseline configuration. The energy restituted to the impactor during the unloading phase is generally lower in the non-conventional laminates, possibly indicating a higher energy dissipation by means of damage.

Another way to evaluate the differences between conventional and non-conventional laminates in terms of impact damage is by comparing the values of the maximum impactor displacement, as shown in Figure 6.6. In specimens with similar in-plane and bending stiffness as these are, any significant differences in maximum indentation should be caused by differences in stiffness degradation due to the damage process. However, Figure 6.6 shows very similar values for the three different configurations, hence a definite conclusion about which configuration suffers the less damage is not possible by this method.

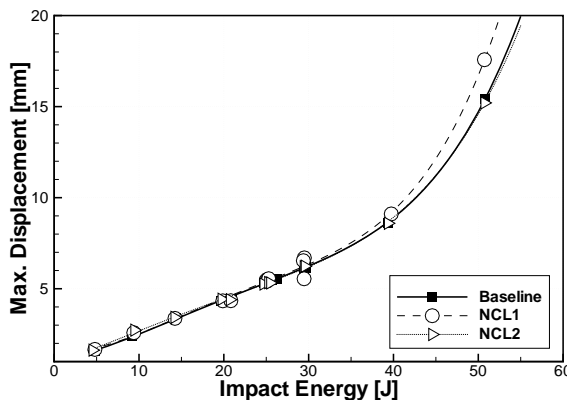


Figure 6.6: Maximum impactor displacement for impacts on the baseline (conventional) and non-conventional laminates.

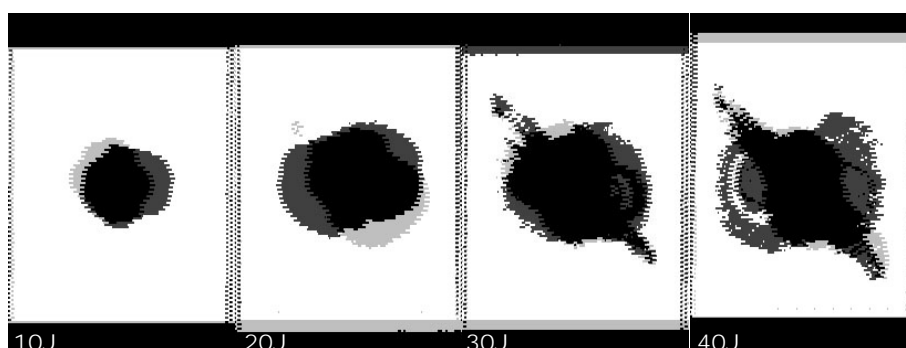
### Non-Destructive Inspection (NDI)

More data is necessary to evaluate the difference in impact damage between the baseline configuration and non-conventional laminates. The extent of damage was determined by Non-Destructive Inspection (NDI), specifically ultrasonic C-Scan. The results of C-Scans on specimens impacted at four energy levels are shown in Figures 6.7. An attenuation of 6dB is considered the threshold value for damage identification. The area exceeding the threshold attenuation value represents the extent of damage. For a better comparison, the C-scan results for the baseline configuration and both non-conventional laminates are superimposed in Figures 6.7.a and 6.7.b. The exceedance area represents a rough estimation of the extent of damage, mostly delaminations, in the impacted specimens, i.e. the impact footprint.

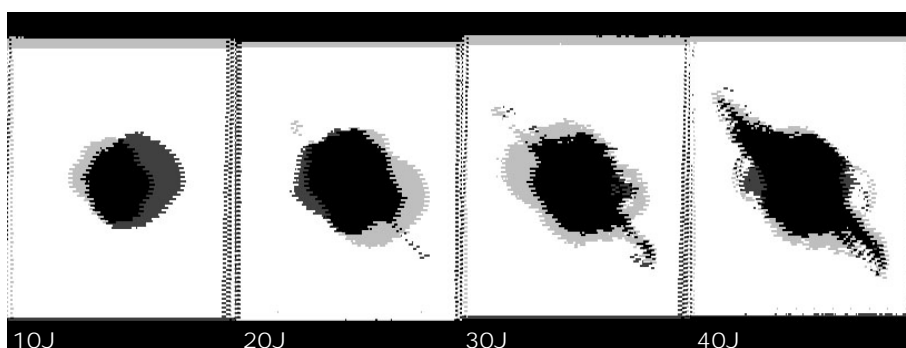
The C-scan evaluation of the specimens impacted at an energy level of 5J did not reveal damage whatsoever, although the hysteresis effect in the load-deflection curves plotted Figure 6.4.a indicates a stiffness reduction due to damage. This mismatch occurs possibly because the ultrasonic C-scan technique used did not have the sensitivity to detect transverse matrix cracks which, together with face ply indentation, might be the only damage mechanisms resultant from such low impact energies. For energy levels of 10J and 20J, damage in the form of interlaminar delamination is detected by the C-scan. Impacts at energy levels of 30J and 40J also produce extensive back face splitting and fibre peeling, as manifested in the C-scan records as elongated regions protruding 45° from the delaminated region.

In general, the NCL1 shows a larger impact footprint than the baseline configuration. However, the trend is opposite if the comparison is made with the NCL2. The impact energy is plotted on Figure 6.8 as a function of the measured exceedance area. An exponential law, crossing the vertical axis at 5J, is fitted to the results. As a rough estimation, 5J was considered the threshold energy level for impact damage, for all the three configurations. In reality, this threshold value should be somewhere between 5J and 10J.

The trendlines on Figure 6.8 indicate that, in general, the NCL2 laminate produces an 8% narrower impact footprint than the baseline design, but the NCL1 laminate exceeds it by 30%. From these results, it is clear that by dispersing the stacking sequence of a laminate while keeping its elastic performance, it is possible to improve its damage resistance. However, this result is not automatically achieved for every non-conventional laminate generated by the current method.



(a) Baseline versus NCL1



(b) Baseline versus NCL2

Figure 6.7: Impact Footprint - area exceeding an attenuation of 6dB, as measured by nondestructive inspection by means of through-transmission ultrasonics. Comparison between baseline (grey) and non-conventional laminate (dark) specimens for four different levels of the impact energy.

### Through-the-Thickness Damage

The intraply damage can be evaluated by visual inspection of the specimens' transverse section at the impact location, as exemplified in Figure 6.9 for 30J impact loads on the baseline and non-conventional laminates. Each image is a side-by-side assembly of about 30 pictures taken by an optical microscope. Besides intraply damage, the images help identifying the location of delaminations through-the-thickness of the specimens. This valuable information is not given by the traditional C-Scan inspection which has limited sensitivity. More delaminations are observed on the laminates with dispersed stacking sequences. However, these are wider on the baseline, particularly on the interfaces close to the back face. This is inline with the NDI results presented in Figures 6.7 and 6.8. Fur-

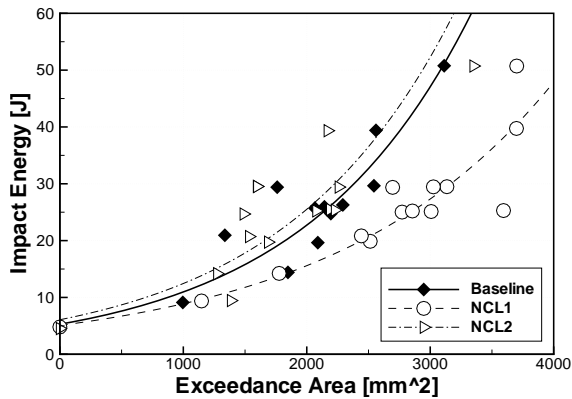
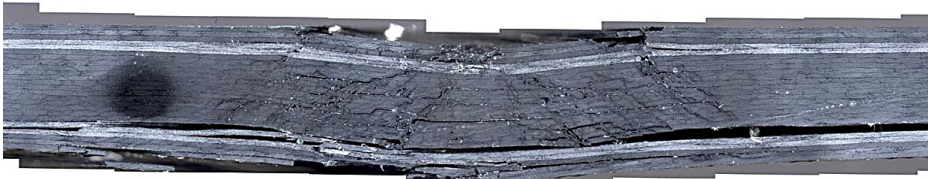


Figure 6.8: Impact footprint area as function of the impact energy. An exponential law is fitted to the discrete results with the 5J energy level showing zero exceedance area.

thermore, the concentration of matrix cracks and broken fibres around the impact zone is visibly higher on the non-conventional laminates.



(a) Baseline



(b) NCL1



(c) NCL2

Figure 6.9: Middle section views of baseline and non-conventional laminate specimens impacted at 30J.

The visual inspection of the transversal section of a specimen at the impact location, as in Figure 6.9, gives an idea of the through-the-thickness damage mechanisms on an impacted laminate such as delaminations. However, there are obvious limitations to the simple observation methods applied on a single section cut. Not only the full extension of damage is impossible to evaluate, but also the lack of image contrast makes the characterisation of delaminations difficult. To overcome these limitations, an enhanced inspection technique was adopted.

The Fluorescent Penetrant Inspection (FPI) is a type of the known Liquid Penetrant Inspection technique and is based upon capillary action, where a low surface tension fluid penetrates into the open cracks of a material. In the case of FPI, the penetrant is applied by dipping the sectioned specimens in a dye that fluoresces when excited by ultraviolet radiation (also known as black light). FPI is performed in a darkened environment, and the excited dyes emit bright yellow-green light that contrasts strongly against the dark background. In these conditions, a high resolution picture of the specimen section is taken for later processing. In order to obtain the required results, the correct type of dye (on a sensitivity scale) and the adequate dipping time must be chosen carefully. Also, a correct cleansing of the section surface is required.

Within the present research, the FPI was performed on three specimens, one per lay-up configuration, previously impacted at an energy level of 30J. In order to evaluate the actual extent of damage, not only layerwise but also in the plane of the laminate, 5mm thick strips of the specimens were cut parallel to the smaller specimen axis, and then inspected at both surfaces. As examples, Figure 6.10 shows pictures of the application of the FPI technique to sections of the baseline and non-conventional laminates close to the impact location. The location of the widest delaminations is identified.

The extension of the larger delaminations was measured at each of the inspected sections. Then, the measurements were interpolated to generate a contour plot of each delamination. Figure 6.11 shows the superimposition of the major delaminations for each of the inspected specimens. For the baseline laminate specimen, there are two major delaminations. The widest one has an ellipse-like shape with its major axis oriented at around  $75^\circ$  and is located between plies 21[ $0^\circ$ ] and 22[ $90^\circ$ ]. The second largest delamination occurs at the interface between plies 19[ $0^\circ$ ] and 20[ $45^\circ$ ] and has a more elongated shape oriented at around  $30^\circ$ . There are still two other delaminations of relative large size, but smaller than the previously described. These are two elongated delaminations along  $0^\circ$  and  $-40^\circ$ , the first one between plies 15[ $-45^\circ$ ] and 16[ $0^\circ$ ] and the second one between layers 14[ $0^\circ$ ] and 15[ $-45^\circ$ ].

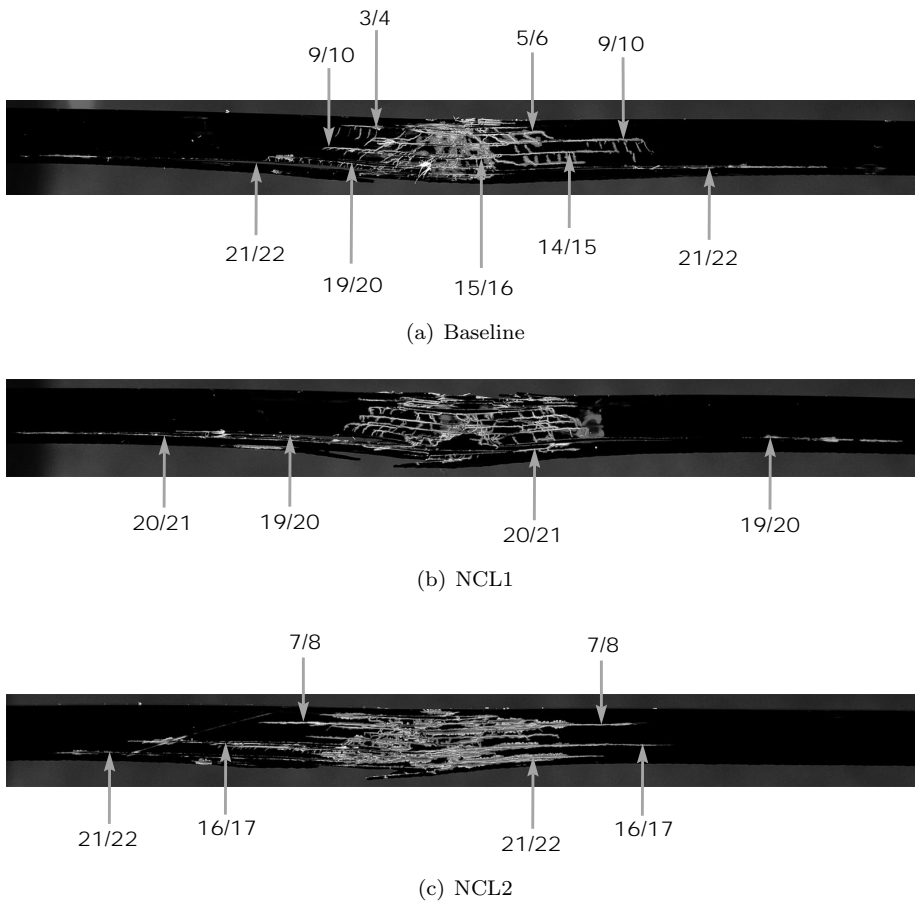


Figure 6.10: Section cut views of the three different laminate specimens impacted at an energy level of 30J. A fluorescent penetrant liquid is applied for better identification of through-the-thickness damage, namely the location and extent of delaminations. Major delaminations are identified by the neighbouring ply numbers.

Regarding the NCL1 specimen, only two major delaminations are observed: one between layers 19[0°] and 20[-70°] oriented at -60°, and the other one between plies 20[-70°] and 21[70°] oriented at around 60°. The NCL2 specimen also suffers from two major delaminations, one square shaped between layers 16[-10°] and 17[-80°] and the other one between plies 21[5°] and 22[80°], elongated along the 60° axis. There is also a smaller, but still relatively large, square shaped delamination between layers 7[10°] and 8[-80°].

From these observations, it is concluded that all major delaminations occur at interfaces close to the back face of each specimen. The plies most prone to



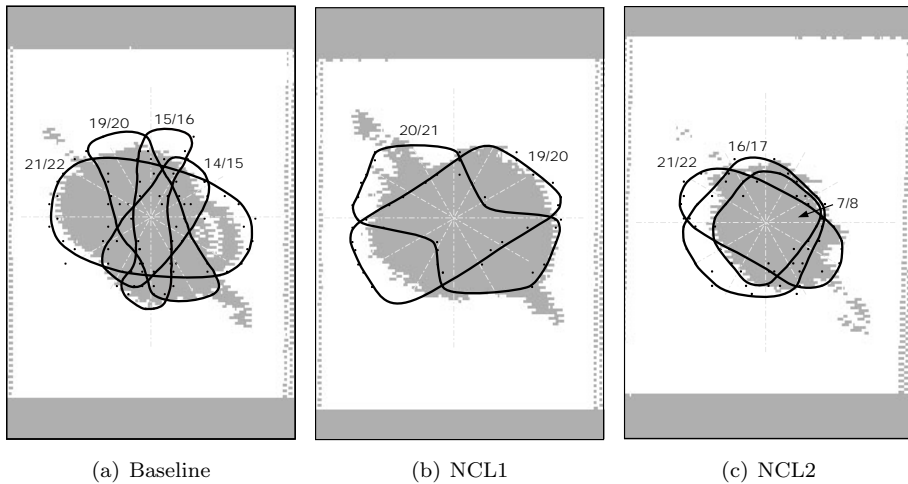


Figure 6.11: Superimposition of the major delaminations on the baseline and non-conventional laminate specimens impacted at an energy level around 30J. Each delamination is identified by the neighbouring ply numbers. The FPI and the C-Scan results (grey area) are compared.

delaminate are the ones with the largest difference in fibre orientations because such interfaces are where the highest interlaminar shear stresses develop. Also, in accordance with previous investigations<sup>103</sup>, delaminations typically develop along an axis which orientation is close or equal to the orientation of the underlying ply.

The superimposition of the major delaminations identified by the FPI is compared, in Figure 6.11, with the results of the C-scan inspection presented earlier. In all cases, the impact footprint area measured by the NDI is smaller than that identified by the FPI. This shows a known limitation in the sensitivity of the ultrasonic C-Scan technique. Far from being 100% reliable, better results are achieved with the FPI. In spite of the accuracy of each method, the results of the FPI are inline with the ones of the NDI and presented in Figures 6.7 and 6.8. Overall, these reveal that the delaminations on the NCL1 are wider than on the baseline configuration whilst the delaminations on the NCL2 are smaller. However, the post-impact strength of each specimen certainly depends on the through-the-thickness location of these delaminations, as well.

### Indentation

The permanent indentation of the impacted specimens, measured immediately after the tests, as a function of the impact energy is plotted in Figure 6.12. For

similar impact energies, the dents are deeper on the non-conventional laminates than on the baseline configuration. This is possibly related with the higher concentration of matrix cracks and fibre breaks around the impact zone in the non-conventional laminates, as shown in Figure 6.9. The energy necessary to produce a 1mm dent depth,  $E_{1mm}$ , considered to be the threshold for Barely Visible Impact Damage (BVID), is determined by interpolation of the results. A value of 26.4J is found for the baseline design whilst for the non-conventional laminates,  $E_{1mm}$  is approximately 25.5J. Therefore, for a given impact energy, damage is easier to identify on the laminates with dispersed stacking sequence.

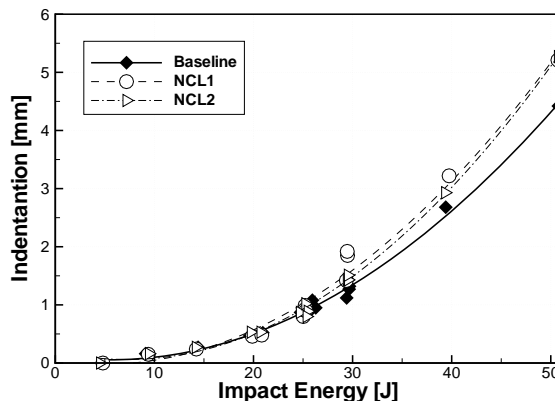


Figure 6.12: Permanent indentation, as measured immediately after specimen testing. Second order polynomials are fitted to the discrete results.

The deeper permanent indentation on the non-conventional laminates is valuable, given the industry requirements for BVID based on this parameter. A wider range of impacts can be identified on a structure designed with dispersed stacking sequence laminates leading to a higher readiness in structural maintenance.

## 6.4 Compression-After-Impact Tests

The *standard test method for compressive residual strength properties of damaged polymer matrix composite plies*<sup>121</sup>, as devised by the American Society for Testing and Materials (ASTM), was carried on the previously impacted specimens. A similar procedure is proposed by the aircraft manufacturing company AIRBUS<sup>117</sup>. This experimental procedure is commonly known as the Compression-After-Impact (CAI) test used to evaluate the residual post-impact strength of composite laminates i.e. their tolerance to damage<sup>102–104</sup>.

### 6.4.1 Test Setup and Procedure

The setup for the CAI test is illustrated, in simplified form, in Figure 6.13. A complete representation is available in the document defining the standard test procedure<sup>121</sup>. A 0-800kN load range compression machine with parallel platens, driven by four hydraulic actuators, was used in the test programme. The previously impacted specimens were loaded along their major axis and the edge displacement was manually controlled. A displacement rate no higher than 0.5mm/s was prescribed throughout all the tests.

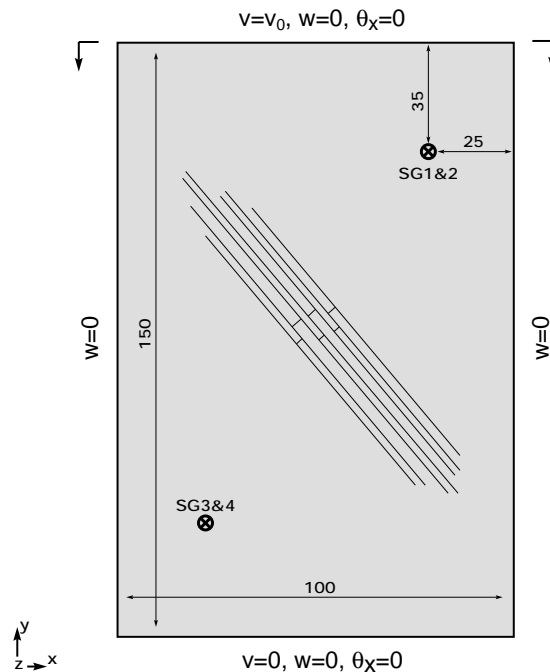


Figure 6.13: CAI test setup (dimensions in mm). View from the back face where fibre splits are visible.

A special purpose fixture<sup>121</sup> was developed for the CAI tests. It applies simply supported boundary conditions to the longer side edges while clamping the shorter horizontal edges (except for the horizontal in-plane displacements). As shown in Figure 6.13, four strain gauges are attached to each specimen in a back-to-back configuration. The strain gauges are placed in opposite corners in order to avoid the large fibre splitting areas on the back face of the specimens as a result of the higher energy impact events. The purpose of using the strain gauges is to check for any out-of-plane bending, abnormal (non-parallel) loading and to determine

the maximum strains achieved before specimen failure.

### 6.4.2 Experimental Results

Twelve out of the fourteen specimens of each configuration which had been previously impacted were compressed up to failure. One virgin (non-impacted) specimen of each configuration was tested as well. From the test matrix presented in Table 6.2, only two of the specimens per configuration, corresponding respectively to  $E_i = 30J$  and  $E_i = E_{1mm}$ , were not compressed after being impacted. The residual strength values and failure strains achieved are presented in the following paragraphs.

#### Compressive Residual Strength

As observed previously, an impact event on a laminate can result in delaminations at multiple interfaces through its thickness. Consequently, the laminate is divided in several thinner sublaminates, overall, having a lower bending stiffness than the original plate. The compressive residual strength of the specimens tested is generally determined by the resistance to buckling of the sublaminates rather than their in-plane strength. Even the compressive strength values obtained for the virgin specimens do not correspond to their failure under pure in-plane compression because of plate instability before those values are reached. While the Hashin criteria<sup>64</sup> predict pure compression first-ply failure of the  $0^\circ$  layers at 1016MPa, under test conditions none of the specimens reached a value higher than 500MPa.

The CAI results, for all the tested specimens, are graphically represented in Figure 6.14. Power-law curves, illustrating the residual strength of the laminates as function of the impact energy, are fitted to the experimental data. In reality, an asymptotic behaviour is expected as the compressive residual strength of completely penetrated specimens does not vary with impact energy. In the present cases, the asymptotes of minimum CAI strength approach the 200MPa level.

The specimens impacted at an energy level of 5J did not show damage under the scrutiny of the ultrasonic C-Scan. In spite of the scatter in results, their CAI strength is, on average, the same as for the virgin specimens. This means that, for low impact energies, there is a plateau in the residual strength plot of each specimen corresponding to its undamaged compressive strength, i.e. there is a range of impact energies which do not cause significant damage to the specimens. In the absence of more data, the threshold impact energy to guarantee specimen damage is considered to be 5J. If more refined data was available, this value would be somewhere between 5J and 10J, possibly different for each of the three

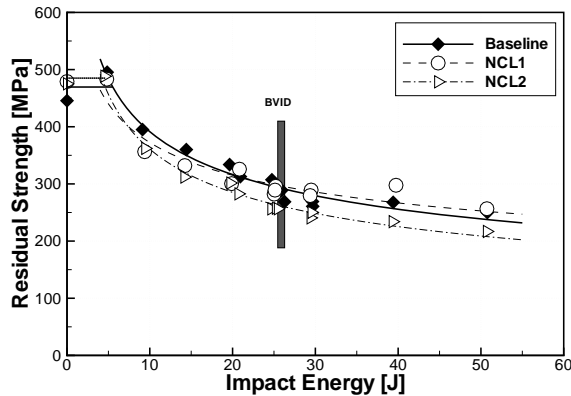


Figure 6.14: CAI strength of the three specimen configurations as function of the impact energy. Power-law curves are fitted to the experimental data.

configurations tested.

Further analysis of Figure 6.14 reveals that the response behaviour of the three laminate configurations is similar. Furthermore, there is no consistent trend that could substantiate the superior performance of any of the non-conventional laminates as compared with the baseline configuration. On the contrary, the NCL2 consistently under-performs the baseline configuration by 10% to 20% even though the NCL2 had shown to have a smaller impact footprint compared to the baseline design. Given the scatter in the results, the compressive residual strength performance of the baseline configuration and the NCL1 cannot be differentiated.

The CAI strength normalised by the average undamaged strength is plotted, in Figure 6.15.a, as function of the impact footprint and, in Figure 6.15.b, as function of the permanent indentation. In general, for a given value of the C-scanned damaged area, the strength reduction is the highest for the NCL2, average for the baseline and lowest for the NCL1. The same trend is observed for the permanent indentation, specially for damage extents larger than BVID, which typically corresponds to a 40% reduction in the strength of the specimens.

### Failure Strains

The designer of composite structures is often more interested in knowing the failure strain of an impacted laminate rather than its residual strength. With this information the designer can fix a minimum bound for the strain that a given structure undergo without failure, supposing that it had suffered any single impact within an expected range of impacts. Hence, increasing the failure strains of a structure is of great importance.

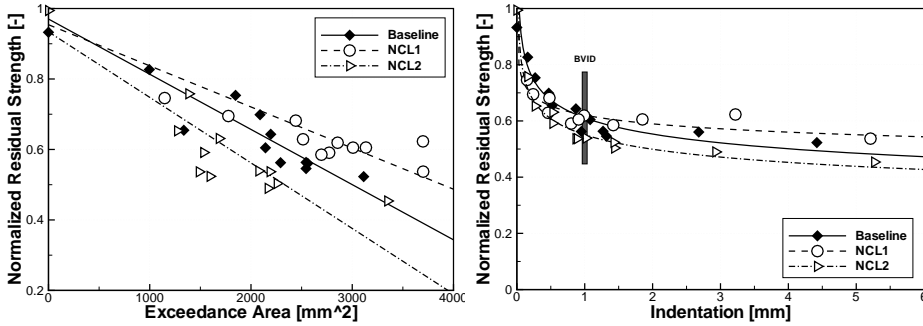


Figure 6.15: Residual strength as function of impact footprint and as function of the permanent permanent indentation.

The CAI failure strains are represented in the form of bars in Figure 6.16. The strain results for the NCL2 slightly underperform the ones achieved for the baseline configuration. However, in general, the NCL1 shows much better performance than the baseline. While the minimum failure strain value reached for the baseline configuration was about  $-2700\mu\varepsilon$ , for the NCL1 this value is in the vicinity of  $-4600\mu\varepsilon$ , i.e. 70% higher in absolute value.

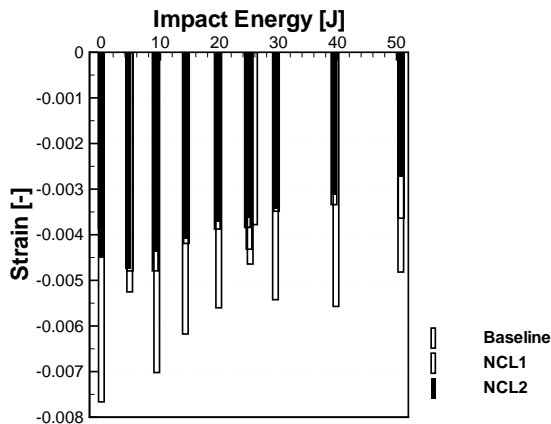


Figure 6.16: Strains reached at failure in the CAI tests. The values shown are the average of the strains measured by the strain gauges at the impact face.

The previous observations are substantiated by the impact damage results. As shown in Figures 6.10 and 6.11, delaminations of considerable size occur at several interfaces through-the-thickness of both the baseline laminate and NCL2 specimens as a result of impact events. This divides each of these laminates into a few sublaminates. Impacts on the NCL1 laminate specimens, on the other

hand, seem to produce relatively large delaminations only on interfaces 19/20 and 20/21. This leaves almost intact one relatively thick sublaminates composed by plies 0 to 19. This sublaminates carries most of the compressive loading on the NCL1 specimens. While the sublaminates on the other configurations fail quite abruptly, in the NCL1 the thicker sublaminates seems to buckle before failure, hence allowing higher strains. This is corroborated by the load versus strain plots on Figure 6.17 for specimens impacted at an energy level of 30J. The buckling of the NCL1 specimen is evidenced by the sudden divergence of measurements made by back-to-back strain gauges SG3 and SG4 before failure.

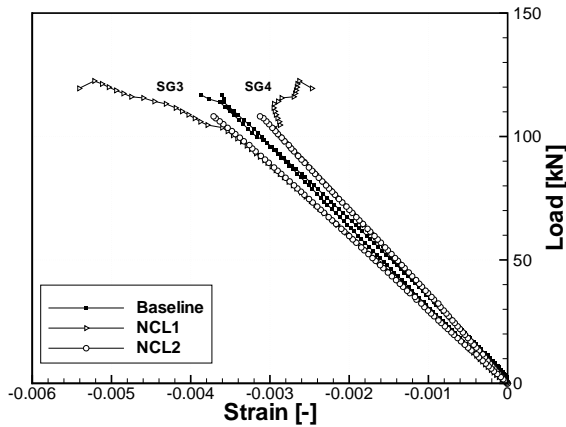


Figure 6.17: Strains measured by SG3 and SG4 during the CAI tests on specimens impacted at an energy level of 30J.

## 6.5 Discussion

As opposed to what was expected, the experiments carried out showed no clear improvements in terms of the impact performance of the non-conventional laminates:

$$[\pm 45/0/70/-70/0/15/10/-10/-15/15/-15]_s \text{ (NCL1)}$$

$$[\pm 45/80/5/20/-20/10/-80/-10/-5/15/-15]_s \text{ (NCL2)}$$

over the chosen conventional configuration

$$[\pm 45/90/0/45/0_4/-45/0_2]_s \text{ (baseline)}$$

even though, there are discernable differences in various impact response variables.

Evaluating by the smaller impact footprint, the NCL2 laminate appears to offer an improved impact resistance, as compared to the baseline configuration. The opposite occurs for the NCL1. According to a general rule of thumb in the impact damage field<sup>103</sup>, the wider the damaged area, the lower the compressive residual strength. However, the experimental CAI results show a reversed trend for the configurations studied, i.e. the damage tolerance of the NCL1 specimens is similar or slightly higher than the damage tolerance of the baseline design, and the opposite is observed for the NCL2. A closer look at the through-the-thickness damage distribution (Figures 6.10 and 6.11) of the impacted specimens reveals the reasons for such unexpected behaviour. The impact footprint in the NCL1 specimens results mainly from the superimposition of only two wide delaminations between layers close to the laminate back face. This leaves an almost intact stiff sublaminates capable of bearing relatively high CAI loads before buckling. On the baseline, and mostly on the NCL2, the multiple delaminations, some of which close to the laminate symmetry plane, subdivide the specimens in several sublaminates with overall less resistance to buckling.

The evidence of more concentrated damage regions around the impact locations (Figure 6.9) as well as the deeper permanent indentations on the non-conventional laminates (Figure 6.12) are signs that the mechanism of fibre bridging is playing a somewhat more prominent role in the prevention of spreading of intralaminar damage in these laminates than in the conventional configuration. This might have advantages in terms of the residual tension strength performance of the specimens.

In general, it can be concluded that the simple strategy of dispersing a traditional laminate stacking sequence while maintaining its in-plane and bending stiffness does not automatically lead to designs having improved impact responses. One of the possible reasons for this is the high difference between the orientation of adjacent plies in the non-conventional laminates. These may easily delaminate due to the high interlaminar shear stresses, specially if they are located close to the back face of the impacted specimens. On the other hand, interface angle differences of  $5^\circ$  are common on the designed non-conventional laminates. Such a small difference between orientations of adjacent layers is probably not enough to promote a significant fibre bridging effect and not enough to trigger delaminations, i.e. such plies behave almost as if they are clustered at the same fibre angle. Delamination is, in any case, unavoidable and actually necessary to dissipate part of the impact energy. The strategy to keep delaminations under controlled size is to spread them among the highest number of interfaces and to prevent high interlaminar shear stresses caused by large differences in the orientations between



adjacent layers. Therefore, constraints regarding maximum fibre angle differences between neighbouring plies should be imposed in the design of laminates with dispersed stacking sequences.

Additionally, an improved CAI response may be achieved with extra control on the through-the-thickness location of delaminations. In terms of residual strength, a delamination at an interface close to backface of a impacted specimen is preferable to one deeper in the laminate.

## 6.6 Conclusions

A new stacking sequence design method is proposed in the study presented herein. This method is inspired by the non-conventional laminates that are generated due to spatially varying fibre orientations in VSP' and the flexibility offered by the AFP technology in terms of permitted fibre angles. It is shown that it is possible to disperse the stacking sequences commonly used on composite applications in such a way that no neighbouring layers have the same fibre orientation angle while the resultant laminate still keeps similar axial and bending stiffness properties. Laminates with dispersed stacking sequences were branded *non-conventional laminates*.

A traditional laminate was compared with two non-conventional laminates in terms of impact performance. This was done by means of drop-weight impact and CAI experiments. In general, it can be concluded that the straightforward dispersion of the stacking sequence does not result in clear improvements in terms of impact resistance or damage tolerance performance. However, there are indications that the strategy might work if constraints in the difference between the orientations of adjacent plies are imposed and attempts are made to condition the through-the-thickness location of delaminations.

Even if the impact response of laminates could be improved by means of a more informed and selective stacking sequence dispersion method, the results of the present investigation can be extrapolated to conclude that the stacking sequence dispersion of variable-stiffness composite panels does not preclude their superiority in terms of damage tolerance because in these configurations the dispersion is a secondary and uncontrolled consequence of fibre-steering.

The impact performance of non-conventional laminates is evaluated in the following chapter by means of dynamic simulations of the impact and CAI experiments. These can provide a better insight on the impact damage phenomena, besides being a valuable tool to replace part of the experimental tests by reliable computational simulations in the evaluation of candidate laminates.



# Chapter 7

## Low-Velocity Impact: Numerical Simulations

### 7.1 Introduction

**T**HE previous chapter reports an experimental programme on the LVI and CAI responses of composite laminate specimens designed according to (i) a traditional methodology, based on  $0^\circ$ ,  $\pm 45^\circ$  and  $90^\circ$  ply angles and ply clustering, and (ii) a non-conventional approach based on the dispersion of the stacking sequence while keeping similar global stiffness properties as the traditional baseline configuration. The present chapter is focused on the numerical simulation of those tests by means of FE tools<sup>122;123</sup>.

Under out-of-plane loads, such as impacts, laminated composites may suffer damage in the form of different mechanisms such as (i) delaminations at ply interfaces and (ii) intraply matrix cracking and fibre breakage. If acceptable accuracy is to be expected from the numerical impact analyses, these damage phenomena need to be taken into account. Several authors have proposed analytical formulations for the prediction of the impact response of composite laminates<sup>102-104</sup>. However, the complexity of the physical phenomena, which includes dynamic structural behaviour and loading, contact, friction, damage and failure, often results in a oversimplification of the problem and limits the analytical models. The numerical approach by means of FE analyses is a more flexible and powerful alternative to the analytical formulations. The possibility of modelling the constitutive behaviour of each material at local (element) level adds to the capacity of simulating complex structures under seemingly complex external loads and boundary

conditions.

Herein, the interfaces between the plies are simulated by means of cohesive elements, as proposed by Turon et al.<sup>124</sup>. Cohesive elements are a reliable numerical tool for the prediction of the initiation and propagation of delaminations under several loading scenarios and have been applied before in the simulation of impact-induced delaminations<sup>125;126</sup>. The intraply damage model used in this work is an extension to three-dimensional scenarios of the plane stress formulation proposed by Maimí et al.<sup>85;86</sup> for in-plane behaviour, which was used in Chapters 4 and 5. The application of these models is limited to the range of quasi-static loading and low strain-rates situations where LVI events can be considered to fit<sup>103</sup>.

## 7.2 Impact Damage Models

Two distinct formulations are used to simulate the damage phenomena occurring in layered composites under out-of-plane, LVI loads: (i) a continuum damage model to address the matrix and fibre damage occurring at ply level and (ii) a cohesive damage model to account for delamination. While in the case of delamination the crack plane is known *a priori*, the location and direction of matrix cracks and fibre breakage bands needs to be determined along with the analysis.

The intraply damage model used in this work is an extension to three-dimensional solid elements of the plane stress formulation implemented by Maimí et al.<sup>85;86</sup> in shell elements and used in Chapters 4 and 5. The cohesive damage model is based on the explicit implementation<sup>127</sup> of the formulation proposed by Turon et al.<sup>124</sup>. Both constitutive models were coded as ABAQUS/Explicit<sup>62</sup> VUMAT user-written subroutines. The main aspects of these models are presented in the following paragraphs.

### 7.2.1 Continuum Damage Model for 3-D Plies

The ply constitutive model used herein<sup>85;86</sup> follows the general form schematically represented in Figure 4.2, for each damage mode. As described in Chapter 4, the material response is linear-elastic until the onset of damage and, at higher strains, it softens according to an exponential law. The complementary free energy density of a three-dimensional transversely isotropic ply ( $E_2 = E_3$ ,  $G_{12} = G_{13}$ , and  $\nu_{12} = \nu_{13}$ ) is defined as:

$$\begin{aligned}
G = & \frac{\sigma_{11}^2}{2(1-d_1)E_1} + \frac{1}{2E_2} \left[ \frac{\sigma_{22}^2}{(1-d_2)} + \frac{\sigma_{33}^2}{(1-d_3)} \right] - \frac{\nu_{12}}{E_1} (\sigma_{22} + \sigma_{33}) \sigma_{11} - \\
& - \frac{\nu_{23}}{E_2} \sigma_{22} \sigma_{33} + \frac{\sigma_{12}^2}{2(1-d_6)G_{12}} + \frac{\sigma_{12}^2}{2(1-d_5)G_{12}} + \frac{\sigma_{23}^2}{2(1-d_4)G_{23}} + \\
& + [\alpha_{11}\sigma_{11} + \alpha_{22}(\sigma_{22} + \sigma_{33})] \Delta T + [\beta_{11}\sigma_{11} + \beta_{22}(\sigma_{22} + \sigma_{33})] \Delta M \quad (7.1)
\end{aligned}$$

where  $d_1$  is the damage variable associated with longitudinal (fibre) failure. The transverse matrix cracking is controlled by  $d_2$ , for in-plane loads, and by  $d_3$  for out-of-plane loads. The damage variables  $d_4$ ,  $d_5$  and  $d_6$  are influenced by longitudinal and transverse cracks.

The strain tensor,  $\varepsilon = \{\varepsilon_{11}, \varepsilon_{22}, \varepsilon_{33}, \gamma_{12}, \gamma_{13}, \gamma_{23}\}^T$ , results from the differentiation of the complementary free energy density with respect to the stress tensor,  $\sigma = \{\sigma_{11}, \sigma_{22}, \sigma_{33}, \sigma_{12}, \sigma_{13}, \sigma_{23}\}^T$ :

$$\varepsilon = \frac{\partial G}{\partial \sigma} = \mathbf{H} : \sigma + \alpha \Delta T + \beta \Delta M \quad (7.2)$$

Here,  $\mathbf{H} = \frac{\partial^2 G}{\partial \sigma \otimes \partial \sigma}$  is the lamina compliance tensor represented as:

$$\mathbf{H} = \begin{bmatrix} \frac{1}{(1-d_1)E_1} & -\frac{\nu_{12}}{E_1} & -\frac{\nu_{12}}{E_1} & 0 & 0 & 0 \\ -\frac{\nu_{12}}{E_1} & \frac{1}{(1-d_2)E_2} & -\frac{\nu_{23}}{E_2} & 0 & 0 & 0 \\ -\frac{\nu_{12}}{E_1} & -\frac{\nu_{23}}{E_2} & \frac{1}{(1-d_3)E_2} & 0 & 0 & 0 \\ 0 & 0 & 0 & \frac{1}{(1-d_6)G_{12}} & 0 & 0 \\ 0 & 0 & 0 & 0 & \frac{1}{(1-d_5)G_{12}} & 0 \\ 0 & 0 & 0 & 0 & 0 & \frac{1}{(1-d_4)G_{23}} \end{bmatrix} \quad (7.3)$$

The longitudinal and transverse (in-plane and out-of plane) damage variables are calculated as:

$$\begin{aligned}
d_1 &= d_{1+} \frac{\langle \sigma_{11} \rangle}{|\sigma_{11}|} + d_{1-} \frac{\langle -\sigma_{11} \rangle}{|\sigma_{11}|} \\
d_2 &= d_{2+} \frac{\langle \sigma_{22} \rangle}{|\sigma_{22}|} + d_{2-} \frac{\langle -\sigma_{22} \rangle}{|\sigma_{22}|} \\
d_3 &= d_{2+} \frac{\langle \sigma_{33} \rangle}{|\sigma_{33}|} + d_{2-} \frac{\langle -\sigma_{33} \rangle}{|\sigma_{33}|}
\end{aligned} \quad (7.4)$$

The damage activation functions are described in Chapters 3 and 4. The damage evolution laws for each damage variable are introduced in Chapter 4 and described in detail by Maimí et al.<sup>85;86</sup>.

## Material Properties

The laminates used in this work were fabricated using a fibre placement machine and Hexply AS4/8552 carbon-epoxy tows. The fracture energies per unit surface, corresponding to each failure mode properties are available for the epoxy resin Hexply 8552 but not for the carbon fibres AS4. The mode I and mode II components of the fracture toughness for matrix cracking used here,  $\mathcal{G}_{2+}$  and  $\mathcal{G}_6$  respectively, were measured by Camanho et al.<sup>97</sup> for IM7/8552 using interlaminar test methods. In the absence of the fracture toughness values for a composite reinforced by the carbon fibres AS4, the properties previously measured for the IM7 fibres are used in this work. The energy dissipated by fiber breakage in low velocity impact tests is normally small compared with other dissipation mechanisms such as delaminations and matrix cracking. Then, the possible difference between the two energies is expected to have negligible effect on the results. The ply properties used in this work are summarised in Table 6.1.

### 7.2.2 Cohesive Zone Model for 3-D Interfaces

The bond between each layer is simulated by means of the cohesive zone approach. In this approach, the fracture behaviour (delamination) is lumped into a thin cohesive region representing the resin rich regions between layers. These resin rich regions are simulated by means of cohesive elements placed between each layer, as shown in Figure 7.1.a. The relative displacement of the two surfaces attached to the adjacent continuum elements that model the layers is a measure of the opening of the delamination crack. The opening is controlled by means of a bilinear cohesive constitutive relation, represented in Figure 7.1.b, that defines the delamination process. The formulation of the cohesive element used here is described by González et al.<sup>127</sup> in full detail.

The free energy by surface unit of the interface is defined as:

$$\psi(\Delta_i, d) = (1 - d)\psi^0(\Delta_i) - d\psi^0(\delta_{3i}\langle -\Delta_3 \rangle) \quad i, j = 1, 2, 3 \quad (7.5)$$

wherein  $d$  is the scalar isotropic damage variable,  $\Delta_i$  are the relative displacements, and  $\delta_{ij}$  is the Kronecker delta. The damage model has a unilateral behaviour in mode I loading because negative values of the relative displacement in this mode,  $\Delta_3$ , have no physical sense, i.e. a crack does not over-close.  $\psi^0(\Delta)$  is a function of the relative displacement defined as:

$$\psi^0(\Delta_i) = \frac{1}{2}\Delta_i D_{ij}^0 \Delta_j \quad i, j = 1, 2, 3 \quad (7.6)$$

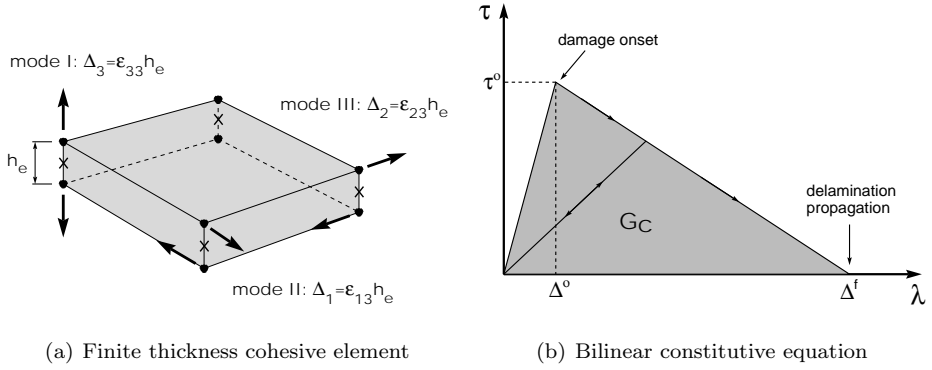


Figure 7.1: Parameters of the cohesive element formulation in an explicit FE code.

$D_{ij}^0 = \delta_{ij}K$  is the undamaged stiffness tensor, wherein  $K$  is the scalar parameter defining the intact stiffness of the interface for each loading mode. The cohesive constitutive equation is defined as:

$$\tau_i = \frac{\partial \psi}{\partial \Delta_i} = (1 - d) D_{ij}^0 \Delta_j - d D_{ij}^0 \delta_{3j} \langle -\Delta_3 \rangle \quad i, j = 1, 2, 3 \quad (7.7)$$

The thermodynamic consistency of the model is ensured by the positiveness of the energy dissipated by the damage process, i.e.  $-\frac{\partial \psi}{\partial d} \dot{d} \geq 0$ . The relative displacement vector,  $\Delta$ , is the free variable of the system and  $d$  is the internal variable that ensures the irreversibility of the model, and whose value has to be evaluated at each time increment during the loading process.

The delamination propagation criterion, based on the work of Benzeggagh and Kenane<sup>128</sup>, is:

$$\mathcal{G}_c = \mathcal{G}_{Ic} + (\mathcal{G}_{IIc} - \mathcal{G}_{Ic}) \left( \frac{\mathcal{G}_{II} + \mathcal{G}_{III}}{\mathcal{G}_I + \mathcal{G}_{II} + \mathcal{G}_{III}} \right)^\eta \quad (7.8)$$

where  $\mathcal{G}_{Ic}$  and  $\mathcal{G}_{IIc}$  are the fracture toughnesses in mode I and II, and  $\mathcal{G}_I$ ,  $\mathcal{G}_{II}$  and  $\mathcal{G}_{III}$  are, respectively, the energy release rates in mode I, II and III. In the present formulation, the shear loading modes II and III are coupled together in a single shear loading mode associated with the energy release rate  $\mathcal{G}_{shear} = \mathcal{G}_{II} + \mathcal{G}_{III}$ . The constitutive loading behaviours in mode II and III are considered the same and the fracture toughness  $\mathcal{G}_{IIIc}$  is assumed to be equal to  $\mathcal{G}_{IIc}$ . This is a reasonable assumption since mode III loading is expected to play a minor role in most of the problems, specifically in impact events. Furthermore, in a FE formulation the distinction between these two loading modes is difficult to establish<sup>129</sup>. The parameter  $\eta$  is found by least-square fit of the fracture toughness

under different mixed-mode ratios.

The delamination propagation criterion can be expressed in terms of displacements by means of

$$\Delta^f = \frac{K_1 \Delta_3^o \Delta_3^f + \left( K_2 \Delta_{shear}^o \Delta_{shear}^f - K_1 \Delta_3^o \Delta_3^f \right) \mathcal{K}^\eta}{K_\beta \Delta^o} \quad (7.9)$$

with the parameter  $\mathcal{K}$  expressed as

$$\mathcal{K} = \frac{K_2 \beta}{K_2 \beta + K_1 (1 - \beta)} \quad (7.10)$$

wherein  $\beta$  is the mixed-mode loading ratio defined as  $\beta = \frac{\Delta_{shear}^2}{\langle \Delta_3 \rangle + \Delta_{shear}^2}$ .  $\Delta_{shear} = \sqrt{\Delta_1^2 + \Delta_2^2}$  is the Euclidian norm of the relative displacements in mode II and III.  $\Delta_3^o$  and  $\Delta_{shear}^o$  are the onset relative displacements for pure mode I and shear mode, respectively. These are calculated by means of  $\Delta_3^o = \frac{\tau_3^o}{K_1}$  and  $\Delta_{shear}^o = \frac{\tau_1^o}{K_2}$ , wherein  $\tau_3^o$  and  $\tau_1^o$  are the interface strengths for pure mode I and shear mode, respectively.  $\Delta_3^f = \frac{2\mathcal{G}_{Ic}}{K_1 \Delta_3^o}$  and  $\Delta_{shear}^f = \frac{2\mathcal{G}_{IIc}}{K_2 \Delta_{shear}^o}$  are the propagation relative displacements for pure mode I and shear mode, respectively.

The parameter  $\Delta^o$  is the general relative displacement at damage onset, determined by means of the damage initiation criterion:

$$\Delta^o = \left( \frac{K_1 (\Delta_3^o)^2 + \left( K_2 (\Delta_{shear}^o)^2 - K_1 (\Delta_3^o)^2 \right) \beta^\eta}{K_\beta} \right)^{\frac{1}{2}} \quad (7.11)$$

In equations 7.9 and 7.11,  $K_1$ ,  $K_2$  and  $K_\beta$  are the penalty stiffness, respectively, for the opening, shear and mixed modes, respectively defined as:

$$K_1 = \frac{E_m}{h_c} \quad (7.12)$$

$$K_2 = \frac{G_m}{h_c} \quad (7.13)$$

$$K_\beta = K_1 (1 - \beta) + K_2 \beta \quad (7.14)$$

wherein  $E_m$  is the Young's modulus and  $G_m$  is the shear elastic modulus of the cohesive layer (resin) material:  $G_m = \frac{E_m}{2(1+\nu_m)}$ . The thickness of the cohesive element is expressed in  $h_c$ .

The correct implementation of a constitutive behaviour for the continuum elements in ABAQUS/Explicit<sup>62</sup> requires the definition of the strain increment vector at each integration point. The cohesive strains are related with the relative



displacements by:  $\Delta_3 = h_c \varepsilon_{33}$  (mode I),  $\Delta_1 = h_c(2\varepsilon_{13})$  (mode II) and  $\Delta_2 = h_c(2\varepsilon_{23})$  (mode III).

### Material Properties

The independent material properties required to completely define the cohesive model are:

- Elastic properties of the interface material,  $E_m$  and  $\nu_m$ . These can be approximated using the ply material properties as  $E_m \approx E_2$  and  $\nu_m \approx \nu_{23}$ .
- Interface strengths for pure mode I and shear modes (II and III),  $\tau_3^0$  and  $\tau_1^0$ , which can be approximated as  $\tau_3^0 \approx X_{2+}$  and  $\tau_1^0 \approx X_6$ .
- Interface fracture toughness for pure mode I and shear modes (II and III),  $\mathcal{G}_{Ic} = \mathcal{G}_{2+}$  and  $\mathcal{G}_{IIc} = \mathcal{G}_6$ .
- The mode interaction parameter  $\eta$ , found by least-square fit of the experimental values of the fracture toughness under different mixed-mode ratios.

Therefore, except for the parameter  $\eta$ , the material properties required for the definition of the cohesive model are common to the ones required to define the intraply damage model<sup>85;86</sup>. The value of the parameter  $\eta$  used herein,  $\eta = 1.45$ , was determined based on experimental data<sup>131</sup> resulting from the Mixed-Mode Bending (MMB) test, as proposed by Crews and Reeder<sup>130</sup>.

## 7.3 Simulations of the Low-Velocity Impact Tests

This section describes the numerical strategy used to simulate the LVI tests reported in Chapter 6. This is followed by a correlation between experimental and simulation results.

### 7.3.1 Numerical Set-Up

Numerical schemes based on explicit time integration are the adequate choice for solving short-time, highly nonlinear dynamic problems. The need to invert the stiffness and mass matrices at every iteration of implicit integration codes makes these impractical in the simulation of nonlinear events with a wide range of sources of nonlinearity. In an impact event, sources of nonlinearity include large displacements, material constitutive behaviour accounting for damage, complex contact interactions and frictional behaviour. Under these conditions, implicit integration

procedures require a large number of iterations in order to achieve an equilibrium solution, hence calling for large computational resources and calculation times, if not impossible at all.

Explicit integration schemes do not require the solution of a global set of equilibrium equations as the accelerations, velocities and displacements are calculated explicitly at each node recurring to a simple central differences rule applied over a time increment. The stable time increment is defined in terms of the highest element frequency in the model, associated with the dilatational mode of deformation. With the element characteristic length,  $l^*$ , and the dilatational wave speed in the material,  $c_d$ , the stable time increment is defined as<sup>62</sup>  $\Delta t_{stable} = l^*/c_d$ . For a linear elastic material with a Poisson's ratio of zero,  $c_d = \sqrt{\frac{E}{\rho}}$ , where  $E$  is the material Young's modulus and  $\rho$  its density.

The stable time steps for explicit dynamic analyses are generally very small and the whole calculation process often requires hundreds of thousands of even millions of increments. However, as an explicit increment is much less expensive than an implicit one, adopting an explicit procedure is often more efficient and preferable.

The FE model developed in this work simulates several physical processes which occur during LVI events on composite laminates. Effort was put on the correct geometrical representation of the structural system, loads, boundary conditions, material behaviour and contact conditions between the bodies involved.

### Geometry and Boundary Conditions

The FE models simulate, in the way shown in Figure 7.2, the geometry and boundary conditions of the experimental tests described in the previous chapter. Laminate test specimens with dimensions of 150mm×100mm are fixed between a steel support and a 10mm thick steel plate which is itself bolted to the support along two lines of three bolts each, parallel to the longer specimen sides. The 4.368mm thick specimens consist of 24 laminated AS4/8552 plies with a nominal thickness of 0.182mm. Both the support and the plate have 125mm×75mm rectangular cuts in the centre leaving part of the specimens free for the impact. In the simulations, the support is considered perfectly rigid, fixed, and in contact with the specimen. The top plate, also in contact with the specimen and simply supported along the bolt lines, is allowed to deform linearly. The modelled part of the steel plate measures 175mm×150mm.

The impactor is modelled as a rigid body with a lumped mass equal to the impactor mass used in the experiments. It has a spherically-shaped impact sur-

face with a diameter of 16mm. An initial velocity in the vertical direction is prescribed to the impactor, simulating the impact velocity measured during the tests. Additionally, a force of magnitude  $M_i g$  in the vertical direction is applied to the impactor to simulate the gravitational force, where  $M_i$  is the impactor mass and  $g$  is the acceleration due to the gravitational force.

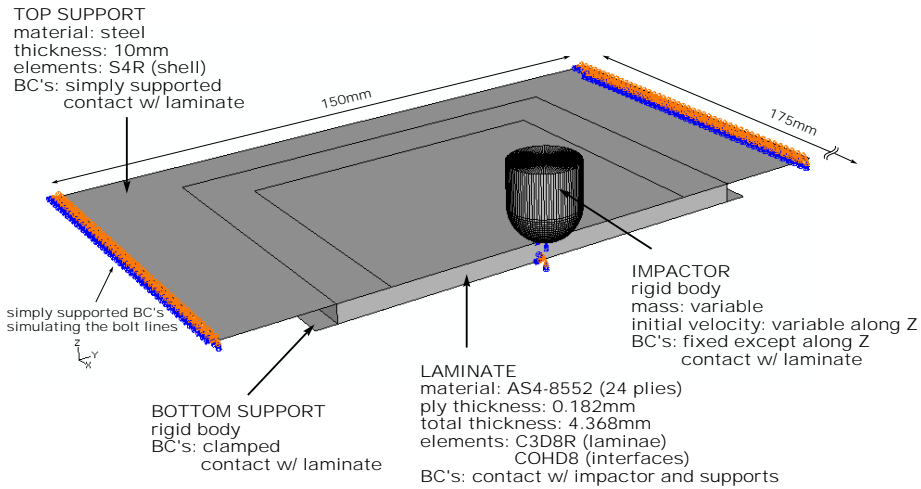


Figure 7.2: Geometry and boundary conditions for the simulation of an impact event on a 24-ply composite laminate specimen. Only half of the structure is represented.

### Element Size and Mesh Regularization

The FE model has four distinct parts: laminate, impactor, bottom support, and top support. The impactor is modelled as a rigid analytical surface associated with a pointwise mass. The bottom support is a rigid body discretised with R3D4 (2mm×2mm) rigid elements. The top support simulates a 10mm thick steel plate with S4R (2mm×2mm) deformable shell elements. Each laminate ply is modelled with one solid C3D8R element through-the-thickness which respond according to the continuum damage model previously described<sup>85;86</sup>. In order to prevent hourglassing of the reduced integration elements, a formulation which combines viscous damping with element stiffness relaxation is used. The resin-rich interfaces between each ply are discretised with COH3D8 cohesive elements that model delamination by means of the traction-displacement laws previously described<sup>127</sup>. Each of these elements has four integration points, as shown in Figure 7.1.a. In the current model, the thickness of the cohesive layer,  $h_c$ , is

0.005mm (about 3% of the nominal ply thickness).

Using the correct element size is of extreme importance in models involving the simulation of damage mechanisms. The continuum damage formulation used in this work models the damage mechanisms occurring in spatially discrete locations as if they are smeared over the finite size of the elements. A zero-thickness mesocrack is simulated by the failure of a single band of solid elements. While damaging, the material energy release rate ( $\mathcal{G}$ ) must be properly computed by the numerical model. Therefore, the damage model<sup>85;86</sup> uses the element characteristic length,  $l^*$ , in a mesh regularisation scheme, as proposed by Bažant<sup>88</sup>. However, there is a maximum size of a finite element that ensures that the energy release rate is correctly computed. If an element is too large, its own elastic energy per unit area is higher than the material fracture toughness and the model will over-predict the energy dissipation. The damage model works around this problem by reducing the strength of the material associated with such an element while maintaining its fracture toughness constant, as illustrated in Figure 4.4. This is acceptable in models, or regions of models, where the determination of the initiation of damage is of secondary importance as compared to the final failure loads or if the objective is the simulation of the global behaviour (e.g. the composite panels simulated in Chapter 4). In the case of impact simulations, one of the main goals is the determination of the impact load that triggers the initiation of damage. Therefore, in the region of impact, the elements should be small enough to guarantee the correct representation of both material strength and fracture toughness. For each damage mode  $M$ , the elastic energy of these elements,  $\frac{1}{2}X_M\varepsilon_M(l^*)^2h_p = \frac{1}{2}\frac{X_M^2}{E_M}(l^*)^2h_p$  should not be higher than the energy dissipated in the fracture process<sup>77</sup>  $\mathcal{G}_M l^* h_p$ , i.e.

$$l^* \leq \frac{2E_M\mathcal{G}_M}{X_M^2}, M = 1\pm, 2\pm, 6 \quad (7.15)$$

wherein  $E_M$ ,  $\mathcal{G}_M$  and  $X_M$  are, respectively, the Young moduli, fracture toughness and ply strengths corresponding to each failure mode. The application of equation (7.15) to the present case dictates a maximum element length of 0.29mm around the impact zone. Approaching the edges, the mesh is coarsened to 1mm in element length, at the cost of the reduction of the ply strength<sup>77</sup> to:

$$X_M = \sqrt{\frac{2E_M\mathcal{G}_M}{l^*}} \quad (7.16)$$

Further increase in element size is not advisable since the simulation of delaminations with cohesive element is also mesh dependent. The cohesive zone, i.e.

the region ahead of a delamination crack tip where damage is occurring, should be correctly discretised in order to capture the correct traction-displacement field and accurately simulate the energy being dissipated. At least two elements should be within the cohesive zone<sup>132;133</sup> whose length can be approximated as:

$$l_{cz} = \frac{E_M \mathcal{G}_M}{X_M^2}, M = 2+, 6 \quad (7.17)$$

The application of equation (7.17) to the present case yields a minimum cohesive zone length (in mode II) of 0.51mm. This means that the discretisation requirement is barely accomplished around the impact zone but not away from it. Inaccurate results may result from such approach. However, the required mesh refinement would make the model computationally untractable.

### Control of the Stable Time Increment - Element Deletion and Mass Scaling

The user-developed FORTRAN routines (VUMAT) that implement the laminae continuum damage model and the interfacial cohesive behaviour<sup>85;86;127</sup>, are run at each time increment for each integration point on each element in the model (over 1 million elements in total). The amount of memory required by the analyses approaches 10GBytes. Each run takes between 4 to 5 days to complete using a cluster of 32 CPU's. Such long calculation times are a direct result of the small stable time increment required by ABAQUS/Explicit<sup>62</sup>.

Due to their small thickness, cohesive elements define the upper bound of the value of the stable time step. However,  $\Delta t_{stable}$  can be increased by artificially increasing the density of these elements. Care must be taken to prevent the change of the total mass balance in which case the physical impact problem would be altered. In the current work, the density of the COH3D8 (cohesive) elements is increased, typically by a factor of 50. This \*MASS SCALING typically improves the calculation speed by a factor of 3 while increasing the total mass of the model by less than 2%

Furthermore, the localised softening associated with damage can cause an excessive element distortion which introduces numerical convergence difficulties and force the reduction of the stable time step. These two factors may cause the analysis to run slowly or even to abort. To prevent excessive mesh distortion and allow the analyses to complete successfully, the elements are removed from the mesh once they reach a given damage threshold. Cohesive elements are removed when the the damage variable,  $d$ , reaches the value of 0.99. They are replaced by contact constraints between plies, with frictional effects. The ply elements are

removed when the damage variable in the longitudinal direction,  $d_1$ , reaches 0.999. The transverse and shear damage variables  $d_2$ ,  $d_3$ ,  $d_4$ ,  $d_5$  and  $d_6$  are limited to a maximum value of 0.99, i.e. under these damage modes the elements always keep some residual stiffness in order to avoid uncontrolled distortion. This technique has, however, limited efficiency. Tenfold reductions in the  $\Delta t_{stable}$  would be no exception during an impact analysis if no other measures were taken. In order to improve the efficiency of the simulations, \*VARIABLE MASS SCALING is applied to the elements undergoing severe deformations due to the accumulation of damage. Since these are only a few in the whole model, the mass balance is only marginally changed without noticeable influence in the response of the global model.

### Contact and Friction

The contact between the impactor and the laminate specimen is simulated by the **general contact algorithm** of ABAQUS/Explicit which uses a penalty enforcement contact method without softening<sup>62</sup>. As the cohesive elements fail and are subsequently removed from the mesh, interpenetration between the newly generated free surfaces must be prevented. ABAQUS/Explicit allows the modelling of contact between eroding bodies by defining new contact constraints on surfaces generated due to element removal. The eventual contact between delaminated plies, and also between the specimen and supports, follow the same formulation as the impactor-laminate contact.

Friction is introduced between all the contacting surfaces. The Coulomb friction model is used according to which there is no tangential motion between two surfaces until the shear component of the surface traction reaches a critical value,  $\tau_{cr}$ , which depends on the normal contact pressure,  $P$ , and a friction coefficient,  $\mu$ , according to the relation:

$$\tau_{cr} = \mu P \quad (7.18)$$

The friction coefficient between surfaces depends on the materials in contact and on the surface quality. Several authors have studied the subject of friction between metals and composite laminates and between delaminated surfaces<sup>134–136</sup>. In the last case, the friction coefficient is a function of the interface angle. For  $0^\circ/0^\circ$  interfaces it can be as low as 0.2 whilst for  $90^\circ/90^\circ$  interfaces it can be as high as 0.8. In this work, an average friction coefficient of 0.5 is applied between ply surfaces independently of the interface angle. For metal-laminate contact (impactor-laminate and laminate-supports) a value of  $\mu=0.3$  is used.

### Damping

Damping is introduced in the model by means of `*BULK VISCOSITY` which introduces damping associated with volumetric straining<sup>62</sup>. This form of damping typically has numerical effects only, i.e. is not considered part of the material constitutive response. Its purpose is to damp high frequency oscillations and prevent elements from collapsing under high-speed stress waves.

High frequency oscillations are observed to have a destabilising effect on the behaviour of the cohesive elements, causing them to damage prematurely. A damping factor corresponding to 6% of the critical damping is used in the current work. The collapsing of heavily damaged elements is a serious issue that severely decreases the stable time increment of the simulations. The `*BULK VISCOSITY` formulation smears a stress wave over several elements preventing the element from collapsing.

### 7.3.2 Numerical Results and Correlation with Experiments

Herein, the most relevant results from the FE impact simulations are presented. History variables such as impactor force, displacement and transferred energy, corresponding to different impact energies, are compared with experimental data. The correlations between experiments and simulations with respect to delamination size and intraply damage are also presented for the three laminate configurations defined in the previous chapter, which are:

$$[\pm 45/90/0/45/0_4/-45/0_2]_s \text{ (Baseline),}$$

$$[\pm 45/0/70/-70/0/15/10/-10/-15/15/-15]_s \text{ (NCL1) and}$$

$$[\pm 45/80/5/20/-20/10/-80/-10/-5/15/-15]_s \text{ (NCL2).}$$

As an example, Figure 7.3 depicts a 29.7J simulated impact on the baseline laminate. This half-specimen plot shows matrix cracking and major delaminations occurring at 2ms after the contact between the impactor and the specimen.

### Impact Dynamics

The experimental and simulated impactor reaction force histories, corresponding to impacts of 4.7J, 9.1J, 19.6J and 29.7J on specimens with the baseline configuration, are plotted in Figure 7.4. The oscillatory behaviour due to the dynamic coupling between the specimen and its support, observed in the experimental tests, is not correctly replicated by the numerical simulations. However, the





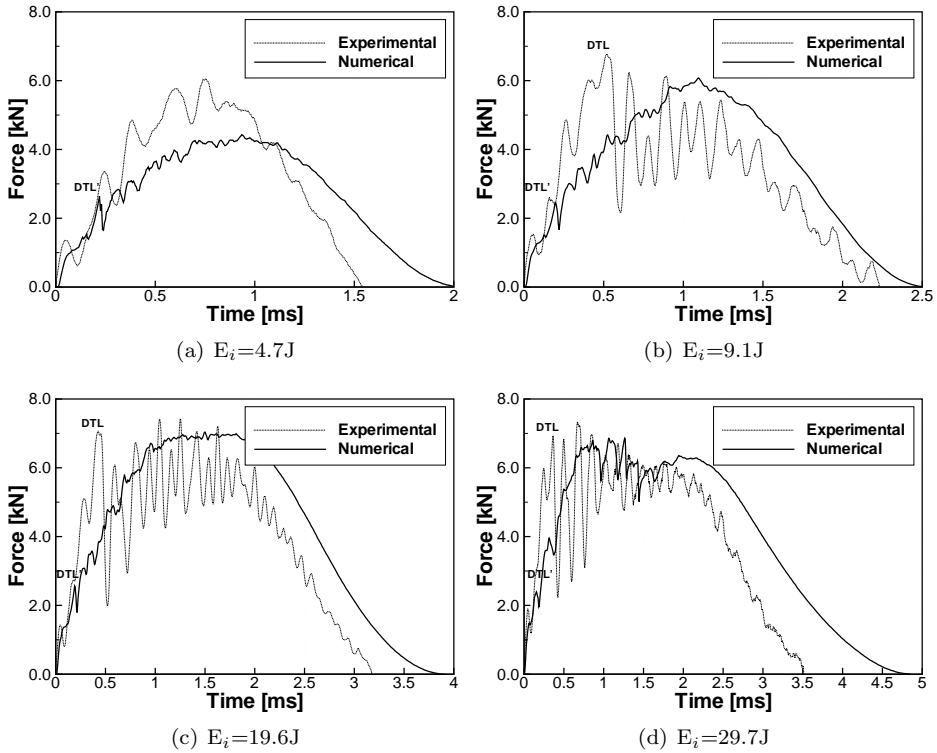


Figure 7.4: Experimental and numerically simulated impactor reaction force histories for four impacts on the baseline configuration specimens. Points DTL and DTL' correspond, respectively, to the measured and predicted delamination threshold loads.

### Delaminations

The predicted delaminations at each ply interface are identified by the cohesive elements deleted from the original mesh. The edges of the remaining mesh can be compared with the experimental data obtained using the Fluorescent Penetrant Inspection (FPI) technique. As examples, the measured and simulated major delaminations on the baseline configuration and non-conventional laminate specimens loaded with similar impacts energies (around 30J), are compared in Figure 7.6. The expected delamination peanut shapes resulting from LVI events on composite laminates are predicted at some interfaces, although due to the limitations on the level of accuracy that can be obtained by the FPI technique, these shapes were not exactly captured experimentally.

Regarding the baseline design, except for the interfaces 10/11 ( $0^\circ/-45^\circ$ ) and 21/22 ( $0^\circ/90^\circ$ ), all major delaminations are well predicted, including their ori-

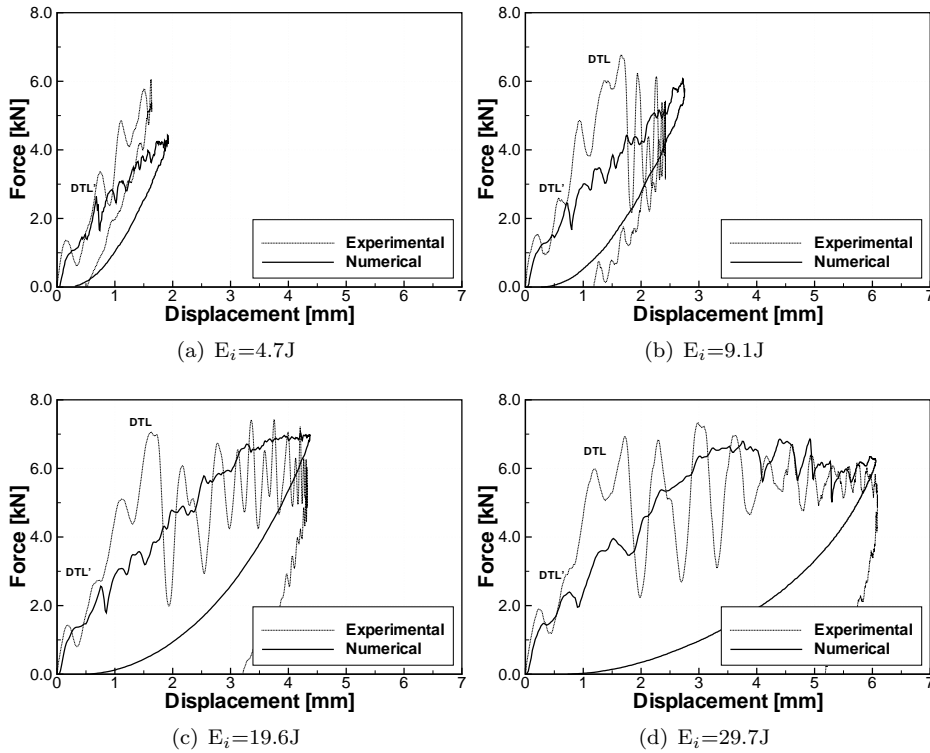


Figure 7.5: Experimental and numerically simulated impactor reaction force versus displacement for four impacts on the baseline configuration specimens. Points DTL and DTL' correspond, respectively, to the measured and predicted delamination threshold loads.

entation. The number of relatively wide delaminations is smaller on the non-conventional laminates, as reported in the previous chapter. Inspection of the NCL1 specimen impacted at 29.5J reveals two major delaminations at interfaces 19/20 ( $0^\circ/-70^\circ$ ) and 20/21 ( $-70^\circ/70^\circ$ ). The shapes of these are not well predicted by the simulations, although their relative size, as compared to other delaminations, is. The same applies to the NCL2 specimen impacted at 29.4J, for which the wider delaminations are at interfaces 16/17 ( $-10^\circ/-80^\circ$ ) and 20/21 ( $20^\circ/5^\circ$ ).

The predicted impact footprint results from the superimposition of all delaminations, since the other damage modes are concentrated on a narrower area. This information is compared with the actual impact footprint obtained experimentally by means of the ultrasonic C-scan technique in Figure 7.7. The simulated projected damaged area (impact footprint) on each configuration agrees well with the experiments for impact energies of 10J and 20J, but it tends to be slightly

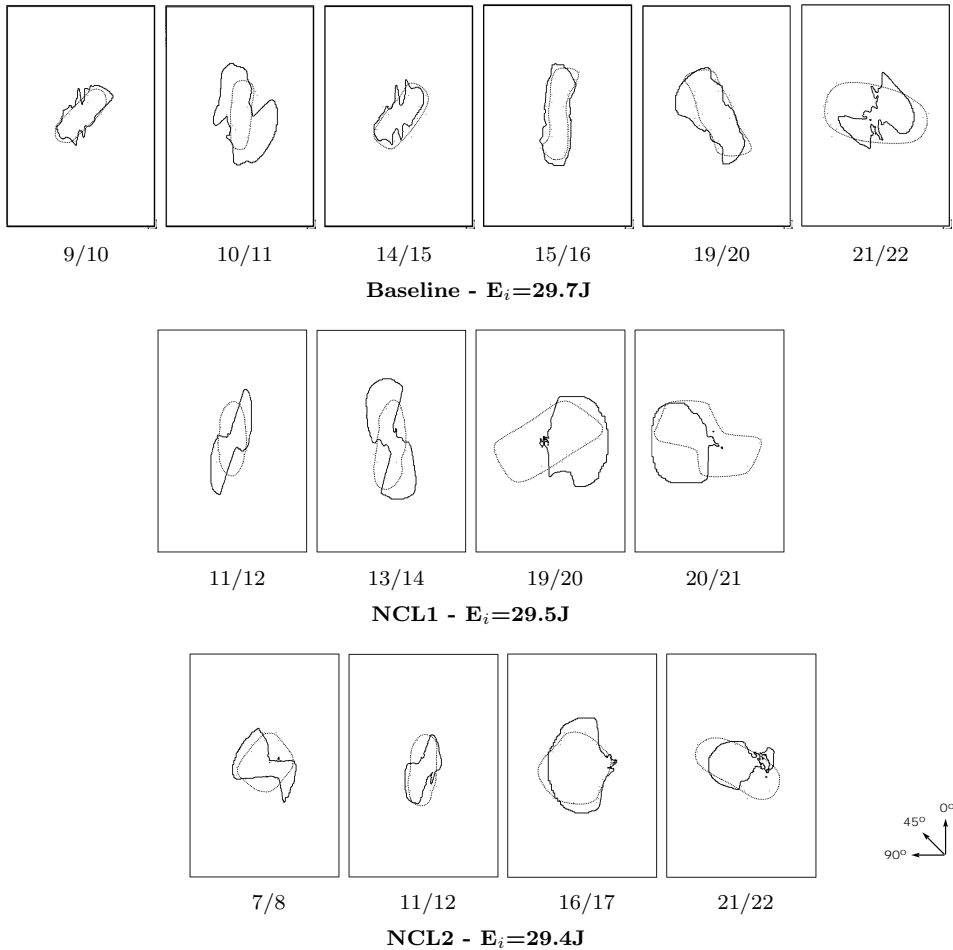


Figure 7.6: Major delaminations, by interface, on the baseline configuration and non-conventional laminates subjected to similar impact energies. Numerical simulation results (solid lines) are compared with experimental data (dotted lines) obtained with the FPI technique. Each delamination is identified by the adjacent ply numbers.

over-predicted for the 30J impact level.

Either separately or together, three factors may be contributing for the mismatch in the results corresponding to 30J impacts. The first one is related to the accuracy of the inspection technique. As reported in the previous chapter, the FPI technique revealed wider delaminations than detected by the ultrasonic C-scan method, specially for the NCL2. The second possible cause is the mesh refinement level, which may be insufficient to predict the delamination front accurately enough at such distances from the impact location where the mesh is

more refined. The third factor is related to the main damage mode. Somewhere between 20J and 30J on the impact energy scale, fibre breakage takes over delamination as the main damage mode. This conclusion is supported by the analysis on the visible damage after impact and the C-scan results, which show a much smaller increase in impact footprint from the 20J to 30J impact level than from the 10J to the 20J. The accuracy of the simulations might decrease when trying to predict the energy dissipated by fibre breakage since not all the loading and failure modes are taken into account by the constitutive damage model. While only fibre tension, compression, and in-plane shear are simulated by the model, under an impact load, the plies are locally subjected to out-of-plane transverse loading and may fail by matrix/fibre crushing as well.

The ultrasonic C-scan inspection captures the back face splitting and fibre peeling protruding  $45^\circ$  from the delaminated region. This failure modes are not captured by the numerical simulations.

The impact energy level of 5J is not addressed in Figure 7.7. For impacts at such a low energy levels, the C-scan inspection does not reveal damage in the form of delamination. However, the numerical models simulate the occurrence of delaminations, though small in size, for 5J impacts. This is inline with the severe underprediction of the DTL value. One of reasons for this mismatch might be related with the inability of the damage model to predict transverse compressive and shear plasticity. At low energy impacts most of the dissipation might actually occur in the form of matrix plasticity, to form a permanent indentation, instead of in the form of delamination. Another reason might be the effect of transverse normal stress on  $\mathcal{G}_{IIc}$ <sup>136;137</sup>, which is neglected in the cohesive model used in this work. However, the strongest reason might be the natural difficulty of cohesive elements in accurately predicting delamination initiation loads without making use of very fine meshes. Furthermore, an accurate description of the interlaminar stresses in the laminate would improve the accuracy of the simulations. Typically, this would also require finer FE meshes than used in the current models, specially along the through-the-thickness direction of the laminate.

### Matrix Cracking and Fibre Breakage

Matrix cracking appears to be the first damage phenomenon occurring on composite laminates undergoing impact loads, specially around the impact point<sup>102-104</sup>. Above an impact energy threshold, which for the present configuration is somewhat between 5J and 10J, matrix cracks propagate along with delaminations. Above a higher energy level, fibre breakage also plays a role in the damage pro-

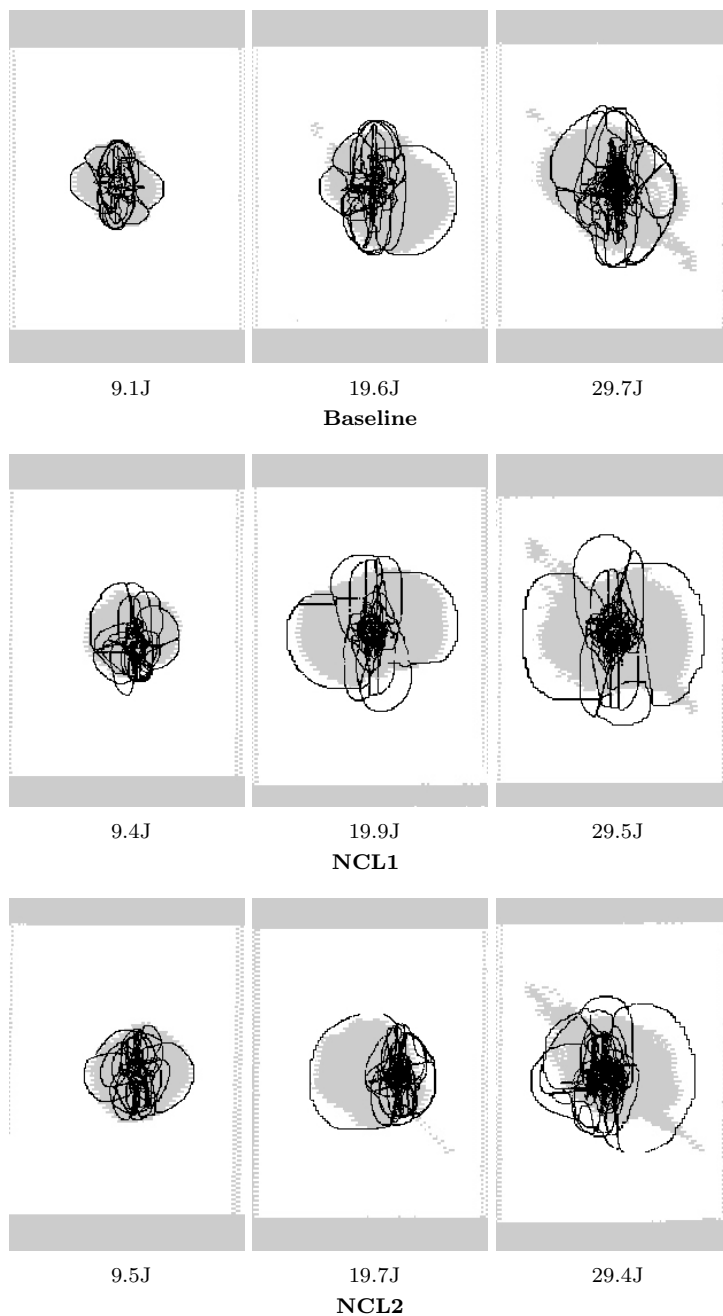


Figure 7.7: Simulated impact footprints (dark lines), for three impact energies per configuration, as compared with C-Scan data (filled grey).

cess. These three damage modes are represented in Figure 7.8, obtained by X-ray tomography on a baseline configuration specimen impacted at 19.6J. The picture shows a planar section cut of the impacted specimen at about a depth of 3.6mm from the impact face. Due to the specimen permanent indentation, plies 20 ( $45^\circ$ ) and 21 ( $0^\circ$ ) are visible on the same picture. Matrix cracking and fibre breakage can be identified on these plies as well as delamination (dark areas).

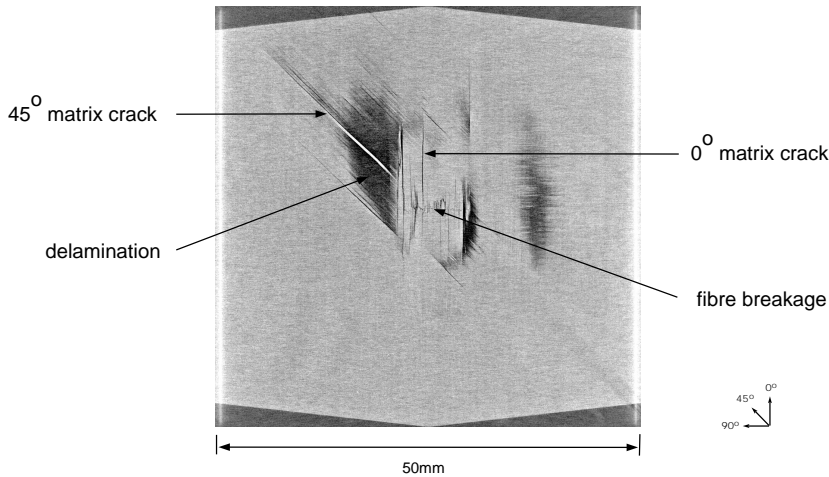


Figure 7.8: X-ray tomography picture of the baseline specimen impacted at 19.6J. The picture shows a planar section cut of the impacted specimen at a depth of 3.6mm from the impact face. Plies 20 ( $0^\circ$ ) and 21 ( $45^\circ$ ) are visible.

The numerical simulations of matrix and fibre failure on some of the plies of the baseline laminate specimen impacted at 29.7J are shown in Figure 7.9, as examples. Matrix cracking is accurately predicted at orientation parallel to the  $0^\circ$  (e.g. clustered plies 6-7-8-9),  $90^\circ$  (e.g. ply 22) and  $\pm 45^\circ$  (e.g. plies 5 and 10) fibre directions. The crack directionality is well simulated for  $0^\circ$  and  $90^\circ$  plies as the mesh conforms to these directions. The accuracy is lower for plies oriented differently. Two single matrix cracks, oriented nearly at  $-45^\circ$ , are predicted in ply 10. These are formed as a result of a 'delamination jump' from interface 9/10 to 10/11, as can be concluded with the help of Figure 7.6. The transverse damage is accompanied by longitudinal damage due to fibre shearing. The same effect is visible on ply 20. On the plies close to the impact face (e.g. 1 and 4), fibre damage is, as expected, concentrated around the impact zone.

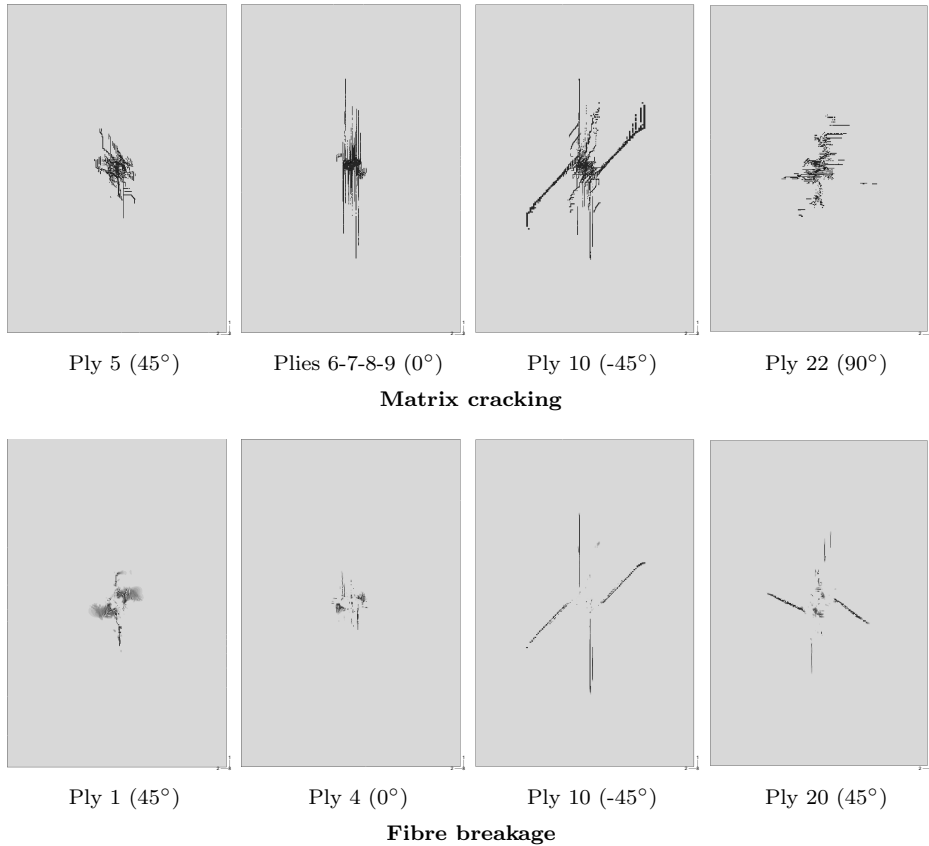


Figure 7.9: Simulation of matrix cracking and fibre breakage on a baseline laminate specimen impacted at 29.7J.

### Energy Dissipation

During an impact with rebound, such as the ones experienced in this work, the impact energy is totally transferred to the laminate. Part of it is accumulated in the form of elastic energy and another part is dissipated in the form of material damage (crushing, delamination, matrix cracking and fibre breakage) and friction. Most of the stored elastic energy is recovered and transferred back to the impactor as it bounces away from the laminate. A smaller part is converted in vibrations which are damped within a larger time scale. According to the numerical predictions, the energy converted in plate vibrations is negligible as compared with the other forms of energy.

The comparison between the measured and predicted energy balance is plotted in Figure 7.10 for specimens with the baseline configuration impacted at 4.7J, 9.1J,

19.6J and 29.7J. The computed energy is the sum of the laminate elastic energy and dissipated energy in the form of delamination, intraply damage and friction, which are also independently shown in the graphs. The values are normalised by the corresponding total impact energy. In general, the energy balance is well simulated and the instant of maximum displacement, corresponding to the peak of the total transferred energy curve, is well predicted, except for the 4.7J impact. In this case, the simulations inaccurately predict some energy dissipation by means of delamination. As a result, the energy restitution coefficient, i.e. the ratio between the energy restituted to the impactor as it bounces back and the total impact energy, is over-predicted by a fraction corresponding to the erroneously simulated delamination energy dissipation. For the 29.7J impact case, a small amount of extra energy (about 7% of the impact energy) is added to the system. This is assumed to be caused by an exaggerated amount of viscous dissipation in the model.

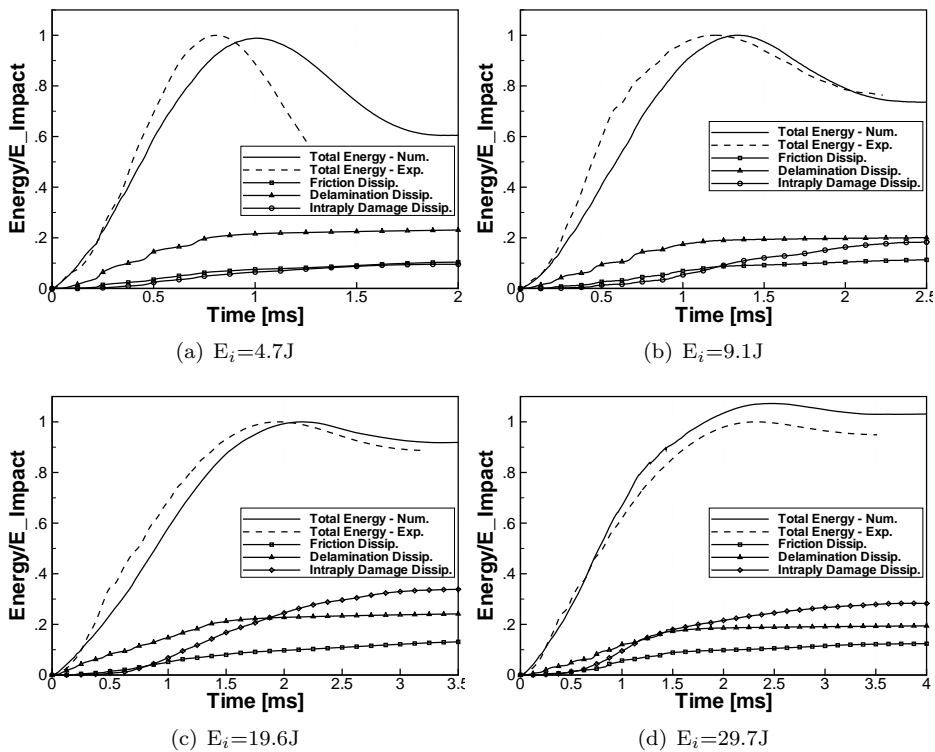


Figure 7.10: Experimental and numerically simulated energy histories for four impacts on baseline configuration specimens. The values are normalised by the corresponding impact energy.



From very low-impact energy levels, delamination dominates over the other dissipation modes until it is surpassed by intraply damage dissipation, but only at relatively high impact energies (e.g. 29.7J). The energy dissipation in the form of delaminations seems to grow proportionably to the impact energy, maintaining a ratio of 20%. The analyses show that although delaminations do not grow after the maximum impactor penetration instant, matrix cracking and fibre breakage do.

The values of the total energy dissipated independently by delamination, intraply damage and friction, for baseline and non-conventional laminate specimens impacted at energies in the 9-30J range, are shown in graphical form in Figure 7.11. Both the delamination and friction dissipated energies show linearly increasing values with impact energy. The energy dissipated by means of intraply damage modes grows faster with impact energy than the other damage dissipation modes, however the trend is difficult to categorise with the available data. The plots confirm that delamination is the primary damage mode up to impact energies of about 20J, after which it is surpassed by matrix and fibre failure. Friction is the mode of lowest energy dissipation. However, this term, representing about 15% of the total impact energy, is far from being negligible.

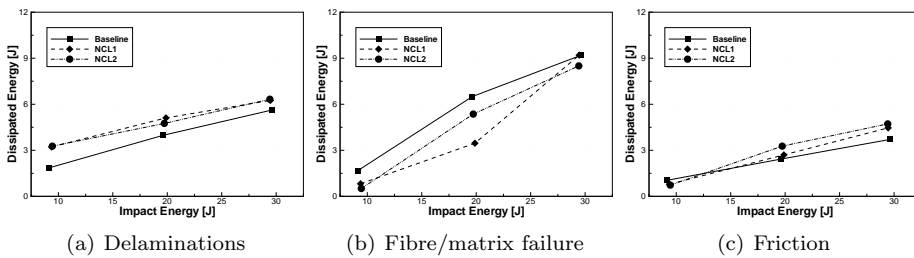


Figure 7.11: Total energy dissipated through several modes for the three investigated configurations and impacts in the 9-30J range.

The simulations show that, in the 9-30J impact energy range, the energy dissipated by means of delaminations is always higher for the non-conventional laminates than for the baseline specimens, which have less ply interfaces. This is balanced by a higher dissipation by in the form of matrix cracking and fibre breakage, although the difference between the various configurations is only clear up to impact energies around 20J.

## 7.4 Additional Non-Conventional Laminates

As concluded in Chapter 6, the simple strategy of dispersing a traditional laminate stacking sequence while maintaining its in-plane and bending stiffness does not automatically lead to configurations with higher performance in terms of impact damage. It was reasoned, on one side, that the high differences in ply orientations allowed between adjacent layers in the non-conventional laminates cause high interlaminar shear stresses which may easily trigger delaminations. On the other side differences between orientations of adjacent layers as small as  $5^\circ$  are probably not enough to promote a significant fibre bridging effect or trigger any delamination, i.e. in practice such plies behave as if they are clustered at the same fibre angle.

The stacking sequence dispersion algorithm described in Appendix A was modified to accommodate extra constraints regarding the minimum and the maximum allowed dispersion between adjacent plies. Three new additional non-conventional laminates were generated based on the baseline configuration considered so far:

$$\text{NCL3: } [\pm 45/75/10/15/ - 10/ - 75/ - 15/10/ - 10/15/ - 15]_s$$

$$\text{NCL4: } [\pm 45/0/70/ - 70/5/ - 5/50/0/10/ - 10/ - 20]_s$$

$$\text{NCL5: } [\pm 45/70/5/0/ - 70/0/15/ - 15/15/ - 5/ - 15]_s$$

In all these cases the target minimum ply orientation dispersion is  $15^\circ$ . The target maximum ply orientation dispersion varied from configuration to configuration, being  $45^\circ$  for NCL3,  $60^\circ$  for NCL4 and  $75^\circ$  for NCL5. The constraints on minimum and maximum fibre orientation dispersion between adjacent layers are merely target rules. They were allowed to be violated, if necessary, to maintain the stiffness properties of the baseline configuration on the newly generated non-conventional laminates, i.e., the priority of the stacking sequence dispersion algorithm was the matching of the lamination parameters of the baseline and non-conventional laminate, as in Chapter 6. In practice, violations of the target constraints occur on all the three newly generated configurations even though the stiffness requisite was somewhat relaxed.

LVI events on the additional non-conventional laminates were simulated by the methods described previously. Experimental tests were not carried out. The response of the specimens impacted at an energy of 19.6J was predicted by means of numerical simulations. The impact footprints are compared, in Figure 7.12, to the results obtained by means of ultrasonic C-scan inspection on the respective baseline laminate specimen.

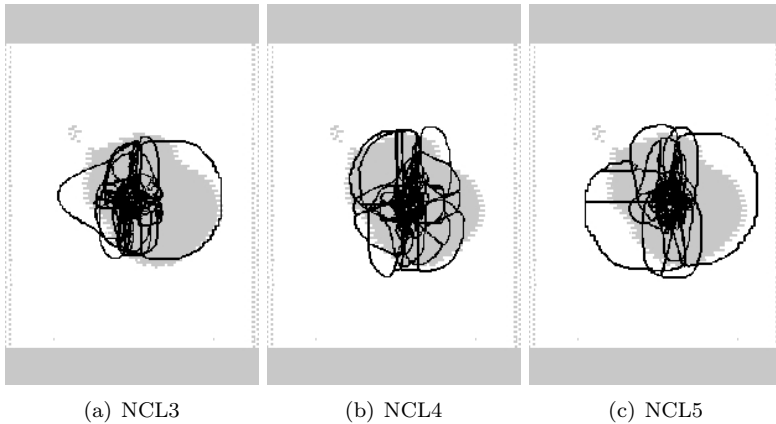


Figure 7.12: Comparison between numerically predicted impact footprints (dark lines) and C-Scan results (filled grey), for the three additional non-conventional laminates ( $E_i = 19.6J$ ).

The predicted impact footprints shown in Figure 7.12 are wider than measured for the baseline configuration, except for the NCL4, though care should be taken when comparing the results of both methods because the ultrasonic C-scan inspection can, in general, only approximate the full extent of the delaminations, as explained see Chapter 6. A closer look at the numerical results allows the identification of two wide delaminations at the interfaces 17/18 ( $-15^\circ/-75^\circ$ ) and 21/22 ( $10^\circ/75^\circ$ ) of the NCL3. In the NCL5, a single wide delamination is predicted at interface 17/18 ( $0^\circ/15^\circ$ ). The NCL4 shows relatively narrower delaminations spread over interfaces 16/17 ( $0^\circ/50^\circ$ ), 19/20 ( $5^\circ/-70^\circ$ ) and 20/21 ( $-70^\circ/70^\circ$ ). The widest delaminations measured on impacted baseline laminate specimens are at interfaces 21/22 ( $0^\circ/90^\circ$ ) and 19/20 ( $0^\circ/45^\circ$ ). The extension of delaminations on the NCL3 and NCL5 and the fact that they occur deeper in the laminate, dividing the respective specimens in thinner sublaminates with overall less resistance to buckling, favours the conclusion that these non-conventional laminates should have a lower CAI strength than specimens of the baseline laminate. For the NCL4 the case might be different since delaminations on these specimens are in general smaller than in the baseline configuration. Furthermore, from the three major delaminations on NCL4, two of them are located at through-the-thickness locations similar to the baseline configuration.

Although the last statements are merely conjecture, since the residual strength of the additional non-conventional laminates was not evaluated either by experimental testing or numerical simulations, it becomes clear that the modifications introduced in the stacking sequence dispersion method do not necessarily lead to

the design of laminates with improved damage tolerance. Furthermore, the results from the most recent simulations reinforce the idea that the baseline laminate is already a design difficult to improve in terms of impact damage resistance and tolerance. The reason for this might be that, up to a certain level, ply clustering might have beneficial effects after all. It can prevent delaminations for occurring in deep through-the-thickness regions of an impacted laminate specimen where their effect on the reduction on the CAI strength is the highest. By forcing wide delaminations to occur at interfaces close to the back face of an impacted specimen, a relatively thick (relatively resistant to buckling) sublaminates results. Also, the lower in-situ transverse and shear strengths of clustered plies, and their smaller resistance to crack opening due to a weaker fibre-bridging effect, lead to an overall higher energy dissipation by intraply damage modes such as matrix cracking at the expense of energy dissipation by means of delamination, as shown in Figure 7.11. Matrix cracks are preferred to delamination because it generally has a lower effect on the reduction of the CAI strength.

## 7.5 Conclusions

The work reported in this chapter shows that it is possible to simulate transient LVI events on composite laminates by means of the explicit FE method together with physically based constitutive models which take into account the progressive failure behaviour of fibres, matrix and interfaces between plies. The simulations are computationally expensive because of the large number of elements required and their small characteristic length, especially at interfaces, which is associated with short stable time increments. However, the effort is rewarded with promising predictions of the impact duration, maximum impact force, maximum displacement, transferred energy, impact footprint, location and size of delaminations, as well as of matrix cracking and fibre breakage. Additionally, predictions of the energy dissipated in the form of delamination, intraply damage and friction become possible.

The model was tested against the LVI experiments on three 24-ply laminate specimens with similar stiffness properties. One of those laminates was composed exclusively of traditionally  $0^\circ$ ,  $90^\circ$  and  $\pm 45^\circ$  oriented layers and exhibit ply clustering. On the other two laminates, the fibre angles are dispersed and ply clustering is avoided. The simulations are reliable under these conditions, for impact energies in the range of 10-30J, although the level of accuracy seems to decrease with the number of interfaces. The simulations underpredict the DTL which has a major influence in the overall specimen response to very low-energy

impacts. In order to overcome this difficulty, future improvements of the damage model should address the nonlinear transverse compressive and shear response of composites to allow for the simulation of permanent indentations. Also, the effect of transverse normal stress on the cohesive fracture toughness  $\mathcal{G}_{IIc}$ <sup>136;137</sup> should be accounted for.

Under high-energy impacts, laminate specimens suffer extensively from failure mechanisms such as matrix and fibre crushing, which the present model does not predict. Actually, although the impact model is based on a three-dimensional stress formulation the damage model only accounts for the in-plane failure modes and the influence of the stress components  $\sigma_{11}$ ,  $\sigma_{22}$  and  $\sigma_{12}$  in the determination of the failure criteria. For a better representation of the damage mechanism occurring under impact loads (e.g. matrix crushing) the stress components  $\sigma_{33}$ ,  $\sigma_{13}$  and  $\sigma_{23}$  should be accounted for the determination of the failure indexes, as well as material characterisation data achieved by means of testing.

The experiments performed revealed some local dynamic effects (e.g. on delaminations), although globally the LVI events can be considered quasi-static. Under these conditions some damage mechanisms, such as transverse compressive and shear cracking, might be influenced by the applied strain rate. Therefore strain rate effects should be characterised and included in the damage model, specially for high impact energies.

Furthermore, it is known that the in-situ strengths<sup>138;139</sup>, the fracture toughness component  $\mathcal{G}_{IIc}$ <sup>140</sup> and the friction coefficient<sup>134;135</sup> are functions of the fibre angle difference between adjacent plies. In the numerical strategy used in this work, (average) constant values were used. However, the accuracy of the simulations can certainly benefit from the implementation of such variations.

The simulations add valuable data to the comparison between the traditionally designed baseline configuration and non-conventional laminates preformed in the previous chapter. The baseline laminate dissipates less energy by means of delaminations than the non-conventional laminates. This is balanced by a higher energy dissipation by intraply damage modes. This favours the traditionally designed configuration since matrix cracking and fibre breakage are less detrimental to the CAI response of the specimens than delamination.

Three additional non-conventional laminates were generated after updating the stacking sequence dispersion algorithm with target constraints on the minimum and maximum ply dispersion. However, the impact simulations on those configurations did not produce promising results. In general, significant sized delaminations on non-conventional laminates are either wider or occur deeper through-the-thickness of the laminate specimens. These two factors contribute to

the reduction of the compressive residual strength of the specimens, as observed experimentally. The CAI tests were not simulated numerically because this would require the use of even finer (and intractable) FE meshes.

Contrary to what was expected, the results from the experimental and numerical studies on non-conventional laminates lead to the conclusion that ply clustering might, in fact, have a beneficial effect on the CAI response of laminates by preventing major delaminations from occurring at inner laminate interfaces and promoting damage dissipation by intraply damage modes rather than delaminations. Hence, the stacking sequence dispersion strategy might produce better results if applied to traditional designs without ply clustering or configurations where ply clustering has a lower significance.

# Chapter 8

## Conclusion

### 8.1 Lessons Learned

**T**HIS thesis covers the structural analysis of non-conventional composite laminate designs of two types: (i) Variable-Stiffness Panels (VSP) in which the orientation of the fibres varies continuously along the in-plane directions of each ply and (ii) straight-fibre laminates with stacking sequences dispersed over the whole  $0 - 90^\circ$  range rather than being restricted to combinations of conventional  $0^\circ$ ,  $90^\circ$  and  $\pm 45^\circ$  fibre orientations. Although they are related in the sense that VSP have a dispersed stacking sequence at any planar location, this characteristic was uncoupled from the fibre-steering, and its particular effect on the damage response of laminates subjected to out-of-plane loads was studied.

In general lines, this thesis demonstrates that it is possible to achieve highly tailored composite structures with higher specific stiffness and strength than the ones designed and produced nowadays. This represents a remarkable step in the development of lighter applications and a more efficient energy usage. Such performance is achieved by in-plane fibre steering, allowed by modern Advanced Fibre Placement (AFP) technology, rather than by a simple stacking sequence rearrangement of straight-fibre plies. A set of more detailed conclusions of this work are presented in the following paragraphs.

#### 8.1.1 Variable-Stiffness Laminates

The in-plane stiffness variation allowed by the variable-stiffness concept revealed a great capacity for load redistribution from the central sections of the panels to their supported edge sections, allowing for more than doubling the buckling

loads as compared to the most efficient straight-fibre designs. The higher the freedom to steer, i.e. the smaller the radius of curvature of the fibres, the higher is the potential for increase in the structural performance. In part, the benefits in terms of buckling are due to the favourable residual thermal stresses installed in curvilinear fibre laminates due to the panel curing cycle, which amplify the effect of load redistribution. The difference in terms of strength performance is also remarkable, specially between straight and curvilinear-fibre panels optimised for the best buckling response. The difference is significantly less remarkable between panels designed for strength.

In the configuration with the highest critical loads, the fibre angles vary linearly, along a direction perpendicular to the vector of the applied loading, from an angle of  $0^\circ$  to an orientation of  $75^\circ$ , which is closely aligned with the loading. This is very similar to the best performing variable-stiffness design in terms of failure. With respect to the postbuckling strength, panels with such fibre angle distributions benefit from higher critical loads and a favourable alignment of the fibres at the edge sections where most of the load is transferred to.

Besides the individual achievements in terms of buckling and postbuckling strength, the relation between both types of responses highly benefits the variable-stiffness concept. With straight fibres, a  $\pm 45^\circ$  arrangement leads to the optimal buckling performance but, for optimal failure performance, fibres closely aligned with the loading are required. This means that a VSP can be designed simultaneously for the optimal buckling and strength responses while a conventional laminate can not.

Because of the capacity for load transfer from the central sections to the edges, it is possible to design VSP that do not develop stress concentrations around central notches and can actually be insensitive to them in terms of buckling and failure. This is a remarkable achievement and a great promise regarding weight savings in comparison to conventional solutions where the thickness is typically increased to overcome stress concentrations around cutouts. Such procedure may actually attract more loads eventually leading to even thicker (and heavier) laminate requirements.

The manufacturability of fibre-steered laminates imposes some design constraints that limit their advantages in terms of failure performance, specifically the fibre angle mismatches at the course edges, due to the finite width of the AFP machine head passes, create zones of elevated stresses. These can be mitigated by using narrower tow courses, ply staggering or hybridisation, i.e. mixing straight and curvilinear fibre plies in the same laminate.

The tow-overlap method shows the most promising failure results for small



fibre angle variations within a ply. For large variations, the thickness (and mass) that builds up outweighs its structural benefits. That is, the specific strength of VSP with overlapping tows decreases with fibre orientation variation, for relatively large values of that variation. In the future, a study should be conducted to find its optimum value. The reason for this evolution in specific strength is the laminate eccentricity caused by single-sided thickness build-ups which promote premature panel buckling. The postbuckling bending induced stresses lead to the premature panel failure. Hence, for large fibre orientation variations, the tow-drop method is the most promising.

The resin-rich spots caused by the individual cutting of tows have a detrimental effect on the failure performance of variable stiffness panels built by such method. The wider the fibre tows, the stronger this effect is. However, the predicted strength reduction, for panels using standard tow widths (3.125mm wide), is limited to single digit percentages when compared with ideally manufactured panels, i.e. without fibre-free areas. Future research should focus on the experimental validation of these findings.

The numerical modelling strategies developed in this work seem adequate for the simulation of the structural behaviour of fibre-steered laminates under static in-plane loads, with remarkable accuracy in terms of buckling and postbuckling final failure loads. The continuum damage model, for the simulation of the onset and propagation of material damage in straight-fibre laminates subjected to in-plane loading, allows the prediction of the postbuckling structural failure of composites panels with moderately curved fibres within a few percent difference from experimental results. Admittedly, such accurate results are possible because the curvature of the fibres does not seem to significantly influence the damage behaviour and the out-of-plane transverse shear stresses, that develop in buckled structures, do not seem to play a dominant role in the formation and propagation of matrix cracking and fibre breakage failure modes.

### 8.1.2 Laminates with Dispersed Stacking Sequences

A new stacking sequence design method is proposed in the study presented in this chapter. This method is inspired by the non-conventional laminates that are generated due to spatially varying fibre orientations in VSP and the flexibility offered by the AFP technology in terms of permitted fibre angles.

The effects of the dispersion of fibre orientations on the Low-Velocity Impact (LVI) damage response of composite laminates were investigated by means of experimental testing and numerical simulations. The non-conventional laminates

achieved by this method were compared to traditional configurations with fibre orientations restricted to  $0^\circ$ ,  $90^\circ$  and  $\pm 45^\circ$ , and plies clustered at the same fibre angles. Both conventional and non-conventional laminates had similar stiffness characteristics, hence the dispersion of the stacking sequence was completely isolated from other variables influencing the laminate impact response. The results indicate that the dispersion of clustered plies does not necessarily lead to an improved impact damage response or damage tolerance. Actually, contrary to what was initially presumed, the research carried out supports the case for ply clustering. This design technique can prevent major delaminations from occurring at laminate inner interfaces, hence avoiding their division in less buckling resistant sublaminates, i.e. with lower compressive residual strength. Furthermore, ply clustering seems to limit damage dissipation in the form of delaminations in favour of intraply damage modes (e.g. matrix cracking) which are less detrimental for the laminate Compression-After-Impact (CAI) strength. The question that remains is: can the dispersion of the stacking sequence improve the impact damage response of composite laminates if ply clustering is left out of the analysis. Future research should focus on this problem.

Independently of the answer to the question above, it is safe to assume that the characteristic stacking sequence dispersion of VSP does not improve their impact damage response in relation to straight-fibre laminates. However, this might be achieved by means of in-plane stiffness variation.

Although not practical as a fast design tool, the numerical simulations of the low velocity impacts exhibit promising results for moderate impact energies (10J to 30J). In such cases, the impact behaviour is generally well simulated and remarkable predictions of the impact footprint and location of delaminations through-the-thickness of the impacted specimens are possible. The possibility of computing the energy expended by means of different dissipative modes adds valuable data to the experimental results. However, the numerical tools still need further development, specifically to allow the simulation of matrix/fibre crushing, nonlinear transverse behaviour, strain rate dependency and fibre orientation effects on in-situ strengths, mode II fracture toughness and friction. This would possibly allow or improve the predictions of the delamination threshold loads, permanent indentations and impactor perforation.

## 8.2 Perspectives and Recommendations

The research work presented in this thesis is open to further developments in several directions of investigation. Experimental work should be carried to confirm

the predicted results for the variable-stiffness panels with central holes as well as to validate the numerical analysis on the influence of tow-drops on panel strength. Variations in tow and course widths should be accounted for in the experimental programme.

Furthermore, the response of VSP to tension and shear loads should be investigated. In this thesis, only compressive loads were addressed. This would certify the variable-stiffness concept in a broader range of applications. Also, the validation of the damage model under different load cases and dominant failure modes would be possible. In the damage and failure analyses performed herein on VSP under in-plane loads, the prediction of the occurrence of ply delaminations was neglected altogether. However, due to the stiffness variation in VSP, large in-plane stress gradients may arise. These may contribute to the amplification of the interlaminar stresses, which are responsible for the initiation of delaminations. Furthermore, it has been observed that VSP develop residual stresses during the curing process and local stress concentrations due to tow-dropping and tow-overlapping which certainly contribute to excite the interlaminar stresses further, potentially rendering delamination the dominant failure mode in these structures. Finally, in the vicinity of free edges of notches and holes, the interlaminar stresses are typically high, and delamination is likely to occur. Hence, future analyses on VSP should take into account the eventual occurrence of delaminations.

One of the most promising characteristics of VSP is their impact behaviour. Although the dispersion of the stacking sequence does not seem to produce an effective improvement of the LVI damage behaviour of laminates, there are strong indications that this can be achieved with an in-plane stiffness variation. Specifically, the insensitivity to central cutouts of some fibre-steered designs indicates that these are certainly more tolerant to damage caused by impact than straight-fibre configuration. Questions remain about their impact damage resistance. These should be answered by conducting an experimental programme. However, such programme is bound to be more complex than the one conducted within the framework of this thesis because the specimens required are much larger. Also, test procedures different from the standard ones need to be developed.

Besides improving the impact damage model by taking into account the suggestions proposed in the conclusions to Chapter 7, and developing a strategy to simulate the CAI tests, it would be interesting to resume the experimental and numerical investigations on the damage resistance and tolerance of non-conventional laminates with dispersed stacking sequences. The research should first focus on the behaviour of conventional laminates with and without clustered plies. Then, their stacking sequences should be dispersed and their impact behaviour anal-

ysed. The stacking sequence dispersion method should be enhanced to account for a more selective process of determining dispersed laminates. The process of selection should be based not only on achieving stiffness characteristics similar to the baseline configuration but also on information about the most effective fibre orientation differences in terms of in-situ strengths, fracture toughness, and friction between delaminated plies.

# Appendix A

## Stacking Sequence Dispersion

### A.1 Introduction

THIS appendix summarises the staking sequence dispersion algorithm<sup>114;115</sup> that was used in the design of the non-conventional laminates presented in Chapters 6 and 7.

### A.2 Dispersion of Ply Orientations

The starting idea about stacking sequence dispersion is to maximise the difference between fibre orientations of two adjacent plies. The ply orientation dispersion,  $\mathcal{D}_i$ , between a pair of successive layers ( $i$  and  $(i + 1)$ ) having fibre angles  $\theta_i$  and  $\theta_{i+1}$ , respectively, is defined by

$$\mathcal{D}_i = \frac{1}{\sin^2(\theta_i - \theta_{i+1}) + \delta} - \frac{1}{1 + \delta}, \quad (\text{A.1})$$

wherein  $\delta$  is a small number used only to make Equation (A.2) stable even when the two successive plies have the same orientation. A value of  $\delta = 0.0001$  is assumed throughout this thesis. From Equation (A.2), it is evident that as the value of  $\mathcal{D}_i$  approaches zero, the fibre orientation angle difference or dispersion between the successive plies approaches  $90^\circ$ .

The dispersion of an  $n$ -ply laminate,  $\mathcal{D}$ , is

$$\mathcal{D} = \sum_{i=1}^{n-1} \mathcal{D}_i. \quad (\text{A.2})$$

### A.3 Dispersion using Genetic Algorithms

The baseline laminate, i.e. the design with traditional  $0^\circ$ ,  $90^\circ$  and  $\pm 45^\circ$  layers is assumed to be known a priori. This baseline laminate may be any existing design optimised for a response characteristic such as buckling or vibration. The idea is to improve the damage resistance and tolerance of the base laminate via stacking sequence dispersion.

The stacking sequences generated are subjected to the following conditions:

- The generated stacking sequences must have the same, or similar, in-plane and flexure stiffness as the base laminate. All the stiffness coefficients are linear combinations of eight lamination parameters. Therefore, the objective is to minimise the difference between the base laminate and the dispersed stacking sequence lamination parameters.
- Both the dispersed stacking sequence and base laminate are symmetric. In the proposed optimisation formulation, only half of the laminate is considered and hence the symmetry requirement is automatically satisfied.
- The dispersed stacking sequence must be balanced. This is imposed via a penalty function approach.
- The external two layers of the baseline and dispersed stacking sequence laminates are fixed to  $\pm 45^\circ$  following standard industrial practice in counteracting eventual shear loads.

A standard Genetic Algorithm (GA) is used to generate dispersed stacking sequences. The design space is discretised into 19 possible ply orientations from  $0^\circ$  to  $90^\circ$  at intervals of  $5^\circ$ . A FORTRAN GA framework developed in an earlier research effort, specifically for composite laminate design, is used in the current work<sup>141</sup>. This framework consists of a GA module, encapsulating GA datastructures, and a package of GA operators like crossover and mutation. The module along with the package of operators constitutes a standard GA. An integer alphabet is used to code the ply genes. The implementation details of the GA modules and GA packages can be found in the work carried by McMahon et al.<sup>141</sup>.

The objective function,  $\mathcal{F}$ , is given by

$$\mathcal{F} = - \left( \sum_{i=1}^{i=8} (W_i - W_i^B)^2 + b \cdot \mathcal{D} \right) p, \quad (\text{A.3})$$

which is to be minimised. In Equation A.3, the  $W_i$ 's refer to the lamination parameters of the candidate designs and the  $W_i^B$ 's to the lamination parameters of the baseline laminate. The parameter  $b$  is a bonus associated with the dispersion of the candidate design. It is imperative to use a small value of  $b$  so that the optimisation process is guided by the error function and not by the dispersion measure of the candidate designs. The variable  $p$  is the penalty due to violation of the balanced laminate condition. A negative sign is added because the GA used maximises the objective function.

The optimisation algorithm developed attempts to keep the in-plane and bending stiffness properties of the baseline laminate selected. Additionally, the algorithm attempts to maximise the global dispersion of the laminate by introducing a bonus factor in the objective function rather than the maximisation of the fibre orientation difference between all adjacent plies. In practice, this results in the modification of the fibre orientation angles of clustered plies.

### A.3.1 Lamination Parameters

Lamination parameters represent the laminate lay-up configuration in a compact form<sup>142</sup>. The in-plane behaviour of composite laminates in the CLT can be fully modelled using only four lamination parameters regardless of the actual number of layers:

$$W_1, W_2, W_3, W_4 = \int_{-1/2}^{1/2} (\cos 2\theta(\bar{z}), \sin 2\theta(\bar{z}), \cos 4\theta(\bar{z}), \sin 4\theta(\bar{z})) d\bar{z} \quad (\text{A.4})$$

in which  $\theta(\bar{z})$  is the distribution of the fibre orientation angle through the normalised thickness  $\bar{z} = z/h_l$  ( $h_l$  is the total laminate thickness). Another four parameter define the bending behaviour:

$$W_5, W_6, W_7, W_8 = 12 \int_{-1/2}^{1/2} \bar{z}^2 (\cos 2\theta(\bar{z}), \sin 2\theta(\bar{z}), \cos 4\theta(\bar{z}), \sin 4\theta(\bar{z})) d\bar{z} \quad (\text{A.5})$$





# List of References

- [1] C. T. Herakovich. *Mechanics of Fibrous Composites*. John Wiley and Sons, Inc., New York, NY, 1997.
- [2] A. Beukers and E. van Hinte. *Lightness: The Inevitable Renaissance of Minimum Energy Structures*. Uitgeverij 010 Publishers, Rotterdam, The Netherlands, 1998.
- [3] M. F. Ashby. *Materials Selection in Mechanical Design*. Pergamon Press, Oxford, UK, 1992.
- [4] A. Beukers and E. van Hinte. *Flying Lightness: Promises for Structural Elegance*. Uitgeverij 010 Publishers, Rotterdam, The Netherlands, 2005.
- [5] Z. Gürdal and R. A. Olmedo. Composite laminates with spatially varying fiber orientations: Variable stiffness panel concept. In *Proceedings of the AIAA/ASME/ASCE/AHS/ASC 33rd Structures, Structural Dynamics and Materials Conference*, volume 2, pages 798–808, Dallas, TX, 1992. AIAA 92-2472.
- [6] Z. Gürdal and R.A. Olmedo. In-plane response of laminates with spatially varying fiber orientations: Variable stiffness concept. *AIAA Journal*, 31(4):751–758, 1993.
- [7] K. C. Wu, Z. Gürdal, and J. H. Starnes Jr. Structural response of compression-loaded, tow-placed, variable stiffness panels. In *Proceedings of the AIAA/ASME/ASCE/AHS/ASC 43rd Structures, Structural Dynamics and Materials Conference*, Denver, CO, April 2002. AIAA 2002-1512.
- [8] D. C. Jegley, B. F. Tatting, and Z. Gürdal. Optimization of elastically tailored tow placed plates with holes. In *Proceedings of the AIAA/ASME/ASCE/AHS/ASC 44th Structures, Structural Dynamics and Materials Conference*, Norfolk, VA, April 2003. AIAA 2003-1420.
- [9] D. C. Jegley, B. F. Tatting, and Z. Gürdal. Tow-steered panels with holes subjected to compression or shear loading. In *Proceedings of the AIAA/ASME/ASCE/AHS/ASC 46th Structures, Structural Dynamics and Materials (SDM) Conference*, Austin, TX, April 2005. AIAA 2005-2017.
- [10] Z. Gürdal, B. F. Tatting, and K. C. Wu. Variable stiffness panels: Effects of stiffness variation on the in-plane and buckling responses. *Composites Part A: applied science and manufacturing*, 39:911–922, 2008.
- [11] S. B. Biggers and S. Srinivasan. Compression buckling response of tailored rectangular composite plates. *AIAA Journal*, 31(3):590–596, March 1993.
- [12] S. B. Biggers and S. S. Pageau. Shear buckling response of tailored rectangular composite plates. *AIAA Journal*, 32(5):1100–1103, 1994.

- [13] M. T. DiNardo and P. A. Lagace. Buckling and postbuckling of laminated composite plates with ply dropoffs. *AIAA Journal*, 27(10):1392–1398, 1989.
- [14] C. Muser and N. J. Hoff. Stress concentrations in cylindrically orthotropic plates with radial variation of the compliances. *Progress in Science and Engineering of Composites*, 1:389–396, 1982.
- [15] S.S. Yau and T. W. Chou. Strength of woven-fabric composites with drilled and molded holes. *ASTM Special Technical Publication*, pages 423–437, 1988. ASTM STP-972.
- [16] C. M. Kuo, H. Takahashi, and T. W. Chou. Effect of fiber waviness on the nonlinear elastic behavior of flexible composites. *Journal of Composite Materials*, 22:1004–1022, November 1988.
- [17] M. W. Hyer and R. F. Charette. Use of curvilinear fiber format in composite structure design. In *Proceedings of the AIAA/ASME/ASCE/AHS/ASC 30th Structures, Structural Dynamics and Materials Conference*, pages 2137–2145, Mobile, AL, April 1989. Also in *AIAA Journal*, 29(6):1011–1015, June 1991.
- [18] S. W. Tsai and E. M. Wu. A general theory of strength for anisotropic materials. *Journal of Composite Materials*, 5(1):58–80, 1971.
- [19] M. W. Hyer and H. H. Lee. The use of curvilinear fiber format to improve buckling resistance of composite plates with central circular holes. *Composite Structures*, 18:239–261, 1991.
- [20] N. V. Banichuk. Optimization problems for elastic anisotropic bodies. *Archives of Mechanics*, 33:347–363, 1981.
- [21] N. V. Banichuk. Optimal orientation of orthotropic materials for plates designed against buckling. *Structural Optimization*, 10:191–196, 1995.
- [22] P. Pedersen. On thickness and orientational design with orthotropic materials. *Structural Optimization*, 3:69–78, 1991.
- [23] P. Pedersen. *Optimal orientation of anisotropic materials, optimal distribution of anisotropic materials, optimal shape design with anisotropic materials, optimal design for a class of non-linear elasticity*, volume 2 of *Optimization of large structural systems*, pages 649–681. Rozvany GIN, 1993.
- [24] G. Duvaut, G. Terrel, F. Léné, and V.E. Verijenko. Optimization of fiber reinforced composites. *Composite Structures*, 48:83–89, 2000.
- [25] P. J. Crothers, K. Drechsler, D. Feltinc, I. Herszberga, and T. Kruckenbergd. Tailored fibre placement to minimise stress concentrations. *Composites Part A: Applied Science and Manufacturing*, 28:619–625, 1997.
- [26] F. Bullock, S. Kowalski, and R. Young. Automated prepreg tow-placement for composite structures. In *35th International SAMPE Symposium*, volume 35, pages 734–743, Anaheim, CA, April 1990.
- [27] M. L. Enders and P. C. Hopkins. Developments in the fiber placement process. In *36th International SAMPE Symposium*, volume 36, pages 778–790, San Diego, CA, April 1991.

- [28] D. O. Evans, M. M. Vaniglia, and P. C. Hopkins. Fiber placement process study. In *34th International SAMPE Symposium*, volume 34, pages 1822–1833, Reno, NV, May 1989.
- [29] J. R. Barth. Fabrication of complex composite structures using advanced fiber placement technology. In *35th International SAMPE Symposium*, volume 35, pages 710–720, Anaheim, CA, April 1990.
- [30] J. P. Martin, R. J. Langone, M. J. Pasanen, and J. A. Mondo. Cost-effective, automated equipment for advanced composite structure development and production. Technical report, Automated Dynamics Corporation, 1997.
- [31] Ingersoll Machine Tools. <http://www.ingersoll.com>.
- [32] M. J. Pasanen, J. P. Martin, R. J. Langone, and J. A. Mondo. Advanced composite fiber placement: Process to application. Technical report, Automated Dynamics Corporation, 1997.
- [33] J. A. Mondo, M. J. Pasanen, R. J. Langone, and J. P. Martin. Advances in automated fiber placement of aircraft structures. Technical report, Automated Dynamics Corporation, 1997.
- [34] D. O. Evans. Fiber placement. Technical report, Cincinnati Machine, 2001.
- [35] R. Measom and K. Sewell. Fiber placement low-cost production for complex composite structures. In *American Helicopter Society 52nd Annual Forum*, Washington, DC, June 1996.
- [36] E. Renner. Best manufacturing practices: Report of survey conducted at northrop grumman corporation. Technical report, Best Manufacturing Practices Center of Excellence, El Segundo, CA, October 1997.
- [37] W. G. Roeseler, B. Sarh, and M. U. Kismarton. Composite structures: The first 100 years. In *Proceedings of the 16th International Conference on Composite Materials*, Kyoto, Japan, July 2007.
- [38] The Boeing Company. <http://www.boeing.com>.
- [39] R. A. Olmedo and Z. Gürdal. Buckling response of laminates with spatially varying fiber orientations. In *Proceedings of the AIAA/ASME/ASCE/AHS/ASC 34rd Structures, Structural Dynamics and Materials Conference*, pages 2261–2269, La Jola, CA, April 1993. AIAA 93-1567.
- [40] M. M. Abdalla, Z. Gürdal, and G. F. Abdelal. Thermo-mechanical response of variable-stiffness composite panels. *Journal of Thermal Stresses*, 32:187–208, 2009.
- [41] S. Nagendra, S. Kodiyalam, J. E. Davis, and V. N. Parthasarathy. Optimization of tow fiber paths for composite design. In *Proceedings of the AIAA/ASME/ASCE/AHS/ASC 36rd Structures, Structural Dynamics and Materials Conference*, pages 1031–1041, New Orleans, LA, April 1995. AIAA 95-1275.
- [42] C. Waldhart, Z. Gürdal, and C. Ribbens. Analysis of tow placed, parallel fiber, variable stiffness laminates. In *Proceedings of the AIAA/ASME/ASCE/AHS/ASC 37rd Structures, Structural Dynamics and Materials Conference*, pages 2210–2220, Salt Lake City, UT, April 1996. AIAA 96-1569.

- [43] C. Waldhart. Analysis of tow-placed, variable-stiffness laminates. Master's thesis, Virginia Polytechnic Institute and State University, Blacksburg, VA, June 1996.
- [44] A. W. Blom, S. Setoodeh, J. M. A. M. Hol, and Z. Gürdal. Design of variable-stiffness conical shells for maximum fundamental eigenfrequency. *Computers & Structures*, 86:870–878, 2008.
- [45] A. W. Blom, B. F. Tatting, J. M. A. M. Hol, and Z. Gürdal. Fiber path definitions for elastically tailored conical shells. *Composites: Part B*, 40:77–84, 2008.
- [46] K. C. Wu and Z. Gürdal. Thermal testing of tow-placed, variable stiffness panels. In *Proceedings of the AIAA/ASME/ASCE/AHS/ASC 42nd Structures, Structural Dynamics and Materials Conference*, Seattle, WA, April 2001. AIAA 2001-1190.
- [47] K. C. Wu. *Thermal and Structural Performance of Tow-Placed, Variable Stiffness Panels*. PhD thesis, Delft University of Technology, The Netherlands, September 2006.
- [48] Z. Gürdal, B. F. Tatting, and K. C. Wu. Tow-placement technology and fabrication issues for laminated composite structures. In *Proceedings of the AIAA/ASME/ASCE/AHS/ASC 46th Structures, Structural Dynamics and Materials Conference*, Austin, TX, April 2005. AIAA 2005-2017.
- [49] B. F. Tatting and Z. Gürdal. Design and manufacture of tow-placed variable stiffness composite laminates with manufacturing considerations. In *Proceedings of the 13th U.S. National Congress of Applied Mechanics (US-NCAM)*, Gainesville, FL, June 1998.
- [50] B. F. Tatting and Z. Gürdal. Analysis and design of tow-steered variable stiffness composite laminates. In *American Helicopter Society Hampton Roads Chapter, Structure Specialists' Meeting*, Williamsburg, VA, October 2001.
- [51] C. C. Rankin, F. A. Brogan, W. A. Loden, and H. D. Cabiness. *STAGS Users Manual*. Lockheed Martin Missiles & Space Co., Inc., Sunnyvale, California, USA, June 2000. Report LMSC P032594.
- [52] B. F. Tatting and Z. Gürdal. Design and manufacture of elastically tailored tow placed plates. Technical report, NASA, Langley Research Center, Hampton, VA, August 2002. NASA/CR-2002-211919.
- [53] B. F. Tatting and Z. Gürdal. Automated finite element analysis of elastically-tailored plates. Technical report, NASA, Langley Research Center, Hampton, VA, December 2003. NASA/CR-2003-212679.
- [54] B. F. Tatting. *Analysis and Design of Variable Stiffness Composite Cylinders*. PhD thesis, Virginia Polytechnic Institute and State University, Blacksburg, VA, October 1998.
- [55] R. E. Rowlands. Strength (failure) theories and their experimental correlation. In G. C. Sih and A. M. Sudra, editors, *Failure Mechanics of Composites*. Elsevier Science Publishers, B.V., 1985.
- [56] P. T. Langley. Finite element modeling of tow-placed variable-stiffness composite laminates. Master's thesis, Virginia Polytechnic Institute and State University, Blacksburg, VA, June 1999.

- [57] K. C. Wu and Z. Gürdal. Variable stiffness panel structural analyses with material nonlinearity and correlation with tests. In *Proceedings of the AIAA/ASME/ASCE/AHS/ASC 47rd Structures, Structural Dynamics and Materials Conference*, Newport, RI, May 2006. AIAA 2006-2165.
- [58] A. Alhajahmad, M. M. Abdalla, and Z. Gürdal. Design tailoring for pressure pillowling using tow-placed steered fibers. *Journal of Aircraft*, 45(2):630–640, 2008.
- [59] A. Alhajahmad, M. M. Abdalla, and Z. Gürdal. Optimal design of tow-placed fuselage panels with cutouts for maximum strength and buckling performance. In *Second International Conference on Multidisciplinary Design Optimization and Applications*, Gijon, Spain, September 2008.
- [60] A. Alhajahmad. *Desing Tailoring of Panels for Pressure Pillowling Using Tow-Placed Steered Fibers*. PhD thesis, Delft University of Technology, The Netherlands, December 2008.
- [61] C. S. Lopes, P. P. Camanho, Z. Gürdal, and B. F. Tatting. Progressive failure analysis of tow-placed, variable-stiffness composite panels. *International Journal of Solids and Structures*, 44:8493–8516, 2007.
- [62] Abaqus, Inc. *Abaqus Version 6.8 User's Manual*. Pawtucket, RI, USA, 2008.
- [63] F. París. A study of failure criteria of fibrous composite materials. Technical report, NASA, Langley Research Center, Hampton, VA, March 2001. NASA/CR-2001-210661.
- [64] Z. Hashin. Failure criteria for unidirectional fibre composites. *Journal of Applied Mechanics*, 47:329234, 1980.
- [65] A. Puck and H. Schürmann. Failure analysis of FRP laminates by means of physically based phenomenological models. *Composites Science and Technology*, 58:1045–1067, 1998.
- [66] C. T. Sun and J. Tao. Prediction of failure envelope and stress/strain behaviour of composite laminates. *Composites Science and Technology*, 58:1125–1136, 1998.
- [67] M. J. Hinton, A. S. Kaddour, and P. H. Soden. A comparison of the predictive capabilities of current failure theories for composite laminates, judged against experimental evidence. *Composites Science and Technology*, 62:1725–1797, 2002.
- [68] C. S. Lopes, Z. Gürdal, and P. P. Camanho. Tow-placed, variable-stiffness composite panels: Damage tolerance improvements over traditional straight-fibre laminates. In *III European Conference on Computational Mechanics: Solids, Structures and Coupled Problems in Engineering*, Lisbon, Portugal, June 2006.
- [69] C. S. Lopes, Z. Gürdal, and P. P. Camanho. Variable-stiffness composite panels: Buckling and first-ply failure improvements over straight-fibre laminates. *Computers & Structures*, 86:897–907, 2008.
- [70] C. G. Dávila, P. P. Camanho, and C. A. Rose. Failure criteria for FRP laminates in plane stress. *Journal of Composite Materials*, 39:323–345, 2005.

- [71] S. T. Pinho, C. G. Dávila, P. P. Camanho, L. Iannucci, and P. Robinson. Failure models and criteria for FRP under in-plane or three-dimensional stress states including shear non-linearity. Technical report, NASA, Langley Research Center, Hampton, VA, February 2005. NASA/TM-2005-213530.
- [72] J. C. Brewer and P.A. Lagace. Quadratic stress criterion for initiation of delamination. *Journal of Composite Materials*, 22:1141–1155, 1988.
- [73] N. J. Pagano and G. A. Schoeppner. Delamination of polymer matrix composites: Problems and assessment. In A. Kelly and C. Zweben, editors, *Comprehensive Composite Materials*, volume 2, pages 433–528. Pergamon, 2000.
- [74] K. J. Saeger, P. A. Lagace, and D. Jin Shim. Interlaminar stresses due to in-plane gradient stress fields. *Journal of Composite Materials*, 36:211–227, 2002.
- [75] N. V. Bhat and P. A. Lagace. An analytical method for the evaluation of interlaminar stresses due to material discontinuities. *Journal of Composite Materials*, 28:190–210, 1994.
- [76] D. J. Shim and P. A. Lagace. Mechanisms and structural parameters affecting the interlaminar stress field in laminates with ply drop-offs. *Journal of Composite Materials*, 40:345–369, 2006.
- [77] P. Maimí, P. P. Camanho, J. A. Mayugo, and C. G. Dávila. A thermodynamically consistent damage model for advanced composites. Technical report, NASA, Langley Research Center, Hampton, VA, March 2006. NASA/TM-2006-214282.
- [78] P. P. Camanho, C. G. Dávila, S.T. Pinho, L. Iannucci, and P. Robinson. Prediction of in situ strengths and matrix cracking in composites under transverse tension and in-plane shear. *Composites Part A: Applied Science and Manufacturing*, 37:165–176, 2006.
- [79] S. T. Pinho, L. Iannucci, and P. Robinson. Physically-based failure models and criteria for laminated fibre-reinforced composites with emphasis on fibre kinking: Part I: Development. *Composites Part A: Applied Science and Manufacturing*, 37:63–73, 2006.
- [80] S. T. Pinho, L. Iannucci, and P. Robinson. Physically-based failure models and criteria for laminated fibre-reinforced composites with emphasis on fibre kinking: Part II: Fe implementation. *Composites Part A: Applied Science and Manufacturing*, 37:766–777, 2006.
- [81] E. Riks, C. C. Rankin, and F. A. Brogan. On the solution of mode jumping phenomena in thin-walled shell structures. *Computer methods in applied mechanics and engineering*, 136:59–92, 1996.
- [82] C. Fagiano, M. Abdalla, C. Kassapoglou, and Z. Gürdal. Domain decomposition and interlaminar stress recovery of multilayer composite structures. In *Proceedings of the AIAA/ASME/ASCE/AHS/ASC 50th Structures, Structural Dynamics and Materials Conference*, Palm Springs, CA, May 2009.
- [83] C. S. Lopes, Z. Gürdal, P. P. Camanho, and B. F. Tatting. Progressive failure analysis of tow-placed, variable-stiffness composite panels. In *Proceedings of the AIAA/ASME/ASCE/AHS/ASC 48th Structures, Structural Dynamics and Materials Conference*, Honolulu, HI, USA, April 2007. AIAA 2007-2010.

- [84] C. S. Lopes, P. P. Camanho, Z. Gürdal, and B. F. Tatting. Progressive damage analysis of tow-steered composite panels in postbuckling. In *16th International Conference On Composite Materials*, Kyoto, Japan, July 2007.
- [85] P. Maimí, P. P. Camanho, J. A. Mayugo, and C. G. Dávila. A continuum damage model for composite laminates - part i: Constitutive model. *Mechanics of Materials*, 39:897–908, 2007.
- [86] P. Maimí, P. P. Camanho, J. A. Mayugo, and C. G. Dávila. A continuum damage model for composite laminates - part ii: Computational implementation and validation. *Mechanics of Materials*, 39:909–919, 2007.
- [87] D. W. Sleight. Progressive failure analysis methodology for laminated composite structures. Technical report, NASA, Langley Research Center, Hampton, VA, March 1999. NASA/TP-1999-209107.
- [88] Z. P. Bažant and M. Jirásek. Nonlocal integral formulations of plasticity and damage: survey of progress. *Journal of Engineering Mechanics*, 128(11):1119–1149, 2002.
- [89] F.P. van der Meer and L. J. Sluys. Interaction between intraply and interply failure in laminates. In P. P. Camanho, C. G. Dávila, S. T. Pinho, and J. J. C. Remmers, editors, *Mechanical Response of Composites*, pages 141–160. Springer, 2008.
- [90] Standard test method for tensile properties of polymer matrix composite materials. Technical report, American Society for Testing and Materials (ASTM), West Conshohocken, PA, USA, 2000. ASTM D 3039/D 3039M-00.
- [91] Standard test method for compressive properties of unidirectional or cross-ply fibre-resin composites. Technical report, American Society for Testing and Materials (ASTM), West Conshohocken, PA, USA, 1987. ASTM D 3410-87.
- [92] Standard test method for in-plane shear response of polymer matrix composite materials by test of a  $\pm 45^\circ$  laminate. Technical report, American Society for Testing and Materials (ASTM), West Conshohocken, PA, USA, 1994. ASTM D3518/3518M-94.
- [93] Standard test methods for mode I interlaminar fracture toughness of unidirectional fibre-reinforced polymer matrix composites. Technical report, American Society for Testing and Materials (ASTM), West Conshohocken, PA, USA, 2001. ASTM D 5528-01.
- [94] S. T. Pinho, P. Robinson, and L. Iannucci. Fracture toughness of the tensile and compressive fibre failure modes in laminated composites. *Composites Science and Technology*, 66(13):2069–2079, 2006.
- [95] R. Martin, T. Elms, and S. Bowron. Characterization of mode II delamination using the 4ENF. In *Proceedings of the 4th European Conference on Composites: Testing and Standardisation*, Lisbon, Portugal, 1998.
- [96] J. R. Reeder. An evaluation of mixed-mode failure criteria. Technical report, NASA, Langley Research Center, Hampton, VA, 1992. NASA/TM-104210.
- [97] P. P. Camanho, P. Maimí, and C. G. Dávila. Prediction of size effects in notched laminates using continuum damage mechanics. *Composites Science and Technology*, 67:2715–2727, 2007.

- [98] D. J. Shim and P. A. Lagace. Damage and delamination characteristics in composite laminates with ply dropoffs under static and cyclic in-plane loads. In E. Armanios and J. Reeder, editors, *Proceedings of the Joint American Society for Composites/American Society for Testing and Materials Comitee D30 - Nineteenth Technical Conference*. American Society for Composites, 2004.
- [99] P. J. Kromwijk, A. W. Blom, and C. S. Lopes. Influence of tow-drop areas on the strength and stiffness of tow-placed, variable-stiffness laminates. In *Proceedings of the American Society for Composites 2007 Conference*, Seattle, WA, USA, October 2007.
- [100] A. W. Blom, C. S. Lopes, P. J. Kromwijk, Z. Gürdal, and P. P. Camanho. A theoretical model to study the influence of tow-drop areas on the stiffness and strength of variable-stiffness laminates. *Journal of Composite Materials*, 43:403–425, 2009.
- [101] P. A. Lagace and K. J. Bonello. Damage accumulation in graphite/epoxy laminates due to cyclic gradient stress fields. *Journal of Reinforced Plastics and Composites*, 12:1111–1135, 1993.
- [102] R. L. Sierakowski and G. M. Newaz. *Damage Tolerance in Advanced Composites*. Technomic Publishing AG, Basel, Switzerland, 1995.
- [103] S. Abrate. *Impact on Composite Structures*. Cambridge University Press, Cambridge, England, 1998.
- [104] S. R. Reid and G. Zhou. *Impact Behaviour of Fibre-Reinforced Composite Materials and Structures*. Woodhead Publishing Limited, Cambridge, England, 2000.
- [105] R. L. Sierakowski. Impact damage-tolerant composite structural design. In S. R. Reid and G. Zhou, editors, *Impact Behaviour of Fibre-Reinforced Composite Materials and Structures*, pages 106–132. Woodhead Publishing Limited, 2000.
- [106] M. Thomas. How damage tolerance issues on spacecraft composite structures can take advantage of experience gained through aircraft programmes. In *European Conference on Spacecrafts Structures, Materials and Mechanical Testing*, Toulouse, France, 2002.
- [107] H. Razi and S. Ward. Principles for achieving damage tolerant primary composite aircraft structures. In *11th DoD/FAA/NASA Conference On Fibrous Composites in Structural Design*, Fort Worth, TX, USA, August 1996.
- [108] P. A. Lagace and E. Wolf. Impact damage resistance of several laminated material systems. *AIAA Journal*, 33(6):1106–1113, 1995.
- [109] W.J. Cantwell and J. Morton. The impact resistance of composite materials - a review. *Composites*, 22:347–362, 1991.
- [110] E.F. Dost, L.B. Ilcewiz, W.B. Avery, and B.R. Coxon. Effects of stacking sequence on impact damage resistance and residual strength for quasi-isotropic laminates. In T.K. O'Brien, editor, *Composites Materials: Fatigue and Fracture*, volume 3, pages 476–500. American Society for Testing and Materials, 1991. ASTM STP 1110.



- [111] L.H. Strait, M.L. Karasek, and M.F. Amateau. Effects of stacking sequence on the impact resistance of carbon fiber reinforced thermoplastic toughened epoxy laminates. *Journal of Composite Materials*, 26(12):1725–1740, 1992.
- [112] E. Fuoss, P.V. Straznicky, and C. Poon. Effects of stacking sequence on the impact resistance in composite laminates - Part 1: Parametric study. *Composites Structures*, 41:67–77, 1998.
- [113] E. Fuoss, P.V. Straznicky, and C. Poon. Effects of stacking sequence on the impact resistance in composite laminates - Part 2: Prediction method. *Composites Structures*, 41:177–186, 1998.
- [114] C. S. Lopes, O. Seresta, M. Abdalla, Z. Gürdal, B. Thuis, and P. P. Camanho. Stacking sequence dispersion and tow-placement for improved damage tolerance. In *Proceedings of the AIAA/ASME/ASCE/AHS/ASC 49th Structures, Structural Dynamics and Materials Conference*, Schaumburg, IL, April 2008. AIAA 2008-1735.
- [115] C. S. Lopes, O. Seresta, Z. Gürdal, P. P. Camanho, and B. Thuis. Impact behaviour of dispersed stacking sequence laminates. Part I: Experiments. *Composites Science and Technology*, 69:926–936, 2009.
- [116] Standard test method for measuring the damage resistance of a fibre-reinforced polymer matrix composite to a drop-weight impact event. Technical report, American Society for Testing and Materials (ASTM), West Conshohocken, PA, USA, 2005. ASTM D 7136/D 7136M-05.
- [117] Fibre reinforced plastics - determination of compression strength after impact. Technical report, Airbus Test Method (AITM), Blagnac, France, 2005. AITM1-0010.
- [118] G. A. Schoeppner and S. Abrate. Delamination threshold loads for low velocity impact on composite laminates. *Composites Part A: Applied Science and Manufacturing*, 31:903–915, 2000.
- [119] P. O. Sjöblom, T. M. Hartness, and T. M. Cordell. On low-velocity impact testing of composite materials. *Journal of Composite Materials*, 22(1):30–52, 1988.
- [120] E. J. Herup and A. N. Palazotto. Low-velocity impact damage initiation in graphite/epoxy/nomex honeycomb-sandwich plates. *Composites Science and Technology*, 57(12):1581–1598, 1997.
- [121] Standard test method for compressive residual strength properties of damaged polymer matrix composite plies. Technical report, American Society for Testing and Materials (ASTM), West Conshohocken, PA, USA, 2005. ASTM D 7137/D 7137M-05.
- [122] C. S. Lopes, Z. Gürdal, P. P. Camanho, P. Maimí, and E. V. González. Simulation of low-velocity impact damage on composite laminates. In *Proceedings of the AIAA/ASME/ASCE/AHS/ASC 50th Structures, Structural Dynamics and Materials Conference*, Palm Springs, CA, May 2009.
- [123] C. S. Lopes, P. P. Camanho, Z. Gürdal, P. Maimí, and E. V. González. Impact behaviour of dispersed stacking sequence laminates. Part II: Numerical simulations. *Composites Science and Technology*, 69:937–947, 2009.

- [124] A. Turon, P. P. Camanho, J. Costa, and C. G. Dávila. A damage model for the simulation of delamination in advanced composites under variable-mode loading. *Mechanics of Materials*, 38:1072–1089, November 2006.
- [125] F. Aymerich, F. Dore, and P. Priolo. Prediction of impact-induced delamination in cross-ply composite laminates using cohesive interface elements. *Composites Science and Technology*, 68:2383–2390, 2008.
- [126] V. Tita, J. Carvalho, and D. Vandepitte. Failure analysis of low-velocity impact on thin composite laminates: Experimental and numerical approaches. *Composites Structures*, 83:413–428, 2008.
- [127] E.V. González, P. Maimí, A. Turon, P. P. Camanho, and J. Renart. Simulation of delamination by means of cohesive elements using an explicit finite element code. *Computers, Materials and Continua*, 9:51–92, 2008.
- [128] M. L. Benzeggagh and M. Kenane. Measurement of mixed-mode delamination fracture toughness of unidirectional glass/epoxy composites with mixed-mode bending apparatus. *Composites Science and Technology*, 56:493–449, 1996.
- [129] P. P. Camanho, C. G. Dávila, and M. F. de Moura. Numerical simulation of mixed-mode progressive delamination in composite materials. *Journal of Composite Materials*, 37(16):1415–1438, August 2003.
- [130] J. H. Crews and J. R. Reeder. A mixed-mode bending apparatus for delamination testing. Technical report, NASA, Langley Research Center, Hampton, VA, 1988. NASA/TM-100662.
- [131] C. M. L. Tavares. Fracture of advanced composite materials: Experimental basis for a constitutive model. Technical report, University of Porto Report SMAP, Porto, Portugal, January 2006.
- [132] A. Turon, C. G. Dávila, P. P. Camanho, and J. Costa. An engineering solution for using coarse meshes in the simulations of delamination with cohesive zone models. *Engineering Fracture Mechanics*, 74:1665–1682, 2007.
- [133] A. Turon, J. Costa, P. P. Camanho, and P. Maimí. Analytical and numerical investigation of the length of the cohesive zone in delaminated composite materials. In P. P. Camanho, C. G. Dávila, S. T. Pinho, and J. J. C. Remmers, editors, *Mechanical Response of Composites*, pages 77–97. Springer, 2008.
- [134] N. Sung and N.P. Suh. Effect of fiber orientation on friction and wear of fiber reinforced polymeric composites. *Wear*, 53:129–141, 1979.
- [135] J. Schön. Coefficient of friction of composite delamination surfaces. *Wear*, 237:77–89, 2000.
- [136] Q. Bing and C. T. Sun. Effect of transverse normal stress on mode II fracture toughness in fiber composites. In *16th International Conference on Composite Materials*, Kyoto, Japan, June 2007.
- [137] X. Li, S. R. Hallet, and M. R. Wisnom. Predicting the effect of through-thickness compressive stress on delamination using interface elements. *Composites Part A: Applied Science and Manufacturing*, 39:218–230, 2007.

- 
- [138] J. Wang and B. L. Karihaloo. Optimum in situ strength design of composite laminates. Part I: In situ strength parameters. *Journal of Composite Materials*, 30(12):1314–1337, 1996.
- [139] J. Wang and B. L. Karihaloo. Optimum in situ strength design of composite laminates. Part II: Optimum design. *Journal of Composite Materials*, 30(12):1338–1358, 1996.
- [140] J. Andersons and M. König. Dependence of fracture toughness of composite laminates on interface ply orientations and delamination growth direction. *Composites Science and Technology*, 64:2139–2152, 2004.
- [141] M. T. McMahon, L. T. Watson, G. Soremekun, Z. Gürdal, and R. T. Haftka. A fortran 90 genetic algorithm module for composite laminate structure design. *Engineering Computers*, 14:260–273, 1998.
- [142] Z. Gürdal, R. T. Haftka, and P. Hajela. *Design and Optimization of Laminated Composite Materials*. John Wiley and Sons, Inc., New York, NY, 1998.



# Curriculum Vitae

Cláudio Saúl Faria Lopes was born on the 13th of October of 1977 in Leiria, a small town in Portugal. There he completed the basic and secondary education levels.

In 1995, he moved to Lisbon to pursue a higher education in aerospace engineering at Instituto Superior Técnico, a faculty from the Lisbon University of Technology. He spent the 5th year (1999-2000) of his *Licenciatura* degree at the Faculty of Aerospace Engineering from the Delft University of Technology (TU Delft), in The Netherlands, as an Erasmus exchange student.



In the following two years (2000-2002), Cláudio Lopes followed a M.Sc. programme at the aerospace structures group from TU Delft, under the supervision of ir. Tom van Baten and co-supervision of ir. Kees Sudemeijer from DutchSpace B.V. His M.Sc. thesis was on the subject of metal thermal protection systems for space reentry vehicles.

Between March 2003 and June 2004, he worked, as an assistant researcher at the Adhesion Institute from TU Delft, on the certification of bonded joints for commercial airplanes.

For a small period of time between September 2004 and February 2005, Cláudio Lopes worked as a stress analysis engineer at GlobalTechnics B.V., a small aerospace company in The Netherlands.

In March 2005, he enrolled in a Ph.D. programme at TU Delft and University of Porto, in Portugal, under the supervision of prof. Zafer Gürdal and prof. Pedro Camanho. His thesis covers damage and failure of non-conventional composite laminates, a subject he would like to continue investigating in the future.

